Novel Cu(II) complexes bearing N,O-donor heteroaromatic ligands as potential anticancer drugs. A redox-active metallic core

Quim Peña

Universitat Autònoma
de Barcelona

Aix*Marseille
université

Novel Cu(II) complexes bearing *N,O*-donor heteroaromatic ligands as potential anticancer drugs. A redox-active metallic core

Quim Peña
PhD in Chemistry

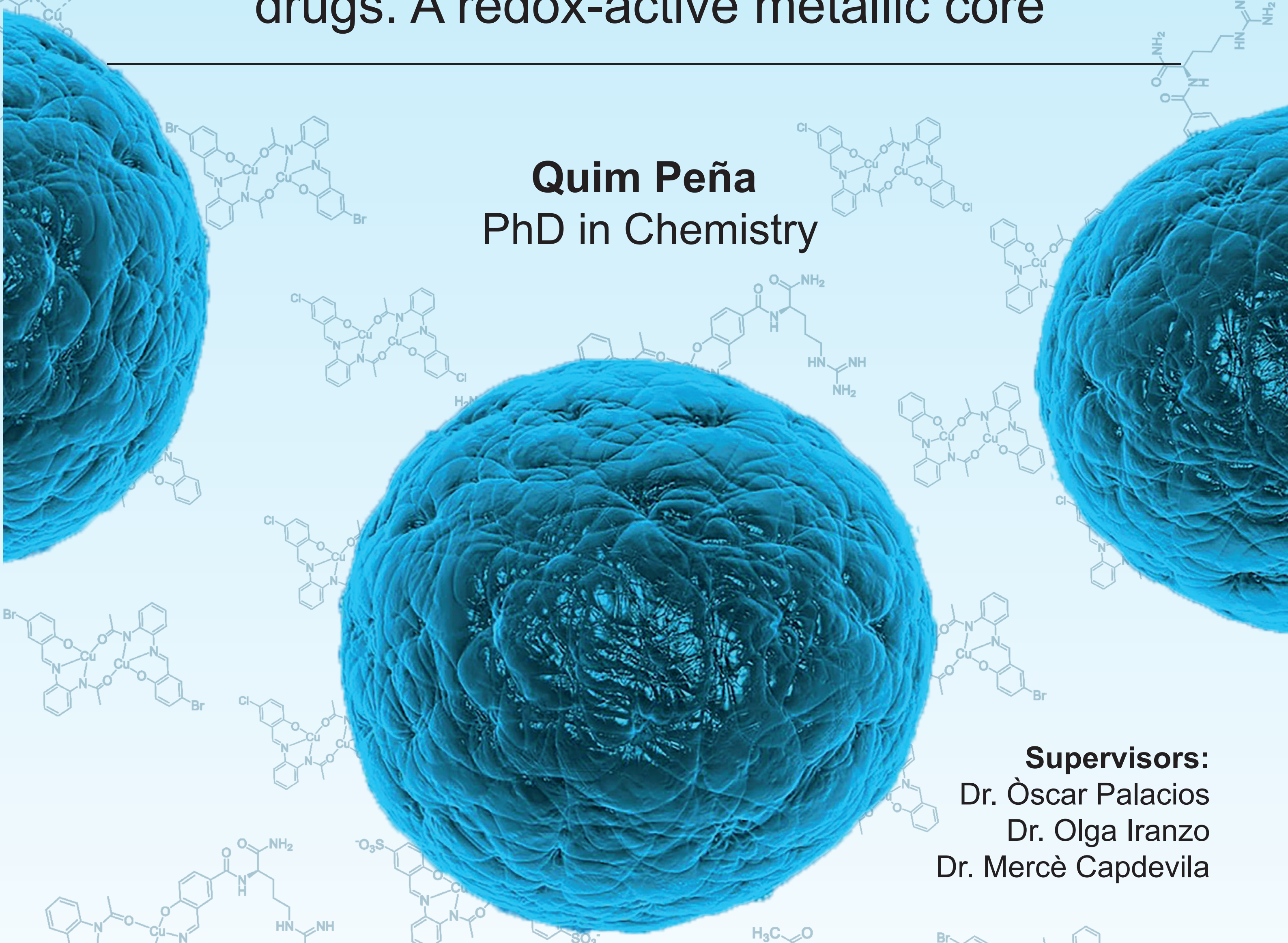

Supervisors:
Dr. Òscar Palacios
Dr. Olga Iranzo
Dr. Mercè Capdevila

2019
PhD Thesis

Universitat Autònoma
de Barcelona

Aix*Marseille
université

Novel Cu(II) complexes bearing *N,O*-donor heteroaromatic ligands as potential anticancer drugs. A redox-active metallic core

Quim Peña
PhD in Chemistry

Supervisors:
Dr. Òscar Palacios
Dr. Olga Iranzo
Dr. Mercè Capdevila

2019
PhD Thesis

Manuscript presented to obtain the PhD Degree by Joaquin Peña Aparicio.

Joaquin Peña Aparicio

With the approval of the supervisors of the Doctoral Thesis entitled “Novel Cu(II) complexes bearing *N,O*-donor heteroaromatic ligands as potential anticancer drugs. A redox-active metallic core”, Dr. Òscar Palacios Bonilla (Universitat Autònoma de Barcelona, UAB), Dr. Olga Iranzo Casanova (Aix-Marseille Université, AMU) and Dr. Mercè Capdevila Vidal (Universitat Autònoma de Barcelona, UAB).

Dr. Òscar Palacios **Dr. Olga Iranzo** **Dr. Mercè Capdevila**

«Toutes les grandes personnes ont d’abord été des enfants, mais peu d’entre elles s’en souviennent.»

-Le Petit Prince-

Antoine de Saint-Exupéry

CONTRIBUTIONS and FINANCIAL SUPPORT

Drs. Òscar Palacios (Universitat Autònoma de Barcelona), Olga Iranzo (Aix-Marseille Université) and Mercè Capdevila (Universitat Autònoma de Barcelona) are kindly acknowledged for the scientific guidance. Quim Peña expresses gratitude to Drs. Pau Bayón (Universitat Autònoma de Barcelona), Julia Lorenzo (Institut de Biotecnologia i Biomedicina) and A. Jalila Simaan (Aix-Marseille Université) for their scientific and experimental support. Drs. Daniel Pulido (CSIC Barcelona) and Míriam Royo (CSIC Barcelona) are also acknowledged for providing the dendritic-based system which has been used in the last part of this work and their scientific advice. Quim Peña also thanks Alejandro García-Torrado and Jordi Bernat Escobairó (Universitat Autònoma de Barcelona), and Sergi Rodríguez-Calado and Sergi Muntaner (Institut de Biotecnologia i Biomedicina) for their experimental support in some synthetic and biological parts of this Thesis work. The *Servei d'Anàlisi Química* and the *Servei de Ressonància Magnètica Nuclear* (at the Universitat Autònoma de Barcelona), and Spectropole facilities (at the Aix-Marseille Université) are kindly acknowledged for allocating instrument time and spectroscopic services. This work was financially supported by the Spanish Ministerio de Ciencia e Innovación and FEDER to the projects BIO2015-67358-C2-2P and CTQ2015-70371-REDT. Quim Peña acknowledges the Ministerio de Educación, Cultura y Deporte for the financial support of a FPU grant and the Ministerio de Ciencia, Innovación y Universidades for the concession of a complementary research stay scholarship. BiosCiences-iSm2 and ED250 (Aix-Marseille Université) are also acknowledged for their support.

TABLE OF CONTENTS

TABLE OF CONTENTS

ABSTRACT

During the last 30 years, Ru, Ir, Pd, Fe or Cu have appeared as promising alternatives to overcome the drawbacks encountered with Pt anticancer compounds. Beyond all of them, and mainly during the last decade, Cu complexes have awakened strong interest as therapeutic agents. Two features make Cu attractive to be used in chemotherapy: its nature as an endogenous metal –which may imply fewer side effects than other exogenous metals- and its Cu(II)/Cu(I) redox pair –which can promote reactive oxygen species (ROS) generation. The production of ROS is not only reported to cause cellular damage, but also to offer a putative discrimination between healthy and non-healthy cells.

On the first part of this thesis work, we report the synthesis, characterization and biological evaluation of a dimeric Cu(II) complex bearing a *N,O*-donor salphen-like ligand ((*E*)-*N*-(2-(2-hydroxybenzylideneamino)phenyl)acetamide, **L1**) specifically designed to promote a fast Cu(II)/Cu(I) redox interconversion. *In vitro* assays outline the high potentiality of the complex to undergo ROS generation inside HeLa cells, and that it shows higher cytotoxicity in cancer than in normal cell lines. Besides, its interactions with some proteins have also been tested, showing that the formed protein-complex adducts do not represent any loss of biological activity respect to the complex itself. From this promising starting point, the Cu(II) complex of **L1** ([Cu(**L1**)]$_2$) serves as the backbone for the synthesis of two *-chloro* and *-bromo* analogs. The presence of electrowithdrawing groups intend to tune the redox behavior of the corresponding Cu(II) complexes, and concomitantly, their ROS generation capabilities. However, one of the main drawbacks faced with these two halogen-derived complexes was their poor solubility and bioavailability. Therefore, several functionalization strategies have been explored to overcome it. The first strategy aimed at increasing the solubility while maintaining the same Cu(II) coordination environment, *i.e.*, the high redox activity observed for the initial [Cu(**L1**)]$_2$ complex. In light of this, a sulfonate group and an Arginine residue have been selected based on their pK_a and biological relevance. Secondly, and in order to enhance the delivery of the complex and the candidacy as future anticancer drug, specific improvement on the cellular uptake -*ergo*, on the cytotoxicity- has been attained by derivatizing [Cu(**L1**)]$_2$ with two specific Arginine-rich Cell-Penetrating Peptides.

Finally, the last part of our work opens the gate to the use of a versatile multimodal dendritic platform as a promising drug carrier. Its potentiality in drug delivery and its copper coordination capabilities have been thoroughly demonstrated. The conjugation approach of the [Cu(**L1**)]$_2$ complex to the platform is also reported as a proof-of-concept of the versatility of this system for future tailor-made anticancer targeted therapies.

SYMBOLS AND ABBREVIATIONS

aa	*Amino acid*
ACN	*Acetonitrile*
ATR	*Attenuated total reflectance*
Boc	*Tert-butyloxycarbonyl group*
β-Ala	*β-Alanine*
CisDDP	*Cis-diamminedichloroplatinum(II)*
CPPs	*Cell-Penetrating peptides*
ct-DNA	*Calf-thymus DNA*
Cyt	*Cytochrome C*
CV	*Cyclic voltammetry*
DCF	*Dichlorofluorescein*
DCFDA	*2',7'-dichlorofluorescin diacetate*
DCM	*Dichloromethane*
DDS	*Drug Delivery Systems*
DIEA	N,N-*diisopropylethylamine*
DMEM	*Dulbecco's Modified Eagle Medium*
DMSO	*Dimethyl sulfoxide*
DMF	N,N-*Dimethylformamide*
DTPA	*Diethylenetriaminepentaacetic acid*
DTPA-5Ac	*Pentaacetylated DTPA-based dendritic monomodal platform*
DTPA-4Ac-NH$_2$	*Tetraacetylated DTPA-based dendritic bimodal platform*
EA	*Elemental analysis*
$E_{1/2}$	*Half-wave potential*
E_{pa}	*Anodic peak potential*
E_{pc}	*Cathodic peak potential*
EPR	*Enhanced permeability and retention*
Eq	*Molar equivalents*
ESR[1]	*Electron spin resonance*
EtOAc	*Ethyl acetate*
EtOH	*Ethanol*
Fc$^+$/Fc	*Ferrocene redox pair*
Fmoc	*Fluorenylmethyloxycarbonyl group*
FTIR or FT-IR	*Fourier-transform infrared spectroscopy*
G	*Glycine (Gly)*
GSH	*Glutathione*
GSSG	*Glutathione disulfide*
HBTU	N,N,N′,N′-*Tetramethyl-O-(1*H-*benzotriazol-1-yl)uronium hexafluorophosphate*
HEPES	*2-[4-(2-hydroxyethyl)piperazin-1-yl]ethanesulfonic acid*
HR ESI-MS	*High resolution electrospray ionization mass spectrometry*
HSA	*Human Serum Albumin*
IC_{50}	*Inhibition concentration of 50% of cell population*

---

[1] *Also named Electron Paramagnetic Resonance (EPR). The ESR abbreviation will be used along this work to avoid confusion with the "Enhanced Permeability and Retention" (EPR) effect.*

i_p	*Intensity of the peak*
K	*Lysine (Lys)*
K_{app}	*Apparent binding constant*
K_b	*Binding constant*
K_{COND}	*Conditional (or effective) binding constant*
m/z	*Mass per charge ratio*
MeOH	*Methanol*
MLCT	*Metal-to-ligand charge transfer*
MOM	*Methoxymethyl ether*
MS	*Mass spectrometry*
Myo	*Myoglobine*
NMP	N-*methyl-2-pyrrolidone*
NMR	*Nuclear magnetic resonance*
Pbf	*2,2,4,6,7-Pentamethyldihydrobenzofuran-5-sulfonyl group*
PEG	*Polyethylene glycol*
PI	*Propidium iodide*
QTOF	*Quadrupole coupled with time-of-flight detector*
Q	*Glutamine (Gln)*
R	*Arginine (Arg)*
ROS	*Reactive oxygen species*
ScdsDNA	*Supercoiled double-strand DNA*
SOD	*Superoxide dismutase*
SPPS	*Solid-phase peptide synthesis*
TAT	*Transactivator of transcription*
TBAP	*Tetrabutylammonium hexafluorophosphate*
TFA	*Trifluoroacetic acid*
TIS	*Triisopropylsilane*
TRIS	*Trisaminomethane*
Trt	*Trityl (triphenylmethyl) group*

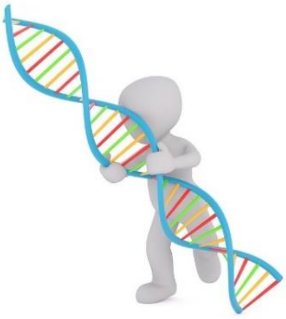

CHAPTER 1
Introduction

This chapter intends to gather the existing literature regarding Medicinal Inorganic Chemistry in cancer therapy to help the reader to get into the topic and fully comprehend the research presented in the following chapters. It describes an overview of the field and details the advances in chemotherapy, specially in the field of Cu(II) complexes since the discovery of cisplatin.

CHAPTER 1

Introduction

1.1 Cancer. A widespread disease

Cancer is a widespread disease, affecting people from all around the world. It is defined as an abnormal growth of healthy cells, which spread out on the neighbor tissues and organs, impairing their normal functioning.[1]

According to what the World Health Organization (WHO) estimates, cancer is the first or second leading cause of death before age of 70 years in 91 of 172 countries in the 21st century.[1] It also ranks third or fourth in 22 additional countries. Cancer incidence and mortality are rapidly increasing in the world, basically due to aging and population growth factors.[2] The majority of cancers belongs to three main classes: carcinomas, sarcomas and leukemia. However, 90% of the human cancers registered until 2000 were classified under the genre of carcinomas, being then epithelial cell malignancies the most abundant type of cancer in the world.[3] According to the American Cancer Society, around 500,000 people died in the United States from cancer in 2000.[4] Only 15 years later, in 2015, the number of deaths rise up to about 600.000,[5] underlying the impact of this disease in life expectancy of world population and the need for research in cancer treatment.

1.2 Tumor and cancer. The angiogenic cascade

The term *tumor* is not synonymous with cancer.[6] Tumor can be benign, premalignant or malignant, whereas a cancer is defined by itself as malignant. Benign tumors can be removed by surgery; malign ones normally require the application of radiotherapy, chemotherapy, surgery and other more sophisticated techniques. A tumor is defined as a neoplasm characterized by a failure in the regulation of tissue growth. As an ancillary proposition, it is noteworthy to state that tumors are more than just insular masses of uncontrollable proliferating cancer cells. Instead, they are considered complex tissues composed of several distinct cell types that participate in heterotypic interactions with one to another.[6,7]

The abnormal proliferation of the tissues is originated by gene mutations.[6,8,9] These gens fall essentially into two main categories: (i) oncogenes that promote cell growth and reproduction and (ii) tumor suppressor genes that inhibit cell division and survival. What is observed is that cancer primarily develops *via* formation of novel oncogenes, overexpression of regular oncogenes and/or malfunctioning of tumor suppressor genes. Changes in different genes transform what can be considered as a “normal” cell into a “cancer” cell. Several models of multistep tumorigenesis, *via* discrete genetic changes, have been proposed to explain this transformation.[6,8,9] The generation of a tumoral cell is one of the topics that have attracted a lot of research during the last 15 years. In light of this, in 2000 Douglas Hanahan and Robert Weinberg reported 6 underlying principles which intend to explain the complexity of cancer cells transformation.[7] Later on, in 2011, they were updated with two new more.[8] These are the so-called “Hallmarks of Cancer”, which can be summarized as follows:[7,8]

(1) Cancer cells stimulate their own growth (*Self-sufficiency in growth signals*).
(2) They have abnormal metabolic pathways (*Abnormal metabolism*).
(3) Cancer cells resist inhibitory signals that might stop their growth (*Evading growth suppressors*).
(4) They resist their programmed cell death (*Evading apoptosis*).
(5) They can constantly multiply themselves (*Enabling replicative immortality*).
(6) Cancer cells stimulate the growth of blood vessels to supply nutrients to tumors (*Inducing angiogenesis*).
(7) They invade local tissues and spread to distant sites (*Activating invasion and metastasis*)
(8) They evade the immune system.

One of the key steps in tumor propagation is related to the induction of angiogenesis, *i.e.* what is termed “Angiogenic switch”.[9] Angiogenesis can be switched on at different stages of tumor progression, depending on its nature and the microenvironment (**Figure 1.1**). This complex process requires a series of steps: from the dilation of existing vessels until the formation of *de novo* ones around the tumor mass. This cascade of steps is not just a prerequisite for the transformation from a dormant cluster of cancer cells to a solid tumor[2], but also participates in the spread of the mass.[6,9] Therefore, it has logically become one of the targets of interest in cancer therapy nowadays.[10,11]

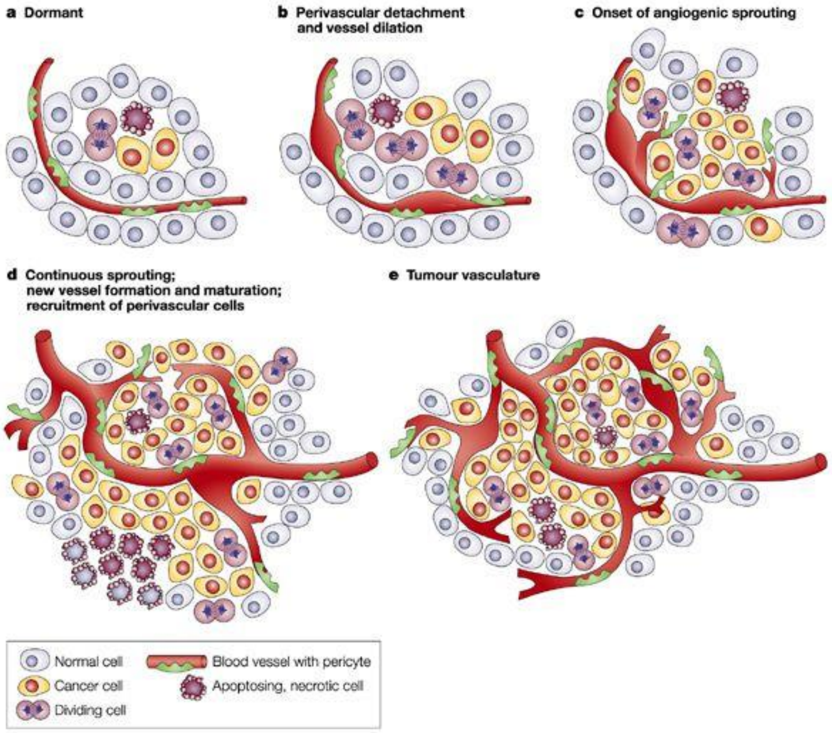

Figure 1.1. Steps of the "angiogenesis cascade" in tumoral cells. Figure from literature.[9]

Special mention must be pointed out also in the metabolism of cancer cells. As commented before, they are characterized by showing abnormal metabolic processes. In this regard, fully comprehension of the metabolic pathways ongoing in tumoral cells might provide useful information for future treatments. In contrast to normal differentiated cells, which rely on mitochondrial oxidative phosphorylation to primarily generate the energy required, most cancer cells do it on aerobic glycolysis instead. This phenomenon is known as the “Warburg effect”.[12,13] In the presence of oxygen, most differentiated cells firstly metabolize glucose to CO_2 by oxidation of glycolytic pyruvate in the mitochondrial tricarboxylic acid (TCA) cycle. The product of this reaction, NADH, undergoes an oxidative phosphorylation to maximize ATP production, with minimal formation of lactate. Only under anaerobic conditions, differentiated normal cells generate large amounts of lactate. Nonetheless, most cancer cells produce mainly lactate products regardless of the availability of oxygen. This “aerobic glycolysis” is in fact an inefficient way to generate ATP, but it seems to be the preferred pathway to obtain the energy for cancer cells. The idea arises from the fact that the metabolism of cancer cells is adapted to facilitate the

---

[2] *According to National Cancer Institute (NIH, www.cancer.gov), solid cancers are defined as abnormal cellular growths that do not usually contain cysts or liquid areas, such as in breast, prostate, etc. These types of cancer are different from those found in blood like leukemia.*

incorporation and uptake of nutrients into the biomass in a conducive manner to cell proliferation rather than efficient ATP generation.[12] It was firstly thought that mitochondria developed a defect that led to glycolysis.[14] However, it was latterly proven that the mitochondrial function was normal and that it was not the cause of the metabolic change, yet not fully understood.[15,16]

This elevated glucose metabolism, and the subsequent generation of lactate, cause an increase of the concentration of protons in the tumor environment. This leads to a pH decrease in and around the tumoral cells. Moreover, the Warburg Effect has also implications in the mitochondrial redox potential, affecting the homeostasis of reactive oxygen species (ROS) inside these cancer cells. pH and ROS levels are differentiating factors between normal and cancer cells. This issue might arise as an important factor to consider in cancer therapy.[13]

1.3 The era of chemotherapy

Chemotherapy is one of the main strategies to cure cancer. Paracelsus was a pioneer in the application of chemicals and minerals in medicine and one of the firsts talking about Chemotherapy, even before the discipline itself existed in the medical community. He wrote a theorem in the 16th century where he mentioned: “How can I treat and hopefully cure a cancer patient with a drug at a nontoxic or acceptable dose without the risk of conversely overdosing and risking severe side-effects or even the death of my patient?”.[17] The use of chemotherapy to treat this disease basically started at the beginning of the 20th century. A summary of the different advances achieved by this discipline since it began is depicted in **Figure 1.2**.[18] The term “Chemotherapy” was coined and defined by Paul Ehrlich in the early 1900s. It was originally defined by him as ‘the use of drugs to injure an invading organism without affecting the host’, similar to what Paracelsus already reported 400 years earlier.[19] Ehrlich was also the first person to document the effectiveness of animal models to screen chemicals for their potential activity against diseases. His research was focused on drugs like alkylating agents and aniline dyes to treat cancer but he is indeed well-known for the discovery of the arsenical drug Salvarsan in the treatment of the syphilis.[19,20] Some years later, the use of sulfur mustards (mustard gas) in the World War I and II led to the observation that mustard compounds may offer therapeutic effects on lymphomas.[21] Nitrogen mustard was rapidly used for lymphomas after the work of Gustaf Lindskog in 1946. The activity of this compound (together with the discovery of other drugs like methotrexate) provided an upsurge of new synthetic drugs in addition of alkylating agents and antifols.[18]

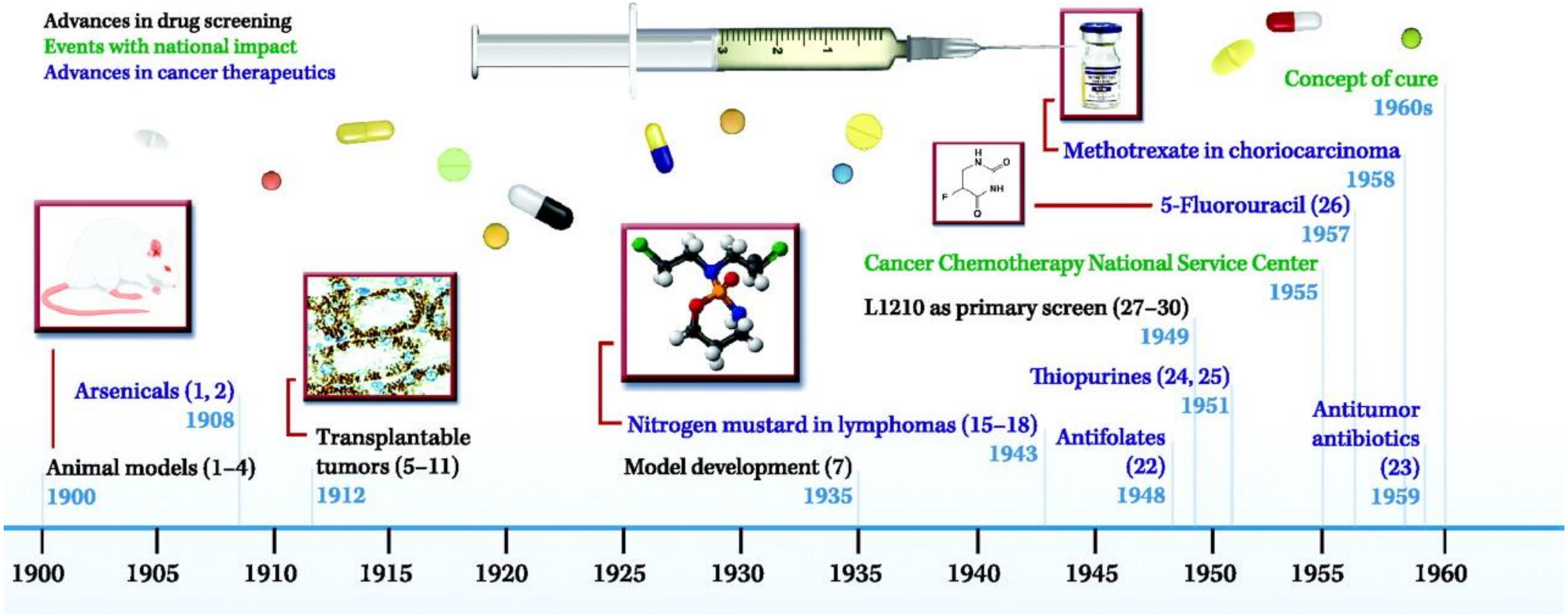

Figure 1.2A. Breakthroughs in the history of chemotherapy from 1900 till the 1960s. Figure from literature.[18]

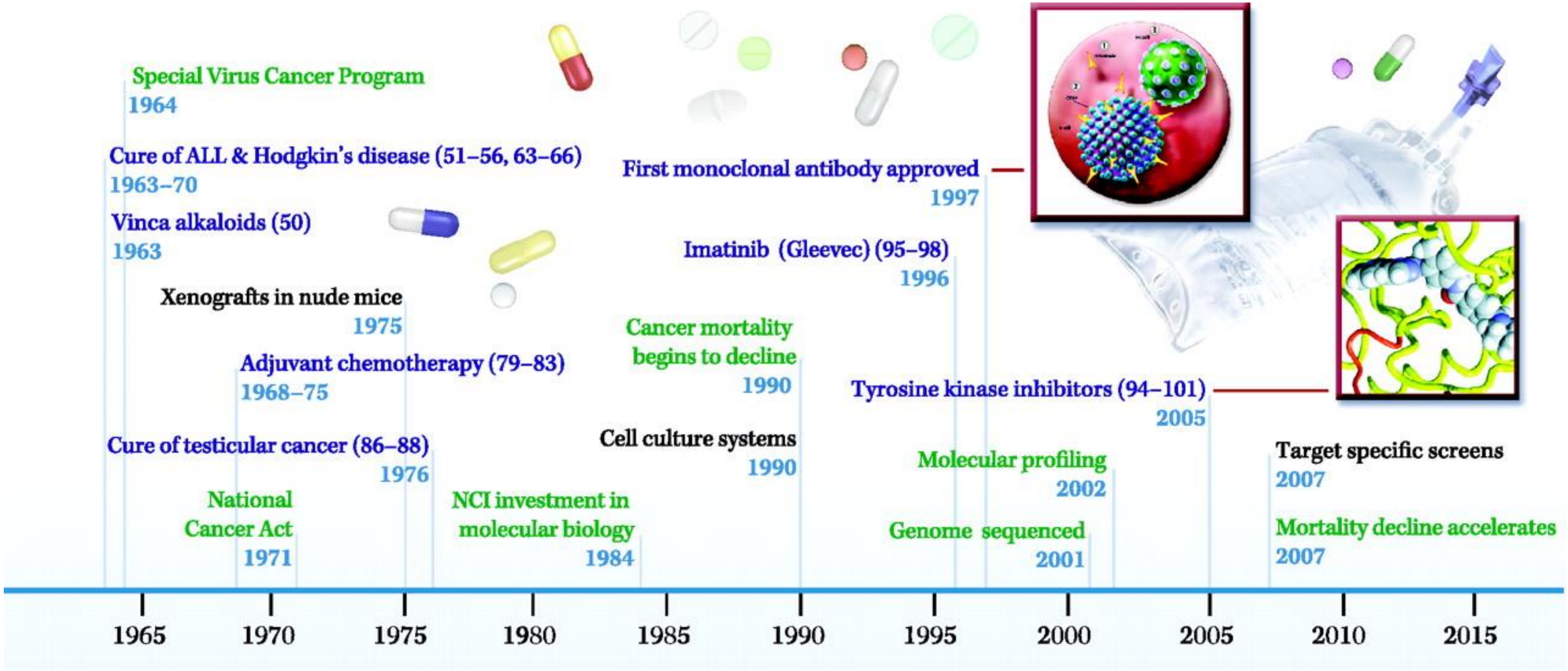

Figure 1.2B. History of Chemotherapy in the last 50 years. Figure from literature.[18]

However, surgery and radiotherapy dominated the field of cancer therapy until the 1950s. The observation that cure rates had plateaued at about 33% showed that combination of these therapies with chemotherapy could cure advanced cancers in a more efficient manner. However, chemotherapy as a real strategy gained relevance in the 1950s, after alkylating agents, antimetabolites and Pt compounds proved to be effective against hematological malignancies and certain solids tumors.[6] From that point on, many progresses were made in this field. Special mention is awarded by the 1970s -the Age of Adjuvant Chemotherapy- and after the 1990s, with the transition into the era of the so-called “targeted therapy”.[18]

1.3.1 The use of metals in chemotherapy. The serendipitous discovery of cisplatin

Metals can offer an enormous versatility and a vast myriad of properties to be tuned. The history of metals in medicine dates back to the most ancient times of recorded history.[20,22,23] As mentioned, the 20th century saw metals making a strong impact on Medicinal Chemistry with the discovery of the organometallic drug Salvarsan, by Paul Ehrlich. Despite “metal potions” -“magesterium bismuti”, gold flakes in suspension, etc. - had been used since long for therapeutic purposes,[24] the discovery of cisplatin and its incredible properties represented a milestone in the history of the use of metal-complexes in cancer treatment. This propelled Medicinal Inorganic Chemistry to the front of the fight against cancer.

Cisplatin (**Figure 1.3**) was serendipitously discovered in 1965 by Barnett E. Rosenberg and Loretta Van Camp,[25] when they were applying some electric current to cultures of *E.coli* bacteria, observing the inhibition of cell division due to the formation of a platinum substance that derived from the platinum electrode. The compound was found out to be *cis*-diamminedichloroplatinum(II) (CisDDP or cisplatin), which was rapidly tested and administered to the first patients less than ten years later. Hilary Calvert, a doctor of the UCL Cancer Institute at the University College of London, related how he was asked in 1972 for cisplatin by a patient suffering from ovarian cancer. She was one of the first people administered with the Pt complex, only after 7 years of the discovery of its properties. “The patient vomited profusely and went into renal failure, but her ovarian cancer melted away” said the doctor.[26]

From that starting point, cisplatin became one of the most outstanding advances in chemotherapy and in the fight against cancer. Since then, many efforts have been devoted to create new metal-based drugs, based on cisplatin structure like carboplatin (**Figure 1.3**). Combining both -metal ions and ligands- provides further possibilities in drug design, thus allowing to treat more and more specifically different types of cancer. Nowadays, metal-based drugs, in contrast to purely organic compounds, have further and more varied properties to be tuned in order to attain the desired function. The versatility of metals (several oxidation states, different coordination environments, etc.) offers a broader spectrum of options to modulate and work with.[27]

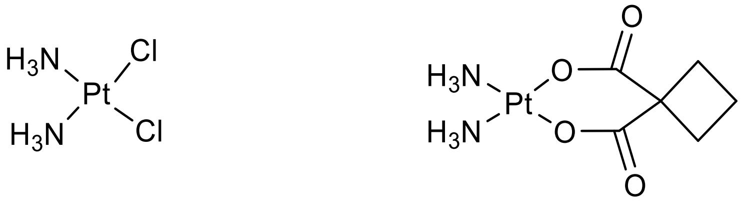

Cisplatin **Carboplatin**

Figure 1.3. Structure of two of the first platinum anticancer drugs and, nowadays ones of the most widely used: cisplatin and the second-generation Pt drug carboplatin, approved for clinical use in 1978 and 1986, respectively.[20]

The overwhelming reactivity of Pt in treating many solid cancers, the evidence that the interaction between Pt and DNA is crucial to undergo cell death and, the inexistence of an organic compound showing the same lesion degree as platinum, heralded a new era to the use of metal ions and their related complexes for anticancer purposes.[28]

Cisplatin toxicity is mainly attributed to the covalent adducts formed preferentially with guanine N7 residues in DNA (**Figure 1.4**).[29] When Pt anchors DNA, the latter is strongly altered to accommodate the platinated lesion. However, no fully comprehension of the lesion mode of Pt-drugs has been achieved yet. In any case, DNA was then considered as one of the main targets in chemotherapy in that moment. Indeed, it is known as a big ligand with many coordination sites.[30] The resolution of the crystal structure of Pt-DNA adducts and the Pt-DNA NMR studies, where Pt was observed to bind the guanine residues, confirmed DNA as the main target. All of this, stimulated the design of cisplatin-like compounds with the ability of entering the cell, going to the nucleus and showing DNA reactivity. In the case of cisplatin, the proposed mechanism is based on the hydrolysis of the complex as the crucial step to activate the drug and to enhance its affinity towards DNA (**Figure 1.4**).

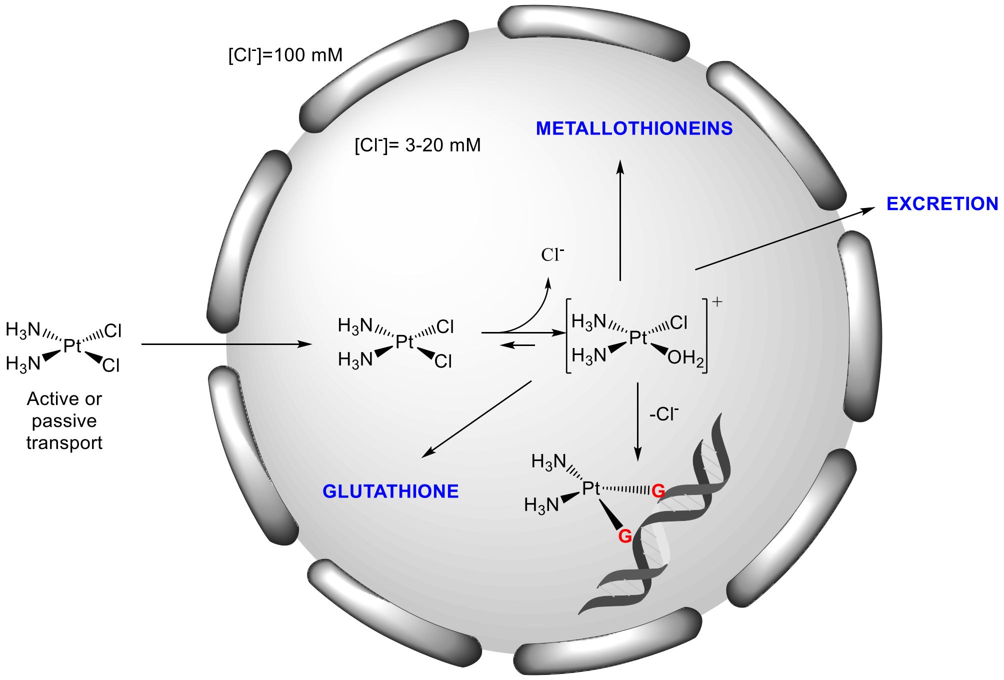

Figure 1.4. Cisplatin mechanism of internalization and interaction inside the cell with biomolecules.

Putative Pt-drugs were widely synthesized and assayed after the discovery of cisplatin due to their high toxicity and they are still a hot topic of research nowadays.[31–37] Nevertheless, they are not generally characterized by offering specificity towards cancer cells. In fact, their effect relies on the antiproliferative activity shown both in normal and affected tissues. Furthermore, the strong affinity of platinum drugs towards other biomolecules apart from DNA has been demonstrated, retaining the compound into the blood stream.[38,39] Intracellular sulfhydryl biomolecules such as glutathione (GSH) and metallothioneins (MTs) have been reported to react and bind Pt in some cases, preventing some Pt-drugs from reacting with the intracellular targets.[40] Therefore, their toxic side-effects, their strong interaction with biomolecules (proteins and non-proteins)[39,41,42] and the resistance observed in many other kind of cancers,[40,43–45] triggered the exploration of new approaches: the use of other metal ions in chemotherapy,[20,46,47] novel Pt(IV) prodrugs[3],[48–50] improved targeted drug delivery,[51] and new photochemotherapeutic agents for light-driven therapies.[33,52–54]

One of the strategies mentioned above is devoted to the use of Pt(IV) complexes. They are recognized as promising anticancer agents since the last decade.[50] Their higher stability, inertness and expanded coordination sphere act as an inherent advantage to overcome the side-effects encountered with the Pt(II) compounds. The six

---

[3] *A prodrug is known as an inactive drug that after a chemical modification inside the body, either on the ligand or on the metallic centre, becomes active, and shows cytotoxic activity.*

saturated sphere of low spin d^6 octahedral geometries makes the Pt(IV) complexes less reactive towards biomolecules than those of Pt(II) and, thus, with higher efficiency in cancer cells. There, Pt(IV) prodrugs are reduced -biologically or with an external stimulus- into an active Pt(II) complex. This is, in fact, the species which causes the damage into cells.[48,52]

1.3.2 Overcoming the Pt drawbacks. The use of exogenous non-Pt metals in cancer

In order to reduce the undesired side-effects and the acquired resistance of some tumors to Pt compounds, Pd, Ru, Rh, Au, Ti and Ir, among others, appeared as promising alternatives after the 1970s. During the last 40 years, several non-Pt based complexes (some of them currently under clinical trials), have been designed and synthesized in order to overcome the problems found with the Pt-drugs.[47,55–61] **Figure 1.5** provides an overview of some representative reported non-Pt anticancer complexes, surpassing the Pt paradigm and demonstrating that Medicinal Inorganic Chemistry has still many things to offer within cancer treatment.[62]

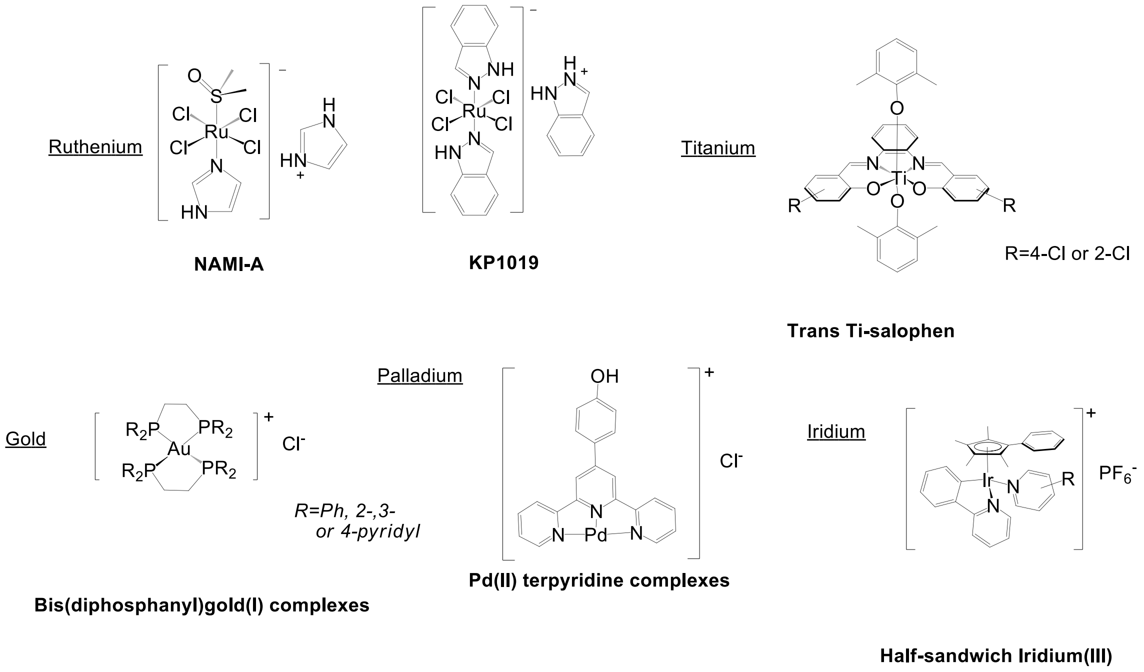

Figure 1.5. Non-Pt based anticancer drugs. Ruthenium based drugs in clinical trials: NAMI-A[63] and KP1019. Salen-Ti(IV) complexes (Trans Ti-salophen) have shown efficient antitumor activity.[64] A bis-chelated phosphine gold(I) complex has been reported to selectively induce apoptosis.[65] Pd(II) terpyridine complexes, such as that water-soluble reported by Darabi *et al.*, exhibits greater cytotoxicity than cisplatin.[66] Organoiridium compounds (a half-sandwich Iridium(III) complex) have demonstrated high antiproliferative activity and to be even more potent than the clinical drug cisplatin.[67]

One of the first metals whose anticancer properties were assessed was Pd. The significant similarities between Pt(II) and Pd(II) triggered the interest of the latter as potential anticancer agent. Pd(II) compounds exchange ligands 10^4-10^5 times faster than the respective Pt compounds. This feature has made them also interesting to be used in chemotherapy, expecting higher reactivity.[34,60,61] However, similar dose-limiting side-effects, as the ones observed for Pt compounds, have been witnessed.

Another largely studied non-Pt metal in cancer treatment has been Ru. This transition metal has a kinetic spectrum of ligand exchange similar to that found for Pt(II), but with a higher number of available and biologically tunable oxidation states (Ru(II), Ru(III) and Ru(IV)).[19] Contrarily to Pt, Ru has attained successful results in the treatment of metastatic cancers, specially two Ru compounds, now under current clinical trials: NAMI-A[63] and KP1019 (**Figure 1.5**), which represented an important breakthrough in the development of metal-based drugs. Dyson, Sadler, Hartinger *et al.* developed some structure-activity relationships for Ru complexes bearing arene, *p*-cymene, cyclopentadienyl and ethylenediamine ligands.[68–71] Current research on this field is highly devoted to light-sensitive Ru compounds. Indeed, and perhaps unexpectedly, the main actor of this issue during the last decade has been light. An increasing number of scientists are focusing their research into the interactions of metal complexes -mainly Ru(II)- with light to control their activity. Several Ru(II) polypyridyl or porphyrin complexes have shown photoinduced promising anticancer activity.[52,72–74]

Whereas both Ru and Pt appear to have the same target (DNA), Ti[62,64,75] and Au[59,65,76] have been reported to show multiple ones such as thioredoxin reductase (TrxR) or mitochondria. Iridium, by its turn, and particularly organoiridium complexes, as the one depicted in **Figure 1.5**, have been reported to exhibit high antiproliferative activity.[64,77] Owing to their fine-tuning control of the coordination sphere, they are able to modulate the production of ROS inside cells. They are reported to damage DNA and mitochondria with high cytotoxic effect.

1.3.3 Endogenous metals in cancer therapy. Towards a softer chemotherapy era

Biological systems have many excretion pathways in order to remove non-beneficial or toxic substances from our body. Several biomolecules such as metallothioneins (MTs) or glutathione show affinity towards metal ions and act by excreting and controlling the amount of toxic and non-toxic metals inside the organisms.[78] For these reasons, Pt and the recent exogenous non-Pt drugs are normally rapidly released and excreted from the body, diminishing effectivity or not reaching the desired target. As a consequence, side-effects (nephrotoxicity, haematogenesis, hepatoxicity, etc.) are still witnessed. Last tendencies in chemotherapy are driving research towards endogenous metals. They offer an advantage in terms of lower intrinsic toxicity and bioavailability, leading to what is called “softer chemotherapy”. In this regard, Fe and Cu have attracted increasing interest to be used in cancer therapy, mainly due to their endogenous nature.[79–85]

Regarding Fe, both Fe(II) and Fe(III) complexes have been synthesized exhibiting anticancer properties, mainly during the last 15 years.[85–88] The anticancer potency of iron complexes was firstly encountered in ferrocenium picrate and ferrocenium trichloroacetate salts in 1984.[89] It was attributed to the formation of ROS, giving rise to oxidative DNA damage. Phototoxic and redox-active iron complexes have also recently shown an interesting cytotoxicity in order to seek for a selective therapy.[86–88] However, and despite the growing interest of Fe in chemotherapy, Cu has been by far more exploited in this field during the last 20 years. This will be detailed in *Section 1.3.3.2*.

1.3.3.1 Copper and its biological role

About 4.6 billion years ago, at the beginning of life and before the rise of O_2 in the atmosphere, Fe(II) was the main metallic ion in primitive oceans and involved in redox and electronic transfer reactions in biological systems. Later, after the rise of oxygen into the atmosphere, Fe(II) reacted to form Fe(III), which precipitated as oxides. Conversely, Cu became more soluble thanks to this oxidizing environment. Cu(I) was oxidized into Cu(II), which was then more available for living organisms. This led to the “copper/iron age”, where both metals shared an important role in biological processes. This drastic change in O_2 and metal bioavailability -prototypically exemplified by Fe(II) and Cu(I)- constrained early life forms to adapt, detoxify, etc. This feature made organisms adapt to different metals homeostasis.[90]

Copper is an essential biometal, being widely present in many biomolecules and playing a remarkable role in a diversity of biochemical processes, partially due to its interesting Cu(II)/Cu(I) redox pair.[91–93] It has two main oxidation states: Cu(I) and Cu(II), each one modulating the affinity towards ligands: Cu(I) is a softer Lewis acid than Cu(II) and displays higher affinity towards ligands with softer donor atoms, such as S or P. With a d^{10} configuration, it shows no *d-d* transition bands in UV-VIS, is ESR[4] silent and

---

[4] *Electron Spin Resonance (ESR) will be used along this work to refer to Electron Paramagnetic Resonance (EPR) technique, whose abbreviation, despite being more extensively used, can confuse the reader with the Enhanced and Permeability Retention (EPR) effect.*

typically adopts trigonal or tetrahedral coordination environments. Cu(II), instead, is preferentially coordinated by harder donor atoms (typically N, O) in square-planar derived or octahedral geometries. It has a d^9 electronic configuration, intense *d-d* transitions at around 600 nm and characteristic ESR signals.[94]

Cuproproteins carry out several functions (as electrons transferases, reductases, oxidases, etc.) and can be generally classified into four basic types (**Table 1.1**):[30,95–97]

- Type I (Electron transfer): copper is normally coordinated by three inert ligands (two His and one Cys) and one or two labile ligands (Met) in a distorted tetrahedral coordination. Type I Cu centers have a coordination environment which does not suit either for Cu(I) or for Cu(II). It is indeed close to the transition state between Cu(I)-Cu(II). This is the so-called *entatic state*, which favors a fast and efficient electronic transfer. They are commonly known as “Blue Copper Proteins” due to its characteristic blue color. One example is Plastocyanin.

- Type II (Catalysis, redox): copper is coordinated by 4 N_{His} in a rather square-planar configuration, exhibiting available coordinating positions and characteristic ESR spectrum. Type II Cu centers generally control de generation and elimination of ROS. The most common are the oxidoreductases, like Superoxide Dismutase (SOD).

- Type III (O_2 transport): dinuclear copper antiferromagnetically coupled centers, each one coordinated by three histidines with a bridging ligand (oxygen or hydroxyl anion). Hemocyanin is one of the prototypical examples of this class of Cu centers.

- Cu$_A$ (Electron transfer): dinuclear copper center with mixed valence, coordinated by histidines and two bridging ligands (cysteines). Axial donor atoms O, S complete the coordination spheres of this particular Cu center found only in Cytochrome C oxidase, in a subunit of this big protein.[97]

-

Table 1.1. Classification of the Cu centers in biomolecules regarding the coordination features metal.[30,95–97]

TYPE I (mononuclear)	TYPE II (mononuclear)	TYPE III (dinuclear)	Cu$_A$ (dinuclear)
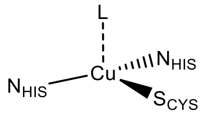 *L=Met*	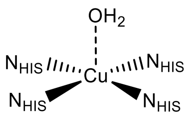	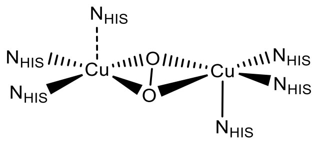	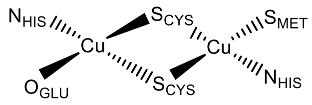

Metals playing crucial roles in many metabolic processes, like copper, are present at trace levels in living systems. The concentration of free copper has to be kept low since changes in the disruption of the homeostasis of copper are responsible for some disorders such as the Wilson and Menkes disease.[98] As a consequence, the levels of copper are highly controlled inside and outside the cell. As highlighted in **Figure 1.6**, several metalloproteins regulate its amount and control the well-functioning of the cell and of the organism in general. This is important to be considered when designing compounds with potential anticancer purposes, and has to be taken into account to improve their pharmacokinetics.

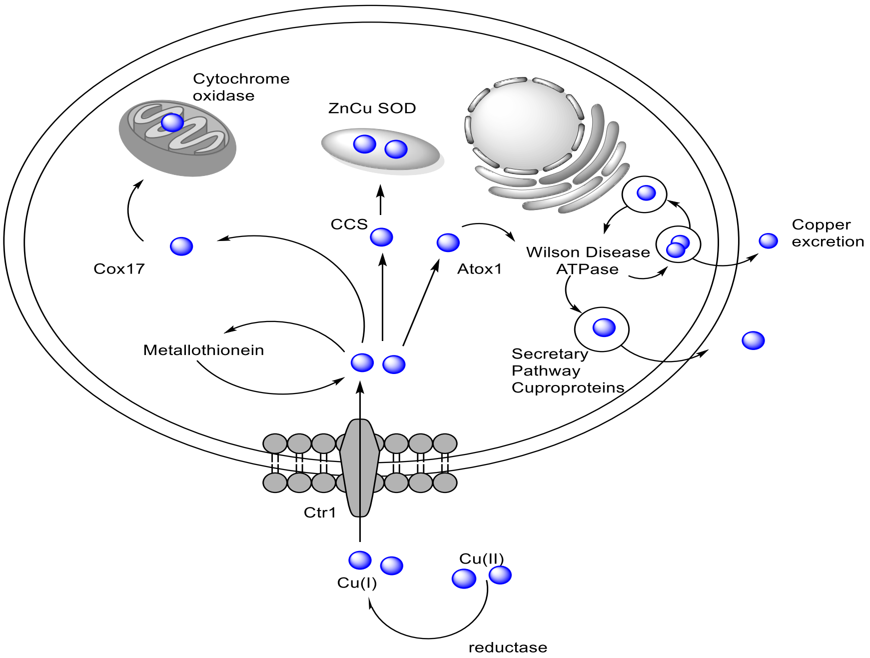

Figure 1.6. Trafficking of Cu inside a mammalian cell, where the three principal copper chaperons (Cox17, CCS and Atox1) deliver it to its targets (Cytochrome Oxidase, Superoxide Dismutase (SOD), and the Wilson and Menkes transporting ATPases). Notice the previous reduction of Cu(II) into Cu(I) to enter into the cell *via* the Ctr1 transporter. Cuproproteins and vesicular pathways excrete the excess of copper inside the cell. Metallothioneins also regulate the amount of copper storing it in the form of Cu(I)-MT since free copper is toxic. Figure adapted from the work published by Bartnikas and Gitlin.[99]

1.3.3.2 Copper in cancer treatment

Experimental evidence has established a strong connection between copper and both the development and progression of cancer. Some studies have placed Cu as a central modulator of normal and malignant angiogenesis. First, the pro-angiogenic role of copper is mediated through various specific pathways.[100–102] Furthermore, this metal can also influence the capacity of cancer cells to invade surrounding tissues and to spread to distant organs (metastasis). Therefore, recognizing that copper serves as a limiting factor for many aspects of tumor growing and progression has encouraged the development of copper complexes as therapeutics and, thus, several interesting and attractive anticancer strategies that target copper have also appeared.[80,81,84,103–105]

In this scenario, anticancer Cu complexes have been reported to be strictly classified into two general groups: (i) copper chelators and (ii) copper ionophores.[106] The firsts (i), which are rarely considered as anticancer agents, consist of chelators that sequester copper ions from cells, disrupting the homeostasis of copper in order to limit the cancer progression.[103,105] The second group (ii) involves those compounds that transport copper inside the cell, increasing intracellular levels and exerting cytotoxic effects through a myriad of pathways.[107] The latter are those commonly named as “anticancer copper complexes”.[81]

The role of Cu and its complexes as anticancer agents -namely, “copper ionophores”- have awakened increasing interest specially during the last 20 years. The main hypothesis supporting Cu is that an endogenous metal might be less toxic for normal cells and not rapidly excreted from the organism.[81] In fact, the number of articles containing both the concepts “copper” and “anticancer” has increased from less than 20 per year to more than 400 since 2000 (**Figure 1.7**).[108] During the last two decades, the reported complexes are mainly Cu(II),[42,79–81,83,109–115] but Cu(I) compounds have also shown a potent anticancer activity.[116,117] A selection of some representative Cu(II) complexes reported in the last two decades is depicted in **Figure 1.8**.

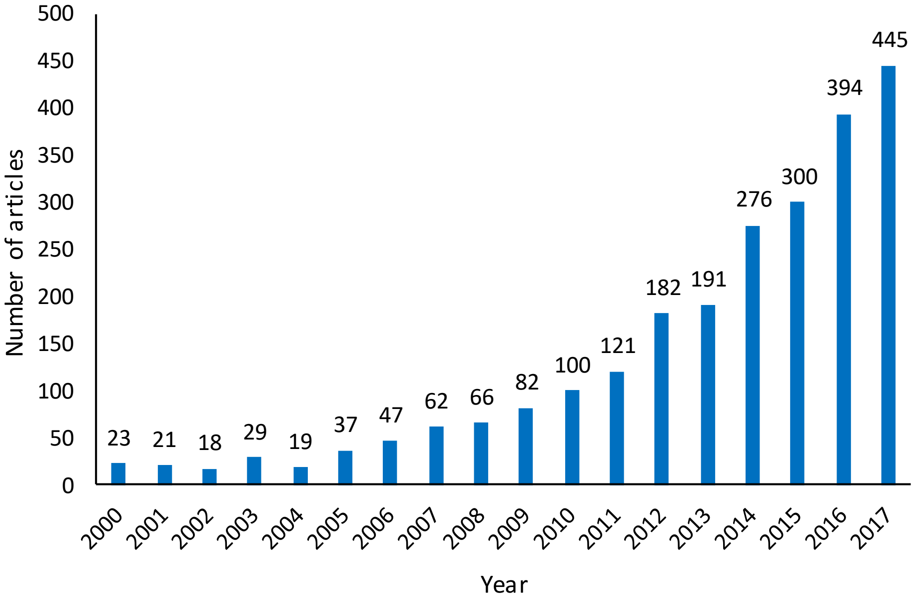

Figure 1.7. Number of articles in Web of Science containing the concepts "copper” and “anticancer" from 2000 until 2017.[108]

Several modes of action have been proposed for Cu anticancer drugs. Even though copper itself is reported to be highly reactive towards DNA, Cu complexes have been observed to lead to apoptosis by several mechanisms. Besides DNA binding, intercalation or direct cleavage,[81] cell damage caused by the production of ROS, mitochondrial disruption or SOD mimetic activity must be strongly remarked.[109,118] Furthermore, it is reported that sugar-directed cleaving chemistry of copper (abstracting H from the deoxyribose moieties of DNA) is also a significant cell-death pathway.[82] Nevertheless, the biologically accessible potential of the Cu(II)/Cu(I) pair appears as one of the principal mechanisms of action -*via* ROS production- and, as this will be an important feature along this thesis work, it will be further detailed in *Chapter 3*.

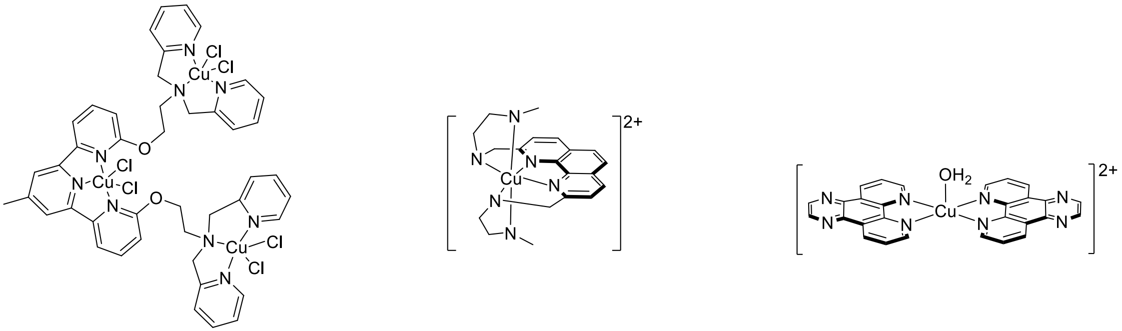

a

Terpyridine Cu(II) complex

b

Neocuproine based Cu complex

c

$[Cu(dpq)_2(H_2O)](ClO_4)_2$

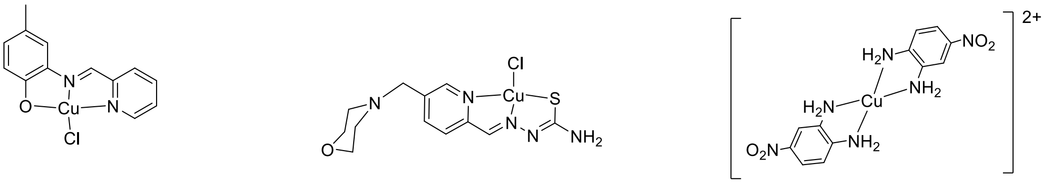

d

[CuII(pyrimol)]Cl

e

Cu(II) thiosemicarbazone-based complex

f

$[Cu(nbda)_2]^{2+}$

Figure 1.8. Some representative anticancer copper complexes reported during the last two decades. A terpyridine Cu(II) complex, **a**, has been reported by Suntharalingam *et al.* to improve the anticancer properties of the mononuclear analog and to show high DNA cleavage.[79] Phenanthroline moieties and planar derivatives have been extensively used for the last ten years, demonstrating high DNA intercalation: **b**.[119] Cu(II) compound **c** has shown red-light induced oxidative cleavage due to its dypiridoquinoxaline (dpq) moiety.[120] Hpyrimol was reported in 2006 to form a highly cytotoxic copper complex **d** without the need of a reducing agent, opening the gate to promising 'self-activating' anticancer compounds.[121] Recently reported water-soluble Cu(II) complexes with morpholine-thiosemicarbazone hybrid ligand showing interesting dual activity: cytotoxicity and antimicrobial, **e**.[115] Q.Peña *et al.* repurposed redox-active Cu(II) complexes with potential anticancer properties, some, **f**, exhibiting potent cytotoxicity in mammalian cancer cells.[113]

As commented above, besides the metal ion itself, the features of the ligand are indispensable to confer the desired properties to the metal center. In light of this, C. Santini *et al.*[80,81] reviewed twice the existing information regarding Cu anticancer drugs and some structure-activity relationships. Phenanthroline ligands and other planar systems such as dipyridophenazine and dipyridoquinoxaline are reported to be good Cu chelating agents and efficient intercalating structures. Moreover, they present high nuclease activity.[82] This, together with the presence of *N*-donor groups, specially imine moieties, appear to enhance the anticancer properties of Cu complexes according to the reviewed literature by C. Santini and coworkers. Thiosemicarbazone has been also widely used as specific ligand to confer remarkable anticancer properties to Cu(II) (**Figure 1.8**), as exemplified by several thiosemicarbazone Cu(II) complexes reported in the literature.[42,104,114,115,122]

New trends are driving research towards a selective therapy, where a thorough design of the ligand allows tuning the properties of the metal center. This allows modulating the physicochemical properties of the complex, endowing selectivity and improving the pharmacokinetics and targeting.[27,112] One of the main drawbacks among these metal-based drugs normally relies on their water solubility. Therefore, the search for biological medium soluble compounds is also a topic of high interest. Indeed, some phenanthroline and thiosemicarbazone-based Cu(II) drugs have been recently reported to be soluble in aqueous media (**Figure 1.8**).[109,115,123]

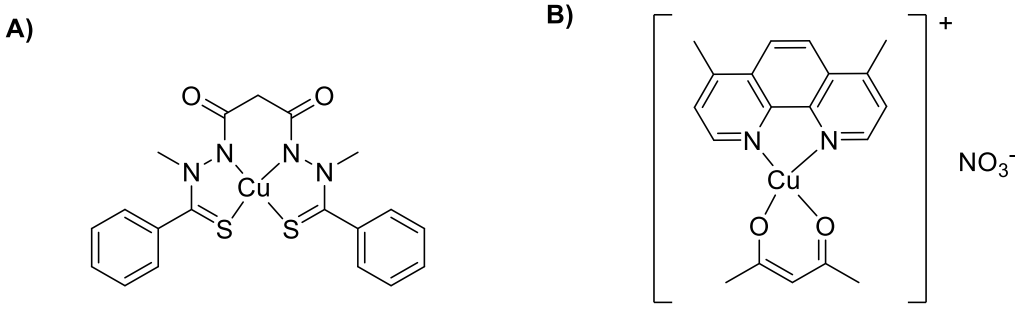

Cu(II) Elesclomol

Casiopeína IIIia

Figure 1.9. Cu(II) compounds in clinical trials. (**A**) Cu(II) Elesclomol[124] and (**B**) Casiopeína IIIia.[125]

Moreover, and from a clinical point of view, an increased number of copper compounds showing efficiency against a variety of tumors in animal models has been also observed.[84] It is worthwhile to mention two Cu(II) complexes, which have entered clinical trial phases. On one side, Cu(II) Elesclomol (**Figure 1.9A**), which has arrived to be examined in phase II trial against ovarian, fallopian and peritoneal cancers, showing a high DNA cleavage and the formation of ROS in larger amounts that in non-cancer cells.[124,126–129] On the other side, Casiopeína IIIia (**Figure 1.9B**) has also entered a phase I clinical trial against acute myeloid leukemia with a similar mechanism to Cu(II) Elesclomol.[125] Both have shown more activity in normal than in cancer cells, *i.e.* promising results to propel Cu as a metal of interest in cancer therapy.

1.4 Drug Delivery Systems

1.4.1 An overview of the drug delivery field

Two branches of pharmacology (pharmacokinetics and pharmacodynamics) play a crucial role on the research and development of a potential anticancer drug, and specially, on its application in clinical assays. The first branch is dedicated to determine the fate of substances administered to a living organism, *i.e.*, the effect of the body in the administered drug. The second attempts to evaluate the effect of the drug on the body, *ergo*, its biological activity.[130,131] One of the most interesting aspects to study with chemotherapeutics is related to their pharmacokinetics. Commonly, many people are strictly focused on the design and synthesis of novel and improved compounds which can offer high cytotoxic activities in tumoral cells. However, not many of them give the required importance to the processes inside the body until reaching the desired target. Five main steps can summarize the pharmacokinetics of a drug: administration, absorption, distribution, metabolism and excretion.[130,132]

For a drug to exert its bioactivity, it has to definitely enter the target cells. First, it has to dissolve in aqueous solution to have any chance of being bioactive. Once a drug is in solution, it has to be delivered to the target cells throughout the body *via* the blood stream.[133]

Advances in biomedical research have significantly enhanced the capability to identify drug targets for medical intervention. Since the milestone of cisplatin, several compounds (inorganic, organic and organometallic) have been discovered, designed and/or synthesized aiming at exhibiting anticancer activity. Despite all the progress made in the chemotherapeutic field, two major obstacles need to be overcome before moving from basic research into clinical application. The first of these obstacles is the lack of specificity and selectivity towards the different targets. This usually leads into undesirable toxic effects, as beforehand mentioned.[134] The inability of most drugs to cross the cell membrane and enter into the cytoplasm is the second main obstacle encountered.[6,133]

Indeed, cellular uptake is precisely considered as one of the main bottlenecks regarding the bioactivity of a compound.[133]

Achieving therapeutically relevant drug concentrations in the tumor mass, specially in the case of solid tumors, for a time sufficient to allow activity of the drug is another important consequence of the second obstacle. The poor solubility and penetrability observed for many drugs leads to residual tumoral cells even after prolongated treatment with these cytotoxic agents.[6,133] Moreover, drug release rates, cell- and tissue-specific targeting, and drug stability are also difficult to predict.

All these troubleshoots found in cancer treatment have been attempted to solve with improved drug delivery systems (DDS). DDS are defined as technologies/methods or processes of administering a pharmaceutical compound with the objective of improving its specificity by: (i) *in vivo* stabilization, (ii) controlling its release, and (iii) localizing its effect.[6]

Specially in the last two decades, the field of drug delivery has experienced a growing interest. The number of publications containing the concept “drug delivery systems” have exponentially increased between 2000-2018 (**Figure 1.10**),[108] highlighting the potentiality of this field in cancer treatment, specially towards selective and more efficient chemotherapy. During the last three years for instance, the number of papers related to DDS have risen up more than 2000 per year. This outlines the key role of these systems in improving the current treatments, as will be exemplified in *Section 1.4.3*.

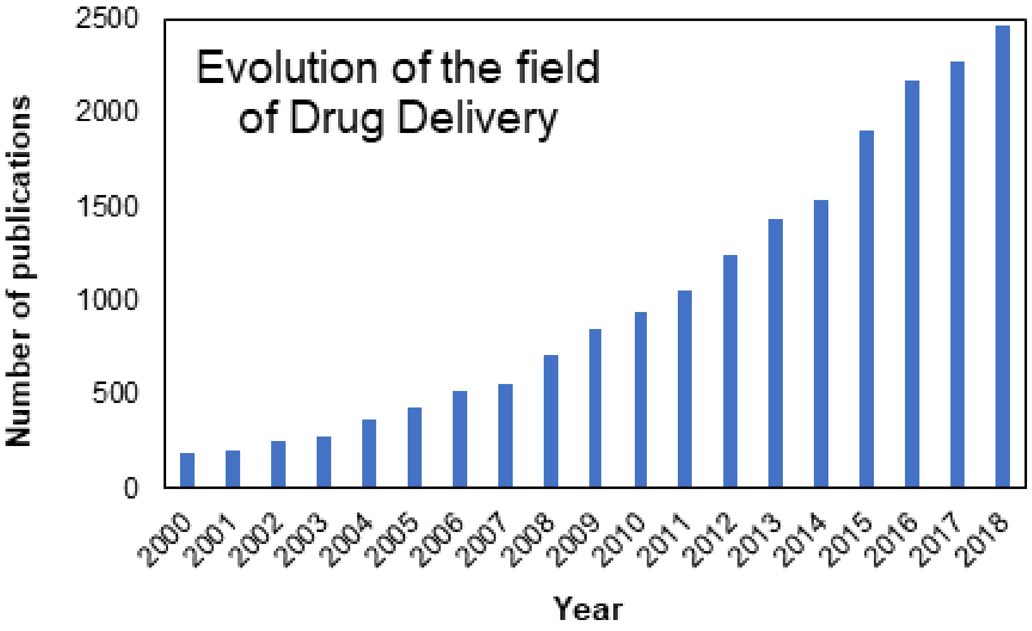

Figure 1.10. Evolution of the field of Drug Delivery. Number of articles containing the concept "drug delivery systems" since 2000. Data from Web of Science database.[108]

1.4.2 Pharmacokinetics of a drug

First of all, and before entering into the different types of designed DDS, understanding and gaining insights into the tumor cell biology, microenvironment of tumor cells and growth patterns allow developing effectively targeted drug delivery options. Hurdles to delivery and DDS design criteria also vary depending on the route of administration. Three main routes are distinguished: systemic, local and oral. Each one has specific requirements. Systemic delivery needs the drug to avoid clearance by the reticuloendothelial system and enter the right tissue. In the case of local delivery, avoiding the surrounding tissue and controlled release are indispensable requirements for the corresponding DDS. Finally, oral delivery systems must overcome extreme changes in pH as well as accommodate changes in biomolecule concentrations that vary with food intake.[135] All these requirements are important to take into account any potential drug for pre-clinical treatments and are an important factor to choose the appropriate DDS for each particular situation.

Despite being aware that pharmacokinetics is an extensive field of study and that it is not the main goal of this thesis, certain preliminary pharmacokinetic characteristics of some new complexes will be explored in *Chapter 3* to provide valuable information regarding their candidacy as putative drugs.

1.4.2.1 Serum proteins in the blood stream

Once the drug is administered into the body, it is distributed and reaches the different organs and tissues. One of the most interesting features to evaluate involves the interactions of these agents with the biomolecules present in the blood stream. Blood is a complex mixture of a multitude of cells and low- and high-molecular weight compounds. The human serum proteome is comprised over 100,000 proteins. In the blood plasma, albumin is by far the most abundant protein with a concentration of around 35-50 mg/mL.[136,137] Transferrin and low-density lipoprotein (LDL) are around 3 and 10-20 mg/mL, respectively.[138] Human serum albumin (HSA) is one of the smallest proteins present in the blood plasma, but it is reported to interact with many metabolic compounds and drugs.[139,140] It has many binding sites and it is a pivotal player to take into account in the final effect of any designed and synthesized drug.[141]

Besides the interactions with drugs, these three proteins (HSA, transferrin and LDL) show an enhanced uptake in tumor cells to cover their needs of proliferation. Therefore, they have also been used as potential drug carriers.[142–144] This dual role of the bloodstream proteins makes them meaningful to be assessed in the evaluation of a drug.[145]

1.4.2.2 Drug Targeting

Drug targeting can be achieved by taking advantage of the distinctive pathophysiological features of a tumor tissue or by actively targeting drug carriers making use of some targeting specific ligands. Two main approaches can be differentiated in drug delivery: passive and active drug targeting.

1.4.2.2.1 Passive targeting. The EPR effect

This approach makes use of the anatomical differences between the normal and the tumor vasculature. This allow a selective accumulation of the drugs at the tumor site through the so-called Enhanced Permeability and Retention (EPR) effect, championed by Maeda and colleagues.[146] The EPR effect is a phenomenon resulting from multiple causes and effects such as anatomical defects in vascular architecture and higher vascular density as a result of active production of angiogenic factors, mainly when tumors are at early stage and express growth factors. As a result, they facilitate extravasation of macromolecules in solid tumors. Normal vasculatures show no such leakage due to their complete architecture of the blood vasculature as well as little production of vascular mediators, which facilitate the extravasation: nitric oxide, vascular permeability factor (VEGF), prostaglandins, collagenase, peroxynitrite, etc.[146]

These anatomical features make the vasculature of a tumoral tissue permeable for macromolecules or even larger nanosized particles like liposomes and micelles. It has been determined that the pore size of tumor microvessels ranges from 100-1200 nm diameter depending on the anatomic location of tumor. This value differs radically from the tight junctions between endothelial cells of microvessels in normal tissues, which is around 2 nm in diameter (exceptions of 150 nm found in kidneys, liver and spleen).[146,147]

This effect is universally observed in rodent, rabbit and human solid tumors, and typically when the tumor size is less than 1 cm. At larger sizes, the tumor exhibits heterogeneity and this makes regular distribution through passive effect more complicated to predict. In any case, the EPR effect has been predominantly used for passive targeting of drugs more than 40 kDa and of low molecular weights presented in drug carriers such as polymeric drug conjugates, polymeric nanoparticles, micellar systems and liposomes.[148,149]

For instance, two liposomal formulations have been made to target drugs to tumor *via* EPR-mediated effect. These formulations are currently commercially available and highlight the potentiality of this effect: Daunosome^{TM} liposome (NeXtar, Inc.) -which encapsulates daunorubicin- and Doxil^{TM} (Sequus Pharmaceuticals) -based on doxorubicin encapsulation. This passive targeting gives rise to a reduction of the drug levels in plasma and a concomitant minimization of the cardiac adverse effects encountered with these drugs.[150]

1.4.2.2.2 Active targeting. Protein receptor

Active targeting employs some kind of strong interaction such as ligand-receptor or other molecular recognition to confer more specificity to the delivery system. Therefore, it relies on accumulating drug in the tumor through interaction with some over-expressed receptors on the tumor surface/microenvironment.[141,147]

Two main strategies are approached: (i) tumor vascular endothelium and (ii) over-expression of proteins on tumoral cells.

The first case (i) uses targets that are easily accessible and endothelial cells that are genetically stable and do not develop resistance against therapeutic agents. For instance, endoglin (CD105), which is the receptor for tumor growth factor (TGF-α), is the most favored target for tumor imaging and therapy.[151] Integrins are also another promising and interesting target since they are exclusively expressed during angiogenesis and not found on normal mature blood vessels.[152,153] The second approach (ii) utilizes protein receptors in cancer cells. Cancer cells express new (and over express existing) proteins in comparison to normal cells. These can serve as a biomarker for the progression of the disease. They are named “tumor associated antigens”.[154] Antibodies or ligands, specific to these antigens can be used to target drugs to tumoral cells.

Further, a variety of cell surface receptors for peptide, hormones and essential nutrients like iron and folic acid are over expressed in many cancer cells, *i.e.* providing a differentiating opportunity to target tumors. Concretely, folate and low-density lipoprotein (LDL) receptors have attracted special attention over the scientific community.[147] Folate receptor is a highly specific tumor marker, frequently overexpressed in more than 90%

of ovarian carcinoma patients and in many other types.[155] LDL, by its turn, can be mimicked by thorough-designed liposomes, increasing the uptake of the drug inside cancer cells.[156]

1.4.3 An overview of the different types of Drug Delivery Systems

Since the early 1950s, many different types of DDS have been developed in cancer therapy.[135,147,157–165] Along the last decades, DDS have been proven to show promising results as carriers in clinical trials and some of them have been approved for clinical use.[158,159,162,166] DDS are expected to achieve easy drug administration, enhanced drug accumulation at the tumor site, minimized side-effects and optimized therapeutic efficacy.[166–170] Antibody drug conjugates,[171–173] liposomal drug delivery systems,[160,161,174] micellar and polymeric systems,[175,176] nanoparticle-based delivery technologies[162,177,178] and dendritic-based systems[179,180] have been some of the most studied and reported ones (**Figure 1.11**).

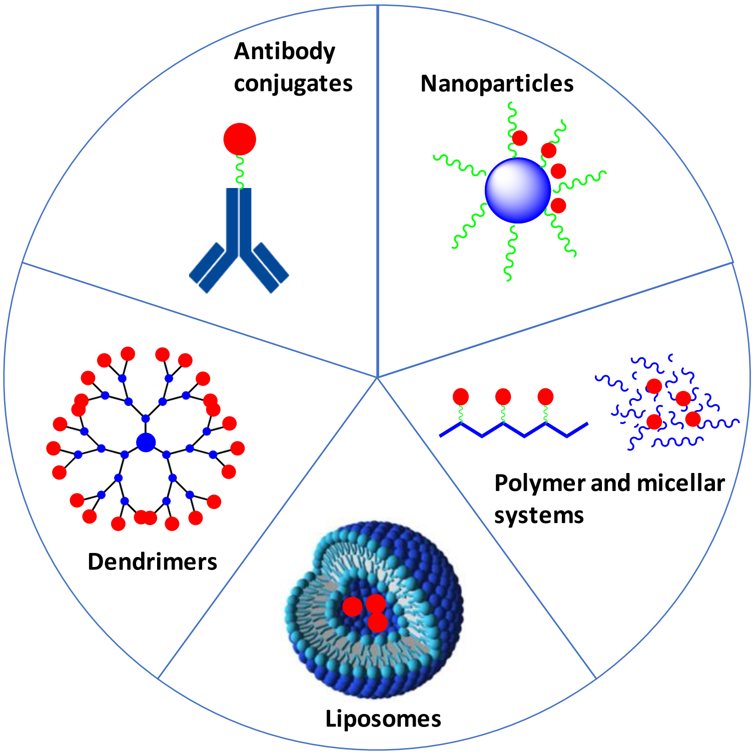

Figure 1.11. Representation of some of the main drug delivery platforms, extensively investigated in clinical trials. Blue represents DDS; green, biocompatible stabilizers or linkers; and red, the drug.

To give some brief examples, Doxil® is a liposomal formulation of doxorubicin (already mentioned in section 1.4.2.2.1), which has found to have a beneficial effect in Kaposi's sarcoma.[181] SP1049C, by its turn, is a Pluronic® L61 and F127 mixed micelle formulation incorporating also doxorubicin as a drug payload. It completed phase II clinical trials in 2011.[182] Finally, the first antibody drug conjugate, an anti-CD33 monoclonal antibody calicheamicin conjugate (Mylotarg®), was approved in 2001 for treating acute myelogenous leukemia.[183]

Several examples of DDS can be found in the literature,[159,184] enhancing and highlighting the potentiality of this field in future drug formulations in the pharmaceutical industry. The main objective is to overcome the side-effects, enhance the cellular uptake and improve the targeting of current drugs. Aspects that might be highly considered to increase the clinical applicability of any potential chemotherapeutic.

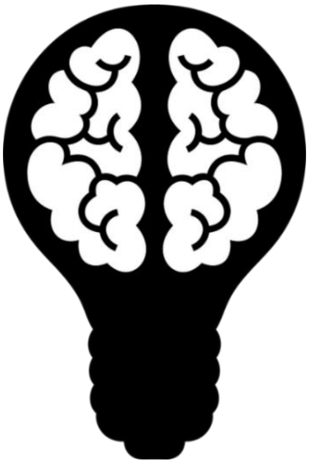

CHAPTER 2

Objectives and outline

This chapter sets up the objectives that will be approached in this PhD thesis. It also shows a chapter breakdown to introduce the reader into the contents of the following chapters.

CHAPTER 2

Objectives and outline

2.1 Objectives

The rather recent discovery of Cu and its complexes as softer but efficient anticancer drugs has opened the gate to explore these endogenous metals in Chemotherapy. Exploiting the Cu(II)/Cu(I) redox pair awakens salient interest within this field,[185,186] specially due to its putative selectivity towards cancer cells and its key role in the final biological activity.[113]

The main goal of this thesis is to develop a new family of functionalized copper(II) complexes based on a salphen-like *N*,*O*-donor heteroaromatic ligand, capable to exert anticancer activity through a ROS-mediated mechanism. The different functionalization strategies will attempt to (i) improve their biological activity and their candidacy for reliable pharmacological doses, and (ii) rationalize and propose structure-activity relationships to design tailor-made future Cu(II) anticancer drugs. Several objectives have been set up to fulfil the final goal:

OBJECTIVE I: To synthesize and characterize a novel *N,O*-donor planar heteroaromatic ligand for Cu(II), able to induce a fast Cu(II)/Cu(I) redox cycle inside cells. This main scaffold will serve as starting point for different functionalization strategies.

OBJECTIVE II: To attain the functionalization of the previously synthesized ligand with different groups, without changing the Cu(II) binding site. Several derivatives have been proposed:

Subobjective II.1: *chloro-* and *bromo-* analogs, to tune the Cu(II)/Cu(I) redox potential.

Subobjective II.2: *sulfonate* and *arginine (Arg)* groups, with the idea of increasing the solubility and bioavailability in biological medium using two opposite electrical charges.

Subobjective II.3: *Cell-Penetrating peptides (CPPs)*, in order to specifically enhance the cellular uptake of the final complex.

OBJECTIVE III: To synthesize and characterize several novel Cu(II) complexes containing the different derivatives of the initial ligand.

OBJECTIVE IV: To study the electrochemical behavior of the synthesized complexes and assess the thermodynamics of the Cu(II)/Cu(I) redox cycle.

OBJECTIVE V: To evaluate the biological activity and uptake of the different complexes (specially those with CPPs) in different cancer and normal cell lines, and to stablish a comparative depending on the type of functionalization carried out to unravel its role into the final biological activity.

OBJECTIVE VI: To study their mechanism of action and correlate it with the chemical potentiality to generate ROS *in vitro*. This includes the evaluation of the interactions with DNA.

OBJECTIVE VII: To examine the interactions of the complexes with proteins and their stability in biological medium to shed light into their pharmacokinetics and value as promising candidates for future pre-clinical *in vivo* models.

OBJECTIVE VIII: To study and evaluate a multimodal DTPA-based dendritic platform as DDS. To conjugate the ligand to this carrier and complex it with Cu(II) to form a potential dinuclear Cu(II) anticancer drug.

2.2 Thesis outline

The results of this thesis are presented in *Chapters 3-6*. The chapter breakdown goes as explained below and is summarized in **Scheme 2.1**, attempting to fulfil the previously outlined objectives as follows:

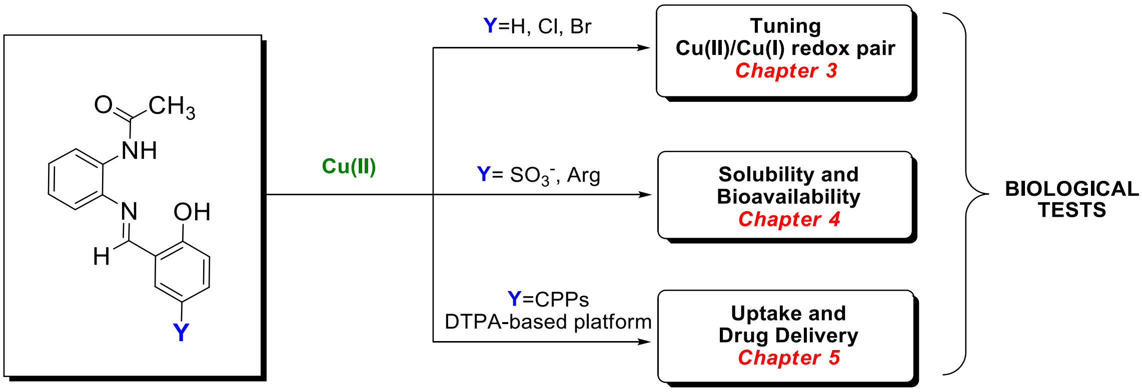

Scheme 2.1. Chapter breakdown of the thesis and summary of the work presented in *Chapters 3-5*.

Chapter 3 describes the synthesis and characterization of the imine-based *N,O*-donor heteroaromatic ligand of interest and its complexation with Cu(II). From this starting point, two chloro- and bromo- analogs are synthesized and characterized. Their high ROS generation capabilities, both thermodynamically and *in vitro*, are compared to evince the drift on the redox potential due to halogen functionalization. Their anticancer activity is confirmed based on cell-viability assays and their oxidative mechanism of action is studied. Final part focuses on a pharmacokinetics study, showing interesting interactions with some plasma proteins and the perspectives to improve the candidacy of the Cu(II) complex as a future anticancer drug. This chapter attempts to target **Objectives I**, **II.1**, and **VII**; and, partially, **III-VI**.

Chapter 4 comprises all the work devoted to the sulfonate and Arg functionalization of the previous synthesized ligand and proves the increase of the solubility and bioavailability of the final Cu(II) complex, which enhances its potentiality as future chemotherapeutic. This chapter details the optimization of the synthetic strategy for both functional groups and shows the synthesis of the final sulfonate- and Arg-derived ligands. Cu(II) complexation and characterization of the complexes is presented, with no alteration on the coordination environment of the Cu(II) ion. Their anticancer activity is comparatively assessed. Final part investigates the role of the functionalization in cell membrane recognition with cellular uptake experiments, and evidences the need of other more specific sequences to increase the translocation properties of a compound through the cell membrane. The work proposed in this chapter was designed to specifically accomplish **Objectives II.2** and **III**. It involves also partial achievement of **Objectives IV-V**.

Chapter 5 is divided into two parts. The first part describes the bioconjugation approach of the initial ligand synthesized in ***Chapter 3*** with Cell-Penetrating Peptides

(CPPs). This work shows the synthetic strategy followed as well as the obtention of the final conjugated ligands and their Cu(II) complexation together with their characterization. The comparison of their cellular uptake reveals the role of the CPPs in the improvement of the internalization and cytotoxicity, and allows to evaluate the appropriateness of the obtained copper(II) complexes as future chemotherapeutics. This first part encompasses **Objectives II.3**, **III** and **V**. The second part concentrates on proving the Cu(II) binding abilities of a dendritic DTPA-based platform and its feasibility to be used as DDS. The work also details the synthetic procedure to anchor the ligand scaffold synthesized in ***Chapter 3*** to the platform and its Cu(II) complexation to form a new dinuclear Cu(II) complex. This second part essentially approaches **Objective VIII**.

Chapter 6 gathers the main remarks of the previous chapters, and summarizes the general conclusions drawn from the work. It also provides the scope for future work.

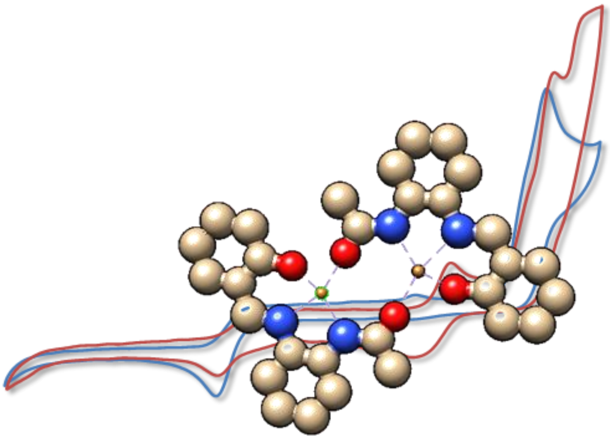

CHAPTER 3

Designing Cu(II) complexes bearing *N,O*-donor heteroaromatic ligands (L1, L2, L3). Promoting oxidative mechanism and ROS generation

The synthesis of a novel salphen-based *N,O*-donor heteroaromatic ligand for Cu(II) and of the two bromo- and chloro- derivatives are shown in this chapter, attempting to achieve a facile Cu(II)/Cu(I) redox conversion to trigger *in vitro* ROS generation. This chapter also summarizes the synthesis and characterization of the corresponding Cu(II) complexes. The evaluation of their ROS production capabilities, as well as of their biological activity in cells, is also included here. Some pharmacokinetic properties are also examined to assess the potentiality of the compounds in future *in vivo* tests.

CHAPTER 3

Designing Cu(II) complexes bearing *N,O*-donor heteroaromatic ligands (L1, L2, L3). Promoting oxidative mechanism and ROS generation

As previously mentioned in *Section 1.3.3.2*, the mechanism of action for Cu complexes against cancer is not fully elucidated yet. Many proposals have been made related to the cell-death pathways provoked by complexes of this metal ion.[81] Interestingly, ROS generation arises as one of the potentialities of Cu as anticancer agent, and it is one of the most widely accepted mechanisms of action for this metal (**Scheme 3.1**).[81] ROS are species like H_2O_2, $O_2\cdot^-$, $HO\cdot$, etc., which are toxic for the organism because they cause oxidative damage to cells.[187] These ROS are released *via* a Cu(II)/Cu(I) catalytic cycle triggered by the presence of agents like ascorbic acid or biological redox buffers such as $NADH_2$, glutathione, etc.

All the cells are sensitive to ROS levels, and they can only cope with a certain maximum concentration of those species before dying. The production of ROS is not only reported to induce cellular damage, but also to offer a putative discrimination between healthy and non-healthy cells. Considering that (i) cancer cells exhibit abnormal and higher basal ROS levels, and that (ii) they show higher vulnerability to ROS level changes than healthy cells do, the modification of those levels represents a unique opportunity to selectively target cancer cells.[188,189] This idea is important to keep in mind during this chapter, because it is one of the pursued objectives in our work.

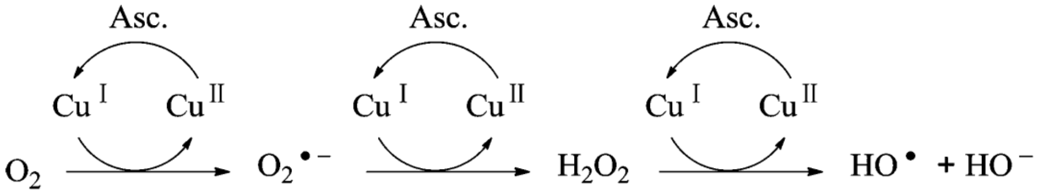

Scheme 3.1. Cu(II)/Cu(I) redox cycle for the formation of ROS species. *Asc.* refers to ascorbic acid.

In this regard, a novel salphen-based ligand **L1** (**Scheme 3.2**) has been designed to easily coordinate Cu(II), with a fourth labile coordination position in the equatorial plane, and with the main purpose to attain a facile redox conversion from Cu(II) to Cu(I).[80,81] The interest of this ligand is twofold. On one side, the presence of *N*-heteroaromatic planar scaffolds promote efficient DNA binding/intercalating action and cleaving properties.[81,190] On the other hand, the use of a redox-active ligand (π-conjugated aromatic coordinating scaffolds) has attracted considerable attention. Its versatility to expand the electron transfer reactivity of the coordinated metals beyond the mere inherent metal activity is interesting in terms of potential redox-mediated anticancer pathways, *i.e.* ROS generation.[191] This is based on the synergy of the ligand and the metal ion, which facilitates multi-electron transfer processes.[191] Indeed, this feature is also observed in nature, where various metalloenzymes contain a redox-active ligand that works conjointly with the ion of the active site, enabling biological reactions to occur near thermodynamic potentials.

This chapter is divided in three main parts. The first part comprises the synthesis of the novel ligand **L1** and its related Cu(II) complex, which serves as the backbone for the project of this thesis. Secondly, functionalization of this ligand with halogen groups (**L2** and **L3**) will be broached in order to observe their effect in the electronic environment around the Cu(II) center. Finally, the last part of this chapter will be devoted to the biological studies and the mechanism of action of the three Cu(II) complexes (**C1**, **C2** and **C3**), altogether with the evaluation of their interactions with proteins.

3.1 Synthesis of the *N,O*-donor heteroaromatic ligand L1

The synthetic strategy followed to obtain ligand **L1** is depicted in **Scheme 3.2**. It is based on a common condensation reaction between the *-CHO* group of *o*-hydroxybenzaldehyde and the *-NH$_2$* functional group of compound **1**.

Prior to this imine bond formation, the synthesis of **1** was carried out by following reported literature.[192] Asymmetric protection of the amino group of the benzene-1,2-diamine was successfully achieved by dropwise addition of acetic anhydride at low and controlled temperature to avoid the *bis*-protected compound. The obtained product was confirmed by ^{1}H NMR (**Figure A1**). Data was in good concordance with the reported structure.[192] The mono-acylated compound **1** reacted with the commercially available *o*-hydroxybenzaldehyde in absolute EtOH in equimolar conditions to give rise to **L1**.

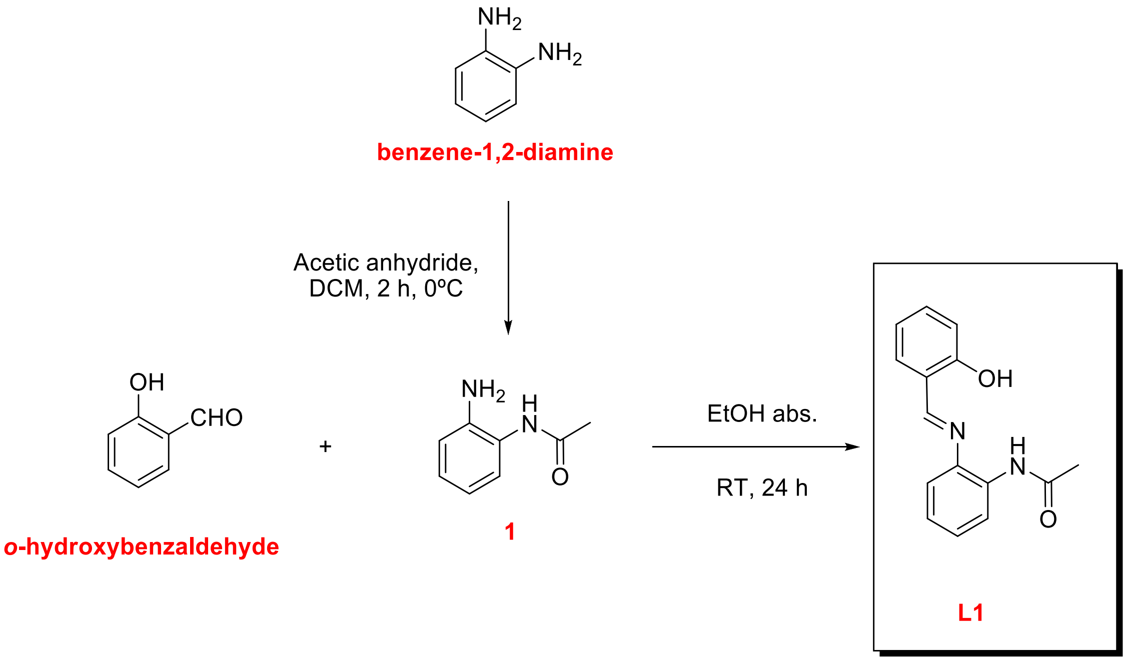

Scheme 3.2. Synthetic strategy to obtain ligand **L1**.

L1 was eventually obtained after purification through silica column chromatography in 40% yield. It was confirmed and characterized by ^{1}H NMR (**Figure A4**), ^{13}C NMR (**Figure A5**), IR (**Figure A6**) and MS (**Figure A7**). Although imines are not highly water-stable functional groups, the conjugated system with the aromatic rings enhance its stability for biological purposes with respect to the use of aliphatic amines.

3.2 Synthesis and characterization of the Cu(II) complex of L1 (C1)

The corresponding Cu(II) complex was obtained after the reaction of the ligand **L1** with Cu(OAc)$_2$. The latter, apart from providing the metal ion, favors the deprotonation of both the phenol and the amide groups in one due to the basic nature of the anion. **C1** was isolated after precipitation from the reaction medium.

The proposed structure for the complex **C1** ([Cu(**L1**)]$_2$) is shown in **Figure 3.1**. It consists of a dimeric Cu(II) structure with a 1:1 (Cu(II):**L1**) stoichiometry in a final neutral species. **L1** has three donor atoms (N, N, O) which are able to chelate Cu(II) in a tridentate fashion. The formation of two chelate rings (five- and six-membered rings) are expected from this scaffold, providing stability to the final complex and, hence, to the iminic bond too. The fourth coordination position around the metal ion would be occupied by an *O*-donor atom from the carbonyl group (C=*O*) of the second complex subunit. This proposal is supported by the data obtained from MS, ESR, IR and Elemental Analysis (EA) experiments, as will be detailed below.

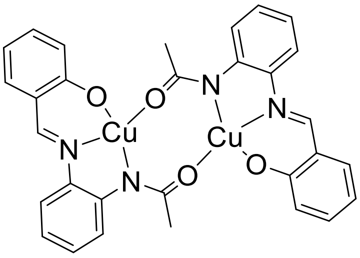

Figure 3.1. Proposed structure for complex **C1**.

3.2.1 Characterization of the complex **C1**

ESR experiments were carried out to confirm the presence of Cu in the +II oxidation state in the complex and the coordination environment around the metal ion. The geometry of the metallic center affects to the electronic properties of the metal ion, including the ground levels for a given geometry. In Cu(II) complexes with elongated octahedron, tetragonal, square pyramidal and square-planar geometries, the electronic density is axial and therefore $d_{x^2-y^2}$ orbitals are the ground state for the single electron. For complexes with compressed octahedron or trigonal bipyramid the ground state is d_{z^2}.[193] The two main parameters to determine the response of the electrons to the applied magnetic field are the *g* and the *A* parameters. Shifts in the *g* value are caused by the influence of spin–orbit coupling. In normal situations where $\mathrm{d}_{x^2-y^2}$ and d_{z^2} are the ground states, the ESR spectra are axial, with equivalent x and y axes and two g values: $g_{//}$ or g_z (parallel region) that is related to the z axis; and $g_\perp$ (perpendicular region), which is related to the x and y axis ($g_x = g_y$). The A tensor (hyperfine coupling constant) is related to the magnetic interactions of the electronic spin (S = 1/2) with the Cu(II) nuclear spin (I = 3/2).[193]

ESR spectrum of complex **C1** (**Figure 3.2** and **Table 3.1**) confirms that Cu is in the +II redox state. The presence of only one ESR signal suggests a sole Cu(II) species in solution for complex **C1**, at least at detectable concentrations for the ESR instrument. Based on $g_{//} > g_{\perp} > g_e$, the ground state for the single electron is a $d_{x^2-y^2}$ orbital and, thus, we expect a square-planar or square-pyramidal derived geometry.[193] This supports the proposed complex structure (**Figure 3.1**), according to the ligand constraints.

The $g_{//}/A_{//}$ ratio (**Table 3.1**) is lower than 140 cm, which indicates a non-distorted structure from planarity.[5] Empirical correlations have been established between the $g_{//}$ and $A_{//}$ parameters and the coordination around the Cu(II) ion. These values match with a N_2O_2 coordination environment,[194] fitting with the proposed structure for complex **C1**. This coordination environment can be easily explained by the presence of three donor atoms (N, N, O) of the chelating ligand **L1**, and a fourth oxygen atom either from the C=*O* of the amide group or from a solvent molecule (DMS*O*) in the coordination sphere.

It is important to critically state here that a dimeric structure will most-likely not be observed in ESR due to metal-metal interactions, which would yield to silent species. Therefore, the N_2O_2 coordination proposed from the ESR signal of **C1** could be probably corresponding to the presence of a DMSO molecule, coordinating the metal ion with an O donor atom in the fourth position of the equatorial plane, and leading to a mononuclear species. This would be supported by the coordinating abilities of the DMSO molecule,[195] which can promote the breakage of the dimeric structure in solution.

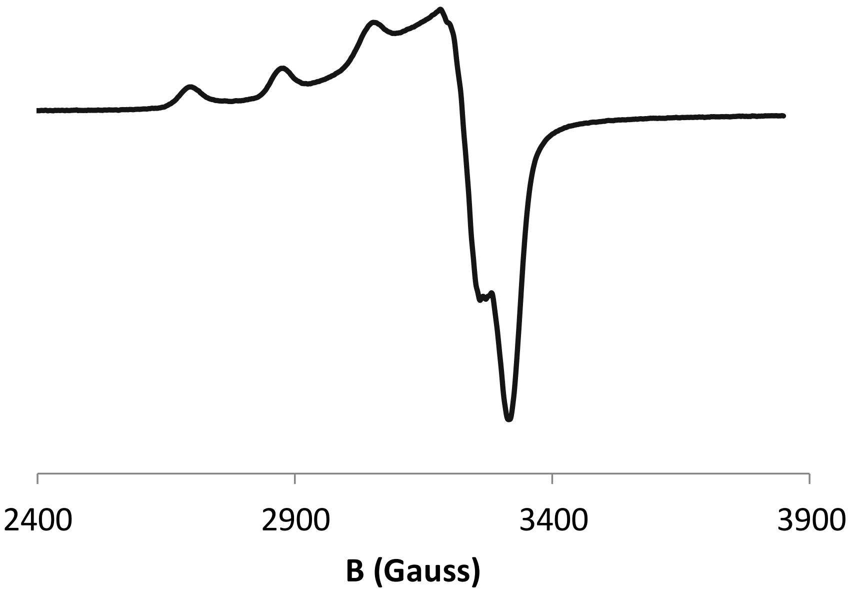

Figure 3.2. X-ESR band of the complex **C1** in frozen DMSO.

---

[5] *The quotient is a convenient empirical parameter to evaluate the tetrahedral distortion. For square-planar structures with no significant distortion, it ranges from 100 to 140 cm.*[314]

Table 3.1. ESR parameters for complex **C1**, extracted from **Figure 3.2**.

Complex	**$g_{//}$**	**$A_{//}$ (10^{-4} cm^{-1})**	**$g_{\perp}$**	**$A_{\perp}$ (Gauss)**	**$g_{//}/A_{//}$ (cm)**
C1	2.248	175	2.055	<20-30	128

Elemental analysis of the isolated precipitate fits perfectly with a 1:1 stoichiometry (Cu:**L1**), with both the *-OH* and *-NH* (amide) deprotonated, and it also confirms a high purity of the obtained complex. No additional counterions or solvent molecules in the coordination sphere of Cu(II) were assumed. IR spectra of **L1** (**Figure A6**) and complex **C1** (**Figure A8**) provide useful information regarding the deprotonation of **L1** to coordinate the Cu(II) ion. The band assigned to the stretching of both *O-H* (phenol) and *N-H* (amide) bonds at 3500-3300 cm^{-1}, as well as the peak related to the bending mode of the *N-H* bond at about 1660 (scissor bending) have disappeared from **L1** to **C1**. This reinforces the deprotonation of both the amide (-N*H)* and the phenol (-O*H*) groups upon metalation.

Based on the proposed N_2O_2 coordination from the ESR experiments and on the EA, the fourth coordination position (O atom) in the solid must be occupied by a donor atom of the same **L1** ligand structure -*ergo* acting in a tetradentate fashion- to avoid altering the chemical composition. At this stage, two possible coordination proposals could be conceived, with distinct nuclearity (**Figure 3.3**).

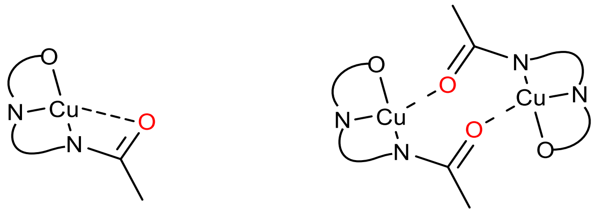

Mononuclear

Binuclear

Figure 3.3. Nuclearity proposals of the final complex as a function of the coordination of the -C=*O* (in red) of the amide functional group.

Structural constraints of the planar ligand, the predisposition of the donor atoms, and the square-planar derived coordination preferences of the Cu(II) ion with *N*,*O*-donor ligands[94,196] point to a binuclear structure. Besides, to our knowledge, there is no reported structure in the literature to support the mononuclear coordination environment of **Figure 3.3**.

Final confirmation was achieved by HR ESI-MS (**Figure 3.4**). At least two peaks can be found attributed to the dimeric complex. Peaks [**C1**+H]$^+$ (*m/z* 631.0456) and its corresponding Na adduct (*m/z* 653.0294) can be assigned to the dinuclear form and, hence, to the proposed structure (**Figure 3.1**). Experimental and theoretical patterns match perfectly (**Figure 3.4**).

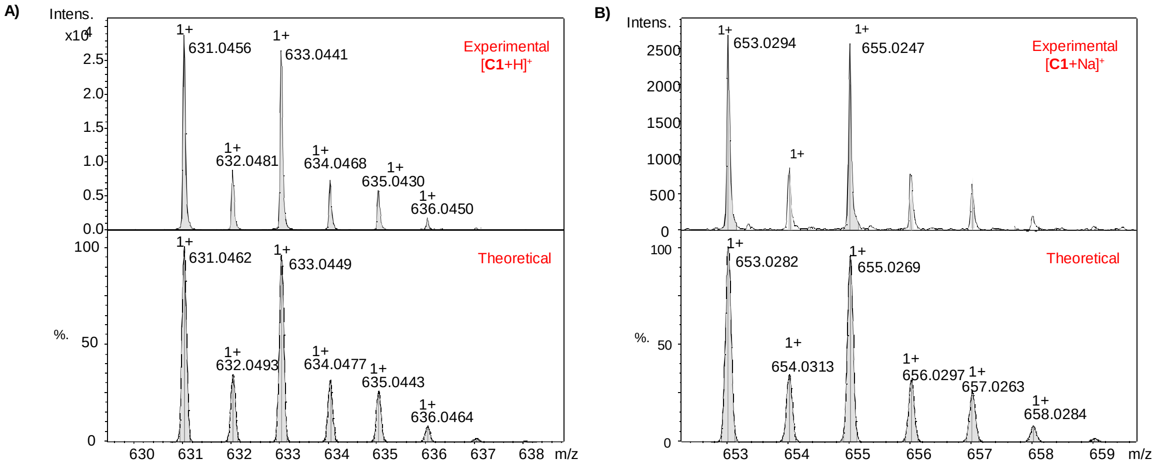

Figure 3.4. Experimental (top) and theoretical (down) HR-MS (ESI$^+$, DMSO-MeOH) spectra of complex **C1** for (**A**) [**C1**+H]$^+$ and (**B**) [**C1**+Na]$^+$.

At this stage, the structure of the complex was consistent and fitting with that shown in **Figure 3.1**. Different crystallization attempts have been tried to obtain crystallographic data and to additionally reinforce all the beforehand presented results. Slow evaporation in different solvents (MeOH, DMF) and temperatures and slow diffusion with a two-solvent system (MeOH-DCM, MeOH-Et_2O, DMSO-DCM, DMSO-Acetone) have been assessed. Most of them resulted in precipitation of the complex without crystallizing and only slow precipitation at 4 ºC in a mixture of DMSO-DCM rendered some crystals. However, they were not suitable for X-Rays analysis due to their too small size.

3.2.2 Redox studies of **C1** and its biological implication

As stated at the beginning of this chapter, one of the cell-death pathways reported for Cu(II) complexes implies oxidative damage and ROS generation.[107] Therefore, knowing the redox properties of complex **C1** is relevant for its putative future biological application. Indeed, cyclovoltammetry studies (CV) can give insights into structural-activity relationships. Some recent reported research in our group proposed a relationship between the Cu(II)/Cu(I) redox potential of some Cu(II) compounds bearing *N*-donor heteroaromatic ligands with their potentiality as *in vitro* ROS generators, *ergo*, as cytotoxic agents.[113]

CV was performed with both **L1** and **C1** in DMSO (**Figure A9**). The ligand **L1** is electroactive in the assayed range (-2 V to 1 V *vs.* Fc^+/Fc). This non-innocence of the ligand may contribute to the final *in vitro* ROS generation activity of the corresponding complex. However, it is important to remind here that the biological redox window approximately ranges from -1.1 V to 0.2 V *vs.* Fc^+/Fc, values arising from the oxidation and reduction of water at pH 7,[197,198] and consequently, this is the interesting region in our study. In this specific range, the ligand **L1** does not show any kind of redox activity The new signal observed on the cyclovoltammograms of **C1** is ascribed to the Cu(II)⇄Cu(I) process. The Cu(II)/Cu(I) assigned potential of -1.07 V (**Figure 3.5**) was confirmed by bulk electrolysis and ESR experiments. Successive scans were performed. The lack of signal change upon the successive collected scans indicates that no disproportion occurred after cycling between Cu(II) and Cu(I). The I_{pa}/I_{pc} ratio close to 1 and the calculated ΔE_p values (**Table A1**) suggest a quasi-reversible one-electron process. The difference between cathodic and anodic peaks is much higher than the expected 0.060 V (ΔE_p of 0.130 V) for fully reversible redox processes, but the recorded voltammogram in the same conditions for the ferrocene (Fc^+/Fc) reference compound also displays similar ΔE_p (around 0.100 V). The linear dependence of the peak currents I_{pc} and I_{pa} *vs.* the square root of the scan rate ($v^{1/2}$) is indicative of a diffusion controlled process (**Figure A10**).[199]

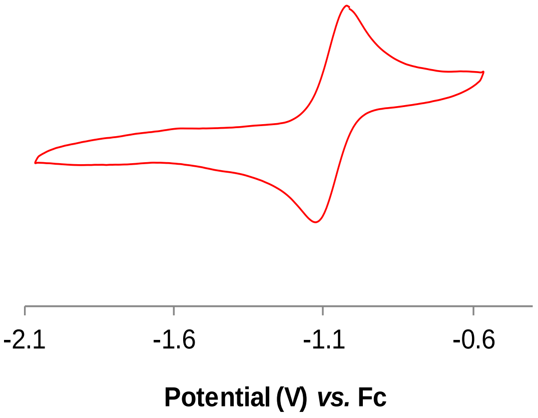

Figure 3.5. Cyclic voltammogram of complex **C1** in DMSO with 0.1 M TBAP recorded at 100 mV/s. The observed signal corresponds to the Cu(II)/Cu(I) redox pair.

The calculated Cu(II)/Cu(I) redox process of **C1** (**Figure 3.5** and **Table A1**) is within the biological range of -1.1 V to 0.2 V *vs.* Fc^+/Fc.[200] The half-wave potential in **C1** ($E_{½}$ = -1.07 V *vs.* Fc^+/Fc) is close to the glutathione (GSH) system ($E°_{(GSH/GSSG)}$ is about -0.95 V *vs.* Fc^+/Fc)[201–203] or the common $NAD^+/NADH$ redox pair ($E°_{(NAD^+/NADH)}$ = -1.0 V *vs.* Fc^+/Fc) in eukaryotic cytosols, and **C1** might be reduced by these two redox buffers.[204]

3.3 *Cl-* and *Br-* derivatization of L1. Understanding the effect of the electronic density in the Cu(II)/Cu(I) redox potential

Although the redox behavior of the metallic core of **C1** makes this copper complex a potential candidate to be used for anticancer purposes,[113] its redox potential value is close to the reduction potential value of water at pH 7. Therefore, distinct chloro- and bromo- analogs have been synthesized in order to observe the effect of the electronic density on the Cu(II)/Cu(I) redox potential, with views of future biological implications. The use of electrowithdrawing groups (halogen atoms) may lower the electronic density around the metal ion, favoring its reduction to Cu(I) by GSH or $NADH_2$. The functionalization intends then to (i) shift the $E_{1/2}$ of the Cu(II)/Cu(I) redox pair towards higher values without altering the coordination sphere of the Cu(II) ion, and (ii) to induce higher redox-mediated toxicity.

3.3.1 Synthesis and characterization of the *Cl-* and *Br-* derivatives of **L1** (**L2** and **L3**)

Chloro- and bromo- derivatives of **L1** (**L2** and **L3**, respectively) have been synthesized following standard procedures (**Scheme 3.3**).

Synthesis of **L2** used *o*-hydroxybenzaldehyde as commercial starting material, followed by the subsequent chlorination with *N*-chlorosuccinimide (NCS) and an acid catalyst.[205] This involves electrophilic substitution *via* formation of positive halonium species. This reaction provides much lower yields than those found with Cl_2 or sulfuryl chloride as common chlorinating agents, but a cleaner reaction.[206] The advantage of this process in front of the use of Cl_2 as chlorinating agent essentially relies on the mild conditions used with NCS. The presence of NaCl slightly increases the yield and the acid reduces the reaction time.[207] However, mono- and di-chlorinated (*orto*- and *para*-) compounds were observed in the reaction crude. Compound **2** was obtained in low yields (14%) after purification through column chromatography. It was then reacted with **1**, as previously done in the synthesis of **L1** (**Scheme 3.2**). The condensation between the *-CHO* group of **2** and the amino (*-NH_2*) group of **1** rendered **L2**, purified *via* silica column chromatography.

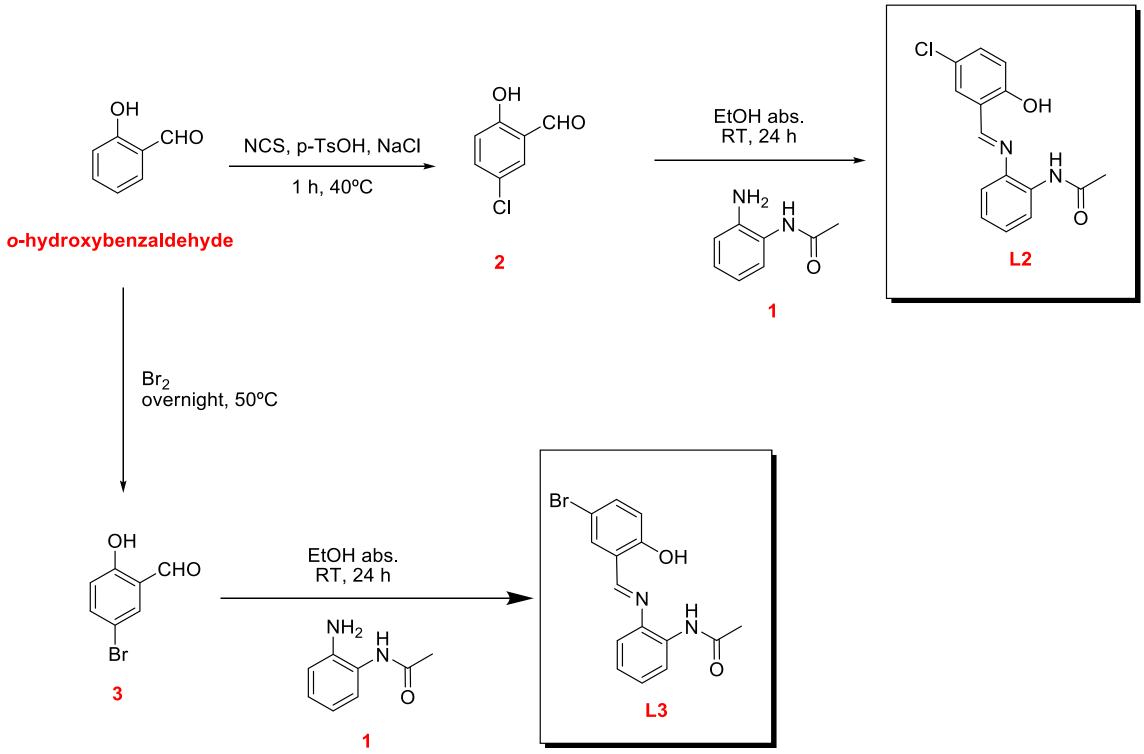

Scheme 3.3. Synthetic strategy towards ligands **L2** and **L3**.

Synthesis of **L3** was performed in an analog manner to that followed for **L2**. In this case, bromination of the starting material *o*-hydroxybenzaldehyde was carried out by using standard bromination procedures with Br_2.[208] **3** was obtained in high yields (55%) and high-purity enough without any further purification step. Final **L3** was synthesized following the same condensation reaction and purification procedure as for **L1** and **L2**. (**Scheme 3.3**).

Compounds **2** and **3** were confirmed by ^{1}H NMR (**Figures A2** and **A3**). Ligands **L2** and **L3** were characterized by NMR (**Figures A11**, **A12**, **A14** and **A15**), IR (**Figures A13** and **A16**) and HR-MS (**Figure A17**), in good concordance with the proposed structures.

3.3.2 Synthesis and characterization of the corresponding Cu(II) complexes of L2 and L3 (C2 and C3)

Once the ligands **L2** and **L3** were isolated in high purity and fully characterized, complexation with Cu(II) was attempted. The procedure was the same than that followed to obtain **C1** (*Section 3.2.1*). The use of the Cu(II) acetate salt provided both the metal and the base to deprotonate the *-OH* and the *-NH* in one. This was again corroborated from the IR spectra (**Figures A18** and **A19**). Both complexes **C2** and **C3** precipitated from the reaction media. The proposed structure maintains the metallic core as that of **C1** (**Figure 3.6**).

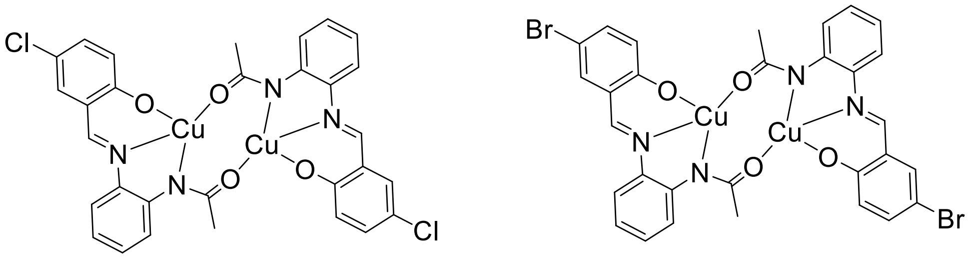

C2 **C3**

Figure 3.6. Proposed structures for complexes **C2** and **C3**.

HR ESI-MS (**Figure A20**) confirms the presence of the dimeric species, with peaks attributed to [**C2**-H]$^+$ (*m/z* 698.9670) and [**C3**+H]$^+$ (*m/z* 786.8678). Moreover, ESR spectra of both complexes demonstrate that they both maintain the same coordination environment around the metal ion than **C1** (**Figure 3.7**). ESR parameters for both complexes are the same as the those obtained for **C1** (**Table 3.2**). This is important because it highlights the fact that the functionalization of the ligands has not altered the final coordination properties and that the metal ion has the same N_2O_2 coordination environment in all three cases (**C1**, **C2** and **C3**). Elemental analyses were also carried out to confirm that both **C2** and **C3** were obtained in high purity.

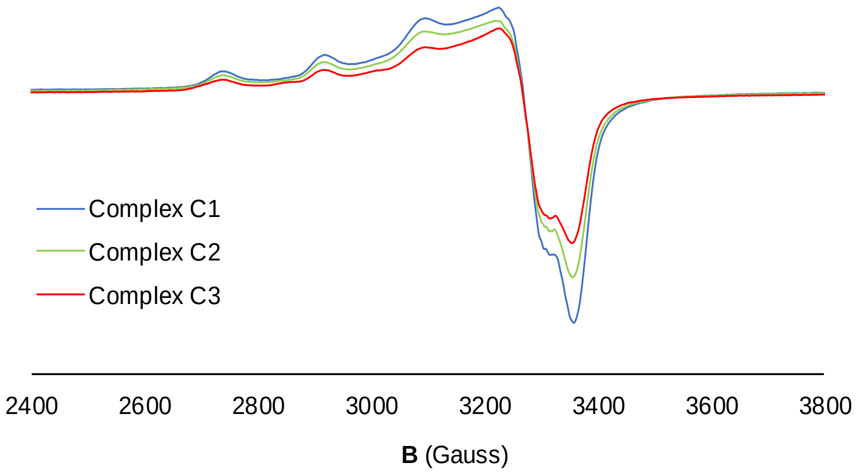

Figure 3.7. X-ESR band of complexes **C1**, **C2** and **C3** in DMSO. ESR spectra were normalized for the sake of comparison.

Table 3.2. ESR parameters for complex **C2** and **C3**, extracted from **Figure 3.7**. **C1** is placed for the sake of comparison.

Complex	**$g_{//}$**	**$A_{//}$ (10^{-4} cm^{-1})**	**$g_{\perp}$**	**$A_{\perp}$ (Gauss)**	**$g_{//}/A_{//}$ (cm)**
C1	2.248	175	2.055	<20-30	128
C2	2.249	178	2.055	<20-30	126
C3	2.251	177	2.055	<20-30	127

3.3.3 Comparative electrochemical behavior of **C1**, **C2** and **C3**

One of the purposes of the ligand **L1** functionalization with electrowithdrawing groups was to shift the redox potential of the Cu(II)/Cu(I) pair to higher values. This shift aims at thermodynamically favoring the reduction of Cu(II) to Cu(I). CV experiments were carried out with **C2** and **C3**, following the same procedure used for **C1** (*Section 3.2.2*). **C2** and **C3** showed a similar redox behavior than that observed for **C1** (**Table A1**), probably due to the fact that they have the same coordination environment around the metal center (**Figure 3.7**).

As observed in the CV shown in **Figure 3.8A**, the presence of electrowithdrawing groups slightly favors the Cu(II) reduction to Cu(I) in complexes **C2** and **C3** (with E_{red} = -1.09 V and -1.08 V, respectively) compared to **C1** (E_{red} = -1.15 V). Both the chloro- and bromo- derivatives have the reduction potential 60 and 70 mV higher than the complex bearing the non-functionalized ligand **L1**. Despite halogen groups make Cu(II) proner to be reduced to Cu(I), the difference is relatively small and this might not have a high influence in the final $E_{1/2}$ value and thus, in their biological activity. The $E_{1/2}$ for the three complexes (**Figure 3.8B** and **Table A1**), in fact, show less differences (just 40 mV), since the anodic peaks are comparatively closer among them (E_{pa} for **C1**-**C3** of -0.99, -0.97 and -0.97 V, respectively).

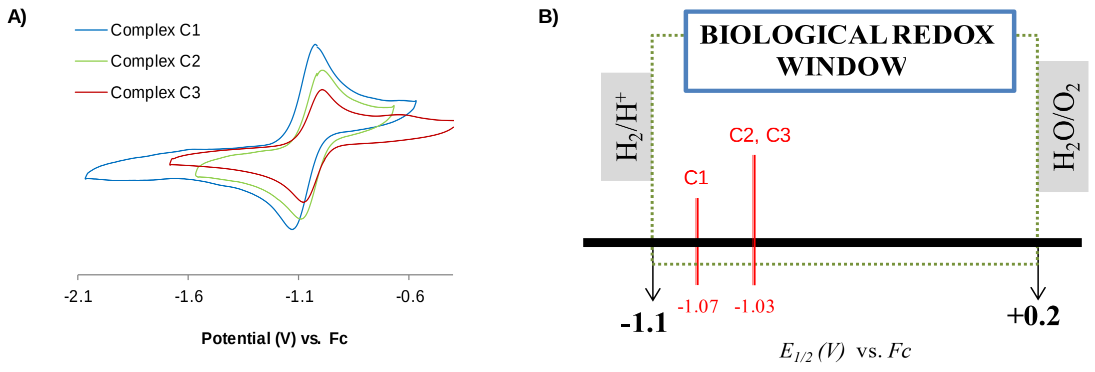

Figure 3.8. (**A**) Cyclic voltammograms *vs.* Fc^+/Fc (Fc) of **C1**, **C2** and **C3** in DMSO with 0.1 M TBAP at a scan rate of 100 mV/s. (**B**) $E_{1/2}$ of **C1**, **C2** and **C3** placed in the biological redox window at pH 7.[200]

In any case, it can be concluded that all three complexes present the half-wave potential of the Cu(II)/Cu(I) redox pair inside the biological redox window, as observed in **Figure 3.8B**. Therefore, they are most-likely able to induce a redox mechanism under biological conditions. This hypothesis can be supported with the ascorbic acid consumption at pH 7.2, monitored by UV-VIS. As seen in the **Scheme 3.1**, Cu(II), in the presence of ascorbate and in an aerobic environment, catalyzes the generation of ROS.[209] Therefore, measuring the evolution of the absorbance of ascorbic acid (265 nm) gives us a first and preliminary idea of the capability of these three complexes to generate ROS. Without any copper catalyst (DMSO control), no decrease on the absorbance at 265 nm can be observed (**Figure 3.9**). This demonstrates that ascorbic acid is stable and the medium does not consume it. In contrast, the presence of a catalytic amount of free Cu(II) ions from the $CuCl_2$ clearly shows a rapid decrease on the absorbance and after just 20 min, ascorbic acid has been almost totally consumed. Complex **C1** is able to consume ascorbic acid at similar rates than free copper ions do. **C2** and **C3** exhibit a slower consumption rate than that of **C1**, which was not expected based on their redox behavior. One possible explanation of the different consumption rate could be related to solubility issues since **C2** and **C3** are less soluble in aqueous media than **C1**.

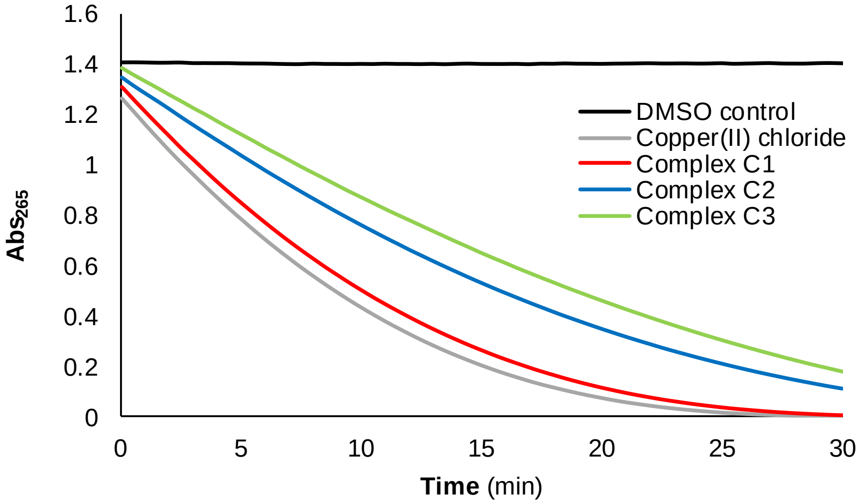

Figure 3.9. Consumption of ascorbic acid (100 µM) mediated by $CuCl_2$ and complexes **C1**, **C2**, **C3** in NaCl and TRIS-HCl buffer at pH 7.2. The four Cu(II) compounds were at a concentration of 2 µM.

Based on the consumption of ascorbic acid by the three complexes, it is expected that they are able to generate ROS inside cancer cells and, therefore, to potentially exert some kind of redox-mediated cytotoxicity. Confirmation of this assumption would be highly interesting since it may provide some kind of selectivity between cancer and normal cells, as explained at the beginning of this chapter.[188,189]

3.4 Biological studies of C1, C2 and C3. Understanding their mechanism of action

The fact that the three Cu(II) complexes (**C1**, **C2** and **C3**) have the Cu(II)/Cu(I) redox pair potential inside the biological redox window encouraged us to assess their biological activity and to elucidate their mechanism of action. Therefore, **C1**-**C3** were evaluated as potential anticancer agents.

3.4.1 *In vitro* anticancer studies. Cytotoxicity towards cancer and normal cell lines

In vitro antiproliferative activity of the three synthesized complexes and of their corresponding free ligands was determined on somatic HeLa and MCF7 cancer cell lines. HeLa refers to an epithelial type of tumor cells from cervix and it is one of the most employed cell lines to test anticancer activity. MCF7 is also epithelial from mammary gland tissue. Both are really useful to be used as testing cell lines because the majority of cancers sprout in epithelial cells owing to their high replication rate.

The IC_{50} values are summarized in **Table 3.3** and the dose-dependent toxicity profiles in HeLa cancer cells shown in **Figure 3.10**. The cell-viability assays obtained in MFC7 (**Figure A21**) exhibit a similar tendency to those observed in HeLa cells. Firstly, it is worthy and interesting to mention the different antiproliferative activity exerted by the three synthesized ligands in HeLa. While **L1** shows poor or negligible toxicity, **L2** and **L3** display significant cytotoxicity (**Figure 3.10A**). This might be a drawback in terms of drug metabolism, even thought they could contribute and add some toxicity to the final Cu(II) complexes. Halogenated aromatic compounds have indeed already been reported to show toxicity in human cells.[210,211] The different cytotoxicity might be attributed to the fact that chlorinated -and by extension brominated- aromatic compounds do apparently interact with an specific receptor found in all human cells: Aryl Hydrocarbon Receptor (AHR). This receptor is associated to transcription factors, affecting to some genes that regulate the metabolism, growth and the clearance of toxic substances from cells.[210] The prototypic toxin that affects this receptor is the well-known 2,3,7,8-

Tetrachlorodibenzodioxin (TCDD), a polychlorinated dibenzo-*p*-dioxin which has been reported to cause severe toxicity in humans.[212]

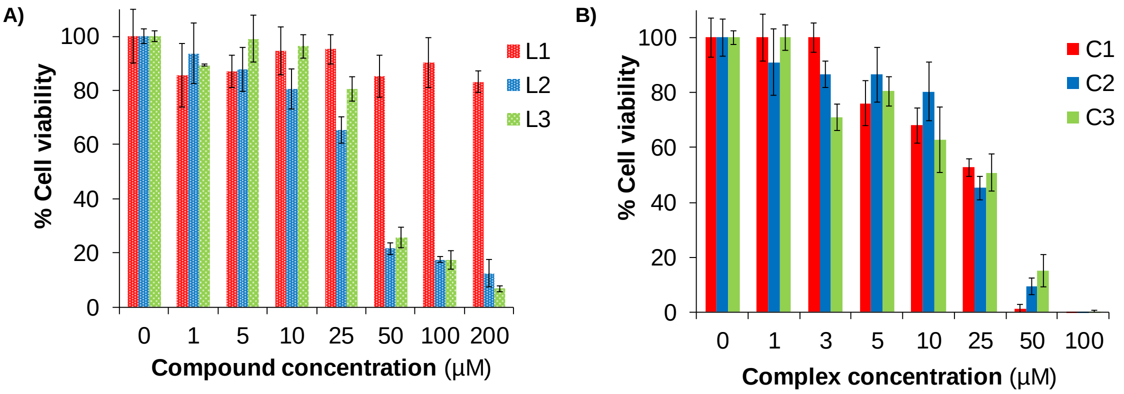

Figure 3.10. Cell viability assays in HeLa cultures of (**A**) **L1**, **L2** and **L3**, and (**B**) their corresponding Cu(II) complexes **C1**, **C2** and **C3** at different concentrations after 72 h of treatment. The obtained values average at least three independent experiments.

Regarding the Cu(II) complexes, it is noteworthy to highlight that CuCl$_2$, used as a Cu(II) control, shows no significant cytotoxicity in none of the assayed cancer cells. Notably, complexes **C1**, **C2** and **C3** display remarkable and dose-dependent cytotoxicity in HeLa cells (**Table 3.3** and **Figure 3.10B**) when compared to CuCl$_2$ and cisplatin (IC$_{50,72h}$ of 15 µM),[213] with IC$_{50}$ around 25 µM. Some considerations are interesting to go into detail. First of all, complexes **C2** and **C3** already bear toxic ligands (**L2** and **L3**) as beforehand mentioned (**Figure 3.10A**). Therefore, cytotoxicity of these complexes probably accounts for an important contribution from the ligand itself. Contrarily, **C1** does exhibit remarkable antiproliferative activity, yet bearing a non-toxic ligand (**L1**). Its toxicity can then only be attributed to a conjoint contribution between the ligand **L1** and the Cu(II) ion, *i.e.* to the entire complex; and not solely to the simple addition of the Cu(II) ion plus the ligand toxicities. In this particular case, this feature may imply an advantage in terms of drug metabolism, since none of the frameworks that constitute **C1** (**L1** and Cu(II) ion) do separately exhibit cytotoxicity.

Results in MCF7 show analogous toxicity profiles (**Figure A21**), with similar IC$_{50}$ values, as observed in **Table 3.3**. This might indicate that they are not specific to any of the two assayed cancer cell lines. Regarding this cell line (MCF7), it is important to mention that some complexes (**C2** and at lesser extent **C3**) showed poor solubility in the biological culture medium. This fact, together with the toxicity already shown by their corresponding ligands **L2** and **L3**, made us discard these two complexes as candidates to be used directly in future *in vivo* tests. In none of the two, the Cu(II) coordination contributes to enhance or provide any additional antiproliferative activity.

C1, by its turn, displays significant and interesting toxicity towards both HeLa and MCF7 cell lines, with less solubility issues than the others two. This encouraged us to assess its cytotoxicity towards normal embryotic fibroblasts (NIH 3T3). This cell line serves as a proof-of-concept of non-cancer cells. As observed in the dose-response cell-viability diagram, complex **C1** exhibits lower toxicity in fibroblasts with respect to both HeLa and MCF7 cells (**Figure 3.11**). This is interesting in terms of selective chemotherapy since they might provide less side-effects, and therefore could represent an *in vivo* advantage.

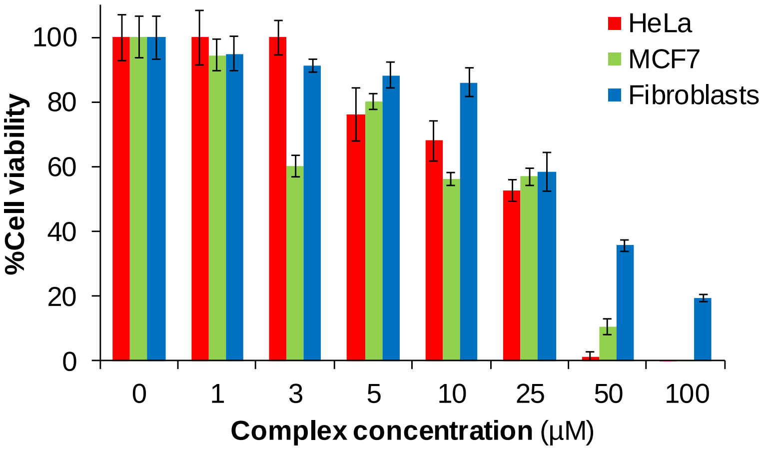

Figure 3.11. Comparison of the dose-response cell-viability diagrams of **C1** in HeLa, MCF7 and NIH 3T3 (fibroblasts) cell lines (0-100 µM) at 72 h. The obtained values average at least three independent experiments.

Table 3.3. IC_{50} (µM) values at 72 h of complexes **C1**, **C2**, **C3** and their corresponding ligands in HeLa, MCF7 and NIH 3T3 cultures, using $CuCl_2·2H_2O$ as reference compound. The results shown are representative of at least three independent experiments (N=3).

Compound	HeLa	MCF7	NIH 3T3
C1	26 ± 4	30 ± 6	n.d.
C2	25 ± 2	-[a]	-[a]
C3	23 ± 10	29 ± 5	-[a]
L1	n.d.	≥ 150	n.d.
L2	≥ 50	-[a]	-[a]
L3	≥ 50	≥ 50	-[a]
$CuCl_2·2H_2O$[113]	n.d.	≥ 200	≥ 200

n.d. (non detected). These cases are those whose dose-response curve does not show cytotoxicity at 200 µM.

[a] Experiments were not carried out due to complex solubility issues in the particular cell culture medium and, hence, to avoid possible biased data. In the case of the non-assayed complexes, their corresponding ligands were not assayed either.

3.4.2 Understanding the mechanism of action for complexes **C1**, **C2** and **C3**

As already briefly stated in the *Section 1.3.3.2*, while Pt complexes can covalently bind to *N*-donor centers in the DNA, as cisplatin does,[29] copper and its complexes have shown a myriad of modes of action. Besides DNA intercalation or groove binding,[81] ROS generation or SOD mimetic activity, among others, are examples of the reactivity observed for some of the current reported Cu(II) complexes.[82,118]

DNA arises still as one of the main targets of chemotherapy and therefore, normally one of the first to be evaluated. In the case of Cu(II) complexes, apart from DNA, ROS have been highlighted as one of the outstanding mechanisms of action for this metal. Therefore, this section will be devoted to evaluate complexes **C1**, **C2** and **C3** with (i) DNA -as the main target of chemotherapy- and (ii) as *in vitro* ROS generators. The idea is to elucidate the most probable mechanism of action for these compounds and, hence, the one mainly responsible for their cytotoxicity. These studies could shed light into the real potentiality of these compounds beyond the cytotoxicity results. IC_{50} values are clearly conditioned and affected by the internalization of the complex inside cells, independently whether they show or not promising activity. Subsequent experiments will then provide us insights into their reactivity and into the putative need to improve their drug delivery in the future.

3.4.2.1 DNA as the main target of chemotherapy. Cleaving experiments and DNA interactions studies

DNA studies that have been carried out in this work involve gel electrophoresis, UV-VIS and circular dichroism (CD) experiments. The idea in the case of compounds **C1**, **C2** and **C3** relies on evaluating the structural damage that they are able to induce towards this biomolecule.

As many Cu(II) complexes have been reported to present cleaving capacity,[79,82,121,214] gel electrophoresis experiments were firstly carried out. The cleaving properties of complexes **C1**, **C2** and **C3** were investigated by following the conversion of supercoiled circular plasmid DNA to opened DNA forms. Gel electrophoresis consists of a gel matrix (agarose gel) which acts as the stationary phase and where biomolecules move along depending on their size and charge due to an applied electrical potential. Shorter DNA fragments would move faster than longer ones. The gel is subsequently stained with ethidium bromide (EB) to reveal the position of the bands. Results are shown in **Figure 3.12**. As observed, complexes **C1**, **C2** and **C3** are only able to partially open supercoiled plasmid DNA (ScdsDNA), leading into its open circular form (ocDNA, form II). This ocDNA is solely seen as a minor band and therefore, they do not possess prominent cleaving capacity by themselves.

Contrarily and remarkably, results under the presence of a reducing agent (ascorbic acid) provide really useful information. The presence of reductants such as ascorbic acid simulates the reducing environment inside the majority of cellular compartments. The generation of Cu(I) stimulates the potential formation of ROS, which have DNA cleaving abilities.[110] In our particular case, the three assayed complexes have an enhanced cleaving capacity in the presence of ascorbic acid, being able to practically transform all the ScdsDNA into ocDNA and, at lesser extent, into its linear form (form III). The almost total vanishing of the band associated to form I suggests a strong cleaving capacity under a reducing environment. This clearly points to a redox-dependent mechanism, triggered by the presence of ascorbic acid, which promotes the Cu(I) generation, the potential formation of ROS and the concomitant DNA damage.

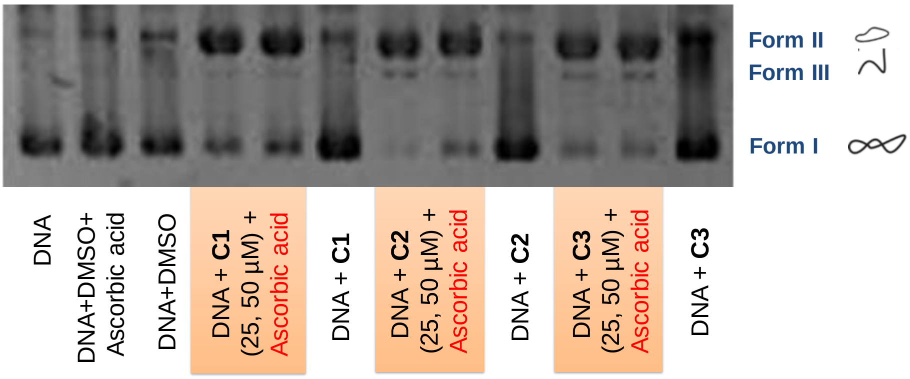

Figure 3.12. Agarose gel electrophoresis of a BlueScript Supercoiled DNA (ScdsDNA) treated with complexes **C1**, **C2**, **C3**. Incubation time of 24 h at 37 ºC. Some samples were incubated for an additional hour in the presence of ascorbic acid.

Apart from the nuclease activity shown by the three synthesized complexes, interactions with DNA have been also assessed. They can be generally classified as covalent or non-covalent. Covalent interactions are highly important in the case of cisplatin and cisplatin-like Pt compounds,[29,39] whose mechanism of action is usually conceived through the formation of Pt-DNA adducts. In the case of Cu(II) complexes, covalent adducts with DNA are less common and normally they do not show this kind of binding.[113] Contrarily, non-covalent interactions are indeed important to be analyzed in our case (**Figure 3.13**).

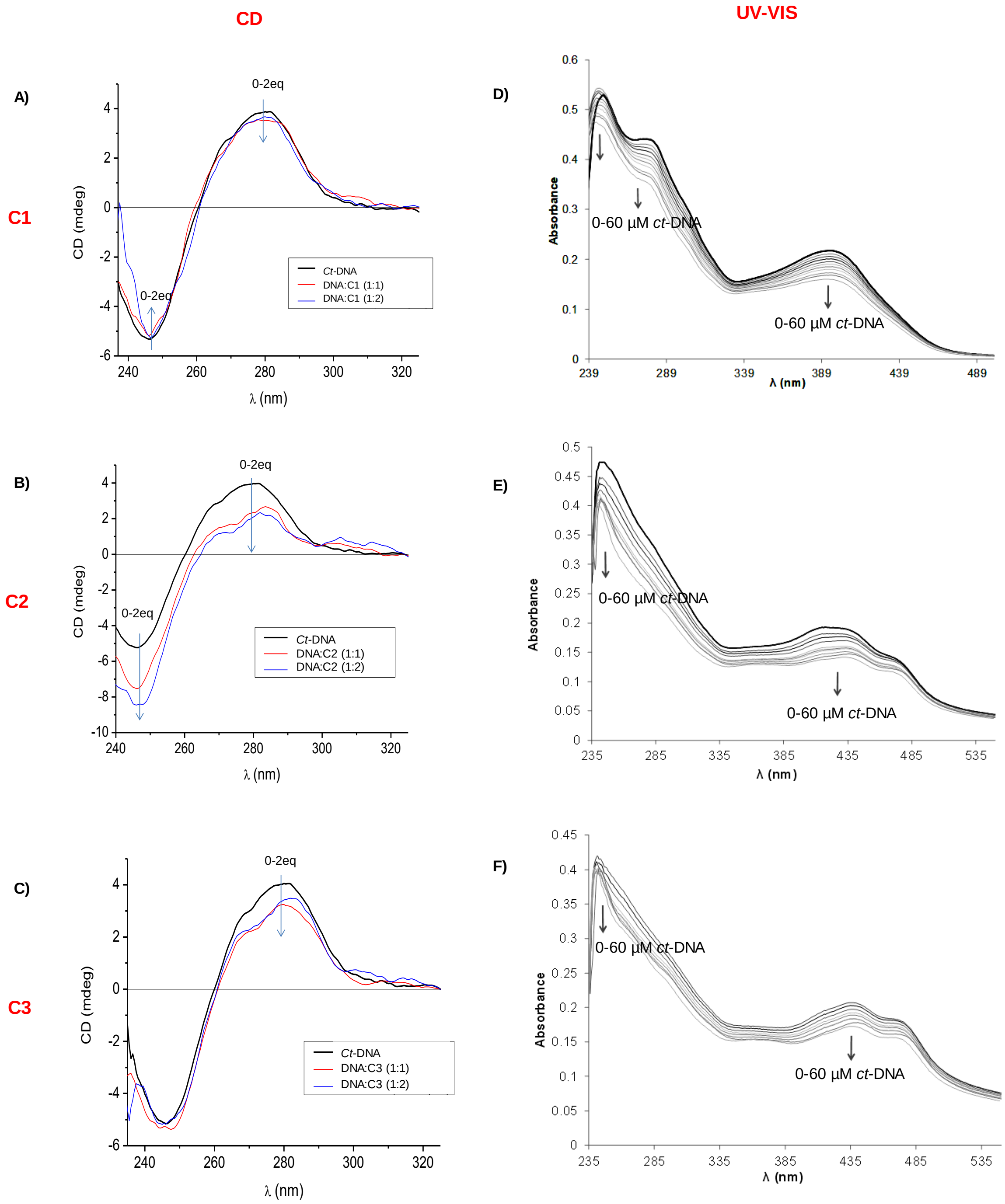

Figure 3.13. DNA-binding studies. On the left, CD studies for **C1** (**A**), **C2** (**B**), **C3** (**C**) at 50 µM of *ct*-DNA and at 1:1 and 1:2 (DNA:Complex) ratios in NaCl/TRIS-HCl at pH 7.2. Samples were previously incubated overnight at 37 ºC. On the right, UV-VIS studies for complex **C1** (**D**), **C2** (**E**), **C3** (**F**) at 30 µM upon *ct*-DNA titration from 0-60 µM in NaCl/TRIS-HCl at pH 7.2. Each spectrum was recorded after 15 minutes of stabilization time. The arrows indicate change upon increasing concentrations of *ct*-DNA.

CD and UV-VIS spectroscopy have been performed in order to enlighten the putative DNA-complex binding modes of **C1**, **C2** and **C3**. Primarily, CD spectroscopy allows to assess the possible structural alterations of the *Calf-thymus* DNA (*ct*-DNA). *Ct*-DNA presents a characteristic feature in the CD spectrum with small amplitude bands: a positive band around 280 nm and a negative band around 245 nm.[215] Changes in the CD spectrum are attributed to conformational changes induced by the presence of the complex.[216] *Ct*-DNA was incubated with **C1**, **C2** and **C3** (from 0 to 2 equivalents) overnight and analyzed by CD (**Figures 3.13A**, **3.13B** and **3.13C**). They show DNA interactions but without inducing important structural changes into the helicity of the *ct*-DNA. Small changes in the intensity of the CD spectra suggest some kind of DNA-drug non-covalent binding. However, both characteristic positive and negative band of the *ct*-DNA are essentially maintained in all the three cases, pointing to no significant structural modifications.

Three main classes of non-covalent bindings have been proposed for metal complexes: intercalation, groove binding and electrostatic interactions with the negatively charged phosphate backbone of the DNA. UV-Vis absorption spectroscopy was used to assess the complex-DNA interactions and their likely nature. The study is based on the changes on the absorbance (typically metal-to-ligand charge transfer absorptions, MLCT, and π-π* ligand transitions) upon increasing additions of *ct*-DNA to a solution of the corresponding metal complexes. Absorption spectra in the range of 225-550 nm were recorded at a constant complex concentration (30 µM) with increasing amounts of DNA. Results for complexes **C1**, **C2** and **C3** (**Figures 3.13D**, **3.13E** and **3.13F**) clearly show a hypochromic effect upon *ct*-DNA addition but no significant bathochromism is observed in any spectra. This points to an interaction with DNA *via* groove binding or electrostatic interactions rather than *via* intercalation.[83,217–219] Compounds showing high DNA intercalating properties do normally produce red-shift due to their π-π interactions with the aromatic bases of DNA,[217,220] an effect that has not been observed in this case. The two other ways of interactions would be actually favored by the opposite electrical charges of the metal compound (cations) in front of the negatively-charged DNA phosphate backbone.

Quantitative data can be obtained from the recorded absorption spectra using the Benesi-Hildebrand equation (Equation 1) that allows to calculate the intrinsic binding constant: K_b. A_o is the absorbance of the complex in the absence of DNA, A is the absorbance at any given DNA concentration, and ε_G and $\varepsilon_{H\text{-}G}$ are the extinction coefficients of the complex and the complex-DNA, respectively.[217,221]

$$\frac{A_o}{A-A_o}=\frac{\varepsilon_G}{\varepsilon_{H-G}-\varepsilon_G}+\frac{\varepsilon_G}{\varepsilon_{H-G}-\varepsilon_G}\cdot\frac{1}{K_b[DNA]} \qquad (Equation\ 1)$$

The plot of the relative variation of the absorbance (*A₀/(A-A₀)*) *vs.* the inverse of the DNA concentration (*1/[DNA]*) allows the determination of K_b (**Table 3.4**). The K_b values obtained for complexes **C1**, **C2**, and **C3** are in the order of 10^4, lower than the values around 10^6-10^7 known for classical and strong metallointercalators (DAPI, HOECHST, etc.).[217,222,223] In any case, these values point to a moderate but non-negligible DNA binding affinity.

Table 3.4. Intrinsic binding constants (K_b) and hypochromism for the interaction of *ct*-DNA and complexes **C1**, **C2** and **C3**. K_b is obtained from the ratio of the intercept to the slope, according to the Benesi-Hildebrand equation (Equation 1),[217] after the fitting of the UV-Vis data from **Figure 3.13**.

Complex	K_bᵃ (M^{-1})	log K_b	% hypochromism (λ in nm)
C1	$2.2·10^4$	4.34	25 (397)
C2	$6.2·10^4$	4.79	27 (424)
C3	$7.2·10^4$	4.86	28 (438)

[a] The calculated K_b values from Equation 1 arise from an approximated DNA-drug model and hence, they should be compared in orders of magnitude, rather than with the exact numbers.

3.4.2.2 *In vitro* ROS production studies

Results obtained in the cyclic voltammetry studies (**Figure 3.8**), ascorbic acid consumption experiments (**Figure 3.9**) and DNA cleaving activity (**Figure 3.12**) undoubtedly indicate an oxidative dependent mechanism of action. In order to detect and confirm the formation of intracellular ROS in HeLa cancer cells, the 2',7'-Dichlorofluorescin diacetate (DCFDA) assay was performed.[112,224] DCFDA is a non-fluorescent and permeable dye that, after cleavage and oxidation by intracellular esterases and ROS, generates dichlorofluorescein (DCF), a fluorescent and non-permeable compound. Having in mind that **C2** and **C3** presented solubility issues in cytotoxicity assays, this experiment was only performed with **C1**, which indeed has the same metallic core as **C2** and **C3** and hence, similar ROS activity are expected. For 4 h treatment, strong DCF fluorescence of up to 3-fold respect to control cells was observed for complex **C1** (**Figure 3.14**), highlighting the ROS production capabilities of this complex. The ROS levels of **C1** are equivalent to those produced by the positive control H_2O_2. On the contrary, **L1** was not able to increase the ROS levels (**Figure 3.14**) respect to the control group. This is in high concordance with the Cu(II)/Cu(I) redox potentials observed previously for **C1** (**Figures 3.8** and **3.9**) and with the results obtained for the toxicity of both compounds (**Table 3.3**). Having the Cu(II)/Cu(I) redox potential inside the biological redox windows, *i.e.* with the thermodynamic potential of Cu(II)/Cu(I) redox cycling in cells, seems to induce a high ROS production level. This fact contributes to undertake a redox-mediated toxicity.

These results confirm the relationship inferred between the Cu(II)/Cu(I) redox potential of **C1**, its ROS production inside the cells, and the exerted biological activity. Furthermore, this ROS cell-death pathway might be a factor to understand the different toxicity profiles observed for **C1** in HeLa and MCF7 cancer cells with respect to normal cell lines (NIH 3T3), shown in **Figure 3.11**. As mentioned at the beginning of this chapter, the production of ROS might appear as a differentiating feature to selectively kill cancer cells in front of healthy cells. Seemingly, **C1** displays a lower toxicity profile in fibroblasts than in the two tested cancer cell lines.

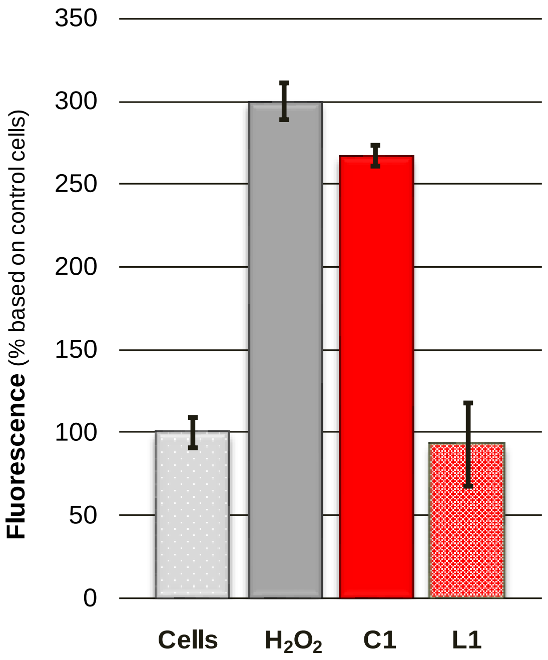

Figure 3.14. *In vitro* ROS production measured with DCFDA assay in HeLa cancer cells for complex **C1** (50 µM), **L1** (100 µM) and H_2O_2 (100 µM) as positive control after treatment during 4 h.

All these data together clearly reinforce the redox mechanism for Cu(II) complexes as one of the most important ones to trigger cell-death and emphasize the strong link between the chemical features of Cu(II) complexes and their biological activity, already proposed in our group.[113] This may be used as an interesting and promising starting strategy to preliminary assess future Cu(II) complexes as anticancer drugs based on their redox features.

3.4.2.3 Cell-death mechanism. *In vitro* apoptosis determination

Once elucidated the mechanism of action of **C1**, it was interesting to examine the cell-death pathway induced by the complex.

Several eukaryotic cell-death pathways have been postulated. However, in general, eukaryotic cell-death has always been dichotomously described as either necrosis or apoptosis.[225,226] Apoptosis is described as an active, orchestrated programmed process of autonomous cellular dismantling that avoids eliciting inflammation. The morphology associated with this phenomenon is characterized by nuclear and cytoplasmatic condensation and cellular fragmentation into membrane-bound fragments, which are taken up by other cells and degraded within phagosomes. Necrosis, by its turn, is defined as a passive, accidental cell death, resulting from external perturbations with uncontrolled release of inflammatory cellular contents. It culminates in the rupture of the plasma membrane and organelle breakdown, which can lead into local inflammation. Therefore, cancer treatment preferentially searches for drugs which are able to induce an apoptotic cell-death pathway.[225,226]

There are different methods to analyze the cellular death pathway.[225] One of them involves the use of fluorescent probes to link specific morphological features of cell death with particular molecular cell death events. For instance, the propidium iodide (PI)/Annexin V-Alexa Fluor 488 assay. This assay is based on the use of two different fluorescent probes that, combined, allows to elucidate the morphology of the cells, *ergo*, their cell-death pathway. First, PI is a fluorescent membrane-impermeant dye that stains the nuclei by intercalating between the stacked bases of nucleic acids. Since PI enters the cell only if its membrane becomes permeable, it is used to measure the integrity of cell membranes. Low fluorescence in the PI probe indicates either alive cells or apoptotic pathway (membrane-bound fragmentation).[225]

Annexin monitors phosphatidylserine (PS) exposure. PS is an aminophospholipid that resides in the inner part of the plasma membrane of living cells. During a cell-death process, it is either actively externalized to the outer surface to be recognized by phagosomes in apoptosis, or released, in the case of necrosis. Therefore, high fluorescence intensity on the Annexin V test points to a dead cell.[225]

Having all of this in mind, PI/Annexin V fluorescent probes were used with **C1** to assess the induced mechanism of HeLa cells death. The obtained dot plots are shown in **Figure 3.15**. The experiment was performed at the IC_{50} value of **C1** for 24 h (about 70 µM), which was determined in cell-viability assays prior to this experiment.

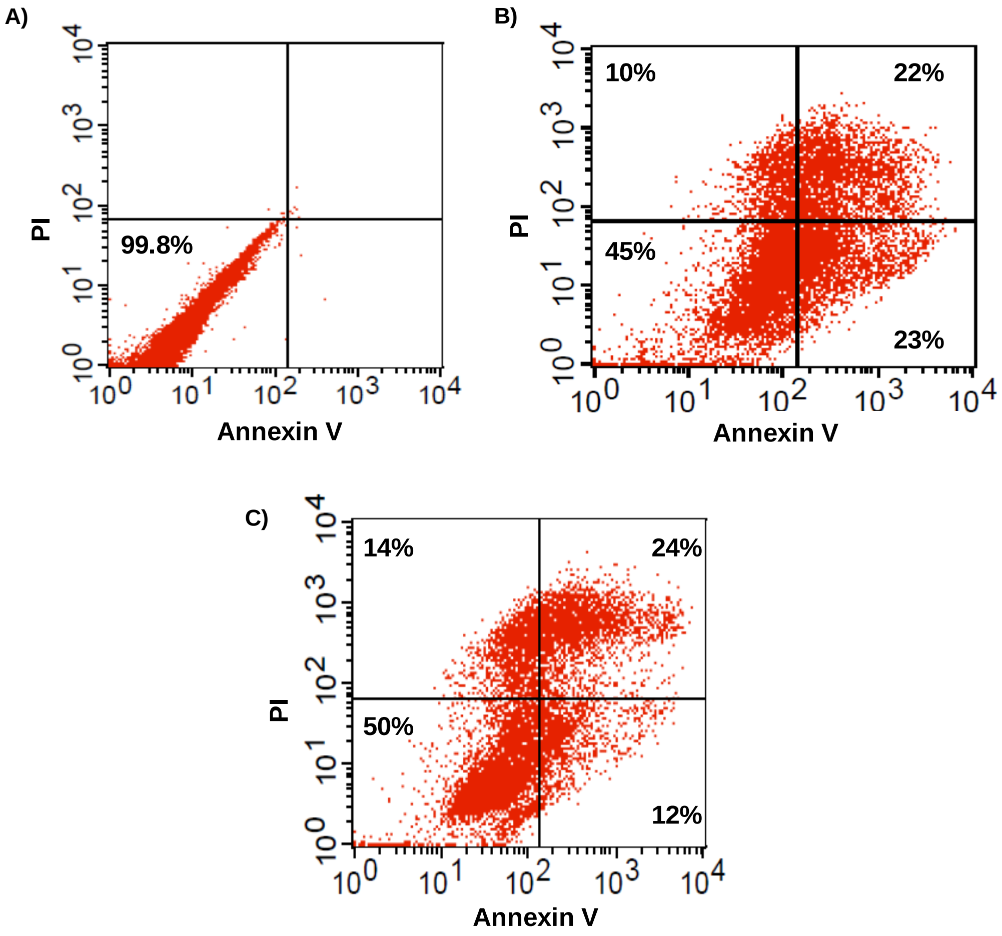

Figure 3.15. Annexin V/PI staining detected apoptosis on HeLa cells by flow cytometry of (**A**) control cells, (**B**) cells treated with cisplatin at 40 µM ($IC_{50,\ 24\ h}$)[213] as control, and (**C**) cells treated with **C1** at 70 µM ($IC_{50,\ 24\ h}$) for 24 h. Axis refer to units of fluorescence. Percentages in each quadrant indicate the cell events respect to the total amount of cells.

First of all, data indicate that about 50% of HeLa cells are dead after the treatment with **C1**, which was already expected using the IC_{50} concentration of the complex. Interestingly, among all the dead cells, at least about 12% of cells are in the early apoptotic stage. This value is in the range of cisplatin, which is well-known to induce apoptotic pathway.[227–229] The rest of death cells (24%) have high fluorescence values of PI, indicating that the membrane is not intact. This might point to a necrosis, with loss of membrane integrity, or to an apoptotic necrosis (late apoptosis). This last mechanism involves an early apoptosis which, with time and the absence of phagocytosis, ends up in the membrane lysis of the already formed apoptotic bodies, and in the organelles breakdown. To enlighten the mechanism of this 24% of cells, kinetics assays would be required.

In any case, results are promising since **C1** induce apoptotic cancer cell-death, at least partially, and this provides an added value to the mechanism of action of this complex.

3.5 Pharmacokinetic features of the potential anticancer drug C1

As detailed in *Section 1.4*, a chemotherapeutic agent has a long journey before reaching the final target: the tumor. Among all the different and complex steps that comprises the pharmacokinetics of a future drug,[130,131] already summarized in *Section 1.4*, body distribution of the compound throughout the blood stream arises as one of the aspects that offers major barriers for the drug to reach the final target. Many developed drugs are degraded along its distribution way throughout the body or are deactivated due to the interactions with proteins, sometimes leading to side-effects.[134,230,231]

In light of this, two main aspects have been considered interesting to be evaluated for any future potential anticancer agent. First of all, the stability of the compound in biological media and/or plasma, and, secondly, its interaction with proteins that can be found along the journey towards the tumoral cell. These are aspects that have been underestimated in many studies, and that indeed will give us valuable pharmacokinetical information regarding the candidacy of **C1** as a future anticancer drug.

As already stated in *Section 1.4*, we are aware of the complexity of this field of study. In our case, first research steps on some pharmacokinetic characteristics of complex **C1** have been explored in this thesis work.

3.5.1 Stability of **C1** in the biological cell culture medium

Minimum Essential Medium (MEM) is usually used for the *in* vitro cytotoxicity studies. It is one of the most widely used of all synthetic cell culture media, developed by Harry Eagle and firstly published in 1959.[232] It is composed of 6 salts ($CaCl_2$, KCl, $MgSO_4$, NaCl, Na_3PO_4, $NaHCO_3$), glucose, and supplemented with 13 amino acids and 8 vitamins. Variations of this MEM, such as Dulbecco's MEM (DMEM), have higher concentrations of vitamins, amino acids and glucose apart from containing Fe(III) salts and phenol red for pH indication.[233] The theoretical pH is around 7.3. Particularly, DMEM was used in the cytotoxicity assays of complexes **C1**, **C2** and **C3** and their corresponding ligands **L1**, **L2** and **L3** (*Section 3.4*).

Consequently, and without going into detail, the DMEM medium contains potential competitor ligands for the metal-containing species that are dissolved in it. Evaluation of the stability of complex **C1** in DMEM has been carried out by using the ESR technique, and comparing it to its ESR spectrum recorded in DMSO (**Figure 3.16**). Complex **C1** was dissolved in DMEM and incubated at 37 ºC for 24h. ESR spectra show that dissolving **C1** in the biological medium does not alter significantly the coordination environment around the Cu(II) ion, and therefore, does not significantly affect the structure of **C1**. Despite some loss of intensity after 24 h and the appearance of a small shoulder, the Cu(II) species of **C1** is mainly maintained based on the spectral features, which match with the ones recorded at the initial time (t = 0). We can affirm then that **C1** remains as the main Cu(II) species in solution after 24 h of incubation in DMEM.

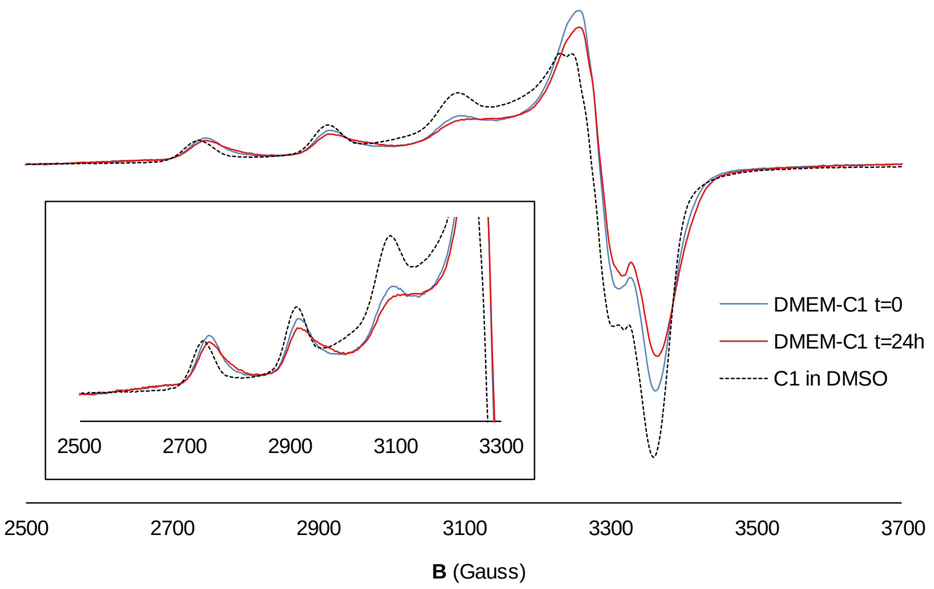

Figure 3.16. X-ESR band of **C1** in DMEM at t = 0 and after 24 h incubation at 37 ºC compared to the X-ESR band of **C1** in DMSO. Samples of **C1** in DMEM were prepared at the same concentration to allow quantitative comparison between them.

3.5.2 Protein-binding studies. A proof-of-concept approach to assess protein-binding influence on the final biological activity of C1

The study of the possible interactions of **C1** with human serum albumin (HSA), Myoglobin (Myo) and Cytochrome C (Cyt) have been monitored by ESI-MS spectrometry. Proteins can easily interact with metal-containing species after their administration and during their biodistribution to the putative targets. HSA (about 66500 Da) was clearly chosen as the most abundant blood stream protein and hence one of the proteins that will surely encounter **C1** once administered. Despite the fact that Myo (about 17600 Da) is only found in humans in the bloodstream after muscle injury, it acts as a model for hemoglobin, a protein highly present in red blood cells. Cyt (about 12000 Da), by its turn, is a small heme protein associated with the inner membrane of mitochondrion, and therefore, found inside cells.

Prior to the incubation of the proteins with the desired complexes, they were characterized by ESI-TOF MS to confirm the absence of any interfering species and to find out their experimental molecular weight (MW). ESI-MS working conditions to ionize and observe proteins must be adjusted and are not the typical ones used for other smaller compounds. In our group, Samper and coworkers reported several studies regarding protein-complex interactions and the specific ESI-MS working conditions.[39,41]

Several ionization states were observed in the m/z working range for the three analyzed proteins. Experimental values determined by ESI-MS are 66550 Da for HSA, 17567 Da for Myo and 12359 Da for Cyt (**Figure 3.17**). In the case of Myo, the experimental value is 615 Da higher than the native apoprotein, which indicates that the heme group is present (616.45 Da).[39]

HSA, Myo and Cyt were incubated with **C1**, at 37 ºC for 24h at different molar ratios, and then each sample submitted to ESI-MS spectrometry. Results evidence that **C1** presents covalent interaction with all the studied proteins, already at a 1:2 (protein:**C1**) ratio (**Figure 3.18**). In general, several peaks can be found corresponding to the complex, or fragments of it, forming adducts with the studied protein.

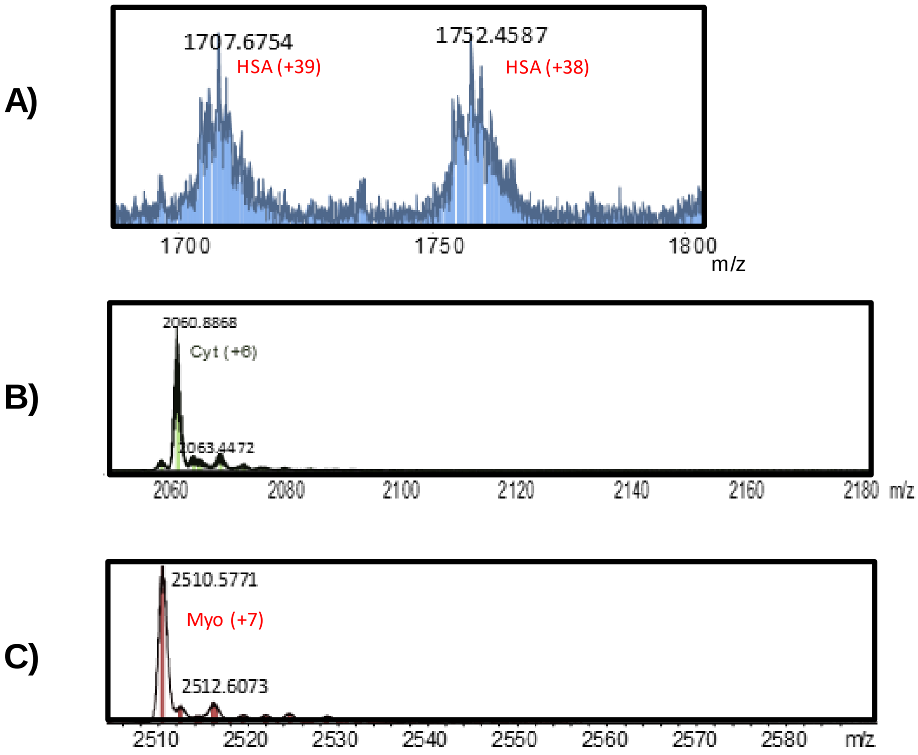

Figure 3.17. Characterization of proteins HSA (**A**), Cytochrome C (**B**) and Myoglobin (**C**) by ESI-MS at selected charge states. Short m/z ranges in each case have been chosen and shown for the sake of simplicity.

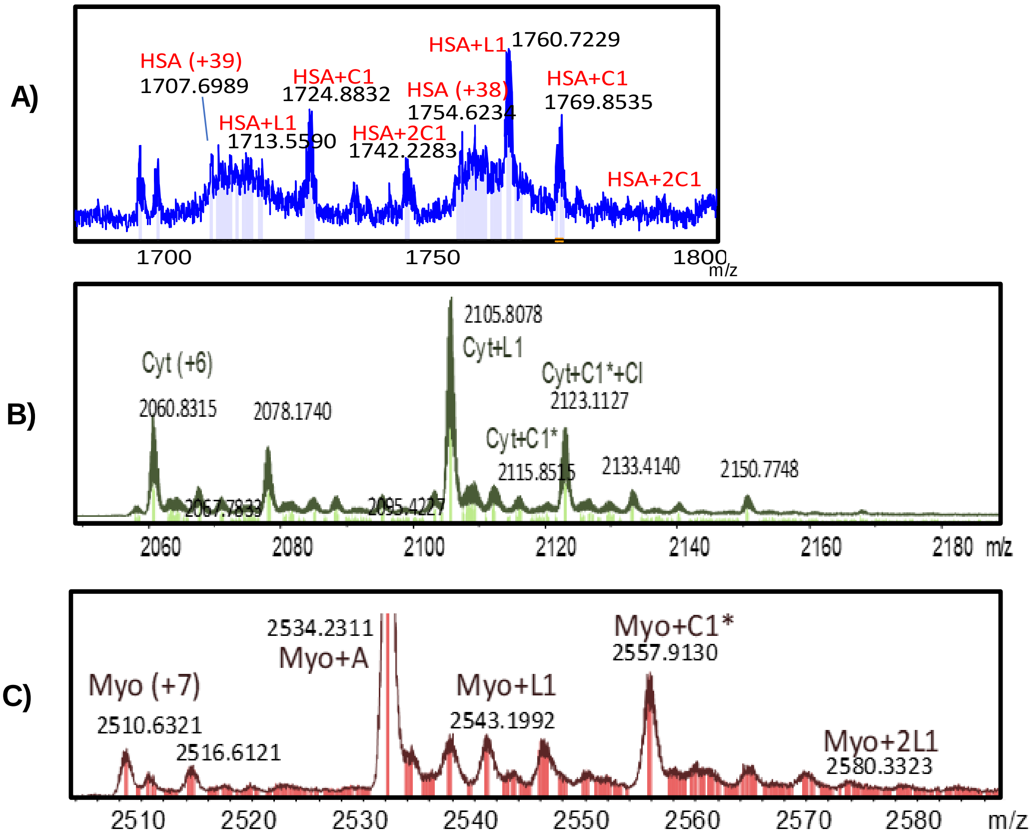

3.18. Protein-**C1** (1:2 ratio) incubations for 24 h at 37 ºC studied by ESI-MS spectrometry. (**A**) HSA-**C1** interactions at the region m/z 1700-1800 (+39 and +38 charge states), (**B**) Cytochrome C-**C1** interactions amplified at the region m/z 2050-2190 (+6 charge state) and (**C**) Myoglobin-**C1** incubation amplified at the region of 2500-2590 (+7 charge state). "C1*" refers to the monomeric unit of complex **C1** and "A" in (**C**) corresponds to compound **1** (**Scheme 3.2**). It is important to note that every "**C1**" in the peaks assignments in HSA (**A**) would equally fit with "2C1*".

Starting with the two smallest proteins, spectra of Cyt and Myo with **C1** clearly show a high interaction of the Cu(II) complex with the proteins (**Figures 3.18B** and **3.18C**). First of all, it is noteworthy the significant decrease on the intensity of the peak corresponding to the free protein at the represented charges of +6 and +7, respectively. In both cases, peaks corresponding to the adduct formed by the protein and the mononuclear framework of **C1** ("C1*") can be identified. The binuclear complex **C1** is cleaved probably due to the binding to the protein. Moreover, adducts corresponding to [Protein+**L1**] can also be assigned, suggesting a possible decoordination of the Cu(II) ion. Both Myo and Cyt structures present several coordinating amino acids for metal ions. Particularly, histidines easily coordinate Cu(II) ions[234,235] and, therefore, these residues might contribute to the formation of the observed adducts (**Figures 3.18B** and **3.18C**). Interestingly, Cyt C has been reported to be related with the apoptotic cell-death pathway,[236,237] which is actually the one preferentially pursued in chemotherapy research. Consequently, interactions of **C1** with cytochrome C could have some implications in the mechanism of death of the cancer cell, *i.e.*, in the apoptosis of the cell.

As a general overview, HSA, a bigger protein than Myo and Cyt, is also able to form several adducts attributed to the protein with **C1** in different charge states at the 1:2 ratio. These adducts contain one and two **C1** entities (or two and four, respectively, in the case of mononuclear frameworks of **C1**: “C1*”) per unit of HSA (**Figure 3.18A**). Cu(II) has been extensively reported to interact with albumin forming Cu(II)-albumin complex or as a ternary complex with amino acids such as histidine.[238] Surprisingly, and despite the fact that there is a Cu(II) specific ATCUN motif in albumin,[239] and that the binding of up to 15 equivalents of Cu(II) has been witnessed (**Figure A22B**), **C1** seems to maintain, at least partially, the structure upon HSA binding (**Figure 3.18A**).

We must take into account that the interaction of a potential metal-based drug with proteins could alter its biological activity. Indeed, *in vivo* studies are absolutely crucial to evaluate the real effect of a drug candidate in a more accurate way than *in vitro* experiments, which solely tests its effect onto attached cells. Cisplatin and Pt-compounds has been reported to be deactivated and cleared from tumoral tissue due to their interactions with proteins.[38,40,41] In our particular case, we propose here a simple assay to monitor the effect of the interaction of a potential drug -in this case **C1**- with proteins in the biological activity.

To the best of our knowledge, this is the first *in vitro* experimental model to simulate and evaluate the effect of the protein-binding on the toxicity of a potential drug towards cancer cells. This represents a further step than just *in vitro* studies, and the idea is to set up a transition model between both *in vitro* and *in vivo* tests. This would enlighten more accurately the real candidacy of a metal-based compound for future *in vivo* assays. To assess it, we incubated the different assayed proteins (HSA, Myo and Cyt) with complex **C1** for 24 h at 37 ºC as for ESI-MS experiments, under sterile conditions. Final mixtures, containing the different [Protein+**C1**] related adducts (**Figure 3.18**) were directly used to perform cytotoxicity assays in HeLa cancer cells. These results were subsequently compared with those obtained for the free complex **C1** (**Figure 3.10**). As observed in all the three cases, cytotoxicity studies clearly evidence that none of the three protein-complex mixtures represent a drawback in the final effect of **C1** in HeLa cancer cell lines (**Figure 3.19**). Special mention must be pointed out in the cases of Cyt and HSA, where the interaction of **C1** with these two proteins does not only do not represent a deactivation of the drug, but indeed implies a significant increase on its cytotoxicity. The calculated $IC_{50,\ 72\ h}$ for the **C1**-HSA adduct is around 15 µM, the same value than that showed by cisplatin, and significantly lower than that calculated for **C1** ($IC_{50,\ 72\ h}$ of 26 µM, **Table 3.3**).

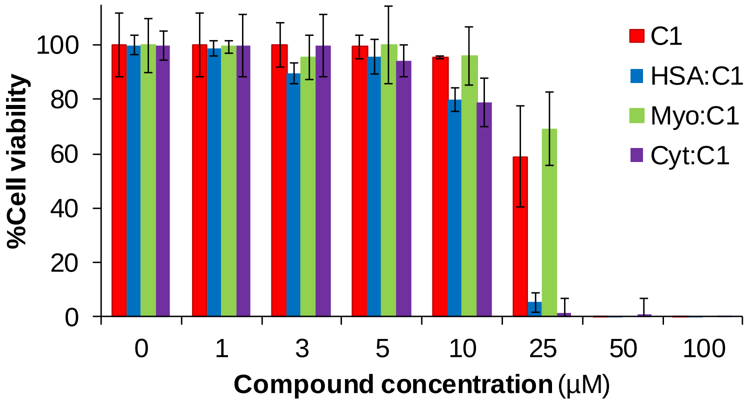

Figure 3.19. Cell viability assays in HeLa cell cultures of HSA:**C1**, Myo:**C1** and Cyt:**C1** mixtures, compared to free **C1** at different concentrations after 72 h treatment. The obtained values average at least three independent experiments.

These data are entirely promising regarding the pharmacokinetic characteristics of **C1**, especially for the case of HSA. As mentioned in the *Section 1.4.2*, HSA is the most abundant protein in the bloodstream, though one of the smallest. A lot of research has been undertaken during the last 40 years with this protein as a potential drug carrier.[143,145,240] Tumors require high doses of nutrients and albumin is observed to have an enhanced uptake around tumoral tissues.[145] This fact is based on the effective hydrodynamic diameter of the albumin (7.2 nm), allowing extravasation into tissue and not into normal tissues: the so-called EPR effect.[145,148] Therefore, HSA outstands as an interesting drug-carrier candidate to load **C1** into tumoral tissues, with even higher cytotoxicity than that found for the free complex **C1** (**Figure 3.19**). Controls with HSA:Cu(II) and HSA:**L1** incubations were also performed (**Figures A22** and **A23**), showing no significant toxicity change respect to free Cu(II) or **L1**. This indicate that the cytotoxicity points to be related to the HSA:**C1** adducts. Ongoing studies are devoted to enhance the applicability of this approach and the scope of the [HSA:**C1**] system for drug delivery.

3.6 Summary and conclusions

This chapter was devoted to the synthesis, biological studies and pharmacokinetics of novel Cu(II) complexes **C1**, **C2** and **C3**, with a high redox-active metallic core and ROS generation capabilities. Here, some important conclusions can be drawn:

1) The synthesis of a novel salphen-based *N*,*O*-donor heteroaromatic ligand **L1** has been described. It has been fully characterized and used to coordinate Cu(II) (complex **C1**). Complex **C1** has been fully characterized. A dinuclear structure and a coordination environment of N_2O_2 about the metal ion is proposed for **C1**, in a square-planar or square-pyramidal geometry.

2) The redox behavior of this novel complex **C1** has been evaluated. The assigned Cu(II)/Cu(I) redox potential ($E_{1/2}$ = -1.07 V) successfully falls into the biological redox window and therefore, the chemical features of **C1** are appropriate to undergo a redox-mediated biological activity.

3) Two novel chloro- and bromo- analogs of ligand **L1** (**L2** and **L3**) have been also successfully synthesized and fully characterized.

4) Ligands **L2** and **L3** have been successfully coordinated to Cu(II), giving rise to complexes **C2** and **C3**. These two new Cu(II) complexes have been characterized, exhibiting the same coordination environment as **C1**. The functionalization of **L1** with halogen groups has not altered the metallic core of the parent complex **C1**.

5) Redox studies have evidenced that **C2** and **C3** have shifted the half-wave potential of the Cu(II)/Cu(I) towards slightly higher potentials ($E_{1/2}$=-1.03 V) with respect to complex **C1**. They both show a more thermodynamically favored reduction from Cu(II) to Cu(I) due to the presence of the electrowithdrawing groups.

6) Potential ROS formation has been evaluated for **C1**-**C3** in a lab-approach by following the consumption of ascorbic acid *via* UV-VIS. The three complexes consume ascorbic acid at a similar or close rate than free Cu(II) ions and, therefore, they show ROS generation capabilities.

7) Cytotoxicity of complexes **C1**, **C2** and **C3** and of the corresponding free ligands has been evaluated in HeLa and MCF7 cancer cell lines. **C2** and its ligand **L2** were not able to be evaluated in MCF7 due to poor solubility. Ligand **L1** showed no cytotoxicity, whereas **L2** and **L3** displayed significant cytotoxicity due to the presence of the halogen groups. The $IC_{50,\,72\,h}$ values for the three complexes are around 25 µM, similar to that found for cisplatin (15 µM). Consequently, the functionalization with chloro- and bromo- groups has not significantly affected the biological activity.

8) **C2** and **C3** have been discarded as potential candidates to be used directly in *in vivo* tests due to their insolubility in biological medium. In any case, they open the gate to

tune the Cu(II)/Cu(I) redox potential *via* functionalization of the ligand and without altering the coordination environment.

9) Cytotoxicity studies in NIH 3T3 as a proof-of-concept for a normal cell line have been also carried out with **C1**. Results highlight a lower toxicity profile with respect to that found in cancer cell lines, which arises as an advantage for future *in vivo* assays and enhances the potentiality of **C1** as a potential future drug.

10) The three complexes exhibit a most-likely oxidative-mediated mechanism of action through ROS generation. Confirmation has been achieved by the *in vitro* ROS generation studies in HeLa cancer cells. **C1** has revealed to generate similar ROS levels than those found for H_2O_2 (up to 3-fold respect to control group), while **L1** has not shown any kind of ROS production.

11) The ROS production capabilities of **C1** are considered to be one of the main factors justifying the higher and apparently selective toxicity observed in the two assayed cancer cell lines (HeLa and MCF7) than in healthy cells (NIH 3T3 fibroblasts). Furthermore, **C1** induces a partial apoptotic cell-death mechanism in HeLa, which is the preferred pathway in cancer treatment.

12) DNA interaction studies have been performed with the three Cu(II) complexes. **C1**, **C2** and **C3** showed high cleaving capacity in the presence of reducing agents. They also interact with DNA *via* non-covalent binding, preferentially groove-binding and electrostatic interactions rather than intercalation. In all cases, no significant DNA structural alterations have been witnessed.

13) A first approach on some pharmacokinetic characteristics of **C1** has been carried out. Complex **C1** is mostly stable in the DMEM cell culture after 24 h of incubation, and therefore it is the species that exerts *in vitro* cytotoxicity. Binding studies with proteins by ESI-MS reveal that the complex **C1** strongly interacts with HSA, Myo and Cyt, based on the presence of peaks attributed to [Protein:$\mathbf{C1}_{\text{(dimer/monomer)}}$] adducts. The interaction of **C1** with these proteins does not represent a drawback in its cytotoxicity. Indeed, **C1** displays higher toxicity in cancer cells when bound to Cyt and HSA, the latter arising then as a promising drug carrier to be explored.

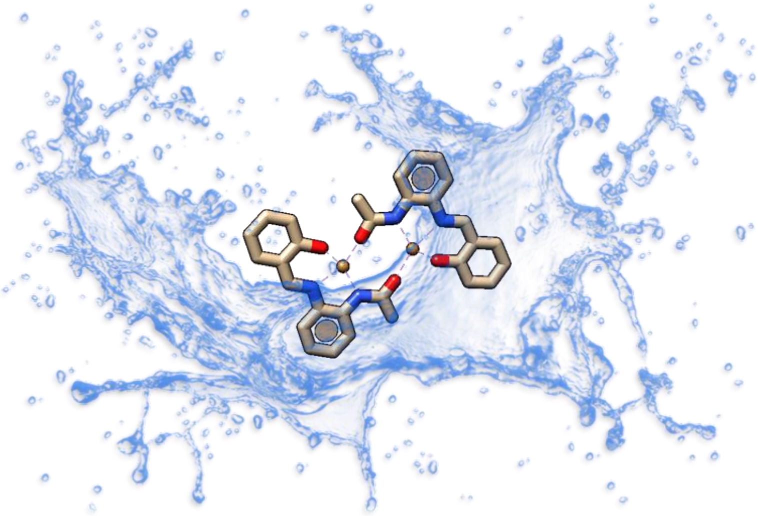

CHAPTER 4

Overcoming the solubility issues of the high redox metallic core of C1: sulfonate and arginine derivatives

This chapters details the functionalization strategies of complex **C1** with sulfonate and arginine groups in order to increase its solubility in water and, therefore, enhance its pharmacological properties. Biological studies (cell-viability assays and uptake studies) are also carried out to compare the activity of the novel derivatives respect to the parent complex **C1**.

CHAPTER 4

Overcoming the solubility issues of the high redox metallic core of complex C1: sulfonate and arginine derivatives.

Previously, we have designed and synthesized three analogous Cu(II) complexes (**C1**, **C2** and **C3**), capable of displaying a high ROS production and showing remarkable anticancer effect in HeLa and MCF7 cells (Chapter 3). **C1** was also tested in fibroblasts cell lines as a proof-of-concept for normal cells, exhibiting lower toxicity than that found for cancer cells. However, some solubility issues were encountered for **C2**, **C3**, and to a lesser extent for **C1** in biological medium. Their poor solubility and the need to use a small percentage of DMSO in the *in vitro* experiments are limiting factors for *in vivo* model assays.

This chapter is focused on the functionalization of the ligand **L1** to increase the water-solubility of the corresponding Cu(II) complex without inhibiting the redox-active metallic core of **C1** (*i.e.* without altering the coordination environment around the Cu(II) ion). Increasing the solubility of the final complexes might enhance their bioavailability and therefore, their activity. Two different strategies have been explored and will be presented here. The first strategy involves the addition of a sulfonate group and the second one, the addition of an arginine (Arg) residue. Both groups have biological relevance and will introduce a charge of opposite sign. Namely, the sulfonate functionalization will provide a global negative charge at biological pH while the functionalization with the Arg residue will lead into a positive charge. This will allow us to gauge the effect of the two opposite charges in the biological activity of the complex. Noteworthy, the interest on exploring the second approach (*i.e.* Arg) is twofold since it also represents a starting point to functionalize the system with Arg-rich Cell Penetrating Peptides[165,241,242], as it will be detailed later on in *Chapter 5*.

4.1 Synthesis of the water-soluble sulfonate Cu(II) complex: C4

4.1.1 Synthesis and characterization of the sulfonate derivative of **L1**: ligand **L4**

The synthesis of the sulfonate ligand (**L4**) has been performed following the strategy depicted in **Scheme 4.1**. The addition of the sulfonate group was done in the aldehyde scaffold before the condensation step with the aromatic amine.

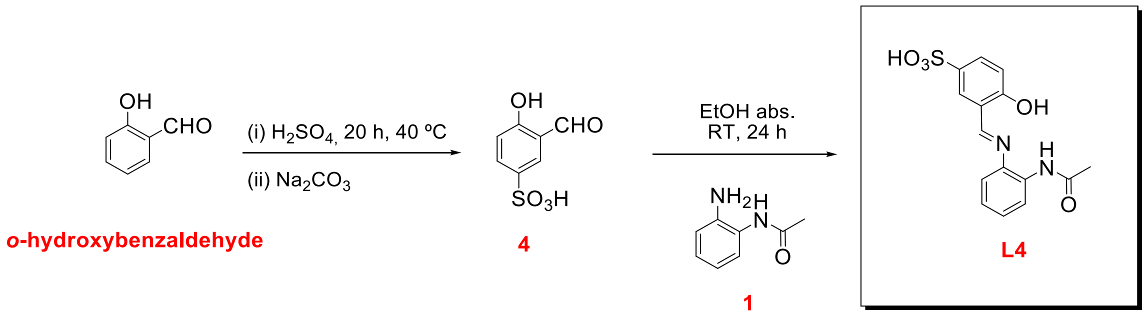

Scheme 4.1. Synthetic strategy to obtain **L4**.

Basically, *para*-sulfonation of the starting material *o*-hydroxybenzaldehyde was achieved *via* S_NAr reaction.[208] Standard sulfonation reactions are normally performed at temperatures around 100 ºC, however, this step was carried out at a maximum of 40 ºC to prevent the oxidation of the aldehyde in such acidic conditions (**Scheme 4.1**).[243] This compromise temperature renders less side-products but also lower yields (11%). Successful *para*-sulfonation was confirmed by ^1H NMR (**Figure A24**).

Afterwards, compound **4** was reacted with **1** to yield **L4**. Obtention of the final ligand was confirmed by ^1H NMR, where the signal at δ 10.26 ppm corresponding to the -C*H*O group of the salicylaldehyde shifted to upfield (**Figure A25**). This shift matches with an imine bond, which is less deshielded due to the lower electronegativity of the *N* atom. ^{13}C NMR (**Figure A26**) and MS (**Figure A27**) data confirmed the identity of **L4**.

4.1.2 Synthesis and characterization of the Cu(II) complex of the ligand **L4**: complex **C4**

Complexation of **L4** was performed by using Cu(OAc)$_2$, as for **C1**, **C2** and **C3** (*Chapter 3*). However, in this particular case, and differently from the synthesis of the previous complexes **C1**, **C2** and **C3** (*Chapter 3*), the use of additional equivalents of acetate anions was required. The sulfonate group (p$K_{\text{a, water}}$ = -2.6) will compete in an acid-base reaction with both the -O*H* of the phenol group (p$K_{\text{a, water}}$ of 9.95) and the -N*H* of the amide group (p$K_{\text{a, water}}$ of 23.3) of **L4**.[208] Even the fact that the given p*Ka* values are in water and the reaction is made in organic solvent, they can be proportionally corrected by using a conversion factor.[244] For the sake of relative comparison, they can be equally used as a guidance to conclude that the sulfonate group will be in any case the first one to be deprotonated.

The crude solid of the complex **C4** was isolated by solvent removal and purified by washing it with DCM and ACN several times. The proposed solid structure is shown in **Figure 4.1**. We expect that **L4** coordinates in a tetradentate fashion as **L1**, with three chelating donor atoms (N, N, O) in a planar structure. The fourth *O*-donor atom of the plane would arise from the second entity of the complex in the dimeric structure, analogous to that found for **C1** in solid state. The dimeric state of the complex **C4** was evidenced by HR ESI-MS (**Figure 4.2A**). Peaks attributed to [**C4**+H]$^+$ (*m/z* = 790.9392, **Figure 4.2A**) and also the corresponding Na adducts could be found (*m/z* = 812.9217). Experimental values fit with the calculated ones for the dinuclear H and Na adduct structures.

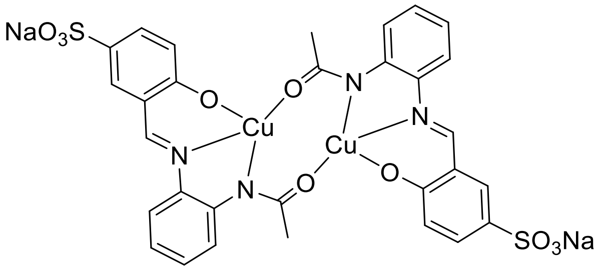

Figure 4.1. Proposed dimeric structure present in the solid for complex **C4**.

It is important to mention that there is also a peak at *m/z* = 395.9831 that can be assigned to the monomeric form of the complex ([**C4**$_{\textbf{monomer}}$+H]$^+$, **Figure 4.2B**). This could co-exist with the dimeric form or arise from fragmentation in the spectrometer, as already seen in *Chapter 3* for **C1**, **C2** and **C3**. In this case, elemental analysis did not unravel solid structural features due to the presence of different counterions for the sulfonate group and salts in the isolated solid. Differences between experimental values and calculated ones were larger than the 0.4% allowed experimental error. Consequently, the presence of the monomeric form (coordinated by a solvent molecule in the fourth position) could co-exist in the solid structure with the dimeric form.

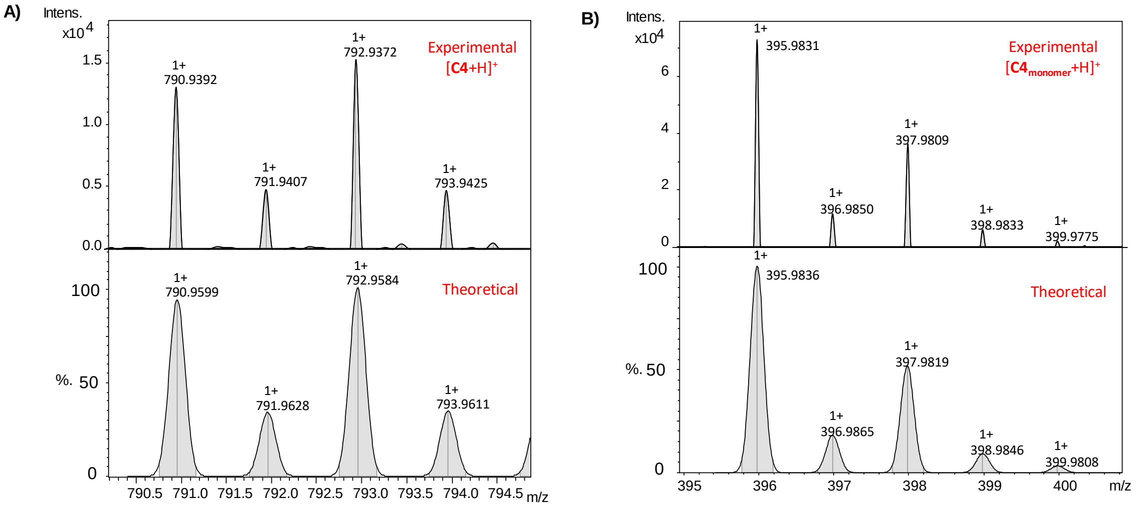

Figure 4.2. Experimental (top) and theoretical (down) HR-MS spectra (ESI$^+$, MeOH) related to **C4**: (**A**) [**C4**+H]$^+$ and (**B**) the monomeric form of complex **C4**, [**C4**$_{monomer}$+H]$^+$.

Therefore, it was crucial to perform ESR measurements to validate the speciation in solution. The ESR spectrum (**Figure 4.3**) showed that there is only one Cu(II) species in solution for **C4**. Both **C1** and **C4** have the same ESR parameters (**Table 4.1**), indicating equivalent electronic environments around the Cu(II) ion, namely a N_2O_2 coordination sphere in a regular square-planar or square-pyramidal derived geometry. These results reinforce the fact that the functionalization has not affected to the Cu(II) center.

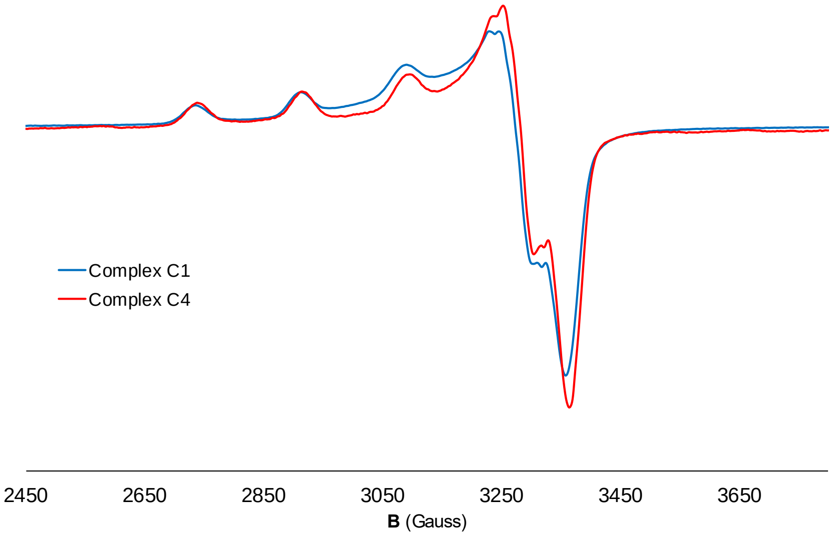

Figure 4.3. X-ESR band of complex **C4** in DMSO.

Table 4.1. ESR parameters for complex **C4** extracted from DMSO solution (**Figure 4.3**). **C1** is placed for the sake of comparison.

Complex	$g_{//}$	$A_{//}$ (10^{-4} cm^{-1})	$g_{\perp}$	$A_{\perp}$ (Gauss)	$g_{//}/A_{//}$ (cm)
C1	2.244	183	2.043	<20-30	122
C4	2.240	186	2.039	<20-30	120

As stated for complex **C1** (*Section 3.2.1*), the proposed N_2O_2 coordination mode in solution based on the ESR data can be explained by the three donor atoms (N, N, O) from the **L4** binding pocket in a tridentate fashion, and a DMSO solvent molecule in the fourth coordination position of the equatorial plane (*via* the O donor atom). This would lead to mononuclear species of **C4** in DMSO solution (**Figure 4.4**), analogous to what has been observed in the ESR data of **C1**-**C3** (*Chapter 3*).

Crystals for complex **C4** have been obtained but they were not suitable to perform X-Ray diffraction analyses. Ongoing attempts are being carried out to get suitable crystals to elucidate and confirm the solid structure of **C4**.

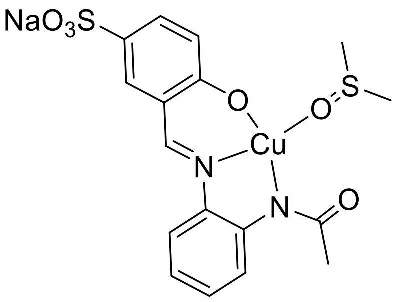

Figure 4.4. Proposed structure of complex **C4** in DMSO solution in a square-planar geometry. The presence of an axial ligand (square-pyramidal geometry) cannot be ruled out according to the ESR data.

4.2 Synthesis of an arginine derivative of ligand L1: L5. A bioconjugation approach

After evidencing that the sulfonation of the ligand **L1** (**L4**) did not alter the coordination environment of the final metal complex **C4** (*Section 4.1*), the second strategy was pursued. The coupling of **L1** with an arginine (Arg) will not only provide a net positive charge to the final Cu(II) complex (in opposition to the negative charge provided by the -

-SO_3^- group), but will also serve as a proof-of-concept to stablish a synthetic strategy for the conjugation of specific Arg-rich CPPs.

In light of this, the first step consisted of designing a synthetic strategy to couple the aminoacid into the organic precursor. Standard solid-phase methodologies,[245] widely used for peptidic synthesis and originally developed by R. B. Merrifield in 1960s,[246,247] were explored. This common technique uses 9-fluorenylmethyloxycarbonyl (Fmoc) or t-butyloxycarbonyl (Boc) protecting groups for the amino terminal groups of the amino acids (*aa*) and the synthesis is carried out in solid-phase (attached to a resin) from the carbonyl group side (*C*-terminus) to the amino group side (*N*-terminus) of the amino acid chain.

4.2.1 Solid-phase synthesis of the Arg(Pbf)-Resin precursor (**6**)

The first step was to attach the commercial Fmoc-Arg(Pbf)-OH to the Fmoc protected resin. We used a Rink Amide MBHA resin (100-200 mesh) to obtain an amide group at the C-terminus upon final cleavage. The strategy is depicted in **Scheme 4.2**. Since this resin is Fmoc protected, the first step was the removal of the Fmoc group with piperidine (20% in DMF). Subsequently, the coupling of the *aa* to the resin was performed using *N,N,N′,N′*-Tetramethyl-*O*-(1*H*-benzotriazol-1-yl)uronium hexafluorophosphate (HBTU) as a coupling agent, which activates the -COOH group in mild conditions.[245,248]

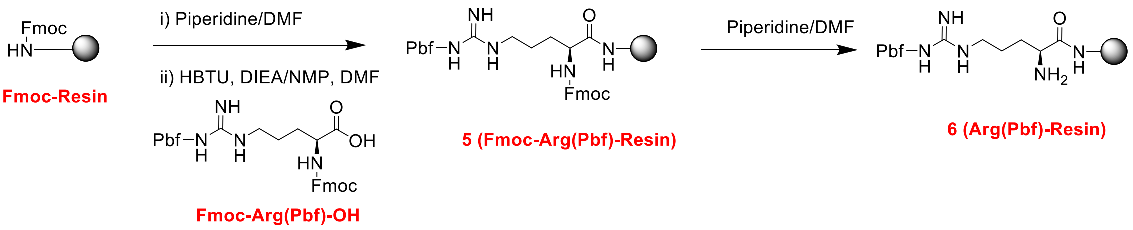

Scheme 4.2. Solid-phase synthesis of Arg(Pbf)-Resin (**6**) precursor. The obtention of **5** has been carried out with *N,N,N′,N′*-Tetramethyl-O-(1*H*-benzotriazol-1-yl)uronium hexafluorophosphate (HBTU) and *N,N*-diisopropylethylamine (DIEA) using a mixture of DMF and NMP as solvents. The deprotection of the Fmoc group was achieved using Piperidine (20%) in DMF. Pbf (2,2,4,6,7-pentamethyldihydrobenzofuran-5-sulfonyl) is a protecting group for the terminal guanidino group of the Arg.

Firstly, Fmoc-Arg(Pbf)-OH was mixed with HBTU to form a good leaving group in the carboxylic of Fmoc-Arg(Pbf)-OH and favor the nucleophilic attack of the amino group of the deprotected resin to the activated -COOH of the Fmoc-Arg(Pbf)-OH to get **5**. Finally, **6** was obtained after removal of the Fmoc group of **5**. To evaluate the achievement of the attachment, an aliquot of compound **6** was taken and the *aa* simultaneously deprotected and cleaved from the resin with a TFA/H_2O/TIS (95:2.5:2.5) mixture.[245] ^1H NMR confirmed the presence of the Arg (**Figure A28**).

4.2.2 Synthesis of Arg-conjugated ligand precursor (11)

Once the Arg is attached to the resin, different coupling strategies to obtain the final Arg-conjugated ligand precursor (**11**) were explored (**Scheme 4.3**).

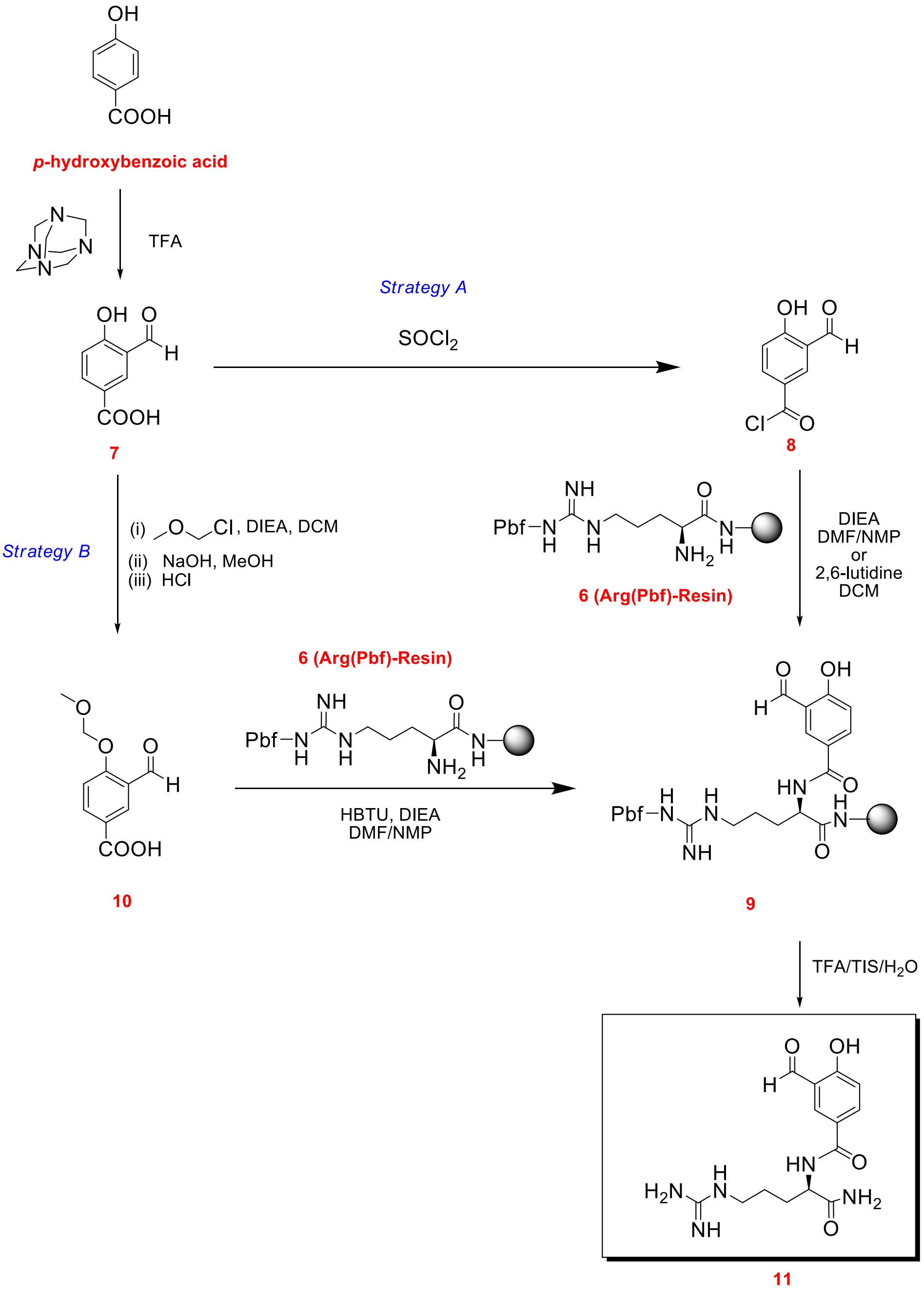

Scheme 4.3. Synthetic strategies to perform the coupling of the Arg(Pbf)-Resin (**6**) to the organic scaffold **7**.

As done for **L4**, the aldehyde scaffold was selected for functionalization. Prior to the election of **7** as precursor, other options were attempted to anchor the *aa* to the aromatic scaffold, such as the use of *p*-(chloromethyl)-*o*-hydroxybenzaldehyde, but without success. The precursor **7** was successfully obtained (**Figure A29**) and two different strategies (*Strategies A* and *B*, **Scheme 4.3**) were carried out in order to activate its -COOH group for subsequent attachment to the Arg(Pbf)-Resin precursor (**6**). Initially, the idea was to avoid the use of coupling agents such as HBTU because previous tests involving the reaction of the compound **7** with only HBTU in basic conditions -and without any compound **6**- had given rise to a mixture of species, according to NMR data. The phenol group of **7** (pK_a of phenol in DMSO is 18.0)[249] could be then reacting with HBTU and interfering in the -COOH activation with HBTU.

Consequently, *Strategy A* was first attempted, which involved the formation of an acyl chloride (**8**), and then the reaction with the Arg(Pbf)-Resin (**6**).

Since compound **8** is highly reactive, it was prepared *in situ* and directly reacted with **6** in basic media using two different bases: DIEA and 2,6-lutidine. After letting the mixture stir overnight, the crude compound **9** was deprotected and cleaved from the resin using TFA/H_2O/TIS (95:2.5:2.5) mixture. The obtained crude of compound **11** was analyzed by analytical reversed-phase HPLC (**Figure 4.5**). Although there are some differences in relative intensities of the observed peaks (*P*, *Arginine*, and *Q*, with R_t = 11.5, 15 and 20 min, respectively) depending on the base, there is still a significant amount of unreacted Arg (R_t = 15 min). Both peaks *P* and *Q* (**Figure 4.5**) were isolated using preparative reversed-phase HPLC and characterized by MS and ^{1}H NMR (**Figure A30**). The first compound matches with **11**, whereas *Q* could correspond to an organic compound analogous to **7** without the Arg moiety (**Figure A30**). However, and despite having successfully obtained **11**, increasing reaction times did not improve the conversion, so we decided to set up another synthetic procedure.

Based on the fact that the coupling required basic media, and that under these conditions the phenol group might compete, *Strategy B* (**Scheme 4.3**) was explored. Protection of the -OH group was attempted with common 2-tetrahydropyranyl (THP) and methoxymethyl (MOM) protecting groups.[250] THP protection reaction gave rise to low yields and therefore MOM group was chosen. Compound **10** was synthesized by reacting **7** with chloromethyl ether (CMME) in anhydrous DCM. In the protection procedure, a MOM ether-ester intermediate was obtained as the carboxylic acid of **7** reacted to form an ester group. Consequently, the -COOH of **10** was recovered after the hydrolysis of the ester intermediate (**Figure A31**).

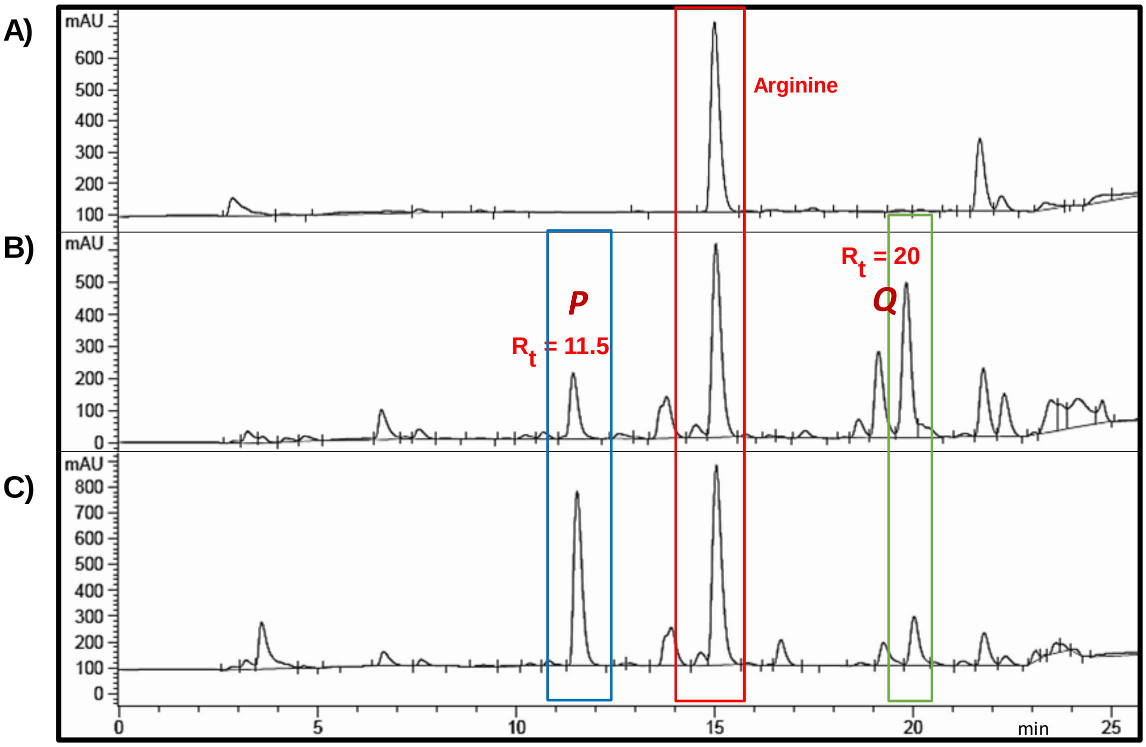

Figure 4.5. Analytical reversed-phase HPLC (8-36 %B in 20 min, C12 Jupiter column) of: (**A**) Arg, (**B**) crude **11** using DIEA as a base and (**C**) crude **11** using 2,6-lutidine as a base. Absorbance at 220 nm was monitored. Peaks *P* and *Q* correspond to those with R_t = 11.5 and 20, respectively.

Compound **10** was used without any further purification for the coupling with Arg(Pbf)-Resin (**6**). In this case, and differently from what we attempted in *Strategy A*, we could try to use HBTU since the phenol group was protected. After 2 h of reaction and subsequent treatment under acidic conditions (TFA/H_2O/TIS), analytical HPLC clearly showed a higher conversion than that from *Strategy A* (**Figure 4.6**). The ratio of the integration between compound **11** (R_t = 11.5 min) and unreacted Arg (R_t = 15 min) in the *Strategy B* is at least about 6 times higher than that found for any of the two approaches in the *Strategy A*. Therefore, this methodology appears to be more useful for this kind of coupling and a better approach for future CPPs attachment.

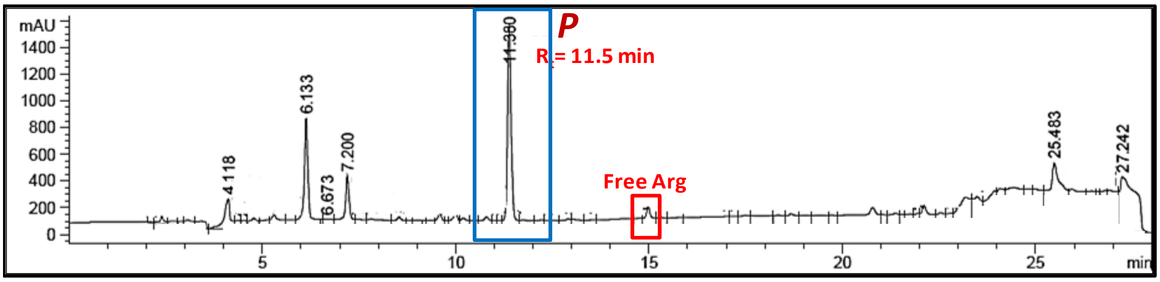

Figure 4.6. Analytical reversed-phase HPLC (8-36 % solvent B in 20 min, C12 Jupiter) of crude **11** from *Strategy B*. Absorbance at 220 nm was measured. *P* corresponds to the peak with R_t = 11.5.

Peak corresponding to compound **11** (*P*, **Figure 4.6**) was purified using preparative reversed-phase HPLC and characterized by ^{1}H NMR (**Figure 4.7**). As observed in the NMR spectrum, there is one proton signal at 9.92 ppm corresponding to the -C*H*O group of **11**, together with three aromatic signals (8.12, 7.92 and 7.01 ppm), which can be attributed to the three aromatic protons of the compound (H_2, H_4 and H_5). The region from 4.5-1.5 ppm is ascribed to the Arg moiety of compound **11**. However, if we consider the integrations of these signals and we compare the ratio between the aromatic and -CHO integrals respect to the Arg moiety, it is clear that there is an excess of Arg with respect to the aromatic scaffold of **11**. In fact, there is another set of three aromatic signals (7.51, 7.46 and 6.83 ppm, identified with an asterisk in **Figure 4.7**) with the same pattern (multiplicity and *J* values) than the respective set of aromatic protons of **11**.

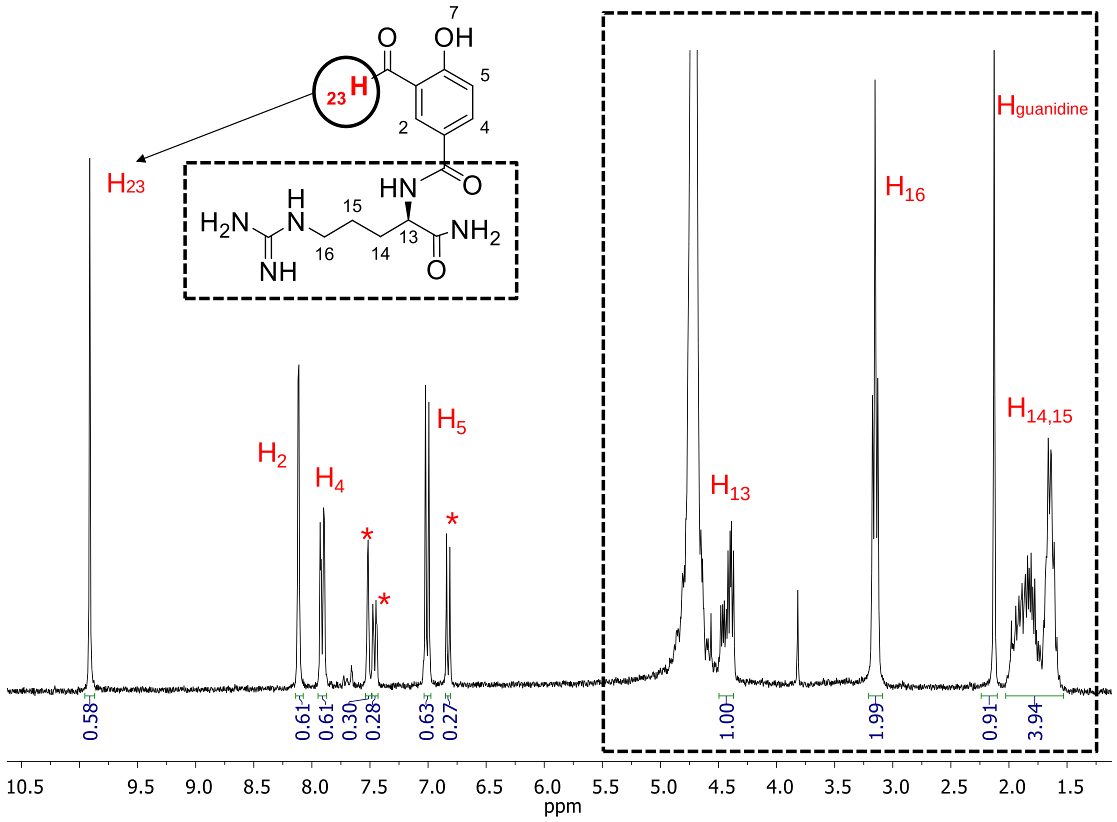

Figure 4.7. ^{1}H NMR (D_2O, 300 MHz) corresponding to the isolated peak (*P*, **Figure 4.6**) of crude **11**. The asterisk refers to another set of aromatic proton signals of a non-identified compound.

This new compound (*, **Figure 4.7**) seems to have the same aromatic scaffold but more shielded than **11**. Moreover, the addition of the integrations of the aromatic protons of **11** plus those belonging to this new unidentified compound (*) matches with one Arg moiety. Therefore, the new compound must be conjugated to the Arg too. The only difference, thus, appears to be in the -CHO group, where a sole ^{1}H signal can be observed in the aldehyde region. This -C*H*O signal is clearly attributed to compound **11** based on the integration values with respect to the set of aromatic protons. The non-identified compound does not have an aldehyde group, yet the same substitution aromatic pattern as in compound **11**.

After the NMR analysis, some aspects still remained unclear. Even though the coupling strategy *B* seemed to give a good conversion from **7** to **11**, there is another non-identified side-product (*, **Figure 4.7**). This has the same aromatic substitution pattern, it is attached to the Arg moiety -probably through amide bond too-, has no aldehyde functional group (**Figure 4.8**) and has the same retention time in the used HPLC conditions as **11**, which difficult its identification. Further studies were performed to unravel the nature of this side-product and to avoid or separate it from pure **11**.

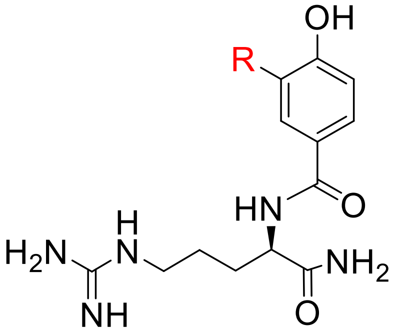

Figure 4.8. Proposed structure for the side-product formed in the synthesis of **11**. ***R*** accounts here for any functional group, excluding aldehyde or imine.

Repetition of the coupling strategy changing concentrations of **10**, **6**, HBTU and DIEA indicated that this side-product was also originated in the formation of compound **10**. We were able to observe its formation either in the hydrolysis step of the intermediate **12** or in the Arg coupling reaction (**Scheme 4.3**). In both reactions, the basic media might be one of the causes of the generation of this side-product.

Subsequent analyses were focused on changing the parameters of the reaction from **12** to **10** (**Scheme 4.4**). The assayed conditions are summarized in **Table 4.2**.

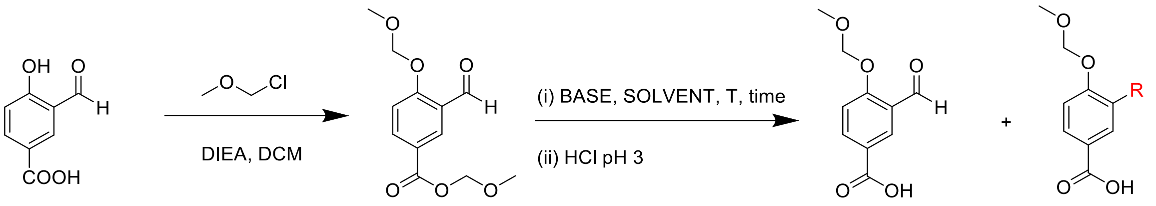

7 **12** **10** **13 (side-product)**

Scheme 4.4. Synthetic strategy of MOM-protection with the intermediate ether-ester **12** and the formation of the unknown side-product, identified as compound **13**. *T* represents temperature. The different assayed conditions of the hydrolysis step of **12** can be observed in **Table 4.2**. *R* accounts here for any functional group (except *-CHO* or *-CHN*).

Table 4.2. Experimental conditions tried for the hydrolysis procedure of **12** (**Scheme 4.4**). All the reactions were carried out in the presence of NaOH as a base (15% in water) for 3-4 h, otherwise mentioned.

Conditions	Cosolvent[a]	Concentration of 12 (mg/ml)	T (ºC)	Yield 10-13 (%)[b]
A	MeOH	3.5	75	90-10
B		3.5	RT	99-1
C[c]		3.5	RT	99-1
D		11	75	25-75
E	THF	3.5	RT	90-10
F[c]		3.5	RT	45-55
G		4	75	35-65
H		9	75	5-95
I[c,d]		3	RT	1-99

[a] *The water:organic cosolvent proportion is always 1:1.5.*
[b] *Based on the integration of the signals of each compound in ^{1}H NMR.*
[c] *The reaction time was ≥ 15 h.*
[d] *LiOH (15% in water) was used as a base instead of NaOH.*

Without going into detail into all the experimental conditions, the formation of the side-product **13** depends on several experimental factors. It is mainly generated at higher concentrations of **12** (*Conditions A vs. D* or *E vs. H*). Secondly, THF also tends to promote the formation of **13** respect to MeOH (*Condition F* respect to *C*). The change on the base also affects the proportion of the side-product **13**. LiOH, which is a weaker base than NaOH, was also attempted. It can be seen that with LiOH the side-product **13** is preferentially formed (*Conditions I* compared to *F*). And, finally, higher temperatures give rise to higher amounts of **13** (*Conditions A vs. B* or *E vs. G*). Finally, it is also worthwhile to mention that *Condition I* was also tested by starting directly from pure compound **10** instead of **12**. From **10**, we were able to obtain 55% of compound **13** too. Consequently, **13** is formed both with the ester (**12**) and with a -COOH group (**10**) in the *para-* position. The -COOH in **10** does not impair the generation of compound **13**.

Based on the results shown in **Table 4.2**, we were able to isolate compound **13** (*Conditions H* or *I*) and characterize it (**Figure 4.9**). ESI-MS (**Figure 4.10A**) and ^{1}H NMR (**Figure 4.10B**) analyses indicate a reduction of the -CHO group of **10** to a benzyl alcohol (-CH_2OH) in **13** (**Figure 4.9**).

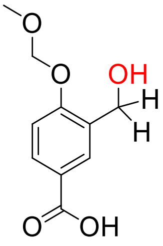

13

Figure 4.9. Proposed structure for the side-product **13**. The highlighted benzyl alcohol comes from the aldehyde reduction of **10** or **12** (**Scheme 4.4**).

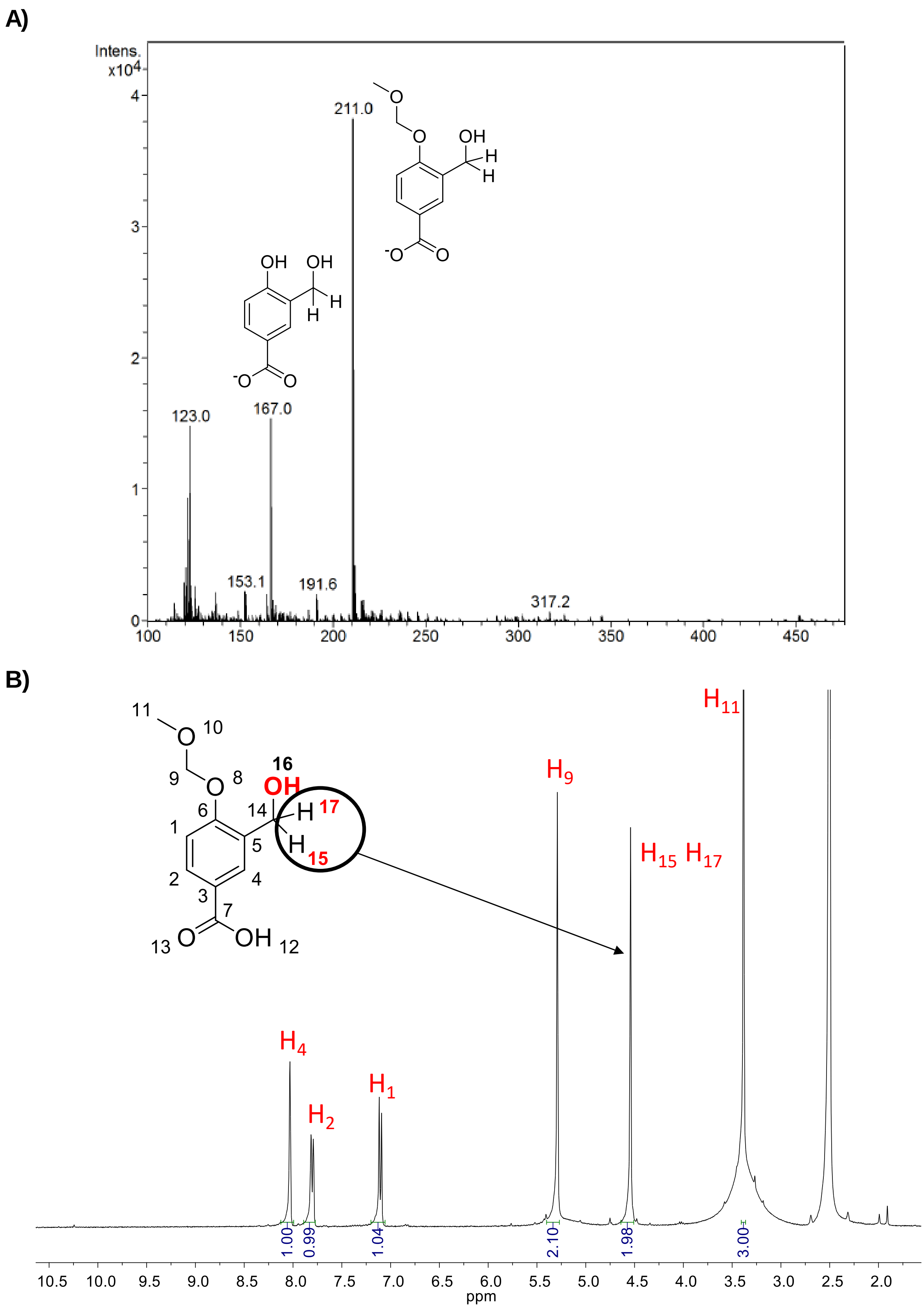

Figure 4.10. (**A**) ESI-MS spectrum (ESI$^-$, MeOH) and (**B**) ^{1}H NMR (360 MHz, d_6-DMSO) of compound **13**.

As observed in the ^{1}H NMR spectrum (**Figure 4.10B**), there is a singlet at δ 4.6 ppm integrating 2H that can be assigned to the two homotopic protons of the benzyl alcohol (H_{15} and H_{17}). These two protons were not observed previously in the spectrum of **11** (**Figure 4.7**) due to overlapping with the peak of the residual solvent (D_2O). As already seen before, no peak corresponding to -C*H*O can be observed. Moreover, ESI-MS peaks (**Figure 4.10A**) at *m/z* 211.0 and 167.0 can be related to compound **13**.

One of the hypotheses that we propose regarding the mechanism of this *in situ* reduction is based on a crossed Cannizzaro.[251] As reported by Swain and coworkers already in 1978, there is a reduction of the benzaldehyde by the methoxide ion in aqueous methanol. This would give rise to the benzyl alcohol and also to an acid compound (H_2CO_3 after acidification), which could be easily removed during the work-up and not seen in the NMR spectrum. However, the fact that **13** is also obtained when using THF rules out this hypothesis. So far, we have no consistent explanation which encompasses both solvents.

To avoid this problem and considering that an analogous side-product was obtained in the synthesis of **11** (**Scheme 4.3** and **Figure 4.7**), we decided to protect the aldehyde group prior to the coupling. Several typical protecting groups for the -CHO group of **10** were considered: acetals, hemiacetals, and thioacetals.[250]

We attempted to protect the aldehyde *via* dimethyl acetals and 1,3-dioxolanes. However, no quantitative reaction was achieved and the conversion was 50% or even lower in both cases. Then, we made a trial reacting compound **10** with an amine. The idea was to mask the aldehyde group by forming an imine bond. To do that, two aromatic amines were assessed. This approach intended to confer stability to the iminic bond *via* conjugation through the aromatic scaffold. First, we tried the simplest option: aniline, but we were not able to obtain the pure product without performing any purification step.

Secondly, the amine precursor **1** was attempted, and this appeared to be a promising strategy both to prevent the reduction of the aldehyde group of **12** and to directly obtain the final ligand after the coupling reaction with precursor **6**. Compound **1** had been easily synthesized using a commercial affordable diamine *via* a reliable and scalable mono-acylation procedure.

Having all this in mind, to render the final precursor **14** (**Figure 4.11**), **7** was protected with the MOM group using the optimized conditions from **Table 4.2** (*Conditions B*), and the imine derivative synthesized by condensation reaction of **10** with the amine **1**.

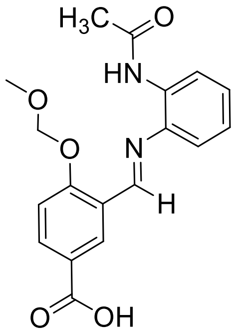

14

Figure 4.11. Final iminic MOM-protected precursor **14** for the subsequent coupling with **6** in HBTU with DIEA.

The imine bond with the precursor **1** did apparently protect the aldehyde group in the basic conditions of the coupling. However, final deprotection and cleavage from the resin with the TFA mixture cleaved the imine bond, yielding pure compound **11** without any trace of aldehyde reduction. ^{1}H NMR (**Figure 4.12A**) showed the presence of only one set of three aromatic ^{1}H signals with total integration of 3 with respect to the singlet of the -C*H*O (9.99 ppm). These integrals match with one moiety of Arg (4.5-1.5 ppm). No additional set of aromatic signals can be observed in this case. We were able to find the optimum conditions for this coupling, and although they are not ideal, they allow for now to obtain the desired product.

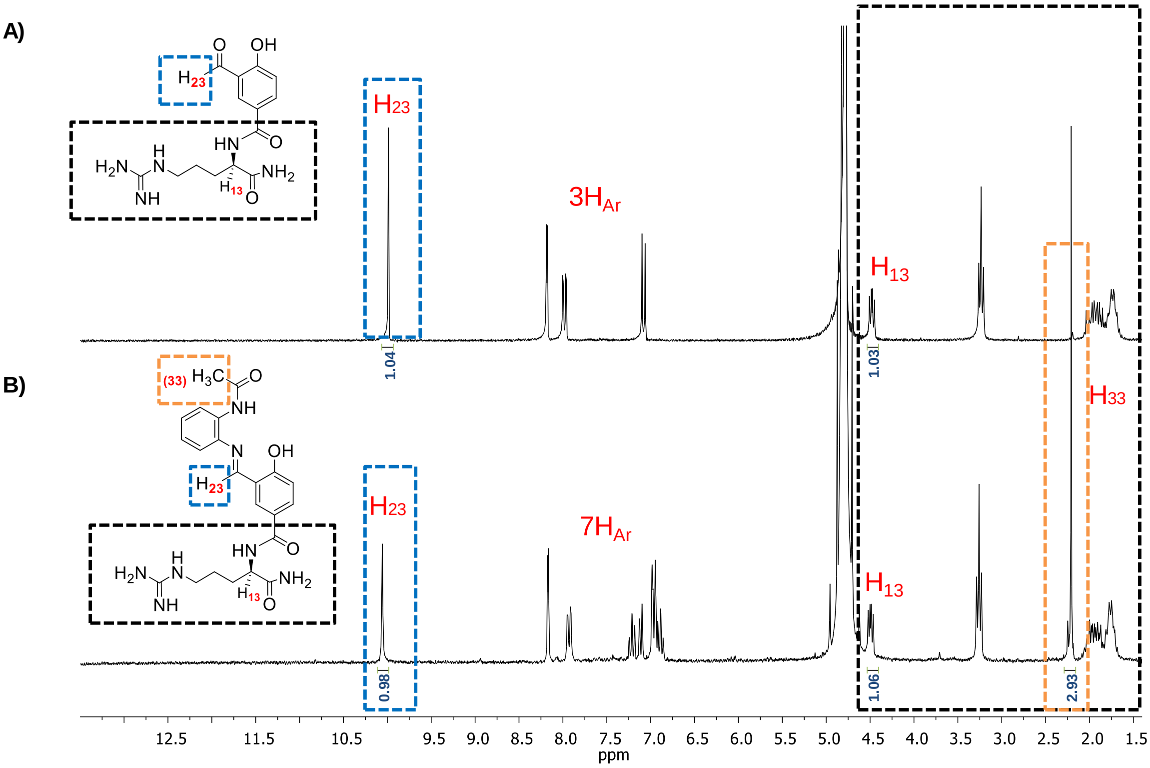

Figure 4.12. ^{1}H NMR (250 MHz, D_2O) of (**A**) compound **11** and (**B**) **L5**.

4.2.3 Synthesis and characterization of the final ligand **L5**

Ligand **L5** was finally obtained as a pure compound after the condensation reaction between **11** and **1** for 24 h (**Scheme 4.5**). After washes of the reaction crude with DCM and EtOAc, pure **L5** was obtained.

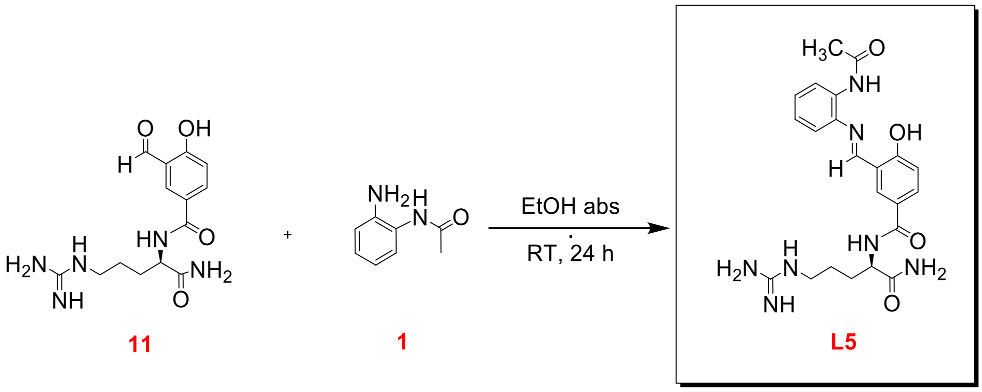

Scheme 4.5. Synthetic strategy to obtain ligand **L5**.

Characterization of the ligand **L5** was performed by ^{1}H NMR (**Figures 4.12B** and **Figure A36**), ^{13}C NMR (**Figure A37**) and MS (**Figure 4.13**). ^{1}H NMR showed the proton signals corresponding to the Arg moiety at the 4.5-1.5 ppm region, whose integration match with the 7 aromatic proton signals. As it can be also observed, the δ of the iminic ^{1}H in **L5** is shifted respect to the -C*H*O of **11** (**Figure 4.12**). HR-MS spectrometry (**Figure 4.13**) confirmed this assignment. The peak at *m/z* 454.2198, attributed to [**L5**+H]$^+$, corroborated the presence of **L5**.

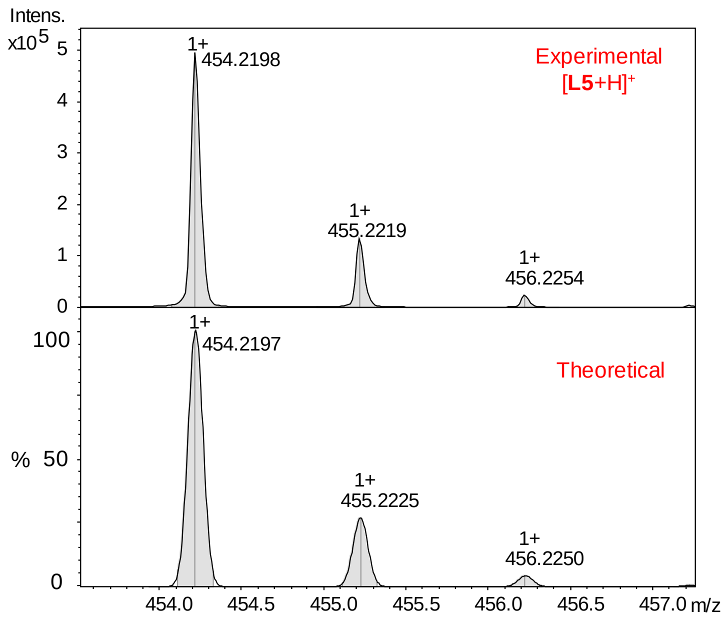

Figure 4.13. Experimental (top) and theoretical (down) HR-MS (ESI$^+$, MeOH) of [**L5**+H]$^+$.

4.2.4 Synthesis and characterization of the Cu(II) complex of ligand **L5** (**C5**)

Cu(II) complexation of ligand **L5** was achieved by using the Cu(II) acetate salt. An excess was used in order to be sure that any protonated Arg residue will not consume the necessary equivalents of the acetate anion to deprotonate the coordinating atoms. The reaction was performed at room temperature for 24 h. The solvent was removed and several ACN washes were carried out to remove the excess of the Cu(II) acetate salt.

The Cu(II) structure in solid state is expected to be analogous to that proposed for **C1**, **C2**, **C3** (*Chapter 3*), and thus, **C5** most-likely has part of the solid structure in a dimeric form (**Figure 4.14**).

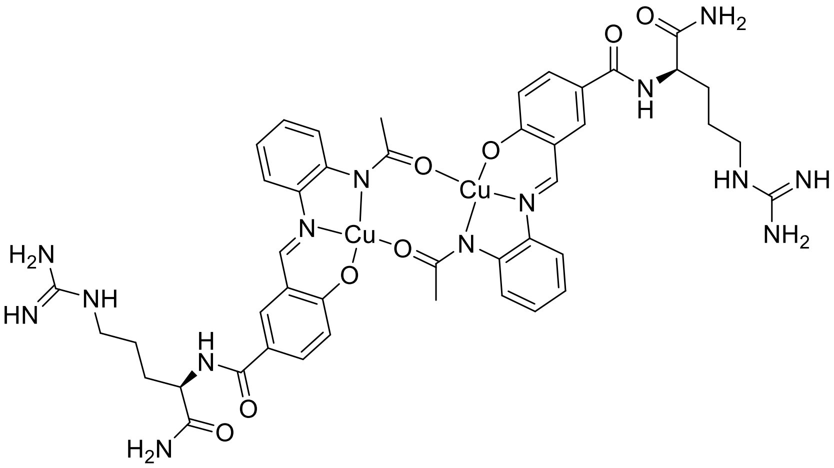

Figure 4.14. Proposed dimeric structure present in the solid of complex **C5**.

MS data confirmed the presence of the dimeric species. Peaks at *m/z* 1029.2550 (**Figure 4.15A**) and 1051.2376 (**Figure 4.15B**) can be attributed to [**C5**+H^+] and [**C5**+Na^+] adducts, respectively. Additionally, as already seen for **C4** (*Section 4.1.2*), there is an intense peak in the MS spectrum that can be attributed to the monomeric form of the complex: [**C5**$_{monomer}$+H]$^+$ (*m/z* 515.1329, **Figure 4.15C**). This monomeric adduct may arise from MS fragmentation under the ionization conditions or, as already discussed for **C4**, it can coexist in the solid state coordinated by a solvent molecule or a counterion, not seen in the MS.

In any case, evidence of the dimeric form is achieved and therefore, our proposal is that in **C5**, as well as for **C4**, the dimer is present in the solid structure of the complex.

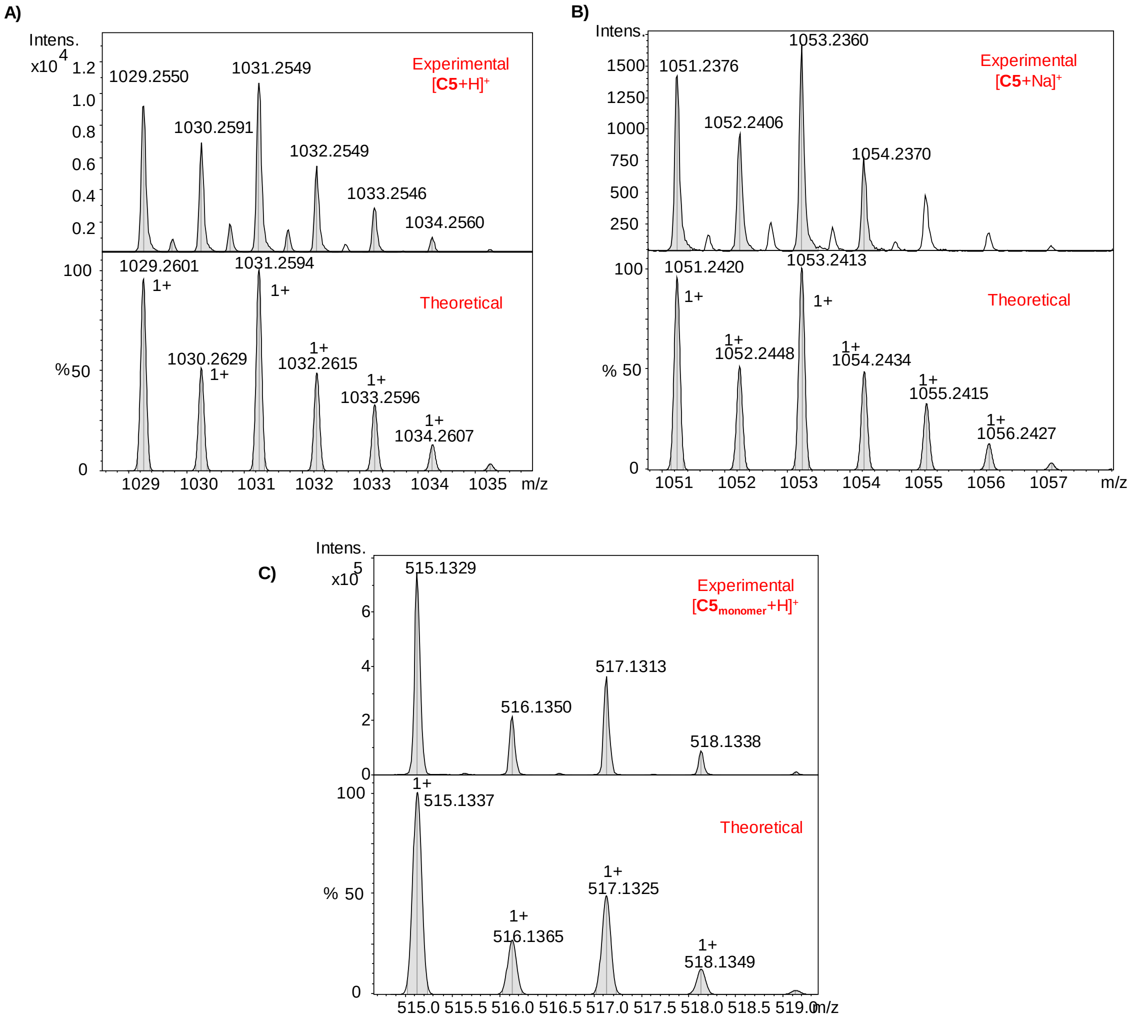

Figure 4.15. Experimental and theoretical HR-MS spectra (ESI$^+$, MeOH) of (**A**) [**C5**+H]$^+$, (**B**) [**C5**+Na]$^+$ and (**C**) the monomeric form of complex **C5**: [**C5**$_{\text{monomer}}$+H]$^+$.

ESR measurements were also carried out with **C5**. As observed from the X-ESR band (**Figure 4.16**), there is only one Cu(II) center, and no signal of free Cu(II) can be observed. The Cu(II) has the same coordination environment in solution as in **C1** and **C4**, *i.e.* a N_2O_2 electronic environment and a non-distorted square-planar or square-pyramidal geometry, based on the ESR parameters extracted from the spectrum (**Table 4.3**). These data highlight that conjugation with the Arg amino acid has not altered the coordination sphere of the metal center.

Table 4.3. ESR parameters for complex **C5** extracted from DMSO solution (**Figure 4.16**). **C1** and **C4** are placed for the sake of comparison.

Complex	**$g_{//}$**	**$A_{//}$ (10^{-4} cm^{-1})**	**$g_{\perp}$**	**$A_{\perp}$ (Gauss)**	**$g_{//}/A_{//}$ (cm)**
C1	2.244	183	2.043	<20-30	122
C4	2.240	186	2.039	<20-30	120
C5	2.248	186	2.046	<20-30	121

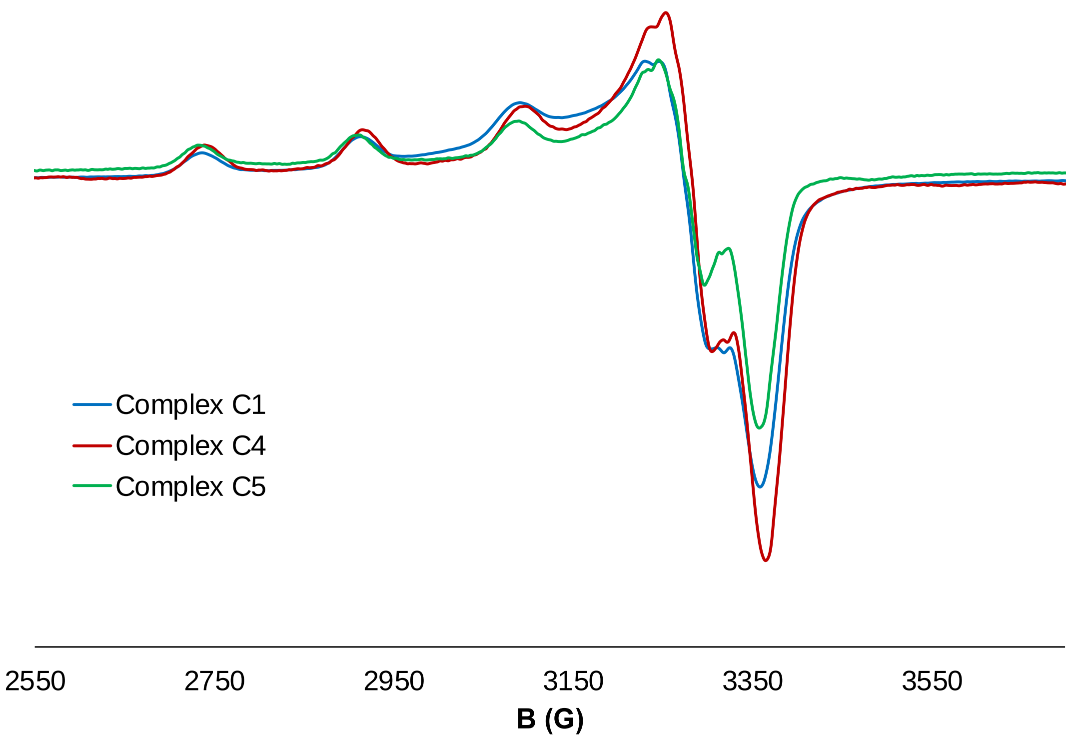

Figure 4.16. X-ESR band of **C5** compared to **C1** and **C4** in DMSO.

4.3 Comparing the redox behavior of C4 and C5 with C1

The goal of functionalizing **L1** with sulfonate (negative charge) or arginine (positive charge) was to enhance its solubility without affecting the high redox activity of the parent complex **C1**.

To verify this, CV experiments were performed with both **C4** and **C5**, and the corresponding ligands, in DMSO with 0.1 M TBAP. Both ligands **L4** and **L5** are electroactive in the assayed window of potentials (**Figure A38** and **4.17B**, respectively).

Regarding **C4**, the Cu(II)/Cu(I) redox potential has the same value ($E_{1/2}$ = -1.07 *vs.* Fc) as that of **C1** (**Figure 4.17A**). Assignment of the Cu(II)/Cu(I) redox pair was done by ESR spectroscopy. The ΔE_p is of *ca.* 130 mV and it can be considered as quasi-reversible based on the value obtained for Fc^+/Fc ΔE_p (100 mV) in the same working conditions. The process is diffusion controlled since there is a linear dependence of the peak currents I_{pc} and I_{pa} *vs.* the square root of the scan rate ($v^{1/2}$) (**Figure A39**). All these data indicate that the sulfonate derivatization of the ligand has not affected the redox behavior of the complex **C4**. The Cu(II)/Cu(I) redox cycling is inside the biological redox window and therefore, **C4** has the thermodynamic potential of generating ROS inside cells (see *Section 3.3.3, Chapter 3*).

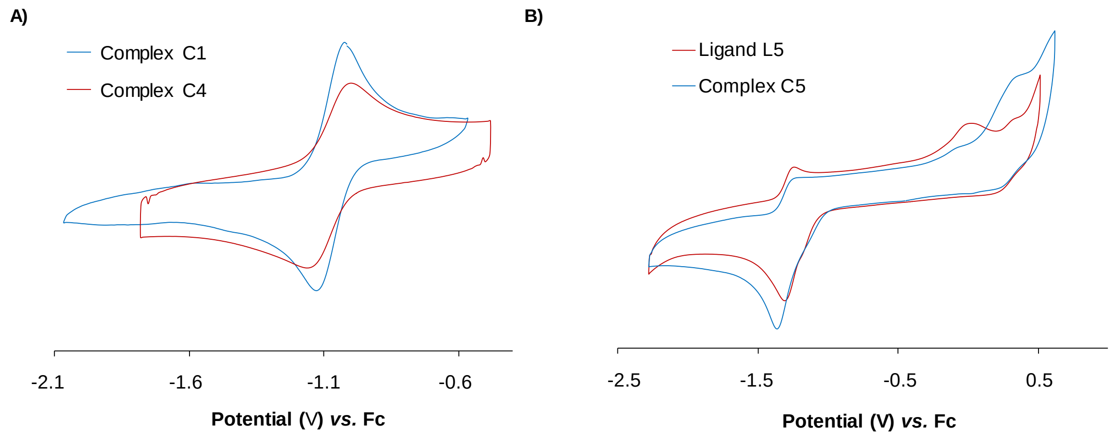

Figure 4.17. Cyclic voltammograms in DMSO with 0.1 M TBAP, at a scan rate of 100 mV/s of (**A**) **C4** compared to **C1**. The observed signals are ascribed to the Cu(II)/Cu(I) redox process. And (**B**) **L5** (1 mM) and **C5** (1 mM).

In the case of **C5**, the presence of the Arg group impaired the clear assignation of a signal to the Cu(II)/Cu(I) redox process (**Figure 4.17B**). The ligand **L5** itself has a similar band about the expected Cu(II)/Cu(I) redox potential region (**Figure 4.17B**). In the complex **C5**, this band appears to be wider and slightly shifted, but cannot be certainly assigned to the Cu(II)/Cu(I) redox pair. There is probably an overlapping between the band corresponding exclusively to the ligand plus the one coming from the presence of the metal ion. Consequently, and despite we expected to have the same half-wave redox potential in **C5**, no clear assignation of Cu(II)/Cu(I) can be done.

At this stage, further studies to shed light into the ROS generation capabilities of **C5** were required. The easiest approach relies on measuring the consumption of the ascorbic acid by UV-VIS (at its characteristic absorbance of 265 nm). As already explained in *Chapter 3* (*Section 3.3.*3), without any copper catalyst (DMSO control), no decrease on the absorbance at 265 nm can be observed (**Figure 4.18**). This demonstrates that ascorbic acid is stable and the medium does not consume it. In contrast, the free Cu(II) ions from the Cu(II) chloride salt produces a rapid decrease on the absorbance and, after 20 min, ascorbic acid has been almost totally consumed.

C4 and **C5** were also examined in these conditions. As observed (**Figure 4.18**), both Cu(II) complexes are able to consume ascorbic acid, *i.e.*, to be potential ROS generators, at similar rates (**C5**) or slightly slower (**C4**) than **C1**. After 25 min, all the assayed Cu(II) complexes are able to totally consume the provided ascorbic acid.

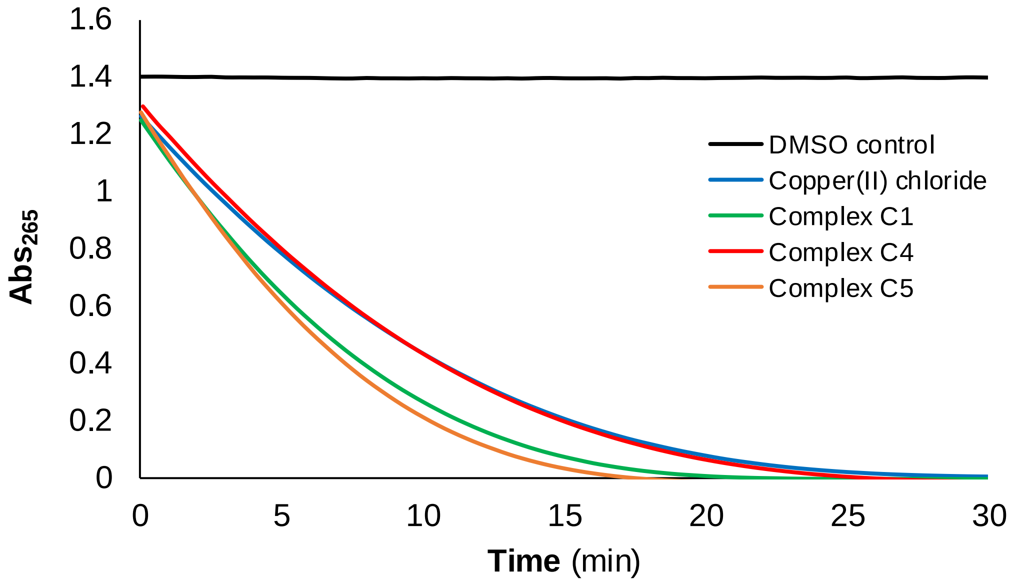

Figure 4.18. Ascorbic acid (100 µM) consumption of $CuCl_2$, **C1**, **C4** and **C5** (2 µM) monitored by UV-VIS at 265 nm, in NaCl/TRIS-HCl buffer at pH 7.2.

These results demonstrate that none of the functionalizations of **L1** have inhibited the ROS generation capabilities in the biological redox window. They also serve as a prove that the Cu(II)/Cu(I) pair of **C5** –to which a value has not been possible to assign in CV experiments- thermodynamically falls into the biological redox window as well.

4.4 Evaluating the effect of *sulfonate* and *Arg* derivatizations onto the biological activity of complexes C4 and C5. *In vitro* anticancer studies and copper cellular uptake assays

Complexes **C4** and **C5** appear as the soluble versions of **C1**. They are highly soluble in the biological medium at 37 ºC (5 g/L for **C4** and even higher for **C5**) without the need of DMSO. Regarding biological applications, these values are greater than the normal dose of administered cisplatin (around 4-5 mg/L).[252] This increment in the solubility limit confirms our success in the strategy chosen to solubilize **C1** and is highly promising to fulfil biological applications.

In vitro anticancer assays were subsequently performed in HeLa cancer cell lines at 24 h and 72 h treatment to compare the activity of the two new Cu(II) complexes with the already studied **C1**. Results are summarized in **Figure 4.19**, **Figure A40** and **Table 4.4**.

As observed from **Figure 4.19** and **Table 4.4**, complexes **C4** and **C5** do not seem to present any improvement in terms of cytotoxicity with respect to **C1**. None of the two new complexes exert higher toxicity in HeLa, despite being more soluble in the medium than **C1**, *i.e.*, theoretically more biologically available. IC_{50} at 24 h are higher than that calculated for **C1** (see **Table 4.4**). Only at 72 h, **C5** does exhibit similar cytotoxicity as complex **C1**, whereas **C4** is still less toxic.

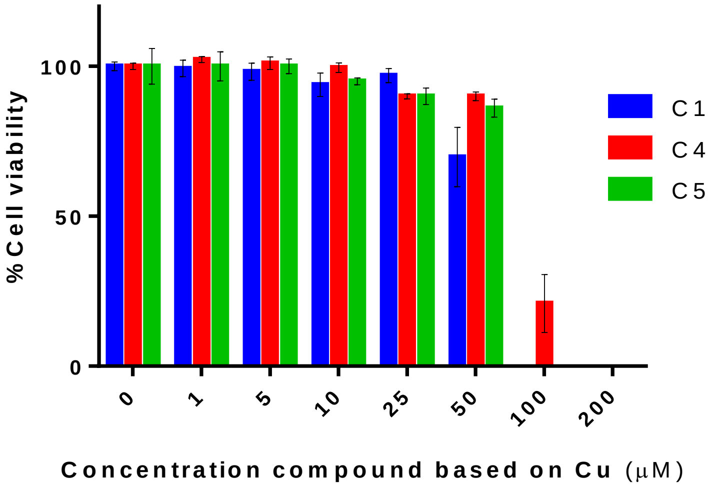

Figure 4.19. Cell-viability assays for complexes **C1**, **C4** and **C5** in HeLa cell lines after 72 h of treatment. Due to the putative presence of dimeric and monomeric forms of the different assayed complexes in the solid structure, concentrations of **C1**, **C4** and **C5** have been normalized in solution based on Cu concentration.

Data so far indicate that having improved the solubility has not provided a better cytotoxicity. Since the initial idea was to increase the bioavailability of the complex **C1** for cells, the next study was to assess the real bioavailability of **C4** and **C5** in cells. Copper cellular uptake experiments were performed in HeLa cancer cells. Treatment with the Cu(II) complexes **C1**, **C4** and **C5** was carried out for 4 h at a normalized Cu concentration of 50 µM for each of the studied complexes. Intracellular uptake was determined by quantifying the Cu amount by ICP-MS after having removed the supernatants, harvested cells and digested the cellular pellets with HNO_3. The chosen concentration and the treatment times are important to avoid cell death. Higher concentrations or treatment times would cause the death of some cells, leading to the release of the intracellular medium –*ergo* the Cu inside. This would render the obtained ICP-MS data inconclusive and meaningless.

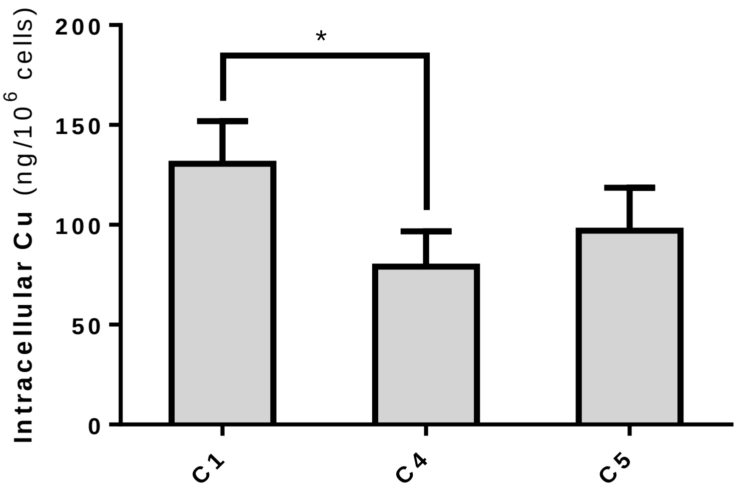

Figure 4.20. Quantification of the copper uptake in HeLa cancer cells after 4 h treatment. Complexes were used at 50 µM concentration based on the metal. The asterisk indicates statistical significance between the values with $p \leq 0.05$.

The amount of Cu uptaken by HeLa cancer cells is significantly higher for **C1** than that for **C4**, and also greater than for **C5**: **C1** > **C5** > **C4** (**Figure 4.20** and **Table 4.4**). This tendency matches with the IC_{50} values obtained for the three complexes in the same cell line, where **C4** showed the lowest toxicity, and **C5** displayed similar antiproliferative activity at 72 h as **C1**, suggesting that their cytotoxicity comes from the metallic core.

Metal uptake for Pt or Cu compounds at the reported literature are highly dependent on treatment times, procedures and techniques that have been used. Cisplatin in HeLa cells, at about 4 h treatment, has been for instance reported to enter about 100-120 ng/10^6 cells at similar treatment concentrations than our complexes.[253] Despite not being directly comparable, the assayed Cu(II) complexes **C1**, **C4** and **C5** are on the same scale as cisplatin, *i.e.* their cytotoxicity.

In regards with the different behavior of the sulfonate and Arg functionalizations (**C4** and **C5**, respectively), it seems that the presence of the negative charge (sulfonate) could hinder more the activity than the positive charged moiety (Arg). This might be related to the fact that the outer membrane of cells generally has a negative-charged surface.[195] This feature would favor the interaction with the Arg moiety (**C5**), concomitantly enhancing its toxicity. Contrarily, **C4** could be somehow partially repelled due to its negatively charged sulfonate group.

All these results highlight that copper uptake is a crucial aspect to consider in the final cytotoxicity of these Cu(II) complexes. Therefore, improving the uptake should enhance their biological activity. Subsequent steps (*Chapter 5*) focused on the improvement of the delivery and uptake of these compounds by functionalization with Arg-rich Cell Penetrating Peptides (CPPs).

Table 4.4. IC_{50} (µM) values at 24 h and 72 h of complexes **C1**, **C4**, **C5** in HeLa cell cultures, and their corresponding copper cellular uptake after 4 h of treatment at a 50 µM of Cu concentration for each assayed complex. The results shown are representative of at least two independent experiments (N=2).

Compound	IC_{50} (24 h)[a]	IC_{50} (72 h)[a]	Intracellular Cu (ng/10^6 cells)
C1	67±2	54±1	130±21
C4	109±1	78±3	79±17
C5	108±4	55±2	97±21

[a] *Normalized for Cu concentration.*

4.5 Summary and conclusions

This chapter was focused on the derivatization of **L1** with sulfonate (**L4**) and Arg (**L5**) residues to enhance the bioavailability of the corresponding Cu(II) complexes **C4** and **C5**, and on evaluating the derivatization effect on their biological activity. Now, some conclusions can be extracted:

1) We have described here the synthesis of a sulfonate functionalized ligand **L4**. It has been characterized and complexed with Cu(II) to yield **C4**. This complex has the same N_2O_2 metal-coordination environment in solution as **C1**. A dimeric form is proposed for **C4** to be present in the solid phase.

2) A synthetic strategy for the bioconjugation of the Arg residue to the aromatic scaffold of ligand **L1** has been designed and synthesized. This bioconjugation approach requires the use of a precursor from 3-acetyl-2-hydroxybenzoic acid (**7**), after protecting the phenol with a MOM group (compound **10**).

3) The use of the non-protected aldehyde compound (**10**) gives rise to a side-product in the coupling reaction with the Arginine. This side-product has been fully characterized and it shows the same retention time as the pure Arg-conjugated product of interest (**11**). We have been able to identify this side-product, which corresponds to the reduction of the aldehyde group into a benzyl alcohol.

4) Optimization of the coupling reaction for the Arg conjugation reaction of **L1** has been successfully achieved to avoid the reduction of the aldehyde group. A conjugated aromatic imine bond has been proven to efficiently mask the aldehyde in such conditions (no reduced -CHO compound has been observed with its use).

5) **L5** has been successfully synthesized and characterized. The corresponding Cu(II) complex (**C5**) has been also obtained and characterized. ESR shows that it has the same coordination environment in solution as **C1** and **C4**. A dimeric structure for **C5**, identified by ESI-MS, has been proposed to be present in the solid phase.

6) Functionalization with sulfonate (**C4**) and Arg (**C5**) has demonstrated not to alter the final coordination environment of the Cu(II) ion in regards to that of the parent complex **C1**.

7) Solubility in biological medium has interestingly increased respect to **C1** at least to 5 g/L for **C4** and **C5** at 37 ºC. Consequently, they both have improved the pharmacological interest respect to **C1** to be tested in future *in vivo* biological assays.

8) Redox studies have corroborated that the Cu(II)/Cu(I) redox potential of **C4** has not been affected by the sulfonate derivatization, *i.e.*, that it still falls inside the biological redox window. For **C5**, the ligand is electroactive and it has a redox response in the region of the expected Cu(II)/Cu(I) redox process, thus impairing the assignation of the latter.

9) Potential ROS formation has been evaluated for **C4** and **C5** by monitoring the consumption of ascorbic acid *via* UV-VIS at 265 nm. They have been resulted to be able to consume ascorbic acid at similar rates as **C1**, confirming that **C4** and **C5** maintain its high ROS generation capabilities.

10) Cytotoxicity of complexes **C4** and **C5** has been evaluated in HeLa cancer cells and compared with that of **C1** at 72 h and 24 h of treatment. Both complexes have shown a decrease on the toxicity respect to **C1**, exhibiting $IC_{50} > 50$ µM based on Cu concentration. Only **C5** at 72 h shows similar effects as **C1** on HeLa cell lines.

11) Cellular uptake experiments demonstrated that the functionalization with sulfonate (**C4**) or Arg (**C5**) does not increase the cell uptake of the complexes, despite making them more soluble in biological medium. Copper uptake in the case of **C4** and **C5** is respectively slightly lower or similar than **C1**, in good correlation with the differences seen in the cytotoxicity of these three compounds.

The Arg group does apparently confer a slightly better uptake to the Cu(II) complexes than the sulfonate group, probably partially due to electrostatic interactions with the negatively charged surface of the cell membranes.

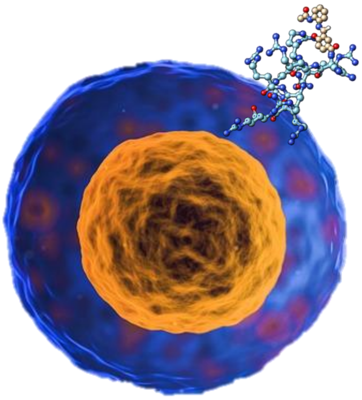

CHAPTER 5

Cell-Penetrating Peptides and Dendritic multimodal platforms to enhance the uptake and delivery of potential anticancer drugs

Drug Delivery Systems are approached in this chapter to enhance the uptake and delivery of the parent complex **C1**. Two different strategies are presented: Cell-Penetrating Peptides (CPPs) and the use of a dendritic DTPA-based multimodal platform. First of all, the coupling strategy with CPPs to obtain the final ligands is detailed, and the corresponding Cu(II) complexes are characterized. Additionally, cell-viability assays and uptake studies are performed to confirm the enhanced complex uptake and, consequently, their improved cytotoxicity. The second part of this chapter reports on the study of the Cu(II) coordination capabilities of the DTPA-based dendritic platform, as well as the synthetic approach followed to conjugate it to the **L1** scaffold (**L9**). Complexation of the new ligand **L9** with Cu(II) is also achieved (**C9**).

CHAPTER 5

Cell-Penetrating Peptides and Dendritic multimodal platforms to enhance the uptake and delivery of potential anticancer drugs

The results shown in previous chapters have already highlighted the redox activity of **C1**, with a significant anticancer activity (*Chapter 3*). Functionalization of **L1** with -SO_3^- and Arg groups has been successfully achieved, leading to an enhancement on the solubility of their complexes in biological medium and therefore, improving their pharmacological interest (*Chapter 4*). However, despite increasing the bioavailability of the corresponding complexes, these two groups attached to **L1** did not account for any improvement either on the cellular uptake or the cytotoxicity of the resulting complexes. In fact, and especially in the case of the sulfonate-derived Cu(II) complex (**C4**), a slight decrease on the cytotoxicity respect to **C1** and **C5** has been observed, which would be attributed to its lower uptake.

Cellular uptake of biologically active molecules is a major obstacle in pharmaceutical drug design and drug delivery. The first barrier towards an efficient intracellular delivery is the plasma membrane, which prevents direct translocation of hydrophilic macromolecules. It is the main barrier for diagnosis and treatment of human diseases. Increasing the intracellular amount of an anticancer complex arises as one of the strategies to improve its cytotoxicity, as well as its efficiency as chemotherapeutic agent. Drug delivery research is a current hot topic,[52,135,159,254,255] and up to date several drug delivery systems have been reported, as summarized in *Section 1.4*.

This chapter will be divided into two sections, where different drug delivery systems will be explored to improve the uptake of **C1**. The first part will be focused on conjugating

Arg-rich Cell-Penetrating Peptides (CPPs) to enhance the intracellular uptake and delivery of the compound of interest. The second part of this chapter deals with the exploration and evaluation of a multimodal dendritic platform as a potential drug carrier.

PART I

5.1 Drug delivery systems (I). Bioconjugation of Arg-rich Cell-Penetrating Peptides: TAT$_{49-57}$ and R$_9$ peptides

CPPs, also known as protein transduction domains, comprise a class of short peptides (< 30 *aa*) that have the ability to cross cellular membranes and mediate the uptake of cargoes into cells.[165,242] They have acquired considerable attention due to their high transduction efficiency and low cytotoxicity.[165,256,257] On the basis of their physical and chemical properties, they are divided into three different classes: cationic, amphipathic and hydrophobic. Cationic peptides represent the majority of the reported CPPs and usually contain more than five positively charged amino acids, which have been reported to enhance translocation through cell membranes. Amphipathic CPPs contain both polar and nonpolar amino acidic regions, and are basically involved in the intracellular transport. They accumulate preferentially in the nucleus.[257] Hydrophobic CPPs contain nonpolar *aa* with high affinity for the hydrophobic domain of cell membranes and can translocate across lipidic membranes in an energy-independent manner.[258]

More than 80% of the known CPPs are cationic peptides and among them, Arg-rich CPPs have been the most widely studied class.[242,259,260] Indeed, the first protein transduction domain, *ergo* CPP, was discovered in 1988, when two independent groups (Green and Lowenstein,[261] and Frankel and Pabo[262]) reported that the transactivator of the transcription (TAT) protein of the Human Immunodeficiency Virus (HIV) can penetrate cells and activate the viral genome replication. Later on, Vivès *et al.,* in 1997, and Choi *et al.*, in 2002, reported that shorter sequences, such as the TAT$_{47-57}$ or TAT$_{49-57}$, cannot only enter cells but are, in fact, more efficient than the full-length protein.[263,264] In general, poly-Arg stretches have shown high levels of cellular uptake, thus offering promising potential for therapeutics. One of the proposed explanations is related to the presence of guanidino groups in Arg, which are reported to form hydrogen bonds with the negatively charged carboxylate, sulfate and phosphate groups of the cell membrane proteins.[265] In this scenario, two prototypical Arg-rich CPPs were chosen for our work as a proof-of-concept: the TAT$_{49-57}$ peptide[264] and R$_9$ (9 Arg residues). It is empirically known that the number of Arg residues affects the translocation ability of the peptide. Peptides having five or less Arg are less effective than those with six or more. Both chosen peptides have more than five Arg residues: six for the case of the $TAT_{49\text{-}57}$ peptide, and nine for R_9. A crucial requirement for the two chosen peptides implied is the fact that they do not contain coordinating residues (such as Cys or His), which could interfere in the future Cu(II) complexation.

Once the two peptides of interest were selected, they had to be attached to **L1**. The followed strategy is depicted in **Scheme 5.1** and it is based on the optimized procedure described in *Chapter 4* for the attachment of **L1** to the Arg residue (*Section 4.2.2*). In accordance, precursor **14** is the one used to anchor the peptide throughout an amide bond.

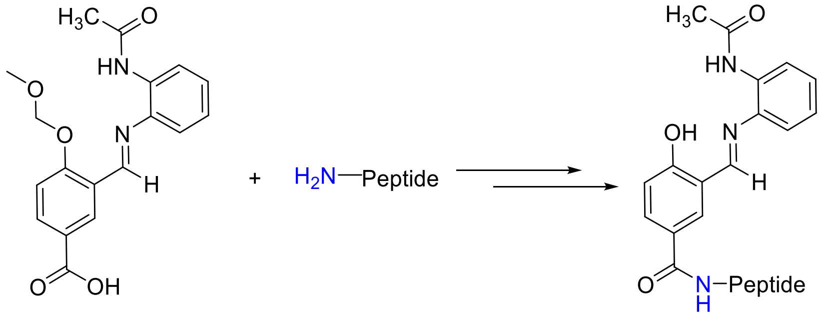

14

Scheme 5.1. Bioconjugation approach to anchor *TAT$_{49\text{-}57}$* or *R$_9$* (R = Arg) CPPs to precursor **14**.

5.1.1 $TAT_{49\text{-}57}$ peptide: the key motif of the TAT protein

The $TAT_{49\text{-}57}$ peptide was the first one to be attempted. As mentioned before, the TAT protein has been extensively studied and was the first discovered with penetrating abilities.[261,262] Park and coworkers demonstrated that the key motif could be reduced without losing its CPP properties to residues 49-57: $TAT_{49\text{-}57}$ peptide (RKKRRQRRR).[264]

5.1.1.1 Solid-phase peptide synthesis and characterization of the $TAT_{49\text{-}57}$ peptide

The $TAT_{49\text{-}57}$ sequence to be anchored to **14** is depicted in **Figure 5.1**. It contains an amide as C-terminus (product of the Rink Amide resin used in the Solid-phase peptide synthesis (SPPS)) and a *β*-Ala as a linker. This spacer is introduced to separate the metallic framework from the peptide sequence responsible of binding to the cell membrane receptors.[266]

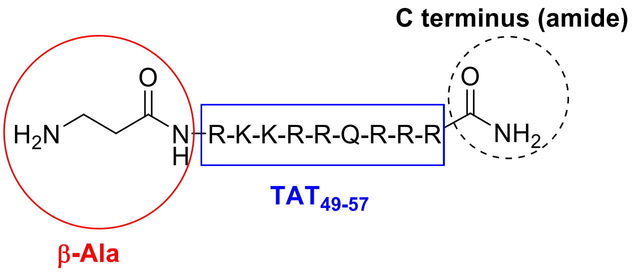

Figure 5.1. TAT$_{49\text{-}57}$ sequence with a *β*-Ala residue as a spacer.

The synthesis of the TAT sequence was carried out by automatic SPPS on a Biotage® microwave assisted peptide synthesizer following standard protocols.[245] The Fmoc protected Rink Amide MBHA resin (100-200 mesh) was used to obtain an amide group at the C-terminus upon final cleavage. Compound **16** (**Scheme 5.2**) was obtained after final Fmoc removal of the last incorporated *aa* (*β*-Ala).

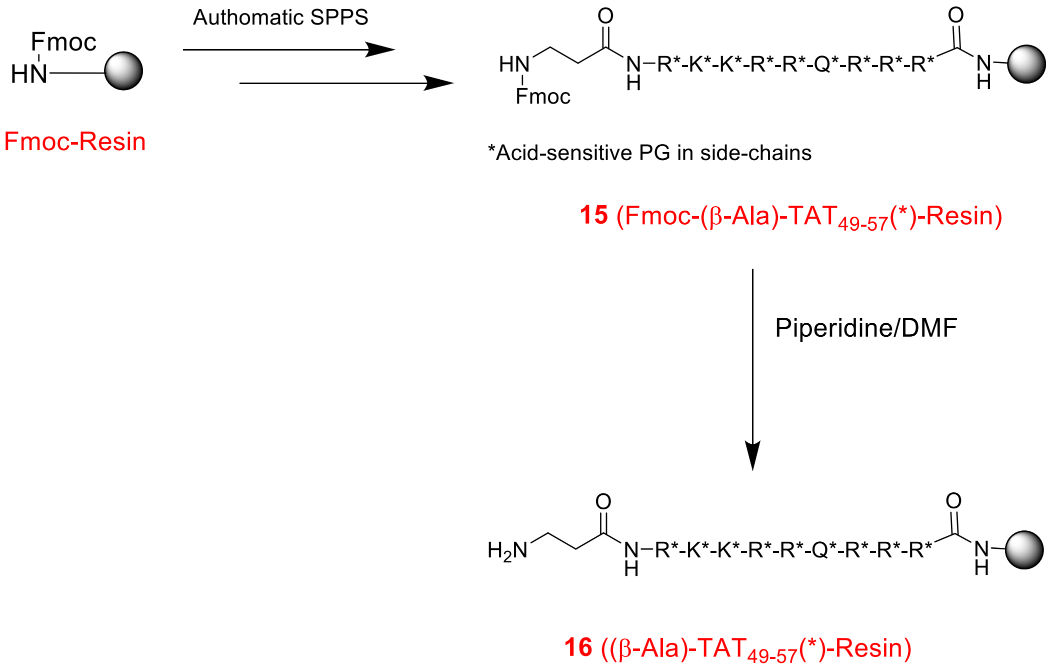

Scheme 5.2. Solid-phase synthesis of **16** as precursor of the final peptidic sequence (**Figure 5.1**) to be attached to **14**.

To evaluate the final peptide, an aliquot of **15** was taken and simultaneously deprotected and cleaved from the resin with the TFA/H_2O/TIS mixture. Only one main peak was observed in analytical HPLC, indicating a high purity. ESI-MS in positive mode (**Figure A41**) confirms the successful peptide synthesis. After final Fmoc removal, an aliquot of **16** (**Figure A42**) was analyzed by ^{1}H NMR spectroscopy and data confirmed its identity too.

5.1.1.2 Synthesis of the ligand **L1** with the (*β*-Ala)-TAT$_{49-57}$ peptide

Attachment of the synthesized TAT peptide to the organic scaffold of **L1** was done *via* precursor **14** (**Scheme 5.3**). As an important reminder, the MOM protection of the phenol group and the formation of the final imine are crucial steps to avoid side-reactions in basic media, and to mask the -CHO group to impair its reduction to a benzyl alcohol (*Chapter 4*).

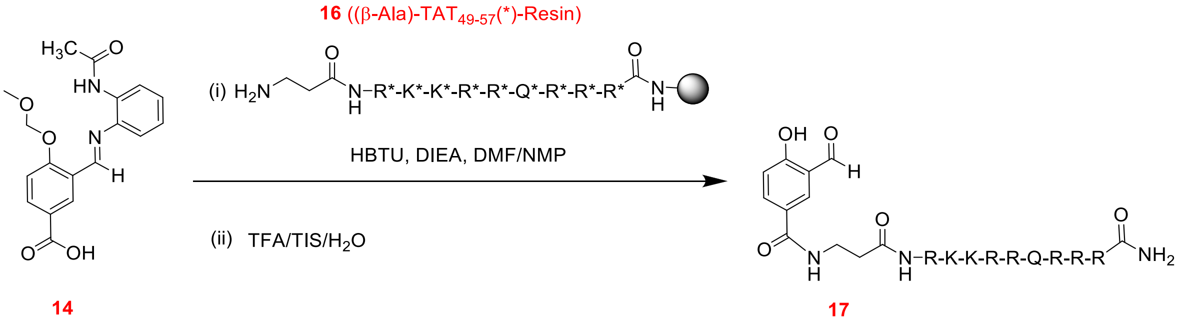

Scheme 5.3. Synthetic strategy of the coupling between **16** and precursor **14**.

Coupling of **14** was performed with HBTU in basic conditions. The simultaneous deprotection and cleavage from the resin with the TFA-containing mixture broke the iminic bond from **14** and a final aldehyde group was obtained in **17**. Preparative reversed-phase HPLC purification yielded pure **17**, as concluded from the ^{1}H NMR spectrum (**Figure 5.2A**).

In the ESI-MS spectrum (**Figure 5.3**) the peaks corresponding to the desired product at +3, +4 and +5 charge states (*m/z* of 520.0, 390.2 and 312.4, respectively) can be observed. However, the peaks with the highest intensity can be attributed to **17** after the loss of a water molecule: [**17**-H_2O]$^{4+}$ and [**17**-H_2O]$^{5+}$ (*m/z* of 385.7 and 308.8, respectively) These can be ascribed to the product of an intramolecular imine bond between the amino (-NH_2) group of the side-chain of any of the lysine residues with the

-CHO of the aromatic scaffold (**Figure 5.4**). Nonetheless, and based on the NMR data (**Figure 5.2A**), this fact seems to be just consequence of the MS working conditions.

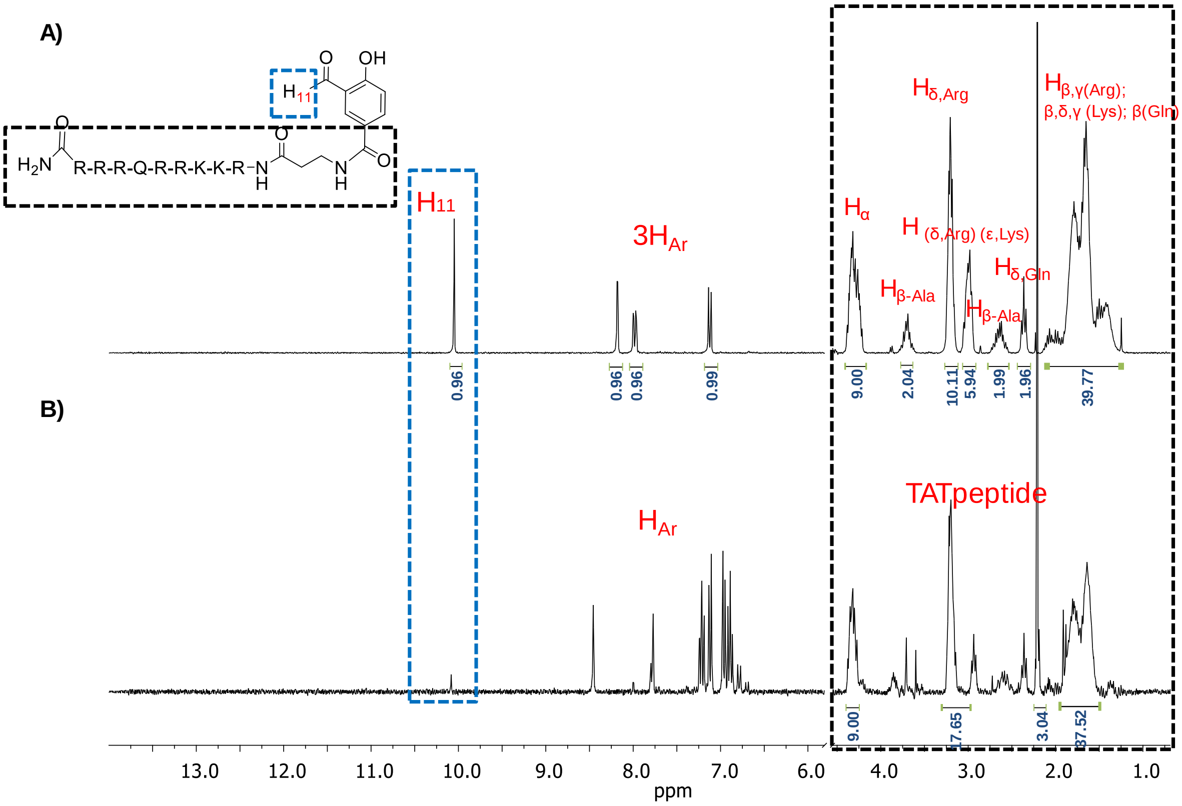

Figure 5.2. ^{1}H NMR (300 MHz, D_2O) spectra of (**A**) compound **17** and (**B**) the reaction crude from mixing **17** and **1**.

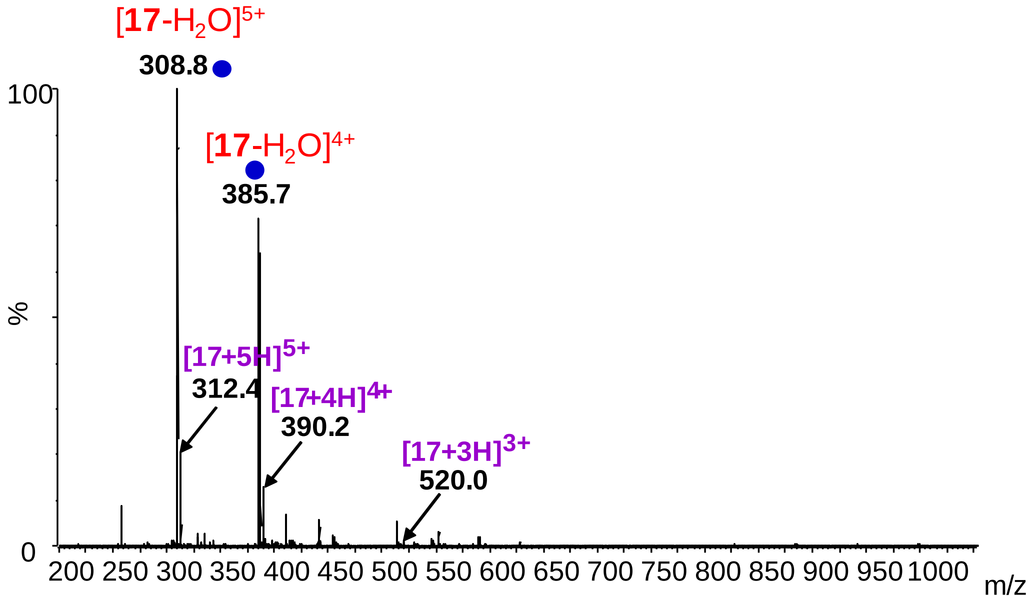

Figure 5.3. ESI-MS (ESI$^+$, MeOH) spectrum of pure compound **17**.

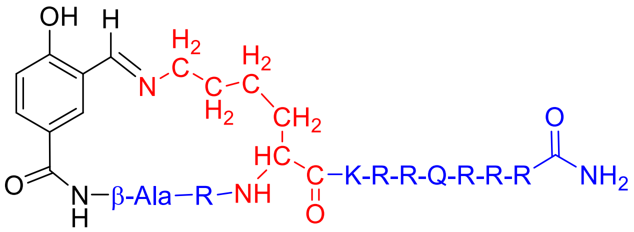

Figure 5.4. Proposed structure for the intramolecular imine bond formation in **17**. In red, one of the two possible Lys residues making the intramolecular bond. In blue, the rest of the CPP.

Once **17** was obtained and characterized, the formation of the final ligand was attempted by making it react with precursor **1**. The reaction was performed in the same conditions as for **L1**-**L5**. Characterization of the reaction mixture was done by ESI-MS (**Figure 5.5**). The observed peaks are attributed to **17** after the loss of a molecule water, *i.e.* intramolecular imine bond formation (**Figure 5.4**): *m/z* corresponding to [**17**-H_2O]$^{3+}$, [**17**-H_2O]$^{4+}$, [**17**-H_2O]$^{5+}$ and [**17**-H_2O]$^{6+}$ (514.0, 385.7, 308.8 and 257.5, respectively). No other peaks were observed, neither from compound **17** nor from any other putative ligand.

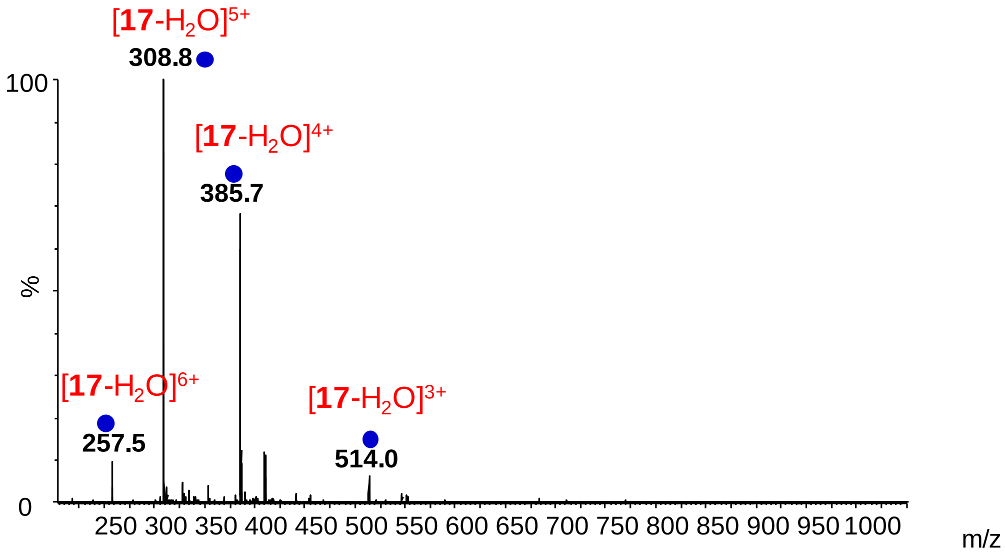

Figure 5.5. ESI-MS (ESI$^+$, MeOH) spectrum of the reaction mixture of **17** with **1**.

Confirmation that the imine bond between **1** and **17** was not formed in our sample, and that the intramolecular formation was not solely due to MS working conditions, was achieved by ^{1}H NMR (**Figure 5.2B**). The spectrum reveals that there is neither a -CHO nor iminic ^{1}H signal at the expected range. For ligands **L1**-**L5**, the iminic proton usually appeared between 10.5-9.5 ppm. This is common for aromatically conjugated imines, which usually give rise to more dieshielded proton signals (δ 8-10 ppm) than aliphatic ones (δ 7-8 ppm).[267] This signal absence at the expected chemical shift in the NMR of **17** suggests that the putative formed imine bond could be intramolecular.

The intramolecular imine formation is competing with the desired intermolecular one of the final ligand. Comparison of the p*K*$_a$ values in water[6] of the -NH_2 of the lysine residue (p*K*$_a$ = 11)[268] and an aniline (p*K*$_a$ = 30.6,[208] as a model for **1**), indicates that the basicity of **1** is higher than that of the side-chain of lysine. Considering that **17** has been purified through preparative reversed-phase HPLC (with 0.1% TFA in mobile phase), **1** will be primarily protonated. This feature will disfavor the intermolecular iminic bond and favor the intramolecular one.

Considering these results, the $TAT_{49\text{-}57}$ peptide was not suitable for the synthetic approach proposed and the R_9 peptide was subsequently explored. The lack of Lys residues, and of any other *aa* with free amino groups in their side-chains, will impair any intramolecular bond formation.

5.1.2 R_9 and $(Gly)_4$-R_9 peptides as Cell-Penetrating Peptides

R_9, also named as $(Arg)_9$, is a well-known CPP. It is also a cationic peptide, as the beforehand mentioned $TAT_{49\text{-}57}$ peptide, and consists of 9 Arg residues. Previous studies revealed that arginine residues contribute indeed more to cellular uptake than lysines do, and have clearly highlighted the uptake efficiency of the nonamers of arginine.[165,260,269,270]

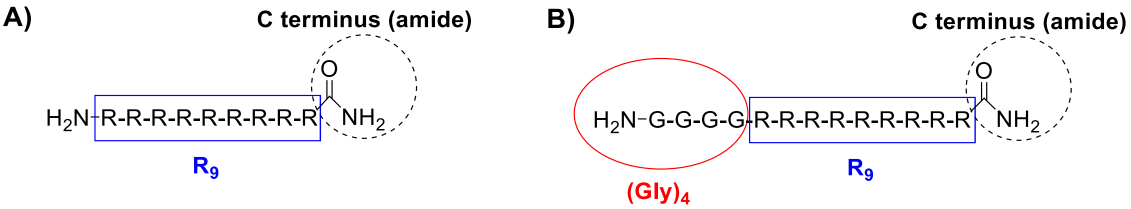

Figure 5.6. Arg-rich CPPs of interest to anchor to **L1**: (**A**) R_9 and (**B**) the corresponding derivative with a linker, $(Gly)_4$-R_9. Both contain 9 Arg residues.

We decided then to synthesize two R_9 sequences, with and without a linker of 4 Gly: R_9 and $(Gly)_4$-R_9 (**Figure 5.6**). They both will have an amide as a functional group in the

---

[6] *A correction factor can be applied to convert the pK$_a$ values in water to organic solvents.*[244] *However, for relative comparison the values in water can be used since the trend is maintained.*

C-terminus, to avoid further cross-reactivity. As already commented for the TAT_{49-57} peptide, the use of spacers might help the recognition of the specific receptors of the cell membrane. A linker of 4 Gly residues separates the CPP peptide sequence from the active site (Cu(II) complex) by a flexible and non-reactive aliphatic chain of an overall of 8C. Gly and Ser, *i.e.*, small amino acids, are simple and suitable choices when certain movements or interactions are required.[271,272]

5.1.2.1 Solid-Phase Synthesis and characterization of R_9 and $(Gly)_4$-R_9

These two sequences were synthesized by automatic SPPS on a Biotage® microwave assisted peptide synthesizer using standard Fmoc methodologies.[245] Following an analogous protocol to that shown in **Scheme 5.2**, amino acids were assembled in a Rink Amide resin and obtained in the Fmoc protected form.

Aliquots of the two resins were taken and simultaneous cleavage and side-chains deprotection were carried out with the TFA/H_2O/TIS mixture. Purity of the cleaved peptides was assessed by analytical HPLC (**Figures A44** and **A46**) and they were characterized by ^1H NMR (**Figures A45** and **A47**). They were used without further purification.

5.1.2.2 Synthesis and characterization of the ligand **L1** conjugated to the R_9 and $(Gly)_4$-R_9 peptides: ligands **L6** and **L7**

Once the two R_9 peptides were successfully synthesized and characterized, attachment of the precursor **14** was made *via* solid-phase methodologies. After Fmoc deprotection, the precursor was linked to the peptides (**18** and **20**) through its aromatic scaffold using an amide bond. The mixture TFA/TIS/H_2O cleaved the peptide from the resin and simultaneously removed the protecting groups (**Scheme 5.4**).

At these conditions, both the MOM protecting group from precursor, as well as the imine bond are cleaved, leading to phenol and aldehyde groups in the final conjugated compounds **19** and **21**. Pure compounds were obtained after preparative reversed-phase HPLC using a H_2O/ACN gradient in acidic conditions (0.1% TFA). **19** and **21** were confirmed and characterized by ^1H NMR (**Figures A48** and **A50**) and MS (**Figures A49** and **A51**).

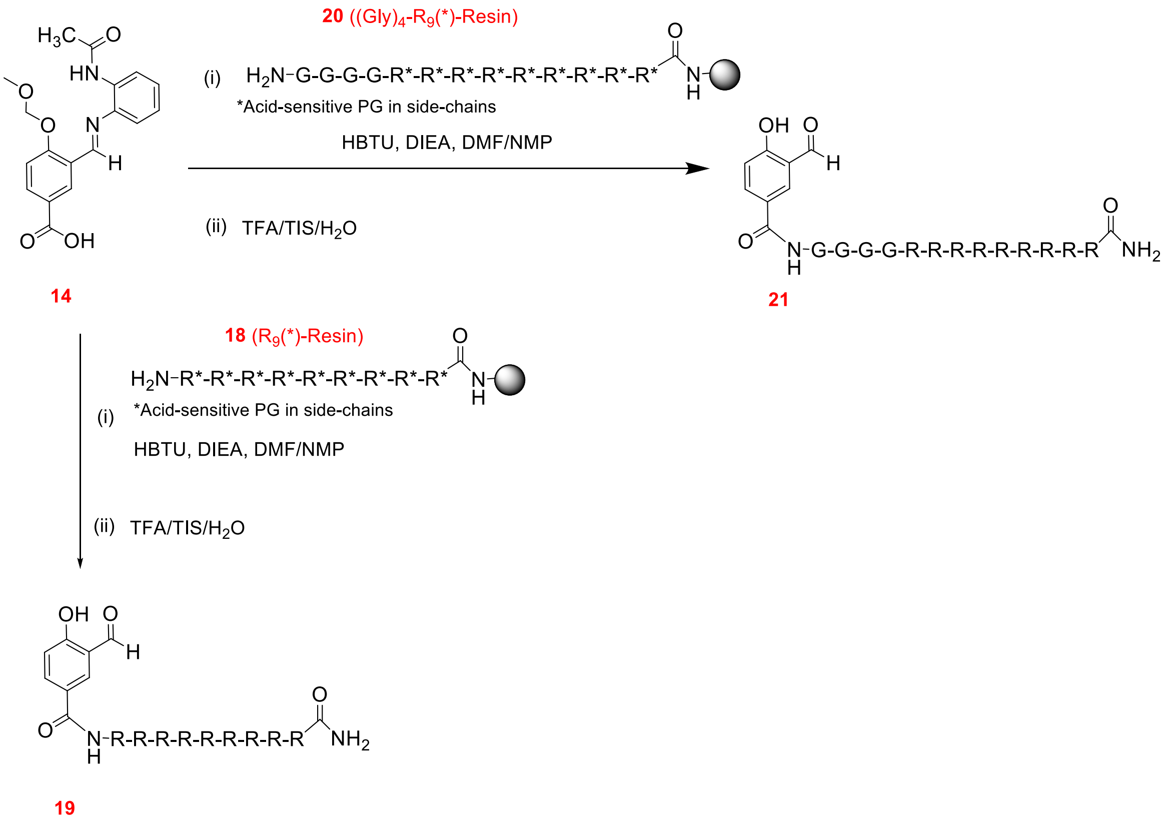

Scheme 5.4. Synthetic strategy to attach the organic precursor **14** to peptides R_9 and $(Gly)_4$-R_9.

Subsequent step involved the imine bond formation between **19** or **21** and an excess of compound **1** to ensure 100% conversion (**Scheme 5.5**). This reaction was carried out in the same conditions as for previous ligands **L1**-**L5**. After 24 h of stirring at room temperature, the reaction crude was washed several times with EtOAc to remove the excess of **1**, yielding pure **L6** and **L7**.

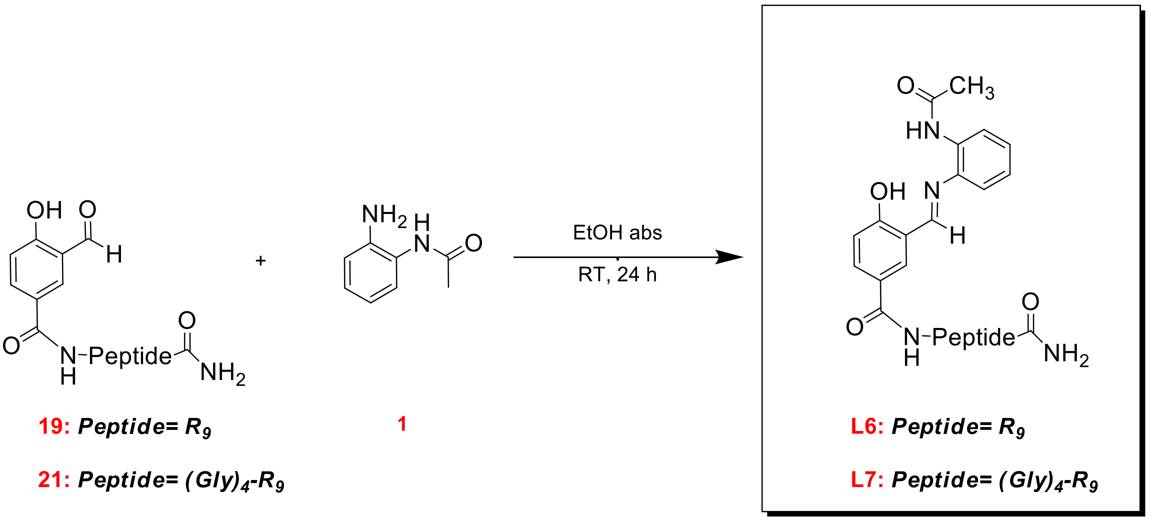

Scheme 5.5. Imine bond formation to obtain final ligands **L6** and **L7**.

Characterization of ligands **L6** and **L7** was done by ^{1}H NMR (**Figures 5.7B** and **A53**, respectively) and ESI-MS. ^{1}H NMR of **L6** (**Figure 5.7B**) shows 7 signals with δ 8.5-6.5 ppm integrating at 7H, which could be ascribed to the aromatic protons of the ligand. Integration of these aromatic signals match well with the presence of 9 Arginine residues for each molecule. This assumption is based on the singlet at 4.26 ppm that integrates 9H, which can be assigned to the *α*-proton of the Arg residues. The comparison between the spectrum of **19** and **L6** (**Figure 5.7**) reveals that there is a new ^{1}H signal in **L6**, with a singlet multiplicity and integrating 3H, which refers to the methyl group of the acetamide (H$_{10}$ at 2.14 ppm). This confirms the linkage between the -NH$_2$ in **1** and the -CHO of **19**. The slight shift on the signal at δ 9.98 ppm for **19** to 10.08 in **L6** can be ascribed to the chemical transformation of the -C*H*O (H$_{11}$) to -C*H*N (H$_{21}$) upon imine formation.

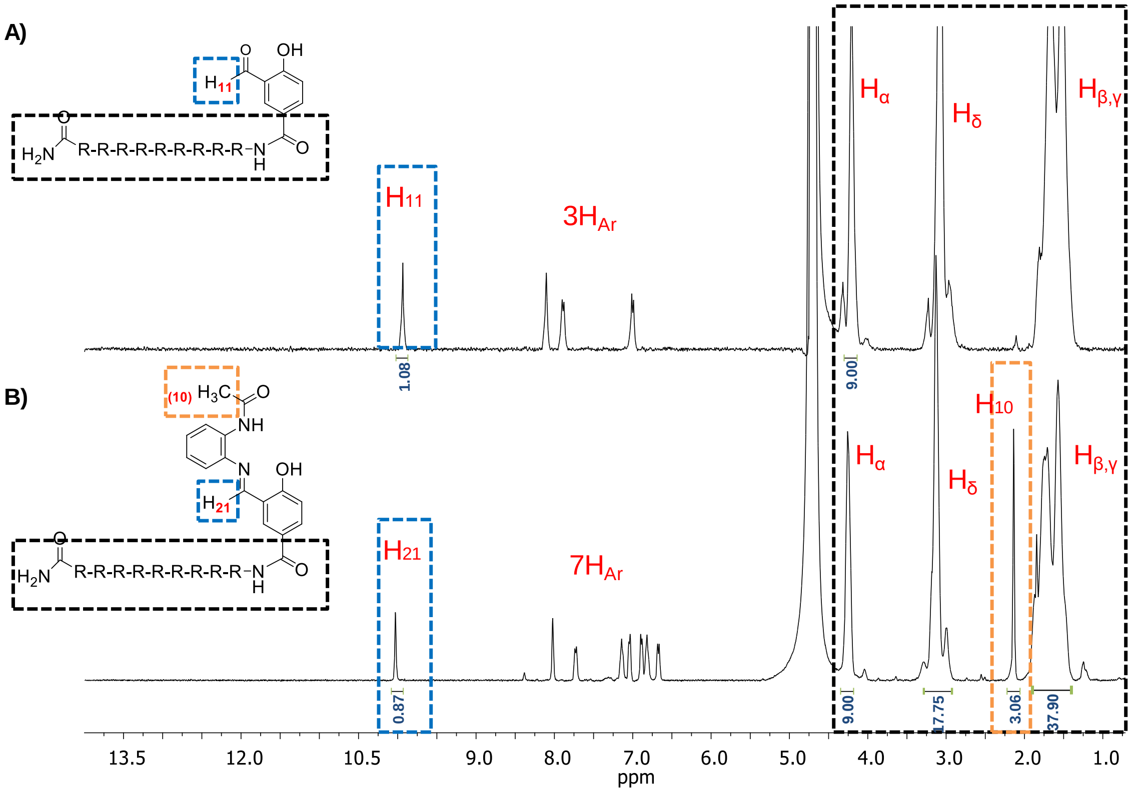

Figure 5.7. (**A**) ^{1}H NMR (D_2O, 360 MHz) of compound **19** and (**B**) ^{1}H NMR (D_2O, 400 MHz) of **L6**.

As both ligands **L6** and **L7** are analogous and just differ in the presence of the (Gly)$_4$ linker, ^{1}H NMR assignation and characterization of **L7** (**Figure A53**) was done in an equivalent manner. The difference relies on the presence of the ^{1}H signals corresponding to the aliphatic protons of the Gly residues at the region between 4.5-3.5 ppm.

Noteworthy, the high positive charge density in the ligands **L6** and **L7** due to the conjugated CPPs has given rise to some conformational equilibria in solution. Since it is not the scope of this work, this behavior was not deeply explored. In brief, both ligands **L6** and **L7** have shown changes in the NMR spectra as a function of sample concentration. As observed in **Figure 5.8**, the NMR spectra of **L6** at 2mg/mL and 8mg/mL contain different set of signals. At high concentrations a new set of ^1H signals appeared in the region 10-6.5 ppm and the singlet of both -C*H*N (H_{21}) and -C$H_{3,\text{amide}}$ (H_{10}) were split into two different signals. This feature was observed to be reversible when diluting again the sample (**Figure 5.8**). In any case, the addition of the integrals of the split signals (H_{21} and H_{10}) perfectly match with one R_9 peptide unit (δ 4.3 ppm, $9H_\alpha$).

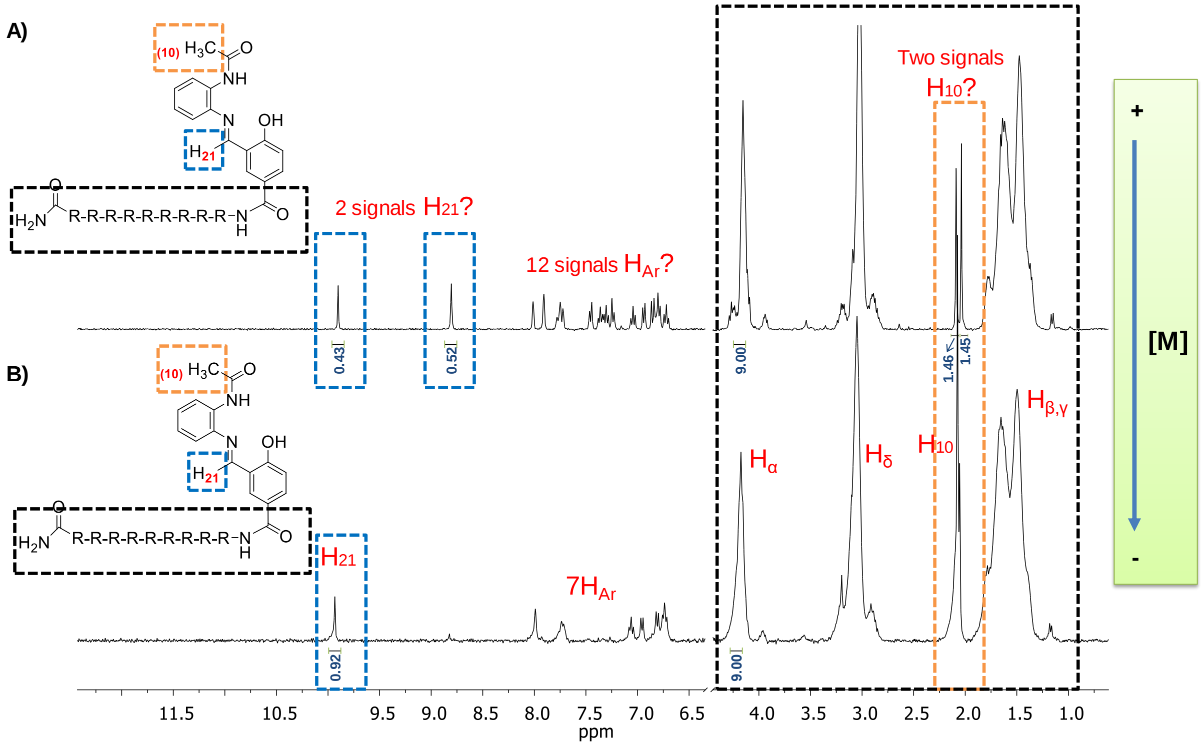

Figure 5.8. ^1H NMR (D_2O, 360 MHz) of **L6** at two different concentrations: (**A**) 8 mg/mL and (**B**) 2 mg/mL at pH between 5-6.

These data suggested a conformational or aggregation effect at high concentrations in solution. Although further studies should be carried out to fully understand this behavior, a recent study revealed that highly charged Arg-rich CPPs, like R_{10} or similar, might undergo self-association in solution.[273] This appears to be a non-specific peptide-peptide interaction characterized by the stacking of some of the side-chains of several arginine residues, specially at the end of the molecular chain. Of course, it is important to mention here that other factors such as pH or temperature may affect this self-association process at some extent but they were not studied since it is not the scope of this thesis.

HR ESI-MS (**Figure 5.9**) confirmed that both ligands were successfully accomplished. Peaks at a +4 charge state (the most intense ones) corroborated the presence of both ligands: [**L6**+4H]$^{4+}$ and [**L7**+4H]$^{4+}$ (426.5133 and 483.5343, respectively). Peaks at +5 and +6 state were also encountered corroborating the same species (data not shown).

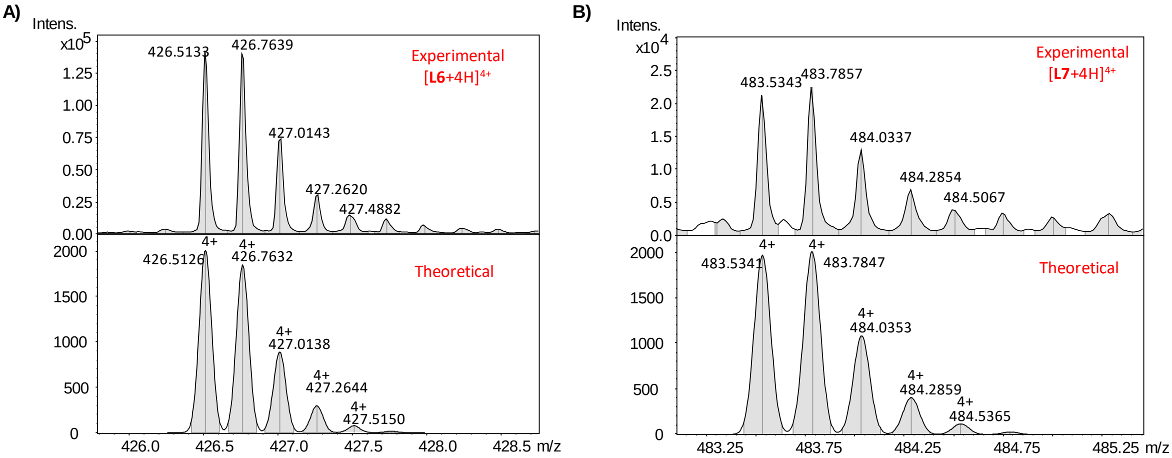

Figure 5.9. Experimental (top) and theoretical (down) HR-MS (ESI$^+$, MeOH) spectra for (**A**) [**L6**+4H]$^{4+}$ and (**B**) [**L7**+4H]$^{4+}$.

At this stage, and having both ligands in hand, the subsequent step was to proceed with their Cu(II) complexation and characterize the obtained Cu(II) compounds.

5.1.2.3 Synthesis and characterization of the Cu(II) complexes of **L6** and **L7**: complexes **C6** and **C7**

Metalation of **L6** and **L7** was carried out in both cases by using Cu(OAc)$_2$ as the copper salt. In this particular case, and since Arg residues are protonated, a higher excess of salt than that employed for the synthesis of **C5** was used. The excess was easily removed *via* several washes with ACN, in which the final complex was not soluble.

C6 and **C7** were characterized by HR ESI-MS (**Figure 5.10**) and ESR spectroscopy (**Figure 5.11**).

HR-ESI MS confirmed that both complexes were obtained in their monomeric form in solution (**Figures A54, A55** and **5.10**). For the case of **C6**, one can observe several peaks corresponding to the complex of interest (**Figure A54**), without considering any putative fourth coordinating molecule in the plane of the Cu(II) ion (**Figure 5.12**): [**C6**+2H]$^{2+}$ (882.4721), [**C6**+MeOH+3Na]$^{3+}$ (621.3109), [**C6**+3H]$^{3+}$ (588.6500), and

[**C6**+4H]$^{4+}$ (441.7483). For **C7**, a similar situation is seen (**Figure A55**). Many peaks can be attributed to H adducts of the complex at different charge states, such as +3 (664.3498), +4 (498.7642), +5 (399.2147). Experimental and theoretical patterns match perfectly in both cases (**Figure 5.10**). Up to now, no X-Ray suitable crystals have been obtained to enlighten the nature of the solid.

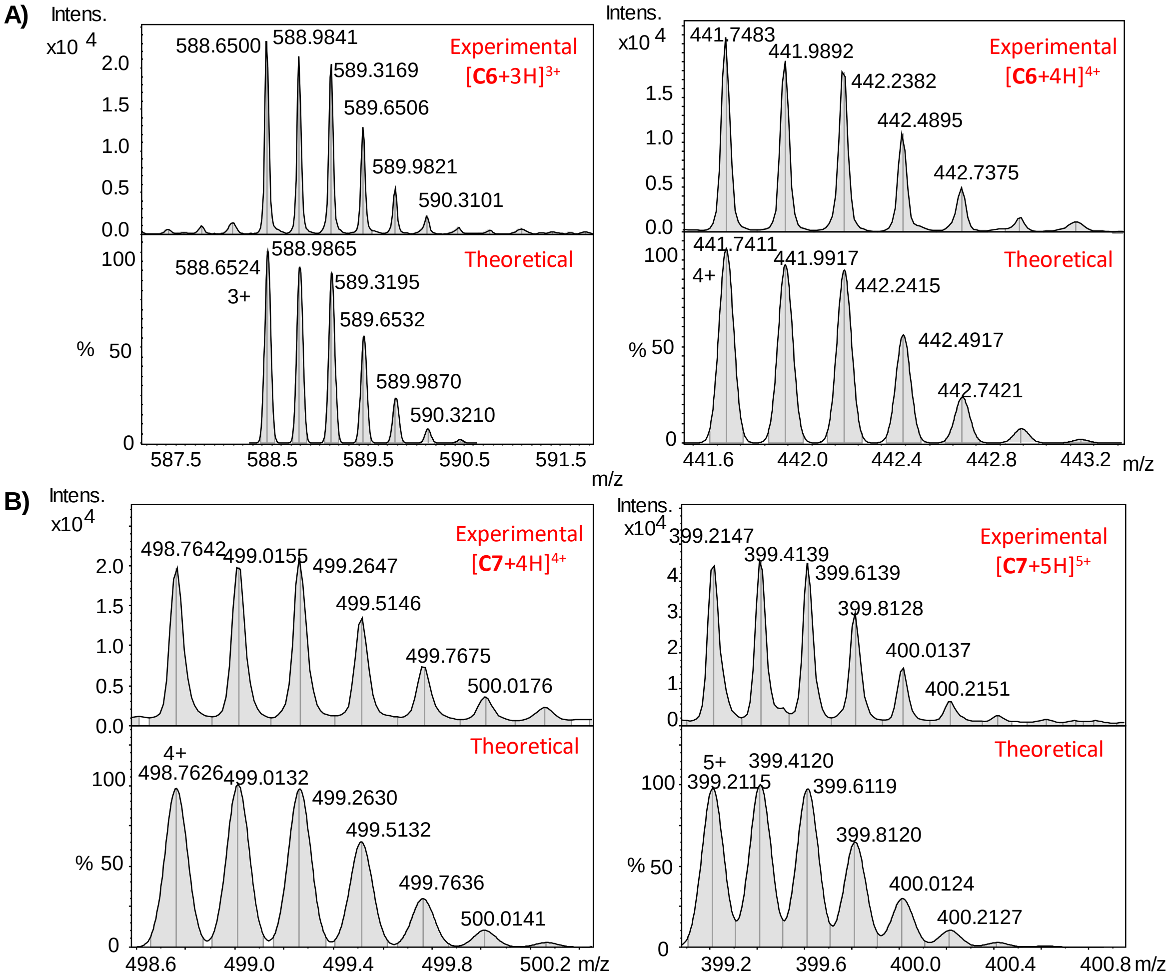

Figure 5.10. Experimental and theoretical HR-MS (ESI$^+$, H_2O-MeOH) spectra of the some of the most intense peaks for (**A**) **C6** ([**C6**+3H]$^{3+}$ and [**C6**+4H]$^{4+}$) and for (**B**) **C7** ([**C7**+4H]$^{4+}$ and [**C7**+5H]$^{5+}$). In all the cases, both **C6** and **C7** represent the complex without the fourth coordinating molecule X (**Figure 5.12**).

ESR experiments of **C6** and **C7** (**Figure 5.11**) clearly outline that there is only one Cu(II) center in each complex with the same coordination environment as that of **C1** (N_2O_2). ESR parameters are analogous in all three cases (**Table 5.1**). Data corroborate that functionalization with both CPPs have not altered the coordination environment around the Cu(II) ion respect to the parent complex **C1**, as it was hypothesized and intended. As seen in previous cases, the N_2O_2 environment in the equatorial plane is given by the ligand donor atoms (N, N, O), while the remaining O is most-likely coming from solvent coordination (a DMSO molecule).

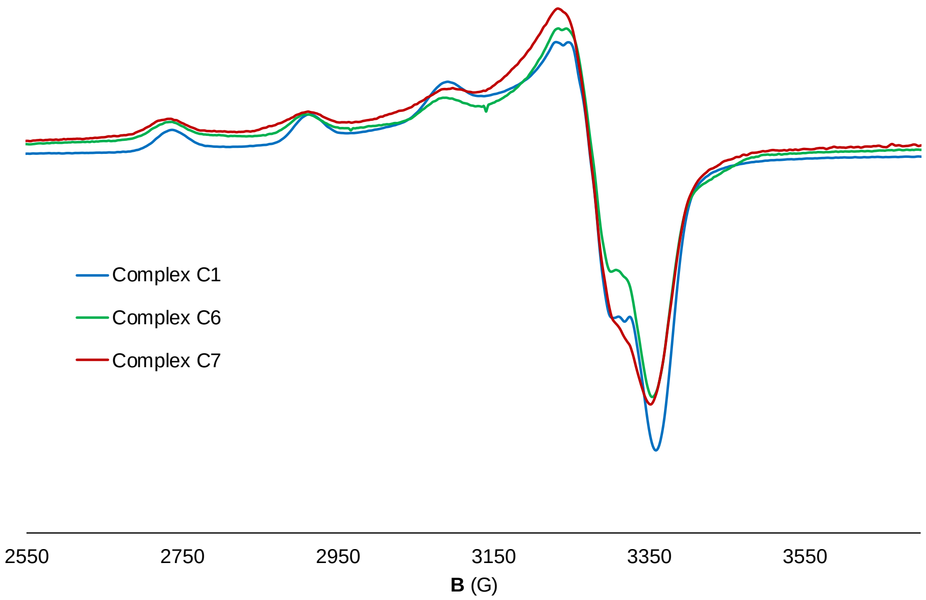

Figure 5.11. X-ESR band for complexes **C1**, **C6** and **C7** in DMSO solution. Spectra were normalized for the sake of comparison.

Table 5.1. ESR parameters for complexes **C6**, **C7** in DMSO solution (**Figure 5.11**). **C1** is included for the sake of comparison.

Complex	$g_{//}$	$A_{//}$ (10^{-4} cm^{-1})	$g_{\perp}$	$A_{\perp}$ (Gauss)	$g_{//}/A_{//}$ (cm)
C1	2.247	180	2.050	<20-30	125
C6	2.244	183	2.043	<20-30	122
C7	2.248	185	2.050	<20-30	122

For **C1**-**C5**, there were always data pointing to the presence of the dinuclear form in the solid phase, either as the unique structure (**C1**-**C3**) or maybe coexisting with the monomeric form (**C4** and **C5**). For **C6** and **C7** neither MS nor ESR were able to prove any dimeric form. This different behavior could arise from the presence of the high-positively charged R_9 peptides, which would difficult the formation of any dinuclear structure. Therefore, **C6** and **C7** are proposed as mononuclear structures (**Figure 5.12**), where the fourth coordination position of the equatorial plane could be occupied by a solvent molecule or any other counterion such as acetate (X).

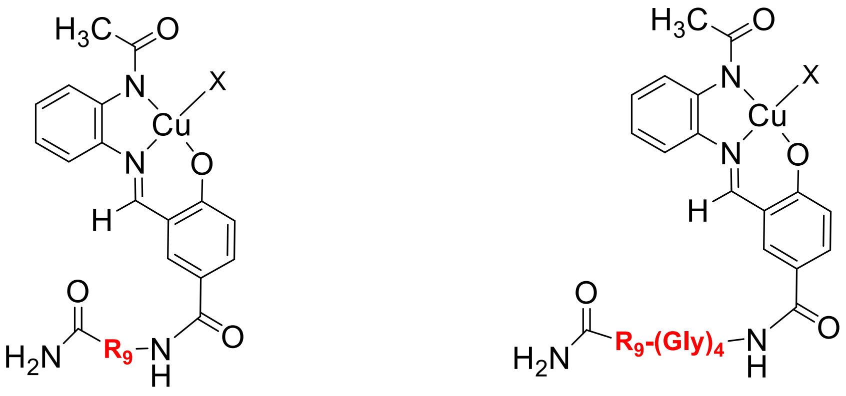

C6 **C7**

Figure 5.12. Proposed structures for **C6** and **C7**. X accounts for any solvent molecule or counterion in a square-planar derived geometry around the metal. The presence of an axial ligand cannot be ruled out (square pyramidal geometry).

5.1.2.4 Biological activity of complexes **C6** and **C7** compared with that of **C5** and **C1**. Evaluating the effect of the Cell-Penetrating Peptides bioconjugation

In vitro assays in HeLa cancer cells were carried out to evaluate the effect of the CPPs onto the final biological activity of the complex. This part will be essentially divided into two main sections. First of all, cytotoxicity experiments will shed light into the antiproliferative activity of the new complexes with respect to the parent one: **C1**. Secondly, uptake studies will also try to elucidate the role of these CPPs and try to correlate it with the toxicity profiles observed.

Cytotoxicity experiments were carried out in HeLa cell lines at both 24 and 72 h for complexes **C6** and **C7**. Results are shown in **Figure 5.13**, **Figure A56** and **Table 5.2**.

Complexes **C6** and **C7** show higher toxicity than that observed for **C1** as a general trend (**Figure 5.13** and **Table 5.2**). As seen from the cell-viability experiments at 72 h, both complexes with the CPPs cause an increase on the cell-death respect to **C1**, especially at 50 µM, where they show significant differences between the cell-viability values (**Figure 5.13**). IC_{50} at 72 h of both **C6** and **C7** are lower (52 and 41 µM, respectively) than **C1** (54 µM). Despite the fact that for **C6** the difference is not as significant as for **C7**, an appreciable change can be observed from the values at 24 h (**Table 5.2**). At shorter times, the differences between their IC_{50} values are more distinguishable and there is a significant increase of cytotoxicity in **C6** and **C7** complexes respect to **C1**. While **C1** shows values around 70 µM, both **C6** and **C7** exhibit IC_{50} values of 50 µM, being a noticeable and remarkable improvement, in the range of the well-known drug cisplatin ($IC_{50,\ 24\ h}$ of 40 µM).[213]

Furthermore, the presence of the glycine linker in **C7** appears to slightly induce higher toxicity than **C6**. This effect is more clearly appreciated at 72 h (**Table 5.2**), where there is a difference in the IC_{50} value of both complexes, being **C7** more toxic. As already mentioned at the beginning of this chapter, this could be justified by the fact that spacers do normally entail a better recognition of the peptides by the specific receptor sites in cells.[266] However, it is important to state here that the difference is not big enough to definitely attribute it to the linker presence. Further experiments with different spacer lengths would be required to confirm this hypothesis.

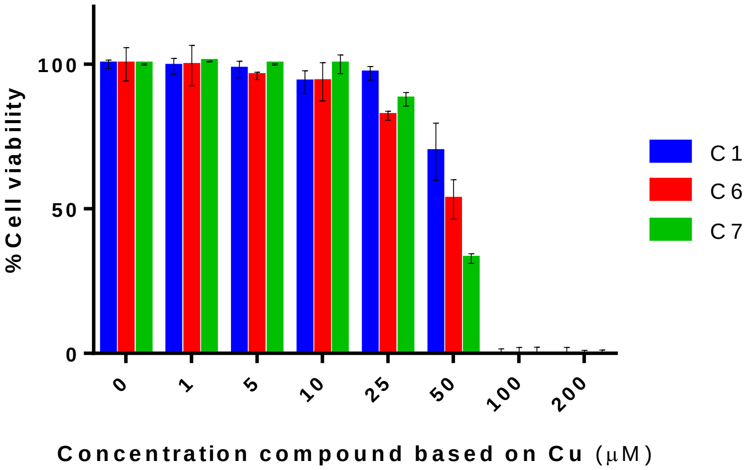

Figure 5.13. Cell-viability assays for complexes **C1**, **C6** and **C7** in HeLa cell lines after 72 h of treatment. Due to the putative presence of dimeric and monomeric forms of the different assayed complexes in the solid structure, concentrations of the tested compounds have been normalized in solution based on the Cu concentration.

Observing that the differences in toxicity between **C6**, **C7** and **C1** are higher at 24 h than at 72 h, points to the fact that time plays an important role in the toxicity of these CPPs conjugated compounds. The presence of the R_9 and $(Gly)_4$-R_9 peptides might have promoted a faster entrance of the complex inside the cell. Basically, even with faster and higher internalizations of **C6** and **C7**, large exposure times (24 h or 72 h) would give enough time to **C1** to enter, even at a slower rate, and reduce the differences in toxicity. Consequently, the next step was to evaluate the effect of the treatment time in the toxicity of these compounds. One of the most important aspects in cancer treatment is focused on the efficiency of a drug in time, *ergo*, its onset of action. If a drug is able to exert the desired activity in a shorter time, any possible clearance pathway from the tumor are diminished, providing an added value to the pharmacodynamics and pharmacokinetics of the drug.

We performed then cytotoxicity assays at two different treatment times to see if differences increased between the three complexes at shorter times. In our case, 30 min and 4 h were chosen to be evaluated. After the selected treatment times with **C1**, **C6** and **C7**, we removed the supernatant (*i.e.*, the remaining complex) and left the cells evolve for 72 h, with the already entered amount of complex in 30 min or 4 h. Results are shown in **Figure 5.14**.

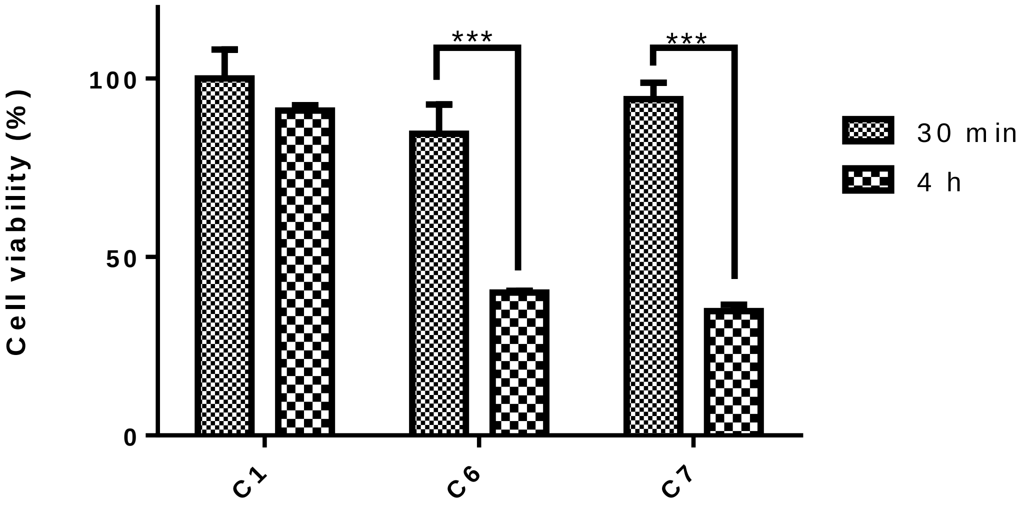

Figure 5.14. Cell-viability assays for complexes **C1**, **C6** and **C7** in HeLa cell lines at 30 min and 4h of treatment time. Compounds were used at 100 µM concentration, normalized based on Cu. The results average three independent experiments. The three asterisks indicate statistical significances between the values with $p \leq 0.001$.

Remarkably, data show that after 30 min there is not enough uptake of any of the complexes to undergo cell-death. However, and interestingly, after 4 h of treatment, the amount of **C6** and **C7** that has been already internalized is able to produce the death of significantly more than 50% of the cell population. Contrarily, **C1** does not show any significant cytotoxicity after the same exposure time, clearly indicating that it needs more time to be able to enter and exert some kind of activity. This experiment stands out complexes **C6** and **C7** as chemotherapeutic agents, where the presence of the CPP makes them much more efficient. This is highly promising and attains a lot of interest in terms of the effective pharmacological dose for pre-clinical assays.

Further information on the activity of **C6** and **C7** can be extracted by comparing these values with those at the same concentration for the 72 h treatment experiments (**Figure 5.13**). In the case of 72 h treatment, both **C6** and **C7** reach the 0% of viability at 100 µM. At 4 h, the uptaken amount is already able to cause the death of more than 50% of the cell population, which represents a significant proportion of the total toxicity, highlighting the penetrability rate of **C6** and **C7** in only 4 h.

The cellular internalization of the complexes **C6** and **C7** was consequently measured at 4 h, and the copper amount inside cells quantified by ICP-MS. Results are shown in **Figure 5.15** and **Table 5.2**. As observed, both **C6** and **C7** penetrate significantly more than **C1** ($p \leq 0.001$). Indeed, the amount of Cu able to enter cells for the conjugated complexes is more than twice the amount found for **C1**. These differences can be attributed to the presence of the CPPs in **C6** and **C7**, which confer an enhanced cellular uptake to the complexes and, hence, an improved cytotoxicity, with salient impact at short treatment times. As already mentioned in *Chapter 4*, cisplatin has shown to enter about 100-120 ng/10^6 cells at similar treatment conditions.[253] In this particular case, **C6** and **C7** are able to have an enhanced penetrability rate, and this could give them higher efficiency at shorter times than the rest of assayed complexes.

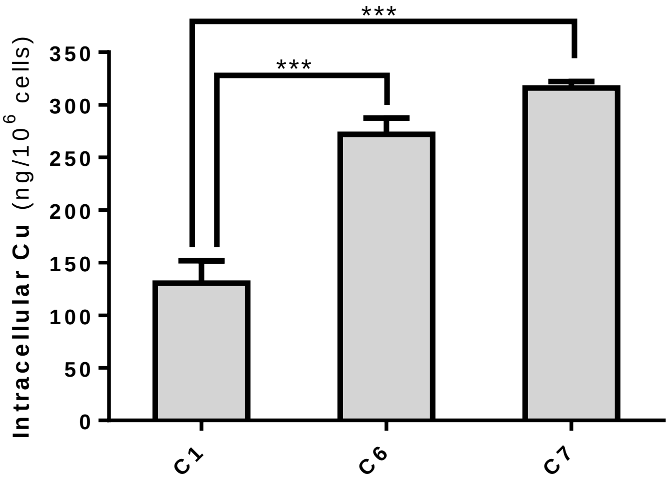

Figure 5.15. Quantification of the copper uptake in HeLa cancer cells after 4 h treatment. Complexes were used at 50 µM concentration based on the Cu metal. The three asterisks indicate statistical significances between the values with $p \leq 0.001$.

Table 5.2. IC_{50} (µM) values at 24 and 72 h of complexes **C1**, **C6** and **C7** in HeLa cell cultures, and their corresponding copper cellular uptake after 4 h of treatment at 50 µM of Cu concentration for each assayed complex. **C5** results (**Table 4.4**) have been included in this table for the sake of comparison. The results shown are representative of at least two independent experiments (N=2).

Compound	IC_{50} (24 h)^a	IC_{50} (72 h)^a	Intracellular Cu (ng/10^6 cells)
C1	67±2	54±1	131±21
C5	108±4	55±2	97±22
C6	51±6	52±4	272±15
C7	50±5	41±4	315±6

^{a}*Normalized for Cu concentration.*

As already appreciated in the cytotoxicity results, the presence of the linker seems to apparently induce some effect on the final complex (**C7**). It also shows a higher uptake in HeLa cancer cells than **C6**, which may explain the differences found in cytotoxicity between them. Nonetheless, these differences are not significant enough yet and more data would be required to assure this putative relationship. Up to now, it remains as a hypothesis worthy to be further explored.

The uptake mechanism of CPPs is in most cases still unraveled. As detailed at the beginning of the section, some reports talk about translocation, others endocytosis, etc. Several mechanisms have been proposed and a lot of research has been carried out during the last 5 years trying to understand the factors that govern the recognition and mechanism of these specific sequences.[242,256,274] To remark it, it is clear that the presence of only one Arginine (**C5**) is not sufficient to improve any cellular uptake of the compound. Increasing the solubility of the complex with only one of the unities of the CPP sequence does not represent any enhancement into the penetrability or activity (**Table 5.2**). Consequently, only very specific sequences of peptides are able to be recognized by the cell and cross the membrane.

In conclusion, the main breakthrough of these two new complexes (**C6** and **C7**) especially arises from the fact that they show higher efficiency than **C1** at short treatment times, due to their enhanced cellular uptake. This is indeed the main advantage conferred by the presence of CPPs, and rise **C6** and **C7** as promising therapeutic candidates for future *in vivo* tests.

PART II

5.2 Drug delivery systems (II): a multimodal dendritic platform

Dendrimers have become attractive scaffolds as drug delivery systems.[275–279] They have gained attention due to their polyvalence, high water solubility and biocompatibility.[180,280] Defined as well-organized 3D-branched nanomeric molecules, the name comes from the Greek work *dendron*, which means *tree*. This highlights their archetypical tree-like branching structure. Their basic structure comprises three main components: a central core, repetitive branching units, and terminal groups, which provide modifiable and surface functionalities. The increase in the number of repeated branching units determines the dendrimer generation.[281,282] The high control level over their architecture makes them promising systems in terms of drug delivery applications where cargoes can be either encapsulated in the internal cavities, mostly hydrophobic, or bound to their surfaces. In this last case, they can be non-covalently attached or covalently linked to the terminal groups.[279]

Several well-known chemotherapeutic drugs, such as methotrexate, cisplatin or doxorubicin,[276,283,284] have been anchored to dendritic structures, improving its tumor targeting capabilities and delivery. One of the advantages that dendrimers provide in terms of drug delivery relies on the EPR effect, which has been already extensively explained in *Section 1.4.2.2.1*. This effect seems to be especially significant when dendritic structures are conjugated with polyethylene glycol (PEG) chains.[285,286] This conjugation has also been shown to reduce the cytotoxicity that the dendritic core offers sometimes, as well as to increase plasma circulation time.[287,288]

The group of Dr. Miriam Royo (CSIC, Barcelona, Spain) has reported several multimodal dendritic platforms based on the diethylenetriaminepentaacetic acid (DTPA) (**Figure 5.16A**), with PEG branching chains.[289] DTPA contains five carboxylic acids (H_5DTPA) and serves as a source of multivalency and, with concrete modifications, also of multimodality. The reported first-generation dendritic platforms can attain several functionalities, giving rise to up to pentamodal structures (**Figure 5.16B**). Their versatility and "*à la carte*" functionalization raise them as highly interesting structures for drug delivery.[289]

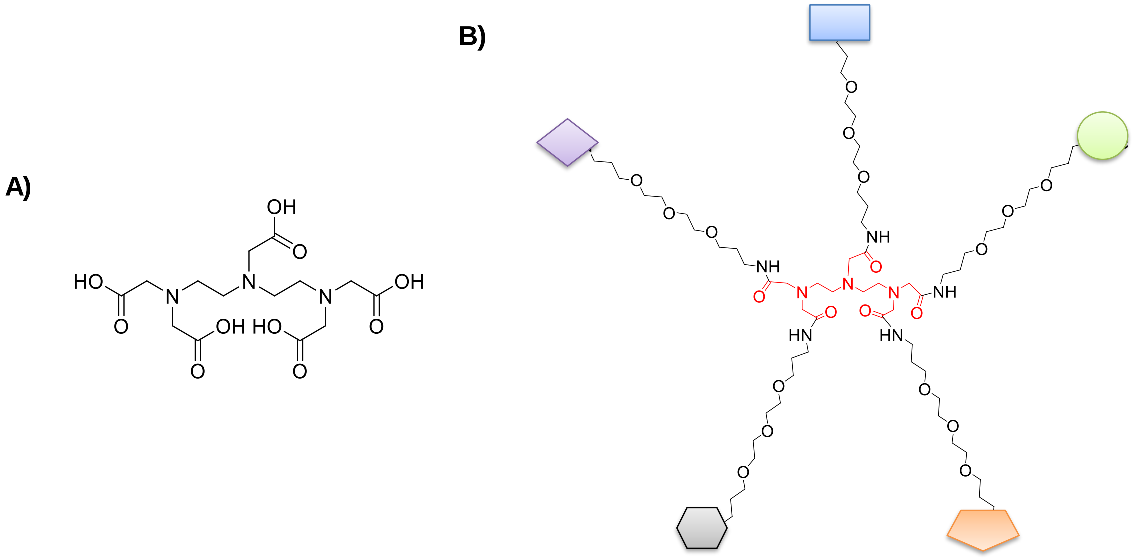

Figure 5.16. (**A**) Diethylenetriaminepentaacetic acid (DTPA) molecule. (**B**) DTPA-based dendritic platform reported by the group of Dr. Míriam Royo, showing its multimodality.[289] In red, the DTPA core.

5.2.1 The monomodal dendritic platform: DTPA-5Ac

The final purpose of the second part of this chapter lies in the attachment of the complex **C1** to the dendritic DTPA-based structure. However, it is important to have in mind that DTPA is a well-known metal chelating agent.[290–295] It has been reported to chelate a vast myriad of different metal ions, among them Cu. Since we are working with Cu(II) ions, before starting with any synthetic route to conjugate the two organic entities (*i.e.* the DTPA-based platform with the **L1** scaffold), we found necessary to evaluate first the Cu(II) complexation abilities of the DTPA core and its potential biological activity. This study was carried out with the simplest dendritic monomodal DTPA-based platform, dubbed DTPA-5Ac (**Figure 5.17**), containing all five terminal amino groups protected in the acetamide form. This platform mimics the final product where the five amino group will be functionalized and therefore not available for Cu(II) coordination. The synthesis of this pentaacetylated DTPA-based platform was carried out and characterized by Dr. Daniel Pulido (Dr. Míriam Royo research group, CSIC, Barcelona, Spain), as reported.[289] We used it directly as received.

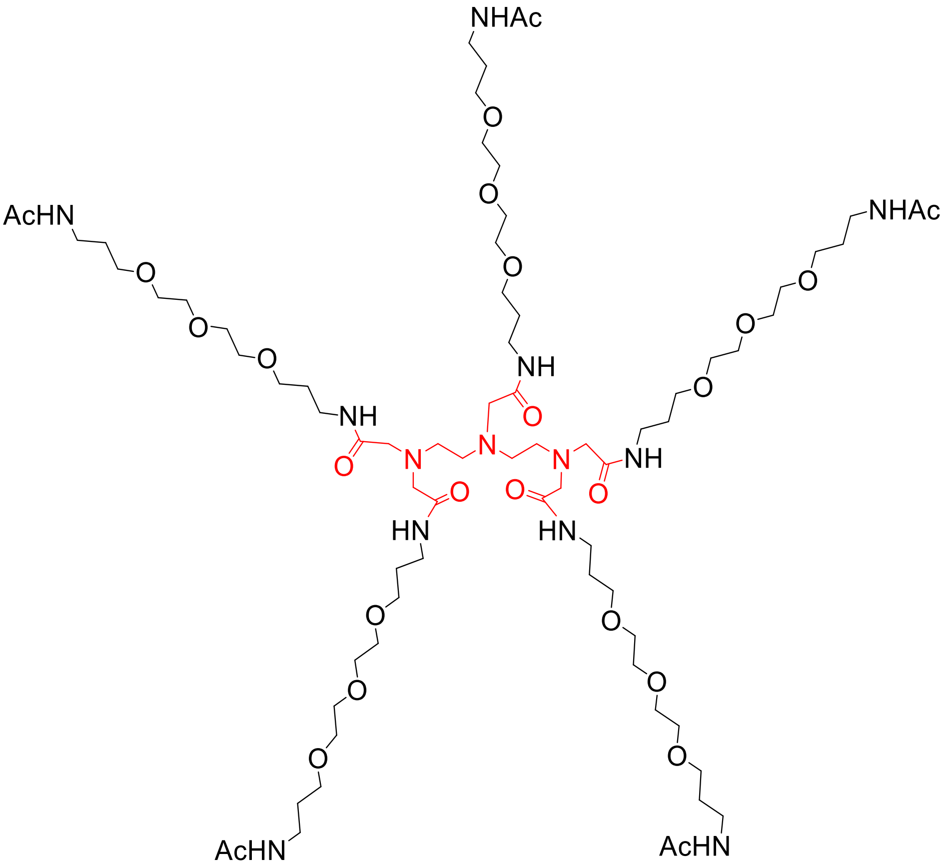

Figure 5.17. Structure of the dendritic monomodal DTPA-based platform: DTPA-5Ac. In red, the DTPA core.

5.2.1.1 Cu(II) coordination abilities of the DTPA core of the dendritic platform DTPA-5Ac

The coordination abilities of the DTPA-5Ac platform have been evaluated by potentiometric studies, VIS experiments, ESR and MS spectrometry.

First of all, potentiometric studies have been carried out with both the DTPA-5Ac alone and in presence of a Cu(II) salt (**Figure 5.18**). As observed from the titration curves of the ligand alone, there is one sloping break at *a* = 1 and at pH around 6. This indicates that it contains one proton able to be deprotonated in aqueous solution at the pH range possible to have reliable values by potentiometry. Since amide groups, as usual, cannot be deprotonated within this pH range, it most likely corresponds to one of the protonated tertiary amines ($-NR_2H^+$) of the central structure (**Figure 5.17**).[296,297] The calculated pK_a for the DTPA-5Ac in the working pH range is 5.6, which is lower than that reported for the DTPA molecule.[298] This is in concordance with the reported literature, where the derivatization of the carboxylic acids of amino-based chelating ligands has been shown to decrease the pK_a of the central N.[298–300]

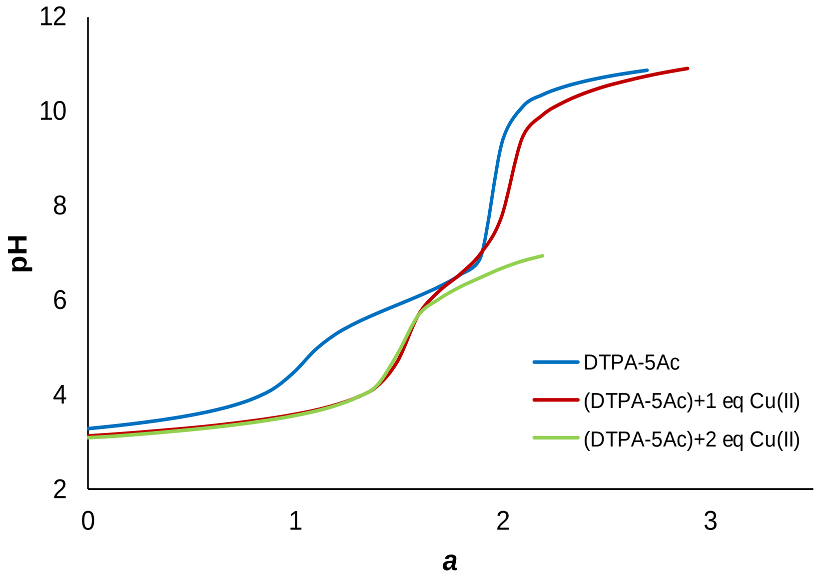

Figure 5.18. Potentiometric titration curves for DTPA-5Ac (1 mM) performed at 298 K and *I* = 0.1 M KNO_3, plotted in the absence and presence of Cu(II). The ***a*** value is the number of moles of base per mole of ligand. The curve corresponding to 2 equivalents of Cu(II) respect to the DTPA-5Ac has been only represented until pH 7 (pH >7 gives rise to the precipitation of $Cu(OH)_2$ and therefore values are misleading).

The presence of 1 equivalent of Cu(II) in the titration experiments (**Figure 5.18**) shows acidification. The buffer region at the acidic pH 3 is longer (until *a* about 2) than that of the DTPA-5Ac alone. This points to an ongoing deprotonation on the ligand, which occurs at lower pH due to metal interaction. At 2 equivalents of the metal ion (**Figure**

5.18), the curve parallels the one at one equivalent of Cu(II) at the acidic pH (pH 3), pointing to the same number of metal ions interacting with the DTPA-5Ac. Besides, at two equivalents of Cu(II), there is the formation of a fine precipitate at pH higher than 7. Isolation, acidification and examination of the precipitate showed that there was no organic matter, thus suggesting that it corresponded to Cu(II) hydroxide. This indicates that DTPA-5Ac is able to only bind one Cu(II) ion.

It is interesting also to mention that a new inflexion point appears in the potentiometric curves of DTPA-5Ac upon metalation ($a = 2$) with a pK_a about 6-7, which could correspond to the deprotonation of an aqua molecule of the metal coordination sphere of the Cu(II) complex with the DTPA-5Ac.

Confirmation of the 1:1 stoichiometry was achieved by ESR, VIS and MS experiments. According to the titration curves seen in **Figure 5.18**, the [Cu(DTPA-5Ac)]$^{n+}$ complex (**C8**) is formed at pH about 6. Several (DTPA-5Ac):Cu(II) mixtures at 1:1 stoichiometry were prepared at different pH (5.5, 7.2 and 8.5) and analyzed by ESR, to confirm the formation of a single Cu(II) species (**Figure 5.19**). As clearly observed, at pH 5.5 there is a mixture of two Cu(II) centers[7], while at pH 7.2 and 8.5 there is a single Cu(II) center in solution. ESR was also performed with a sample containing 2 equivalents of Cu(II) *vs.* the DTPA-5Ac ligand (**L8**) at pH 7.2 (**Figure A57**). The ESR spectrum of what remains in solution matches perfectly with that found with only one equivalent, confirming that it only binds one Cu(II) ion.

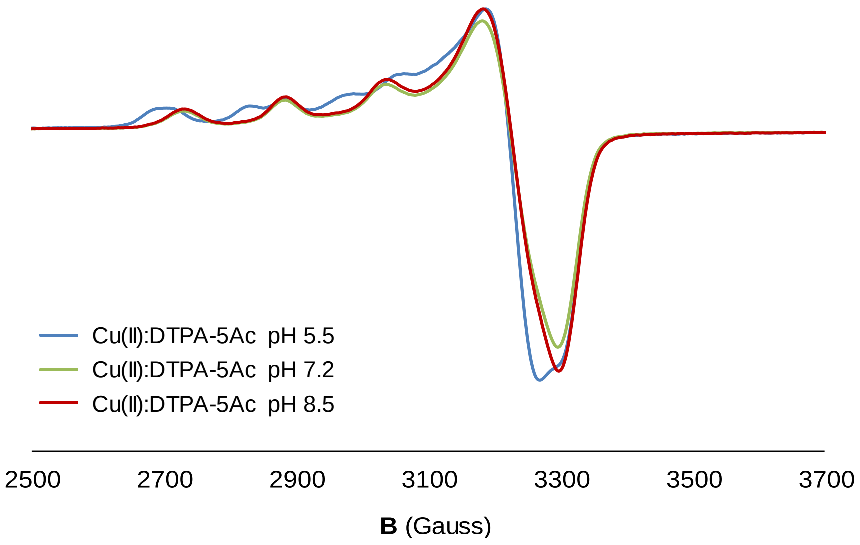

Figure 5.19. X-ESR band of Cu(II):DTPA-5Ac mixtures (1:1 stoichiometry) at different pH in water (with 10% of glycerol).

---

[7] *One of the Cu(II) centers matches with that of ESR at pH 7.2 and 8.5 (**Table 5.3**), while the other one fits with a N_2O_2 coordination environment. The latter would support the hypothesized deprotonation of an aqua molecule of the Cu(II) coordination sphere at pH* ca. *6, observed in potentiometric studies (**Figure 5.18**).*

Extraction of the ESR parameters at either pH 7.2 or 8.5 suggests that the coordination environment around the metal ion might be N_3O or N_4 (**Table 5.3**). The ground state for the single electron is in the $d_{x^2-y^2}$ orbital, and, hence, a square-planar or square-pyramidal derived geometry is expected. However, and according to the $g_{//}/A_{//}$ ratio, which is higher than 140 cm, the complex seems to adopt a slightly distorted structure from planarity. This is indeed in concordance with the high flexibility of the dendritic platform, in contrast to the aromatic-based ligands, such as the ones used for **C1**-**C7**. Based on the proposed environment for **C8**, the DTPA-5Ac (ligand **L8**) could coordinate Cu(II) with at least two of the three tertiary amino groups of the DTPA core. The others N may arise either from the third amino group or from any of the amides adjacent to the central core. If there is any oxygen coordinating, it might come from the amide groups (C=*O*).

Table 5.3. ESR parameters for the complex $[Cu(DTPA\text{-}5Ac)]^{n+}$ (**C8**) at pH 7.2-8.5, extracted from **Figure 5.19.**

Complex	$g_{//}$	$A_{//}$ (10^{-4} cm^{-1})	$g_{\perp}$	$A_{\perp}$ (Gauss)	$g_{//}/A_{//}$ (cm)
C8	2.252	155	2.055	<20-30	145

VIS experiments were also carried out at different pH (**Figure A58**). The *d-d* bands of the Cu(II) ion were observed at different pH (3, 5.5, 7.2, 8.5). Results show that there is a hypsochromic shift on the absorption from pH 5.5 to 7.2, attributed to the complexation of the Cu(II) and in concordance with what we previously observed from ESR and potentiometric studies. At pH higher than 7.2, there is no significant change on the VIS Cu(II) *d-d* band, reinforcing that the Cu(II) complex is already formed. Comparison of the VIS spectrum with one equivalent of Cu(II) and two equivalents results in the same *d-d* band shift, and gives rise to the same final absorbance (**Figure A58**), indicating that only one Cu(II) is bound.

This species was finally confirmed by ESI-MS experiments at pH 8.5 (**Figure 5.20**). Several peaks can be assigned to different adducts of the DTPA-5Ac with the Cu(II) ion both at +2 and +3 charge states. Peak at *m/z* 838.5 corresponds to the $[Cu(DTPA\text{-}5Ac)]^{2+}$ (**C8**), while the rest are adducts of this complex **C8** with H^+, Na^+ or K^+ (849.5, 579.3 574.0, 566.6, etc.).

Once it is clear that the core binds one Cu(II) ion, determination of the binding constant was of interest. As the K_b was unable to be obtained *via* the acquired potentiometric data (**Figure 5.18**) due to the fact that the DTPA-5Ac deprotonation upon metal binding has already occurred at acidic pH,[301] spectrophotometric titrations were performed.

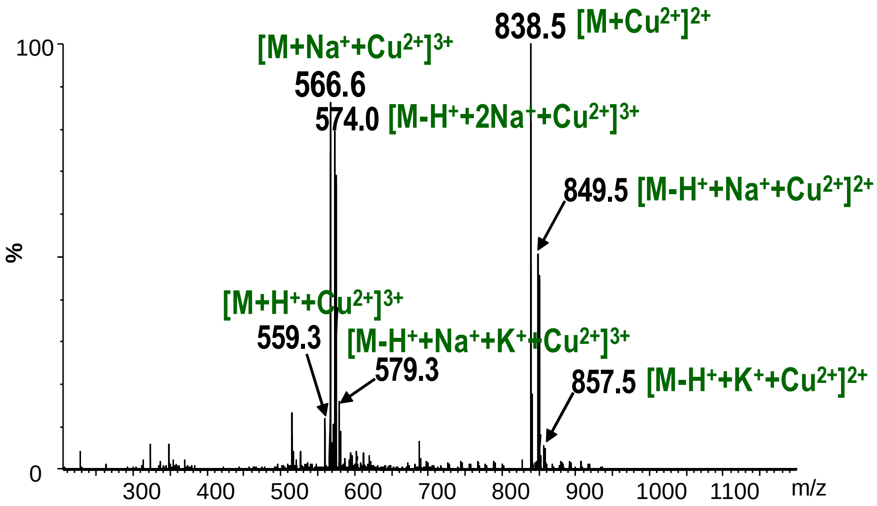

Figure 5.20. MS (ESI$^+$, H_2O-MeOH) spectrum of the interaction of the ligand DTPA-5Ac with 1 equivalent of Cu(II) (**C8**) at pH 8.5. *M* in the spectrum refers to the DTPA-5Ac ligand (**L8**).

Cu(II) titrations to the DTPA-5Ac were performed at pH 7.2 (from 0 to 2 equivalents). They were monitored by following the changes on the *d-d* band at their absorption maximum of 681 nm (**Figure 5.21**). Results show a change in the slope at 1 equivalent of Cu(II), where it starts to decrease, reaching a *plateau*, consistent with the binding of one Cu(II) ion.

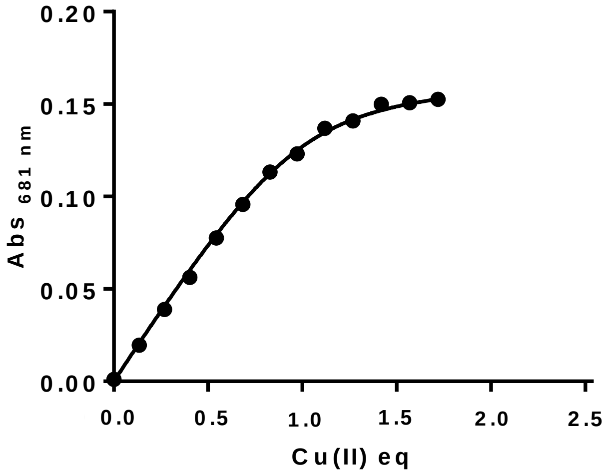

Figure 5.21. Cu(II) titration to DTPA-5Ac (1.5 mM) in 50 mM HEPES buffer (pH 7.2), monitored by the change on the absorbance at the *d-d* VIS maximum at 681 nm. Solid line corresponds to the fit using *Equation 2*.

Calculation of the apparent binding constant was carried out by using a well-known equation (*Equation 2*)[302,303] to determine association constants at different stoichiometry ratios for supramolecular structures, nicely reviewed by P. Thordarson.[304] For each point of the titration, $[Cu]_T$ is increased while the concentration of DTPA-5Ac ([DTPA]) is fixed (1.5 mM). The increase in A_{681} is directly proportional to the amount of **C8** formed, *l* is the cell path-length (1 cm), ε the molecular extinction coefficient ($M^{-1} \cdot cm^{-1}$), and $K_{[Cu(DTPA\text{-}5Ac)],app}$ is the apparent binding constant of the complex **C8**. By plotting the data obtained in **Figure 5.21**, both the extinction coefficient and the $K_{[Cu(DTPA\text{-}5Ac)],app}$ can be calculated (**Table 5.4**).

$$A = \varepsilon l \frac{\left(\frac{1}{K_{[Cu(DTPA-5Ac)],app}} + [Cu]_T + [DTPA]_T\right) - \sqrt{\left(\frac{1}{K_{[Cu(DTPA-5Ac)],app}} + [Cu]_T + [DTPA]_T\right)^2 - 4[Cu]_T[DTPA]_T}}{2} \qquad (Equation\ 2)$$

The calculated apparent association constant between DTPA-5Ac (**L8**) and Cu(II) is 9.6 mM^{-1}, and the extinction coefficient is 0.111 $mM^{-1} \cdot cm^{-1}$. The contribution of HEPES buffer as a metal-binding competitor -it can form a 1:1 complex with Cu(II)- can be corrected by *Equation 3*,[305] to obtain the conditional binding constant (K_{COND}) at the given pH. This conditional metal-binding constant is the affinity constant at a zero-buffer concentration, which would give us a more accurate idea of the binding capacity of the DTPA-5Ac platform.

$$logK_{COND} = logK_{[Cu(DTPA-5Ac)],app} + \log\left(1 + \beta_{Cu-HEPES} + \frac{[HEPES]}{1 + 10^{-pH+pKa}}\right) \qquad (Equation\ 3)$$

Using *Equation 3*, the K_{COND} for the 1:1 complex (pH 7.2) between DTPA-5Ac and Cu(II) was determined. The value is $3.2 \cdot 10^2$ mM^{-1} (**Table 5.4**). This value is much lower than the K_{COND} calculated at same pH for the Cu(II) complex with the DTPA molecule (1:1 stoichiometry)[8]: $K_{COND} = 4.7 \cdot 10^{23}$ mM^{-1}. The presence of the -COOH groups, fully deprotonated at the working pH, contribute to the final chelate stability. The DTPA-5Ac platform has no carboxylic acid group which can coordinate to the metal ion (all the -COOH are in the amido form). Besides, DTPA-5Ac platform has more flexibility than the DTPA molecule due to the PEG branches. All of this would lead to a lower stability of the

---

[8] *The calculated conditional binding constants at each pH for the DTPA molecule (and later for DTPA-BMA too) have been obtained based on the reported overall constants for these two molecules* [295,298] *and by accounting only for the 1:1 (Cu:ligand) species.*[315]

final Cu(II) chelate of **L8**. It is also consistent with some studies performed with the DTPA-derived molecule (2,2-[(carboxymethyl)imino]bis[ethylenebis(methylcarbamoyl-methyl)imino]diacetic acid: DTPA-BMA).[298] This molecule contains two of the -COOH branches of the DTPA in a methyl amido form. Calculation of the Cu(II) binding constant for a 1:1 stoichiometry gives rise to a value already six orders of magnitude lower ($5.6 \cdot 10^{17}$ mM^{-1}) than the analogous one for the DTPA.[298]

Table 5.4. Extinction coefficient (ε), apparent and conditional binding constants (K_{app} and K_{COND}) for the 1:1 complex of Cu(II) with DTPA-5Ac in HEPES (50 mM) at pH 7.2. The results average three independent experiments.

Complex	**ε (mM^{-1} cm^{-1})**	**K_{app} (mM^{-1})**	**$K_{COND} \cdot 10^{-2}$ (mM^{-1})**
C8	0.111±0.004	9.6±3.1	3.2±1.0

Once the coordination abilities of the platform have been studied, it is important to unveil the toxicity of the platform complexed with the Cu(II) ion for future biological purposes. This will allow us to know the real candidacy of this system as a future drug carrier.

5.2.1.2 Cytotoxicity studies of the Cu(II) complex of DTPA-5Ac (**C8**). Evaluating its potential as a future drug carrier

Cytotoxicity studies were carried out in both cancer and normal cell lines. Two cancer cell lines were selected (HeLa and MCF7) while NIH 3T3 fibroblasts cell line was chosen as a proof-of-concept of a normal cell line.

Experiments were carried out at 72 h treatment with both the DTPA-5Ac (**L8**) and the corresponding Cu(II) complex (**C8**) at pH about 7.3. Results (**Table 5.5** and **Figure A59**) highlight that the ligand **L8** alone does not have any significant cytotoxicity in any of the assayed cell lines. However, the presence of Cu(II) endows toxicity to the platform, with some differences depending on the evaluated cell culture. In the case of HeLa cells, **C8** shows poor toxicity, with estimated IC_{50} values of ≥200 µM. In the case of MCF7, this value is much lower. Despite the fact that the cell-viability diagram does not reach the 0% of viability at 200 µM -*i.e.* IC_{50} cannot be calculated-, its estimated value would be ≥50 µM. Finally, the IC_{50} in NIH 3T3 fibroblasts: ≥150 µM.

Given these data, the presence of Cu(II) increases the toxicity of the DTPA-5Ac platform. Nonetheless, and importantly, its toxicity in NIH 3T3 fibroblasts (non-cancer cells) is not high and it can be overcome by functionalizing the platform with cancer targeting systems, which is indeed the long-term purpose.

Table 5.5. IC_{50} values at 72 h for the complex $[Cu(DTPA\text{-}5Ac)]^{n+}$ (**C8**) and the corresponding ligand DTPA-5Ac (**L8**) in HeLa, MCF7 and NIH 3T3 fibroblasts cultures. The results shown are representative of at least three independent experiments (N = 3).

Compound	HeLa	MCF7	NIH 3T3
C8[a]	≥200	≥50	≥150
L8[b]	n.d.	n.d.	n.d.

[a] IC_{50} can only be estimated. These cases are those whose dose-response curve does not reach the 0% of viability at 200 µM.

[b] n.d. (non detected). Experiments that showed no cytotoxicity at the highest assayed concentration of 200 µM.

5.2.2 The bimodal dendritic platform DTPA-4Ac-NH_2

The next step was to functionalize the platform with the **L1** ligand. A single functionalization was chosen as a proof-of concept and to facilitate the development of a synthetic strategy. This approach will allow us to assess the reliability of this system for future tailor-made designed anticancer drugs in targeted therapy. In order to do so, the bimodal DTPA-4Ac-NH_2 (**Figure 5.22**) was used. As mentioned at the beginning of the *Section 5.2*, these platforms have high tunability and can be asymmetrically functionalized by using orthogonal protecting groups. In our particular case, only one of its five terminal amino groups is deprotected and can therefore be conjugated to the ligand.

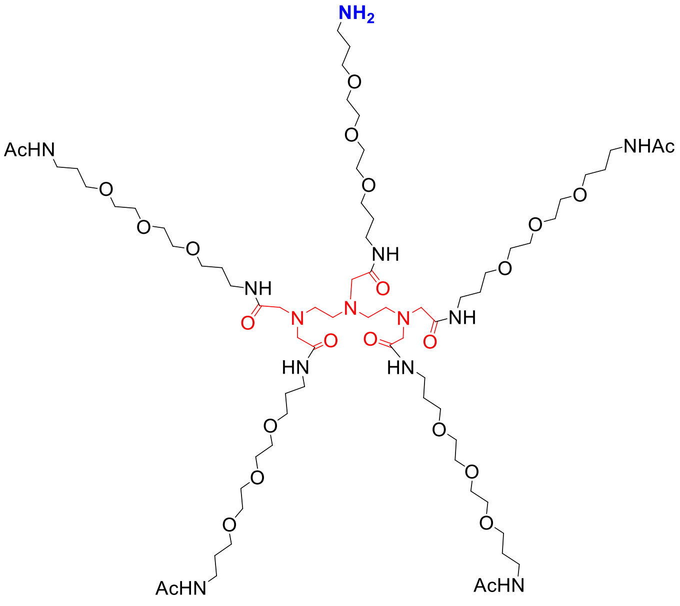

Figure 5.22. Structure of the bimodal dendritic platform DTPA-4Ac-NH_2. In blue, the amino group that will be used to functionalize the platform. In red, the DTPA core.

5.2.2.1 Conjugation of ligand **L1** to the DTPA-4Ac-NH_2 (**L9**).

The designed coupling strategy was based on the procedure followed for ligands **L5**-**L7**, where they were conjugated through an amide bond. Whereas for ligands **L5**-**L7** the conjugation was done while peptides or Arg were still attached to the resin (solid-phase), in the current case, the reaction was performed in solution. The synthetic strategy for the coupling is shown in **Scheme 5.6**.

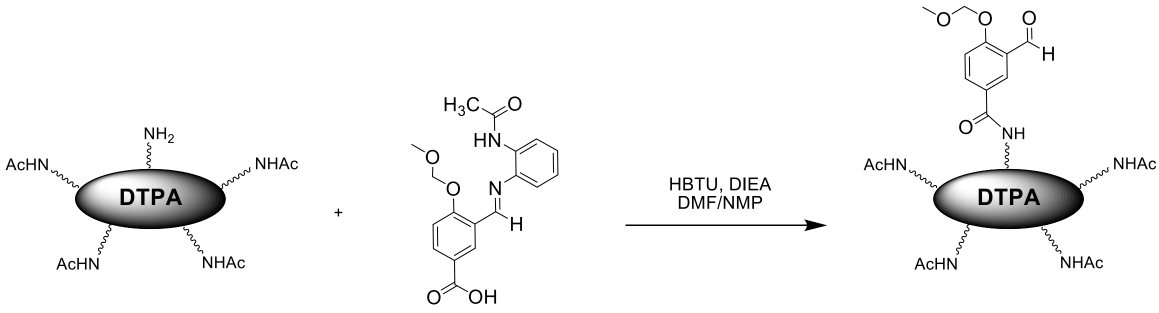

DTPA-4Ac-NH_2 **14** **22**

Scheme 5.6. Synthetic strategy for the coupling of the precursor **14** to the DTPA-4Ac-NH_2. For the sake of simplicity, the DTPA structure shown in **Figure 5.22** will be displayed from now on as shown here.

Compound **22** was obtained *via* formation of the amide bond between the -COOH group of **14**, as standard precursor for these series of compounds, and the free amino terminal group of the DTPA-4Ac-NH_2 by using HBTU as a coupling agent. The precursor **14** was added in excess to ensure full conversion.

In the first attempts, the work-up of the reaction was essentially based on liquid-liquid extractions (water-EtOAc). However, the work-up gave rise to several by-products that could not be removed from the compound of interest. The use of DMF as a solvent also complicated the cleaning procedure. The protocol was furthered optimized, *i.e.* DMF solvent was removed under vacuum and the remaining crude solid washed several times with EtOAc. This protocol allows the removal of the excess of **14** from the reaction crude since compound **22** is not soluble in EtOAc. The compound crude **22** was recovered from water after lyophilization to render a yellowish oil.

The reaction conversion was then checked by analytical reversed-phase HPLC, by following the peak corresponding to the DTPA-4Ac-NH_2 (absorbance at 210 nm, R_t = 20.1 min, **Figure 5.23A**). The chromatogram of the final reaction crude (**Figure 5.23B**) shows the presence of several peaks associated to different products of the reaction and no peak associated to the DTPA-4Ac-NH_2, confirming its total conversion.

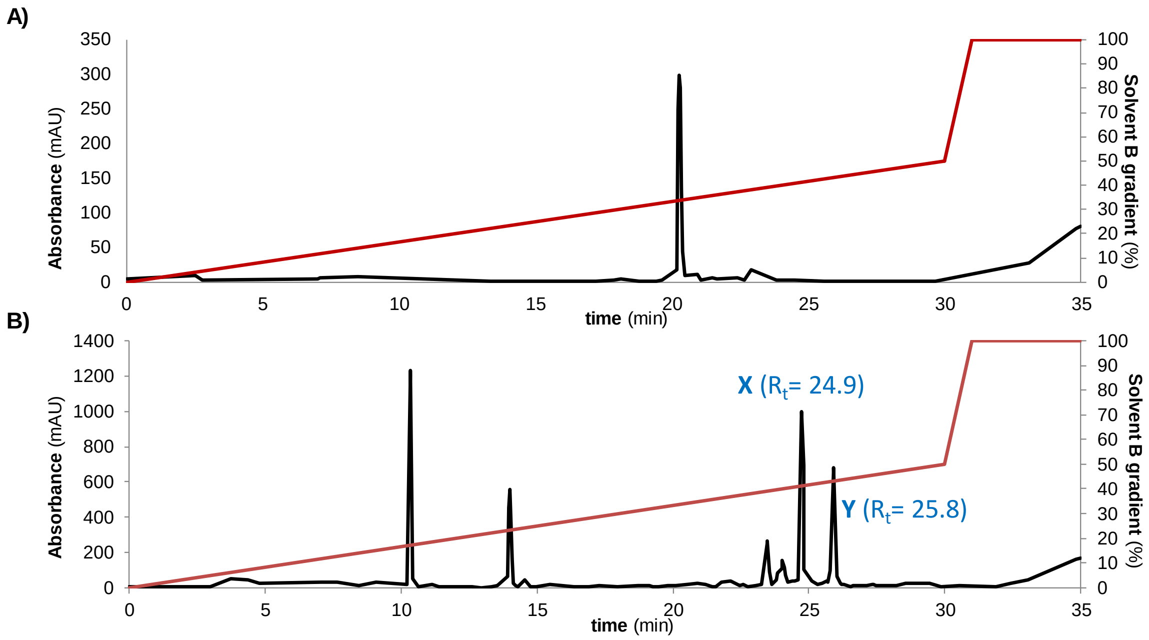

Figure 5.23. Analytical reversed-phase HPLC chromatograms (210 nm) of **A**) pure DTPA-4Ac-NH$_2$ and **B**) reaction crude of the coupling of **14** to the DTPA-4Ac-NH$_2$ (**Scheme 5.5**). Both samples were eluted using a linear gradient of 0 to 50% solvent B in 30 min (solvent A (H_2O with 0.1% TFA) and solvent B (Acetonitrile/H_2O/TFA (90:9.9:0.1)). **X** and **Y** correspond to the peaks of interest.

The reaction crude after the previous work-up was subsequently analyzed by ^{1}H NMR (**Figure A61**). Signals comprised in the chemical shift interval of 4.0-1.5 ppm refer to the aliphatic protons of the platform (**Figure A60**). Some proton signals in the aromatic region, with the expected substitution pattern, confirmed that synthesis of **22** was accomplished. Nonetheless, there were still impurities and the reaction crude needed to be purified.

Purification of the reaction crude was carried out by using preparative reversed-phase HPLC. Compounds **X** and **Y** (**Figure 5.23B**) were isolated by preparative HPLC, yielding compounds **23** (**Figure 5.24**) and **22** (**Scheme 5.6**), respectively, as confirmed by ^{1}H NMR (**Figure A62** for **23** and **Figure A63** for **22**) and ESI-MS (**Figure 5.25**).

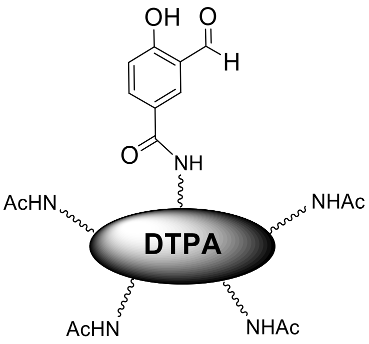

Figure 5.24. Structure of compound **23**.

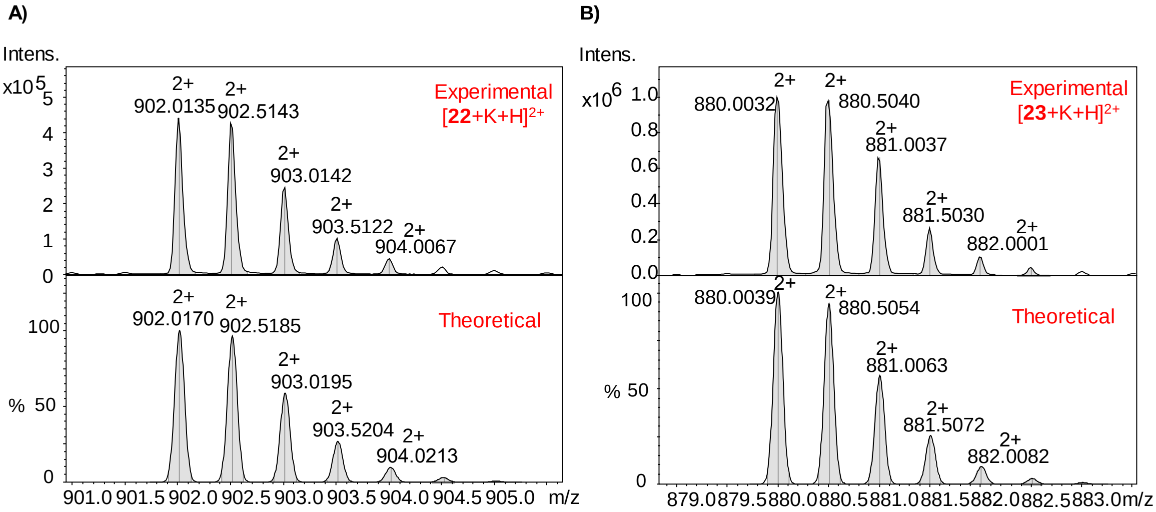

Figure 5.25. Experimental (top) and theoretical (down) HR-MS (ESI$^+$, MeOH) of (**A**) compound **22**: [**22**+K+H]$^{2+}$ and (**B**) compound **23**: [**23**+K+H]$^{2+}$.

The formation of compound **23** (phenol deprotected) after the HPLC purification resulted from the acidic nature of the mobile phase. MOM is a protecting group that is generally removed with strong acid treatment.[306] However, and despite the soft acidic conditions of the mobile phase used during the purification process, the MOM protecting group was partially cleaved. As previously observed, the iminic bond present in the precursor **14** was broken yielding to the corresponding aldehydes **22** and **23**, respectively.

Based on the partial MOM deprotection found under the HPLC conditions, its full removal was attempted prior to HPLC purification. Stirring the reaction crude, after the EtOAc washes, with TFA (5-10% in DCM) resulted in total removal of the MOM group. Afterwards, purification using preparative reversed-phase HPLC was carried out to yield simply compound **23**.

The following step was the synthesis of the final ligand **L9**. This compound was obtained by the condensation reaction of the -CHO group of **23** and the free amino group of **1**, which was used in excess (**Scheme 5.7**). Washes with EtOAc eliminated the excess of unreacted **1**.

L9 was characterized by ^{1}H NMR (**Figure A64**). If we compare the NMR spectra of **23** and **L9** (**Figure 5.26**), the shift of the peak at δ 10.05 ppm (H_{11}) in **23** (**Figure 5.26A**) to 9.99 ppm in **L9** (**Figure 5.26B**) can be ascribed to the imine formation and it is consistent with the lower electronegativity of N *vs.* O atom. At δ 2.11 ppm there is a new singlet integrating for 3H, which can be attributed to the -CH_3 group of the amide coming from **1** (H_{23}). The aromatic region (δ 8.0-6.5 ppm) shows 7 different proton signals integrating for overall 7H, which match with the 7 aromatic protons of the proposed structure. The region with chemical shifts between 4.0-1.5 ppm corresponds to the aliphatic protons of the dendritic platform, whose integrations fit well with the aromatic region of the ligand scaffold (based on the multiplet at δ 1.7 ppm).

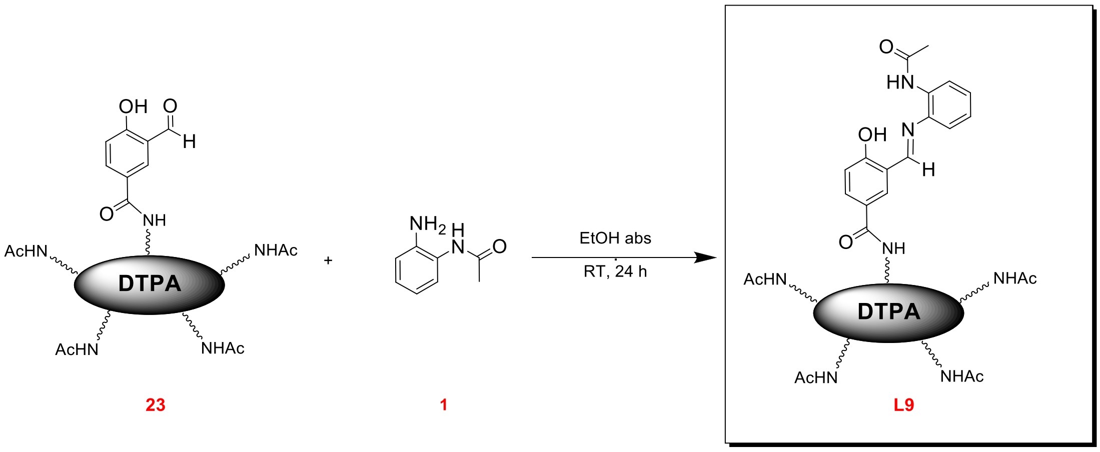

Scheme 5.7. Synthetic strategy towards the final ligand **L9**.

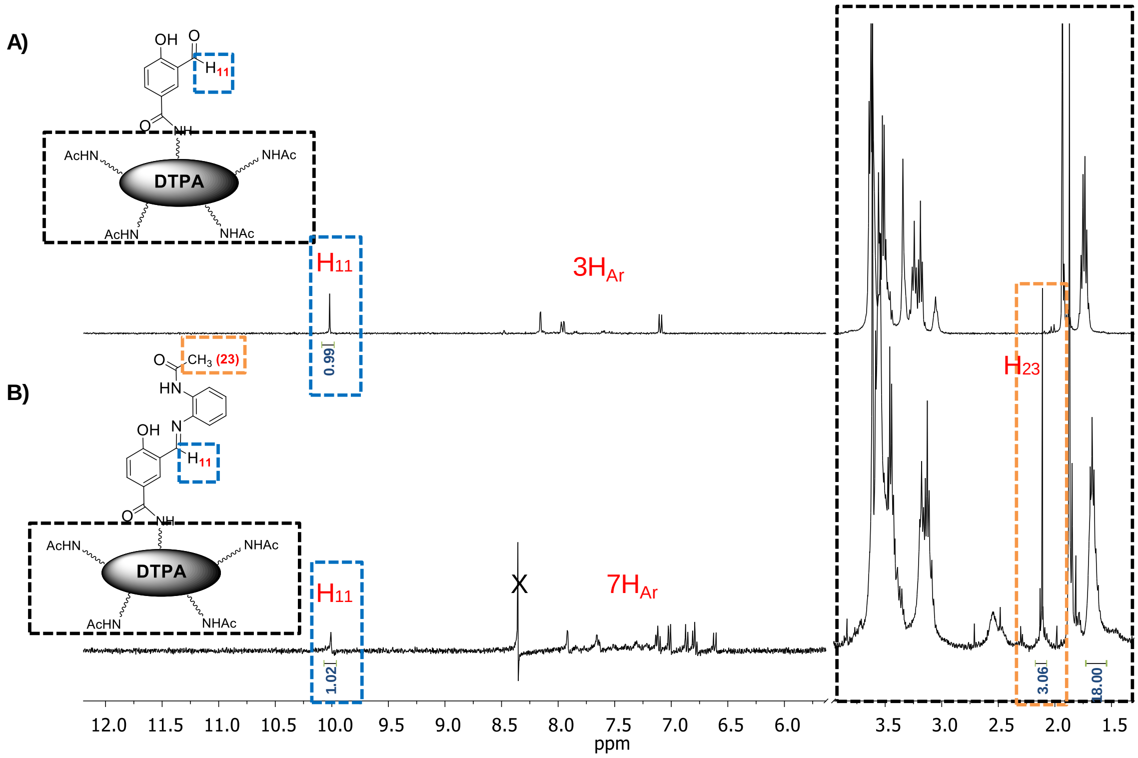

Figure 5.26. (**A**) ^{1}H NMR (300 MHz, D_2O) of compound **23**. (**B**) ^{1}H NMR (400 MHz, D_2O) of ligand **L9**.

Confirmation of the successful synthesis of **L9** was validated by HR ESI-MS. Several charge states can be attributed to the compound of interest. The presence of a major peak at *m/z* = 946.0406 with a +2 charge and a second peak with a *m/z* = 638.3575 with a +3 charge can be assigned to the adducts of the **L9** with Na^+ and K^+ (**Figure 5.27**). Experimental pattern matches well with the theoretical one.

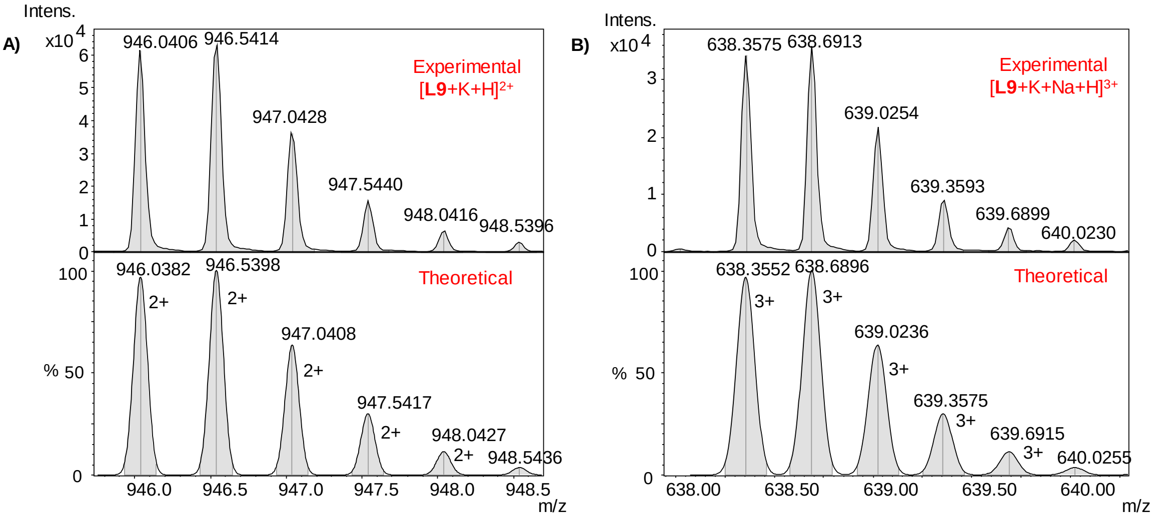

Figure 5.27. Experimental (top) and theoretical (down) HR-MS (ESI$^+$, H_2O-MeOH) of ligand **L9**: (**A**) [**L9**+K+H]$^{2+}$ and (**B**) [**L9**+K+Na+H]$^{3+}$.

It is worth to note that similar to what we found for the cases of both CPPs (*Section 5.1.2.2*), the ^{1}H NMR spectra of this system show different sets of signals depending on some conditions. Indeed, if we have a deeper look at the NMR spectrum of **Figure 5.26B**, there are some small signals that seem to appear between 7.5-7.2 ppm.

These signals do not correspond to any of the reactants used to yield **L9** and they have been observed with different intensities at different concentrations. A clear splitting of some signals (H_{11}, H_{23}) has been observed at higher concentration (**Figure 5.28A**), whose integrals match with one entity of the protons corresponding to the DTPA-based platform scaffold. However, dilution of this sample has not shown reversibility. The ESI-MS spectrum of the same sample (**Figure 5.28B**) mainly shows peaks related to the K, Na and H adducts of **L9** adducted to, and peaks corresponding to the fragmentation of **L9** into compound **23**. No other major peaks are present. Considering that no **23** has been found in the NMR spectrum, the imine fragmentation most-likely comes from the ESI-MS working conditions. Up to now, no plausible explanation has been found for this behavior. Future temperature and diffusion NMR experiments are planned to enlighten the nature of this process.

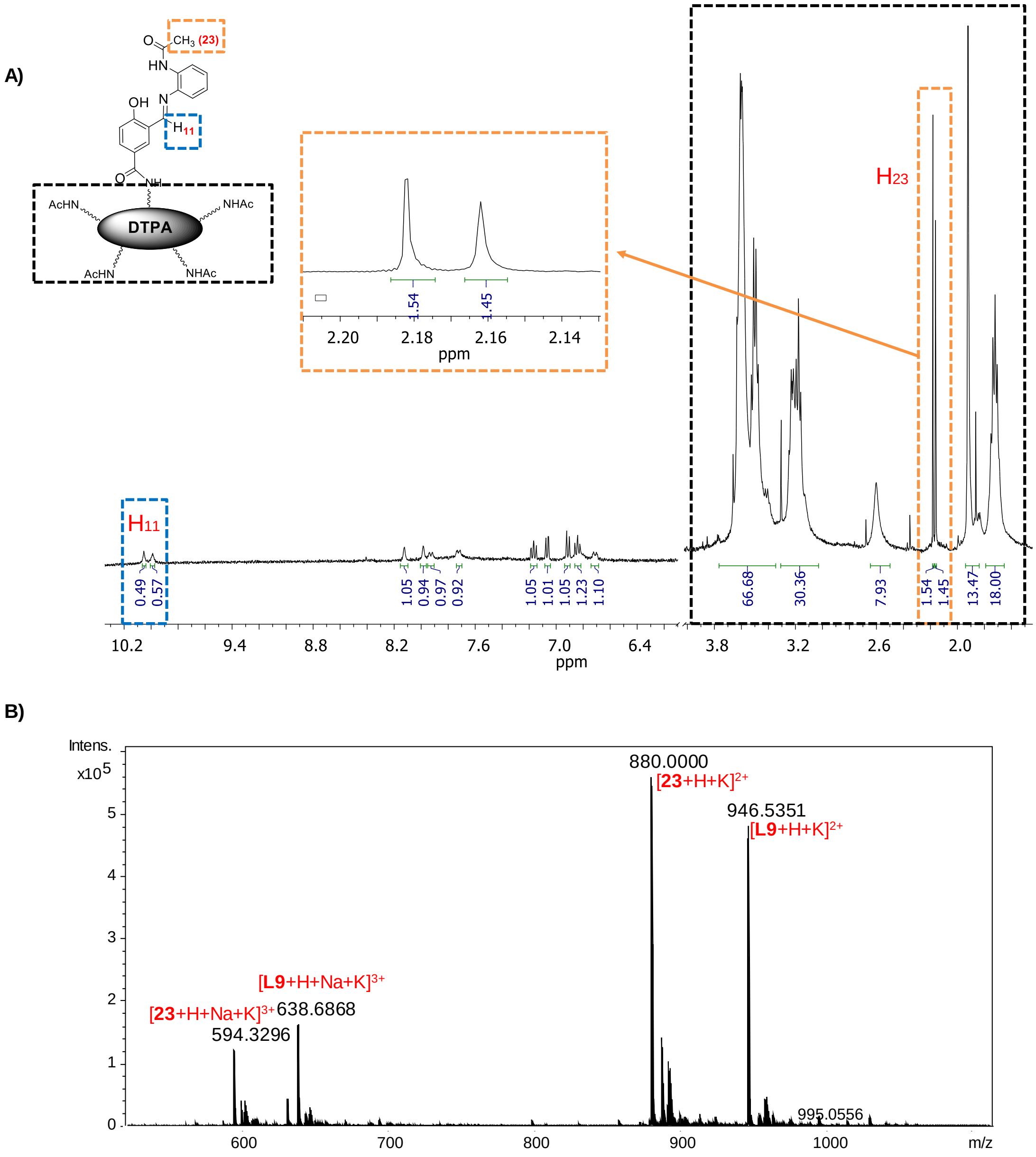

Figure 5.28. (**A**) ^{1}H NMR (400 MHz, D_2O) of **L9** at higher concentration than that of **Figure 5.26B** and (**B**) Full HR ESI-MS (ESI^{+}, MeOH) of the same **L9** sample.

5.2.2.2 Synthesis and characterization of the Cu(II) complex of **L9** (**C9**)

In this particular case, and differently from ligands **L1**-**L7**, the ligand **L9** has two coordination sites for the Cu(II) ion, *i.e.* the DTPA core and the aromatic **L1**-derived scaffold. The idea was to fully occupy both coordination pockets, and therefore, more than 2 equivalents of Cu(OAc)$_2$ were used to ensure full complexation. The complex **C9** was isolated by solvent removal and several ACN washes to get rid of the excess of the Cu(II) salt.

ESR experiments were performed to confirm if the isolated complex has two Cu(II) nuclei (**Figure 5.29**). As observed from the ESR experiments, there are two set of ESR signals (A and B), indicating the presence of two ESR active Cu(II) centers in **C9**. Comparison of the spectral features with those of **C1** and **C8**, *i.e.*, the two respective independent entities, indicates that none of the two Cu(II) centers of **C9** (A and B) fits with the independent complexes.

Simulation of the spectrum (**Figure A65**) and determination of the ESR parameters (**Table 5.6**) clearly highlight that they do not match with those of **C1** and **C8**, indicating a change in the coordination sphere respect to the parent **C1** and **C8** complexes. This change can be due to (i) an increase of the positive charge of the ligand around the copper, (ii) a decrease of the covalency, *i.e.*, spin delocalization from the copper on the ligand donors, or (iii) the presence of one or two axial ligands. In all three cases, $A_{//}$ would be reduced and $g_{//}$ increased, which is what we see in **C9** (A and B) respect to **C1** and **C8** (**Table 5.6**).

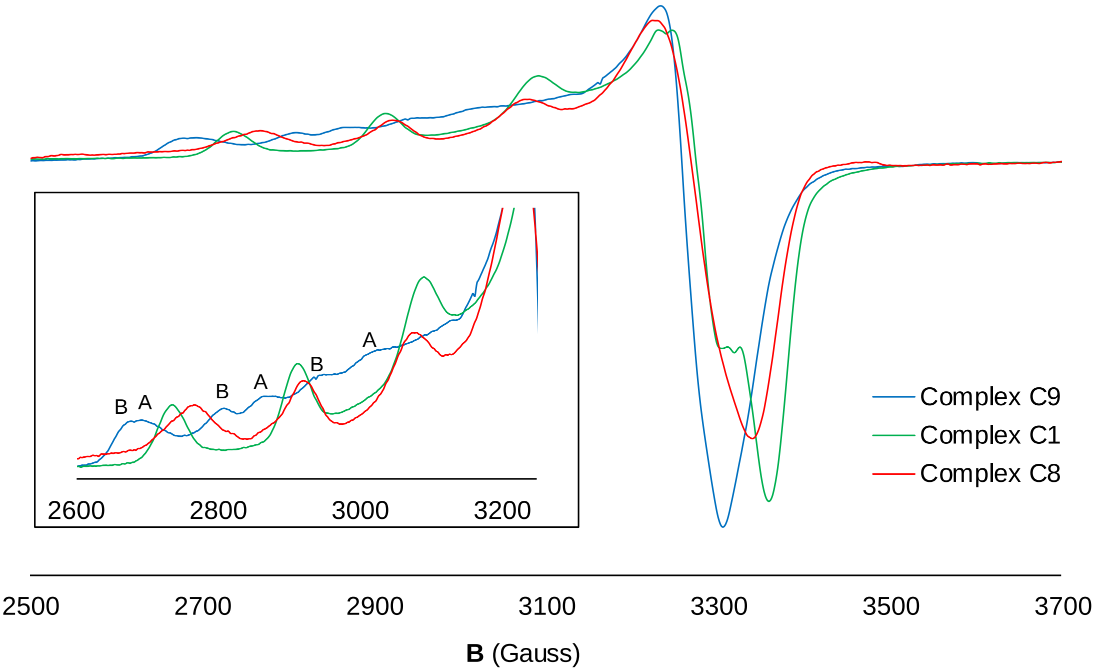

Figure 5.29. X-ESR band of complex **C9** in comparison with **C1** and **C8**. Both **C9** and **C1** have been measured in DMSO, while **C8** in water (pH 7.2, with 10% glycerol).

The Cu(II) center “A” might fall into a N_2O_2 coordination sphere, which coincides with the same donor atoms as for **C1**. Besides, the Cu(II) environment of “A” does not show any significant distortion from planarity according to the $g_{//}/A_{//}$ ratio, as also observed in the parent complex **C1**. The Cu(II) center “B” is more an oxygen-rich species and Cu(II) could be coordinated by one N and several O donor atoms. This site can be ascribed to the DTPA core. ESR data of **C8** (**Figure 5.19** and **Table 5.3**) was collected in water solution, while that of **C9**, in DMSO. Therefore, solvent might be the reason of the different copper coordination sphere in **C9** and **C8**. The “B” site has a slightly distorted structure from planarity that also fits with the distortion observed in the **C8** complex (**Table 5.6**).

Table 5.6. ESR parameters for the complexes **C9** in DMSO extracted from **Figures 5.29** and **A65.** Parameters of **C1** (in DMSO) and **C8** (in water) are placed for the sake of comparison.

Complex		$g_{//}$	$A_{//}$ (10^{-4} cm^{-1})	$g_{\perp}$	$A_{\perp}$ (Gauss)	$g_{//}/A_{//}$ (cm)
C9	A	2.29	170	2.056	<20-30	135
	B	2.34	150	2.052	<20-30	156
C1		2.244	183	2.043	<20-30	122
C8		2.252	155	2.055	<20-30	145

ESR data point to the binding of two Cu(II) ions to **L9**. Calculation of the abundance of each ESR signal (*A* and *B*) accounts for 50% each and this agrees with one molecule of **L9** and two Cu(II) ions bound. However, and strictly, these data could also fit with two independent species at 50% of abundance each and with different coordination environment respect to **C1** and **C8**.

Therefore, HR ESI-MS experiments were then carried out in order to shed light into the putative structure of **C9**. Despite the low ionization capability of the molecule, two peaks were able to be identified corresponding to the ligand and two copper ions, *i.e.* to **C9** (**Figure 5.30**): [**L9**-2H+2Cu]$^{2+}$ ([**C9**]$^{2+}$, *m/z* 987.9684) and [**L9**-3H+2Cu+Na]$^{2+}$ ([**C9**-H+Na]$^{2+}$, *m/z* 998.9641). The loss of two protons from the ligand **L9** can be easily explained by the deprotonation of both the phenol and the amide groups of the aromatic scaffold upon metalation.

MS spectrum shows the presence of another peak containing Cu(II) that can be ascribed to the imine cleavage and the coordination of one Cu(II) ion to the DTPA core site (*m/z* 902.4720, **Figure A66**). This complex will most-likely arise from *in situ* fragmentation in the MS working conditions. However, its presence in the solid state cannot be completely excluded.

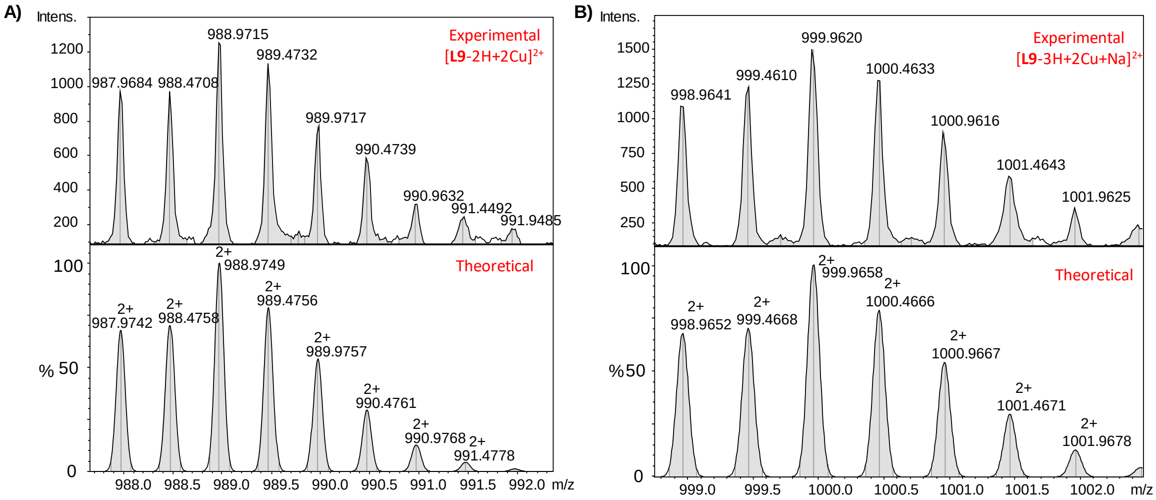

Figure 5.30. Experimental (top) and theoretical (down) HR-MS (ESI$^+$, DMSO-MeOH) spectra of (**A**) [**L9**-2H+2Cu]$^{2+}$ and (**B**) [**L9**-3H+2Cu+Na]$^{2+}$.

Both ESR and MS results are in concordance with the binding of two Cu(II) to **L9**. The proposed structure for **C9** in solution is depicted in **Figure 5.31**. Further studies are currently being performed in order to elucidate the solid structure of **C9**. Clarification of the Cu(II) structure and its purity is important in order to latterly assess its cytotoxicity in cell cultures and stablish future structure-activity relationships.

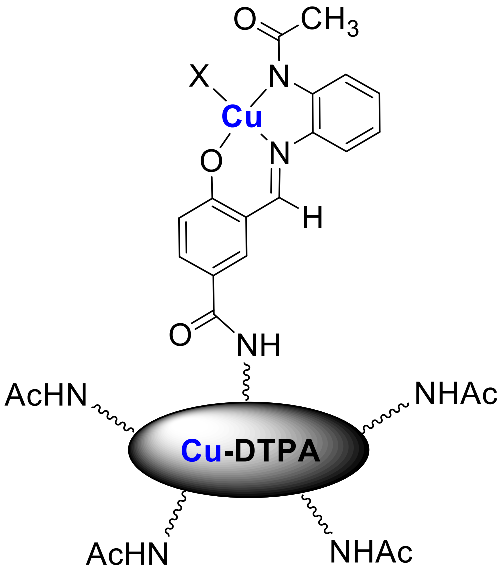

Figure 5.31. Proposed structure of **C9** in solution based on the data gathered from ESR spectroscopy and MS spectrometry. Completion of the coordination sphere of the Cu(II) center of the **L1** scaffold would require a fourth ligand (X) in the same plane and could also account for an axial ligand (in a square-pyramidal geometry). The Cu(II) coordination sphere in the DTPA-based platform will be most-likely formed by two or three *N*-donor atoms from the DTPA core of the platform, and completed by any *O*- (C=O) and/or *N*- (CHN) donor atoms from the adjacent amide groups of the DTPA core or from any solvent molecule.

5.3 Summary and conclusions

This chapter was divided into two parts. The first part was focused in the functionalization of the ligand **L1** with three CPPs ((β-Ala)-TAT$_{49-57}$, R$_9$ and (Gly)$_4$-R$_9$) to specifically improve the uptake inside cells, and their subsequent complexation with Cu(II). Several conclusions can be drawn:

1) We have been able to successfully synthesize the three CPPs by using standard SPPs protocols. The obtained peptides have been characterized by NMR, ESI-MS and their purity assessed by analytical HPLC.

2) The coupling strategy between the **L1** ligand scaffold and the (β-Ala)-TAT$_{49-57}$ peptide has been accomplished. Precursor **14** has been used to form the amide bond between the two moieties. However, trials to obtain the desired final iminic ligand were unsuccessful due to the more favorable formation of the intramolecular iminic bond between the terminal amino group of the Lys side-chain and the -CHO group of the aromatic part of the ligand. This bond was confirmed by ESI-MS. The higher basicity of **1** with respect to the terminal amino group of the Lys side-chains drives the formation of the intramolecular bond in detriment of the desired ligand formation.

3) The R$_9$ and (Gly)$_4$-R$_9$ peptides do not contain any Lys residue, and therefore were used as the alternative to the TAT peptide. Their coupling with precursor **14** has been accomplished in solid-phase. The obtained aldehyde compounds **19** and **21** have been characterized by NMR, ESI-MS and their purity checked by analytical HPLC.

4) Ligands **L6** and **L7** have been successfully synthesized by imine bond formation between **19** or **21**, and the amine precursor **1**. They have been characterized by NMR and MS techniques.

5) **L6** and **L7** experience a concentration-dependent dynamic process in water solution. High concentrations of ligand seem to induce the self-assembly of the molecules due to the stacking of high-positively charged Arg-rich peptidic chains (R$_9$ and (Gly)$_4$-R$_9$).

6) Cu(II) complexation of **L6** and **L7** has been achieved and final **C6** and **C7** isolated and characterized. ESR spectroscopy indicates that both maintain the same Cu(II) coordination environment in solution as that found for the previous complexes **C1-C5**. Nonetheless, no evidence of a dinuclear structure of these complexes has been found in solution since only monomeric peaks have been identified in the HR ESI-

MS spectra of **C6** and **C7**. The high positive charge of the systems may disfavor the dimeric structure formation.

7) **C6** and **C7** show higher cytotoxicity in HeLa cells than **C1**, specially at 24 h with values on the range of the reference inorganic drug cisplatin. Besides, **C7** seems to be slightly more toxic than **C6**. The presence of the linker could play a role in this. Short treatment times emphasize the role of the CPP. At 4 h of treatment, **C6** and **C7** are able to produce the death of more than 50% of the cell population, while **C1** does not exhibit any kind of cytotoxicity. This highlights the higher efficiency provided by the presence of the CPPs and makes both complexes promising candidates for future *in vivo* tests.

8) The higher cytotoxicity of **C6** and **C7** can be attributed to their major cellular internalization. **C6** and **C7** enter the cell membrane two-fold times better than **C1**. Comparison with **C5** reveals that the presence of a single Arg (**C5**) does not enhance the cellular uptake.

The second part of this chapter was devoted to the functionalization of a DTPA-based dendritic platform with the ligand scaffold **L1**, and the synthesis of the corresponding Cu(II) complex.

1) DTPA-5Ac has been used to study the Cu(II) coordination properties of the DTPA core by potentiometry, VIS and ESR spectroscopies and MS. This monomodal DTPA-based platform has a core that is able to bind one Cu(II) (with a $K_{COND} = 3.2 \cdot 10^2\ mM^{-1}$) in a distorted-square planar or square pyramidal derived N_3O geometry (complex **C8**).

2) **C8** is toxic for MCF7 cells, while it shows low toxicity for the normal tested fibroblasts cell line at the assayed concentrations.

3) Functionalization of the DTPA-based dendritic platform with the ligand scaffold of **L1** has been attempted by using the simplest bimodal dendritic platform (DTPA-4Ac-NH_2). The coupling strategy has been successfully accomplished by reacting DTPA-4Ac-NH_2 and precursor **14** using HBTU as coupling agent.

4) Synthesis of the final ligand **L9** has been achieved *via* condensation of the amine precursor **1** and the -CHO of **23**. Characterization of the ligand has been performed *via* NMR and ESI-MS.

5) NMR experiments shows that **L9** experiences some conformational equilibrium in solution. No plausible explanation has been found out yet. Further temperature and diffusion experiments are required to enlighten the nature of this process.

6) The ligand L9 binds two equivalents of Cu(II): one at the DTPA core and the other at the N, N, O pocket of the aromatic **L1** scaffold.

7) ESR shows two active Cu(II) centers in the final complex **C9** with 50% abundance each. None of the Cu(II) nuclei observed in the ESR experiments of **C9** match with the parameters found for the separated analogs **C1** and **C8**, even though they have similarities in coordination environment and geometry.

8) HR ESI-MS experiments have shown the binding of two Cu(II) to the ligand **L9**. Further studies are ongoing to unravel the structural features of **C9** in solid phase.

CHAPTER 6

Final Remarks and Future Perspectives

This chapter gathers the salient conclusions from the previous chapters and shows the potential future prospects of the work.

CHAPTER 6

Final Remarks and Future Perspectives

This thesis work reports on the synthesis, characterization and *in vitro* evaluation of a new family of functionalized Cu(II) complexes bearing an imine-based *N,O*-donor heteroaromatic ligand, capable to trigger a facile Cu(II)/Cu(I) redox interconversion (which could exert anticancer activity through a ROS-mediated mechanism). Three different functionalization strategies have been approached to improve the activity of these complexes: (i) -Cl and -Br groups (*Chapter 3*), (ii) -SO_3^- and Arg groups (*Chapter 4*) and, (iii) CCPs (*Chapter 5*). Additionally, pharmacokinetics and protein interactions have been studied with the non-functionalized parent Cu(II) complex. Finally, a DTPA-based bimodal dendritic platform has been explored as a potential drug carrier. A first approach has been attempted to conjugate it to **L1** and to complex the final system with Cu(II). From the obtained results (*Chapters 3-5*), several conclusions can be extracted:

1) A novel salphen-based *N,O*-donor planar heteroaromatic ligand (**L1**) for Cu(II) and six functionalized analogs (-Cl, -Br, -SO_3^-, -Arg, -R_9 peptide, and -$(Gly)_4$-R_9) have been successfully synthesized and characterized. The seven new ligands (**L1**-**L7**) are shown in **Figure 6.1**.

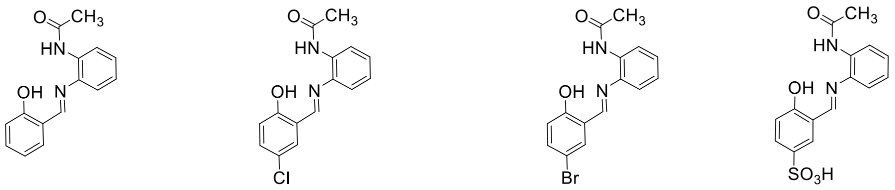

L1 L2 L3 L4

Figure 6.1A. Structure of the ligands **L1-L4.**

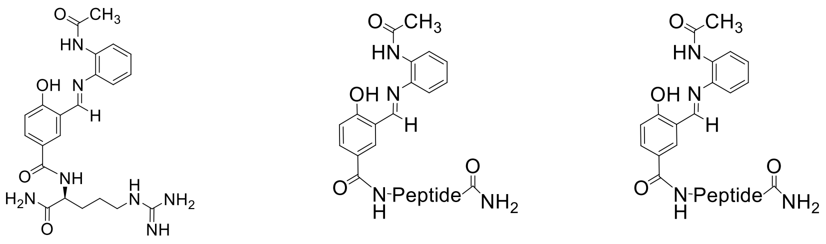

L5

L6: *Peptide= R_9*

L7: *Peptide= $(Gly)_4$-R_9*

Figure 6.1B. Structure of the ligands **L5-L7.**

2) Seven Cu(II) complexes (**C1-C7**, **Figure 6.2**) containing the previous synthesized ligands (**L1-L7**) have been obtained and characterized.

   a. ESR (in DMSO) reveals the presence of a unique Cu(II) species in solution in all the cases. Complexes **C1-C7** are characterized by having a square-planar or square-pyramidal derived geometry, where the ligand chelates in a tridentate fashion (N, N, O). The coordination and geometry around the Cu(II) ion in all seven complexes is exactly the same in solution (N_2O_2), as demonstrated by ESR measurements.
   b. For complexes **C1-C3**, elemental analyses match with either a monomeric or dimeric tetracoordinated structure with no additional counterions or axial ligands, due to the fact that both would share the same empirical formula. However, MS data for **C1-C5** (in MeOH, with 10% DMSO for **C1-C3**) clearly show the presence of dimeric species in solution, pointing to the presence of dimeric structures in solid state.
   c. For complexes **C6-C7**, no evidence of the dimeric structure could be found in solution by MS spectrometry. Only peaks related to mononuclear species could be observed.
   d. Unfortunately, no suitable crystal for X-Ray analyses have been obtained to reinforce what previous data indicate.
   e. Complexes **C4-C7** show an outstanding increase in the solubility in the biological medium respect to **C1-C3**.

3) The Cu(II)/Cu(I) redox behavior of complexes **C1-C5** has been investigated. They show an appropriate thermodynamic potential to undergo a fast Cu(II)/Cu(I) redox cycle inside the biological redox window, *ergo*, to act as potential ROS generators. Functionalization approaches in **C2-C5** have not significantly altered the Cu(II)/Cu(I) redox potential shown by the non-functionalized complex **C1**.

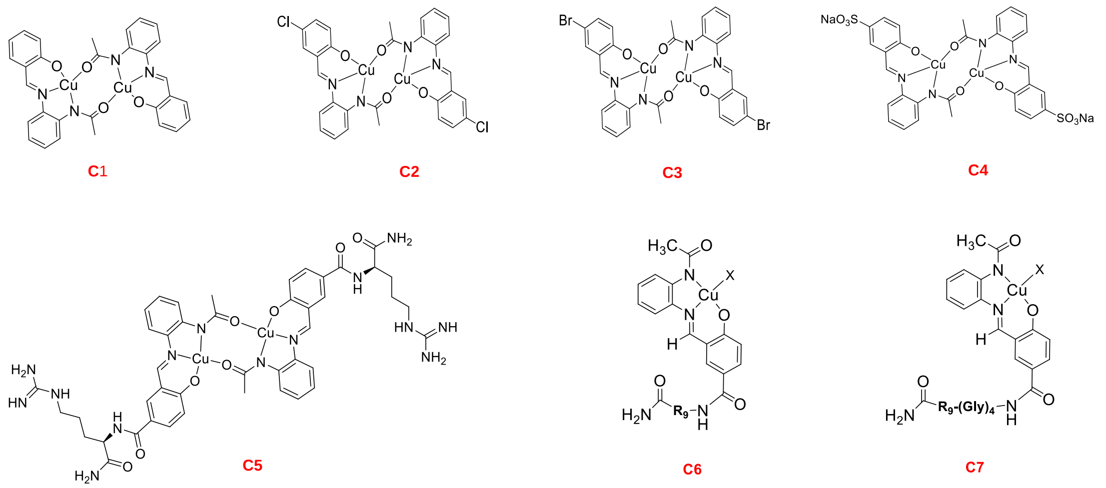

Figure 6.2. Proposed structure for the synthesized complexes **C1**-**C7**.

4) The *in vitro* antiproliferative activity of **C1-C7** in several cell lines at 24 h and 72 h of treatment, and their intracellular copper uptake have been evaluated. Results are summarized in **Table 6.1**.

Table 6.1. IC_{50} values for 24 and 72 h of treatment for **C1**, **C4**-**C7** and their uptake in HeLa cell lines. Values are normalized based on Cu concentration.

Compound	IC_{50} (24 h)	IC_{50} (72 h)	Intracellular Cu (ng/10^6 cells)
C1	67±2	54±1	131±21
C4	109±1	78±3	79±17
C5	108±4	55±2	97±22
C6	51±6	52±4	272±15
C7	50±5	41±4	315±6

a. The parent complex **C1** has been assayed in two cancer cell lines (HeLa and MCF7) and one normal cell line (fibroblasts), showing a promising higher cytotoxicity for cancer cells than for normal ones.

b. Complexes **C2** and **C3** were also tested but unfortunately had to be discarded due to their poor solubility in biological medium.

c. **C1**, **C4**-**C7** have been comparatively evaluated in HeLa cell lines, where they exhibit a remarkable cytotoxicity:

   - Functionalization with sulfonate and arginine groups (**C4** and **C5**) has not represented any improvement in the final cytotoxicity respect to **C1**.
   - Complexes functionalized with the CPPs (**C6** and **C7**) exhibit higher toxicity than the parent complex **C1**, specially at short treatment times

(**C7** > **C6** >>> **C1**). They show enhanced efficacy at short treatment times (4 h), standing out as interesting candidates for future *in vivo* tests.

  d. Copper uptake studies in HeLa cell lines have allowed to infer a relationship between the intracellular amount of copper and the cytotoxicity of the compound. Complexes **C6** and **C7** have shown the highest copper internalization values (about two-fold **C1**, *i.e.* **C7** > **C6** >>> **C1**), while **C4** and **C5** do not show any enhanced uptake respect to **C1**. This is in agreement with the obtained IC_{50} values, and highlights the specificity of CPPs sequences in the recognition of cell membrane receptors, since a sole Arginine residue is not enough to improve membrane penetrability.
  e. The presence of the $(Gly)_4$ linker in **C7** seems to slightly improve the copper uptake respect to **C6**. However, further studies should be carried out to attribute a key role to it on cell membrane recognition.

5) The mechanism of action of **C1** has been evaluated and extrapolated to the rest of complexes -which share the same metallic core-, after observing that the functionalization approaches of **L1** have not extensively affected the redox behavior of the corresponding complexes.

  a. **C1** has been proven to generate high ROS levels inside HeLa cancer cells.
  b. **C1** shows an enhanced DNA cleavage activity in the presence of reducing agents.
  c. **C1** interactions with DNA have been witnessed in a groove-binding or electrostatic mode, but with a moderate binding constant. Therefore, it has been proposed that **C1** most-likely triggers a ROS-mediated cell-death mechanism.
  d. *In vitro* apoptotic studies have revealed that **C1** partially induces a desired early apoptotic cell-death pathway.

6) Some pharmacokinetic features of **C1**, as the main scaffold from which the rest of complexes have been obtained, have also been explored to provide additional information on the pharmacological value of the complex.

  a. **C1** is stable in biological medium for at least 24 h.
  b. **C1** forms covalent adducts with the studied proteins (HSA, Cyt and Myo). In an attempt to model the effect of these interactions into the final biological activity, an experimental approach has been set up. Interestingly, not only

these adducts do not represent a hindrance in the activity of the complex, but they also seem to improve **C1** activity in HeLa cells with HSA or Cyt.

7) A multimodal DTPA-based dendritic versatile platform (**Figure 6.3**) has been explored as potential drug delivery system (DDS).

a. In this regard, the simplest monomodal DTPA-5Ac has been firstly evaluated to get to know the coordination capabilities of the DTPA-based core and its toxicity. The core of the platform has proven to coordinate one Cu(II) ion at physiological pH with an apparent K_b of $3.2 \cdot 10^2$ mM^{-1}. The [Cu(DTPA-5Ac)] complex exhibits low cytotoxicity in normal fibroblasts (NIH 3T3) cell line, placing this platform as a candidate to be used as a drug carrier.

b. As a proof-of-concept to assess the reliability of this platform for future tailor-made anticancer compounds, the bimodal DTPA-4Ac-**NH_2** was used. Conjugation of the **L1** scaffold to the bimodal DTPA-4Ac-**NH_2** has been successfully achieved (**L9**) and the final system characterized.

c. Cu(II) complexation of **L9** has been successfully attempted (**C9**). Two Cu(II) centers have been observed in **C9**: one Cu(II) would coordinate the **L1**-like scaffold, while the other metal ion would be bound in the DTPA-based core pocket, according to ESR parameters.

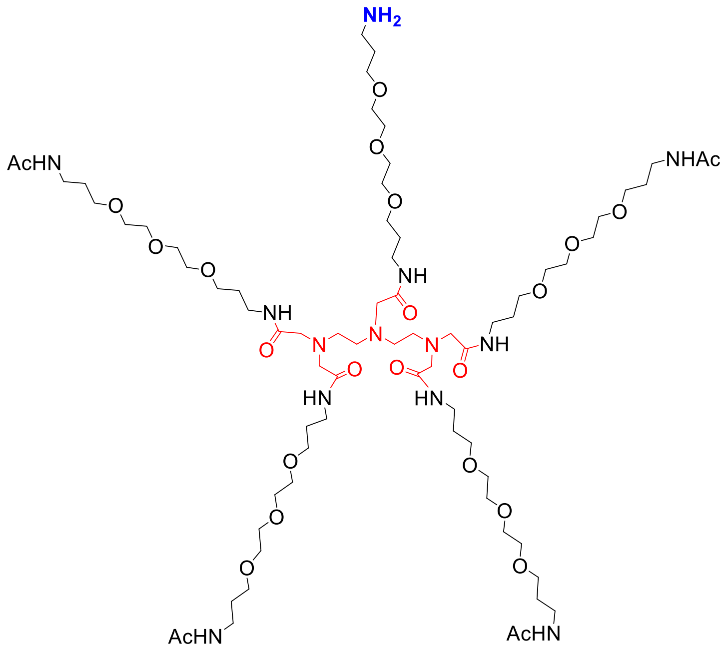

Figure 6.3. Structure of the dendritic DTPA-based platform DTPA-4Ac-**NH_2**. In red, the DTPA core.

In conclusion, the results highlight that the metallic core of **C1** represents an interesting scaffold to explore in future chemotherapeutics due to the high ROS production, which has provided more selectivity toward cancer cells, and the partial induction of apoptosis. It is noteworthy to mention the strategy to conjugate it to the CPPs. **C6** and **C7** have exhibited higher toxicity, uptake and efficiency at short treatment times and arise as promising chemotherapeutic candidates for future pre-clinical tests. Finally, the DTPA-based dendritic platform has shown interesting features to be used as a future drug carrier and the parent complex **C1** has been able to be attached to this platform.

At this stage, this thesis work is a first step that opens the gate to explore different strategies in cancer research. First of all, it would be interesting to further develop and optimize the experimental model that we have set up in *Chapter 3* to *in vitro* assess the effect of protein-binding into the biological activity of a potential drug. Particularly, HSA-**C1** deserves special attention to be further explored in order to take advantage of this protein as a future drug carrier. Besides, cellular biodistribution is worthy to be evaluated to get information regarding the mechanism of these compounds. Whereas the cell-death pathway of Pt(II) compounds has been widely studied, Cu(II) compounds have still many mechanistic features to be unraveled. Taking advantage of the CPPs, immunoassays are planned to provide further insights into the cellular localization of these compounds.

Furthermore, the successful coupling strategy followed in this work with the bimodal DTPA-based dendritic platform encourages us to keep working on this system. Full characterization and biological studies of the Cu(II) complex **C9** must be carried out to assess the effect of this platform into the final cytotoxicity. Moreover, several multimodalities can be attained due to the versatility of the system, leading to a myriad of possibilities to design tailor-made anticancer targeted therapies in the future.

CHAPTER 7

Experimental Section

The details about the methods, experimental procedures, and instruments used in this work are summarized in this chapter.

CHAPTER 7

EXPERIMENTAL SECTION

7.1 Chemicals

Chemicals were purchased from commercial suppliers and used as received. Copper(II) chloride, copper(II) acetate, 2',7'-dichlorofluorescin diacetate (DCFDA), Human Serum Albumin (HSA, A8763), calf-thymus DNA sodium salt (ct-DNA), *N,N*-diisopropylethylamine (DIEA), 4-(2-hydroxyethyl)-1-piperazineetahensulfonic acid (HEPES), 2-amino-2-(hydroxymethyl)propane-1,3-diol (TRIS), triisopropylsilane (TIS), *N*-methyl-2-pyrrolidone (NMP) and piperidine were obtained from Sigma-Aldrich. Solvents such as acetonitrile (ACN), methanol (MeOH), ethanol (EtOH), chloroform ($CHCl_3$), dimethyl sulfoxide (DMSO), ethyl acetate (EtOAc), *N,N*-dimethylformamide (DMF), and dichloromethane (DCM) were used at synthesis grade purity and directly from commercial sources (Scharlab, VWR and Thermofischer). Trifluoroacetic acid (TFA) was purchased from Acros Organics.

The *N*-fluorenylmethoxycarbonyl (Fmoc)-protected amino acids (Fmoc-Arg(Pbf)-OH, Fmoc-Gln(Trt)-Oh, Fmoc-Lys(Boc)-OH, Fmoc-*β*-Ala-OH and Fmoc-Gly-OH), 2-(1*H*-Benzotriazole-1-yl)-1,1,3,3-tetramethyluronium hexafluorophosphate (HBTU) and the Rink Amide MBHA (100-200 mesh) resin were obtained from Novabiochem.

The monomodal DTPA-5Ac and the bimodal DTPA-4Ac-NH_2 were synthesized and characterized by Dr. Daniel Pulido (Dr. Míriam Royo research group, CSIC, Barcelona, Spain) as reported.[289] Both dendritic DTPA-based platforms were used as received.

7.2 Physical Measurements. Instruments and experimental procedures

a) NMR Spectrometry

NMR experiments were recorded on BRUKER DPX-250, 300, 360, 400, and 500 MHz instruments at the *Servei de Ressonància Magnètica Nuclear* (UAB) and *Spectropole* facility (AMU). Deuterated solvents were directly purchased from commercial suppliers. All spectra have been registered at 298 K otherwise noticed. The abbreviations used to describe signal multiplicities are: s (singlet), d (doublet), dd (double doublet), t (triplet), q (quadruplet), bs (broad signal) and m (multiplet). All ^{13}C NMR acquired spectra are proton decoupled.

b) ICP-OES/ICP-MS

Inductively coupled plasma mass spectrometry (ICP-MS) was performed on an Agilent apparatus, model 7500ce. Inductively coupled plasma optical emission spectrometry (ICP-OES) was carried out in a Perkin-Elmer, model Optima 4300DV.

*Stock solutions of complexes **C1**-**C7** for biological assays*. Stock solutions of the assayed complexes **C1**-**C7** were prepared by weighing the appropriate amount of complex and diluting them in the corresponding solvent (DMSO or H_2O). Quantification of the copper concentration was carried out at the *Servei d'Anàlisi Química* (UAB) by ICP-OES. Measurements were performed at least per duplicate.

c) ESI-MS measurements

Routine ESI-MS measurements were recorded at the *Spectropole* facility (AMU) on a SYNAPT G2 HDMS (Waters) instrument with a ionization source at atmospheric pressure (API) pneumatically assisted and with a time-of-flight analyzer (TOF). Ionization conditions: electrospray voltage 2.8 kV, capillary voltage 20 V, dry gas at 100 L/h.

HR ESI-MS measurements were recorded after diluting the corresponding solid complexes in a MicroTOF-Q (Brucker Daltonics GmbH, Bremen, Germany) instrument equipped with an electrospray ionization source (ESI) in positive mode at the *Servei d'Anàlisi Química* (UAB). The nebulizer pressure was 1.5 Bar, the desolvation temperature was 180 °C, dry gas at 6 L min^{-1}, the capillary counter-electrode voltage was 5 kV and the quadrupole ion energy, 5.0 eV.

Protein-complexes interactions by ESI-MS spectrometry were carried out at the *Servei d'Anàlisi Química* (UAB) in positive mode and following a reported procedure in our group.[39] 20 mL of each sample was injected at 40 mL·min^{-1}; the capillary-counterelectrode voltage was 4.5 kV; the desolvation temperature was 100 ºC; dry gas at 6 L·min^{-1}. Spectra were collected throughout a *m/z* range from 800 to 2500. The liquid carrier was an ammonium acetate solution pH 7 in water/acetonitrile (85:15). Stock solutions of the protein were freshly prepared for each experiment. All samples were prepared by incubating the corresponding complex with the protein at a specific ratio for 24 h at 37 ºC in sterilized 25 mM NH_4HCO_3, containing a maximum of 5% of pure DMSO to solubilize complex **C1**. All samples were prepared and kept under sterile conditions in order to directly use the protein-**C1** incubations for *in vitro* cytotoxic assays. **C1** stock solution used for these experiments was quantified by ICP-OES.

d) ESR experiments

Electron Spin Resonance (ESR) (also known as Electron Paramagnetic Resonance (EPR)) measurements were carried out on a BRUKER ELEXSYS 500 X-band CW-ESR spectrometer, with an ELEXSYS Bruker instrument equipped with a BVT 3000 digital temperature controller. The spectra were recorded at 120 K in frozen DMSO solutions otherwise noticed. Simulations with automatic parameter fitting were performed for axial symmetry using a published software.[307] The contribution of naturally abundant ^{63}Cu and ^{65}Cu was considered, but the values given refer to ^{63}Cu. All principal axes were supposed parallel. Typical parameters were: microwave power 10-20 mW, modulation frequency 100 kHz, modulation gain 3 G.

***C1** stability in DMEM.* **C1** was incubated in DMEM biological medium for 24 h at 37 ºC at a concentration of 2 mM. Dilution of this sample to 1.5 mM in DMEM was done prior to ESR measurements (with a 15% of glycerol in the final sample). A control of **C1** (1.5 Mm) in DMEM (15% glycerol) at t = 0 was also considered.

e) Cyclic voltammetry

Cyclic voltammograms were taken on a BioLogic SP-150 potentiostat and EC-Lab 5,40 software. DMSO was used as solvent with 0.1 M of $[NBu_4][PF_6]$ (TBAP) as supporting electrolyte. Measurements were carried out with a three-electrode configuration cell: glassy carbon electrode as working electrode, Ag wire in a 0.1 M TBAP solution in DMSO or DMF as reference and Pt as the counter electrode. Ferrocene

(Fc^+/Fc) system was used as internal standard. The scan rate (v) varied between 500 and 25 mV·s^{-1}. All the experiments were recorded under argon atmosphere.

f) Potentiometric studies

The ionic strength of the experimental solutions was kept at 0.1 M with $NaNO_3$. The temperature was controlled at (25.0±0.1) °C and atmospheric CO_2 was excluded from the titration cell during experiments by passing purified argon across the top of the experimental solution. Additionally, the solution was bubbled with nitrogen before starting the titration. Titrant solutions were added through capillary tips at the surface of the experimental solution by means of a Metrohm Dosino 800 automatic burette and the titration experiment was automatically controlled by a Tritino Ti-Touch 916 unit after selection of suitable parameters. The $[H^+]$ of the solutions was determined by measurement of the electromotive force of the cell, $E = E^{o\prime} + Q \log[H^+] + E_j$. The term pH is defined as $-\log [H^+]$. $E^{o\prime}$ and Q were determined by titrating a solution of known hydrogen-ion concentration at the same ionic strength in the acid pH region. The liquid-junction potential, E_j, was found to be negligible under the experimental conditions used. The value of $K_w = [H^+][OH^-]$ was $10^{-13.77}$ under our experimental conditions. A 0.100 M standard solution of HNO_3 (1000 mL) was prepared from a commercial Merck ampoule and purified water from a Millipore Milli-Q demineralization system. Carbonate-free solutions of the titrant NaOH were obtained at 0.099 M by using freshly prepared solution from a Merck ampoule in water (1000 mL; freshly boiled for about 2 h and allowed to cool under nitrogen flux). This solution was standardized with the standard solution of HNO_3. Measurements during titrations were carried out with DTPA (1 mM) in a total volume of 20 mL, in the absence and presence of Cu(II) (0.5, 1 and up to 2 eq relative to the ligand). The titrations of the free ligand were run between pH 3 and 11, and in the presence of metal between pH 3 to the point of visible precipitation. The calculation of overall equilibrium constants β_l^H and β_{MmHhLl} (being $\beta_{MmHhLl} = [M_mH_hL_l]/[M]^m[H]^h[L]^l$) was done by fitting the potentiometric data from protonation or complexation titrations with the HYPERQUAD program.[308] The Cu(II) stock solution of $Cu(NO_3)_2$ was prepared from analytical grade metal salt and standardized by titration with K_2H_2EDTA following standard methods[309] or by ICP.

g) Elemental analysis

C, H, O analyses were performed at the *Servei d'Anàlisi Química* (UAB) on a Flash EA 2000 CHNS Thermo Fisher Scientific equipment, with a TCD and a MAS 200 R autosampler for solid samples.

h) IR

ATR-FTIR spectra were recorded on a Perkin Elmer spectrometer, equipped with a universal attenuated total reflectance (ATR) accessory, with diamond window in the range 4000–650 cm^{-1}.

i) UV-Vis studies

All the spectra were recorded at room temperature either on an Agilent HP 8453, Varian Cary 50 Bio, a Varian Cary 60 Bio or a Perkin Elmer Lambda 650 spectrophotometer, using 1 cm quart-cuvettes.

Non-covalent DNA-complex interactions were studied by UV-Vis measurements. Solutions of complexes **C1**-**C3** were prepared in 50 mM NaCl/5 mM Tris-HCl buffer (pH 7.2), containing a maximum of 5% DMSO to solubilize them. *Ct*-DNA stock solutions were prepared from its corresponding sodium salt (Sigma Aldrich) and the concentration determined from its absorbance at 260 nm (ε = 6600 cm^{-1}). Blank and dilution effects were corrected.

Ascorbic acid consumption experiments were monitored by UV-VIS at the maximum absorption band of the ascorbic acid (100 µM) at 265 nm for about 45 min. $CuCl_2$ and the assayed complexes **C1-C5** were added at a final concentration of 2 µM in 50 mM NaCl/5 mM Tris-HCl buffer (pH 7.2).

Binding constant determination was achieved by UV-VIS titration. DTPA-5Ac was at 1.5 mM in 50 mM HEPES buffer (pH 7.2) and regular additions of Cu(II) (from a Cu(II) nitrate stock solution standardized by ICP) were added. Absorbance at 681 nm was measured after 10 min stabilization time upon each addition, until 1 eq Cu(II). Higher Cu(II) additions were let stabilized for 30 min and the formed Cu(II) hydroxide precipitate settled down before the measurement.

j) Circular Dichroism

CD experiments were acquired on a JASCO 715 spectropolarimeter. Measurements were carried out at a constant temperature of 20 °C. CD spectra were measured in 50 mM NaCl/5 mM Tris-HCl buffer (pH 7.2). Calf thymus DNA (*ct*-DNA) concentration was 50 µM. Different samples with increasing amount of the complexes to study (0, 50, 100 µM) were incubated at 37 °C for 24 h, containing a maximum of 5% DMSO to solubilize them. *Ct*-DNA stock solutions were prepared from its corresponding sodium salt (Sigma Aldrich) and the concentration determined from its absorbance at 260 nm (ε = 6600 cm^{-1}).

k) DNA cleaving experiments

Gel electrophoresis experiments were performed on agarose gel (1% in TAE buffer, Tris-Acetate EDTA), using a BIORAD horizontal tank connected to variable potential power supply. Samples were stained with EB and revealed with a Super GelDoc PlusImager. Complexes **C1**-**C3** were incubated with the Plasmid DNA (200 ng of BlueScript plasmid per well) in 20 mM NaCl/40 mM Tris-HCl buffer (pH 7.20) medium for 24 h at 37˚C (<10% DMSO in the final mixture to solubilize the complexes). Samples containing the reducing agent ascorbic acid were incubated for 1.5 extra hours in the presence of ascorbic acid (100 µM).

l) Cell-viability assays

The IC_{50} values were evaluated using PrestoBlue Cell Reagent (Life Technologies) assay. Working concentrations of complexes **C1**-**C7** (final amount <0.1% DMSO in biological experiments) were prepared in DMEM medium from the ICP standardized stock solutions of **C1**-**C7**. Human cancer cells (HeLa, MCF7 and CCD112CoN) were obtained from American Type Culture Collection (ATCC, Manassas, VA, USA). The cells were routinely cultured with DMEM (Dulbbeco's modified Eagle's medium, Invitrogen) containing 10% heat-inactivated fetal bovine serum (FBS) at 37 ˚C in a humidified CO_2 atmosphere. HeLa cells were plated at a density of $3{\cdot}10^3$ cells/well in 100 µL of culture medium and allowed to grow overnight. After the required incubation time with different concentrations (0, 10, 25, 50, 100, or 200 µM) of each complex, 10 µL of PrestoBlue® were added following the standard protocol. The fluorescence of each well was measured at 572 nm with a Microplate Reader Victor3 (Perkin Elmer). The relative cell viability (%) for each sample related to the control well was calculated. Each complex was tested per triplicate and averaged from three independent set of experiments. Blank and complex controls were also considered.

For experiments of **C1**, **C6** and **C7** at 30 min and 4 h of treatment, cells were plated and treated following the same protocol. After the treatment time, the supernatant was removed, cells were washed and new DMEM was added. Cells were allowed to grow for 72 h and the cell-viability measured with PrestoBlue®, as beforehand detailed.

m) Intracellular ROS production assays

HeLa cells were plated, grown and allowed to adhere overnight in a 96-wells plate ($20 \cdot 10^3$ cells/well). The 2',7'-dichlorofluorescin diacetate reagent (DCFCDA, 25 µM in DMSO) was then added and the cells incubated at 37°C in the dark for 30 minutes. The DCFDA solution was removed and cells were treated with the compounds at the corresponding IC_{50} values (at 72 h) and incubated for 4 h. The experiments were run in triplicate. H_2O_2 was used as a positive control at 100 µM. The fluorescence of each well was measured at 535 nm with a Microplate Reader Victor3 (Perkin Elmer) after excitation at 485 nm.

n) Cellular uptake studies (Cu uptake)

HeLa cells were plated, grown and allowed to adhere overnight in a 6-wells plate ($200 \cdot 10^3$ cells/well). Cells were treated for 4 h with the different copper complexes at the desired concentration. Medium was removed and cells were washed with PBS and harvested with trypsin for 10 min. The samples were centrifuged and the cellular pellets collected and digested with concentrated HNO_3. Quantification of the intracellular copper was performed by using inductively coupled plasma mass spectrometer (ICP-MS). Measurements were performed at least per duplicate.

o) *In vitro* apoptosis assays

Induction of apoptosis in vitro by **C1** was determined by a flow cytometric assay with annexin V–fluorescein isothiocyanate (FITC) by using an annexin V–FITC apoptosis detection kit (Roche). Exponentially growing HeLa cells in 6-well plates ($300 \cdot 10^3$ cells/well) were exposed to concentrations equal to the IC_{50} for 24 h. After the cells had been stained with the annexin V–FITC and propidium iodide, the percentage of apoptotic cells was analyzed by flow cytometry (FACS Calibur).

p) Peptide synthesis

Peptides ($TAT_{49\text{-}47}$ peptide, R_9 and $(Gly)_4\text{-}R_9$) were synthesized using a microwave assisted Biotage® Initiator+ Alstra synthesizer, following standard Fmoc solid-phase peptide synthesis (SPPS) protocols.[245] They were synthesized on a Rink Amide MBHA resin (100-200 mesh) in a 0.25 mmol scale (0.59 mmol/g). The amino acids (4 eq) were assembled using HBTU (3.9 eq) as coupling agent, DIEA (8 eq, in NMP) as a base and DMF as a solvent. Fmoc deprotection was carried out at room temperature with 20%

piperidine in DMF for about 20 min. Couplings were carried out at 75 ºC for Fmoc-Gln(Trt)-OH (5 min), Fmoc-Lys(Boc)-OH (5 min), Fmoc-Gly-OH (5 min) and Fmoc-*β*-Ala-OH (2 x 5 min). For Fmoc-Arg(Pbf)-OH residues, double couplings were carried out at 50 C (2 x 6.5 min). Cleavage and simultaneous removal of the protecting groups were done manually with a TFA/TIS/H2O (95/2.5/2.5, (v/v/v)) mixture for 2 h at room temperature. The resin was filtered out and washed with TFA. Filtrate and TFA washes were combined and TFA removed under a nitrogen stream. The final peptides were precipitated in cold Et_2O, recovered by centrifugation, dissolved in water and lyophilized.

q) Reversed-phase HPLC

Analytical HPLC analysis were carried out on an Agilent Technologies 1200 Series with a UV-VIS detector. A C12 Jupiter Proteo LC (90Å, 4 µm, 250 x 4.6 mm) was used as a column. Preparative HPLC was performed on an Agilent Technologies 1200 Infinity with a UV-VIS detector. A C12 Jupiter Proteo Axia (90Å, 4 µm, 250 x 21.2 mm) was used as a column.

A two-solvent gradient was used (*Solvent A*: H_2O/TFA (99.9/0.1%); and *Solvent B* (ACN/H_2O/TFA (90/9.9/0.1%)). Absorbance at 220 (peptidic bond), 260 (aromatic scaffolds) and 310 nm (for those containing compound **14**-derived scaffolds) were used to monitor the different compounds. Details of the gradients used are given in the corresponding synthetic procedures.

7.3 Synthetic procedures

Synthesis of precursors for ligands **L1**-**L9**

a) *N*-(2-aminophenyl)acetamide (1)[310]

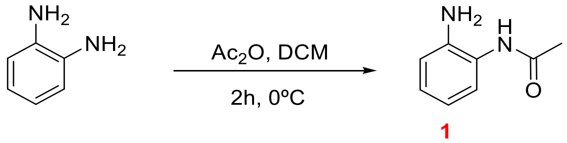

1

Acetic anhydride (5.12 mL, 51.22 mmol, 1 eq) was added dropwise at 0 ºC under N_2 atmosphere to a solution of *o*-phenylenediamine (5.54 g, 51.22 mmol, 1 eq) in anhydrous DCM (75 mL). The mixture was stirred for 2 h at 0 ºC and then stored at -35 ºC overnight. The precipitate was filtered off and washed with cold DCM (3x5 mL) and ether (3x5 mL) to yield 1.01 g of a white solid. The filtrate was furtherly concentrated to the half of its volume and stored at -35 °C for 48 h more. The new precipitate was filtered off to render additional 1.56 g of product. Yield: 2.57 g (38%). **^{1}H NMR** (360 MHz, d_6-DMSO, **Figure A1**): δ 9.12 (s, 1H), 7.14 (d, J = 7.8 Hz, 1H), 6.88 (t, J = 7.4 Hz, 1H), 6.70 (d, J = 8.0 Hz, 1H), 6.52 (t, J = 7.3 Hz, 1H), 4.85 (s, 2H), 2.03 (s, 3H)

b) *p*-chloro-*o*-hydroxybenzaldehyde (2)[207]

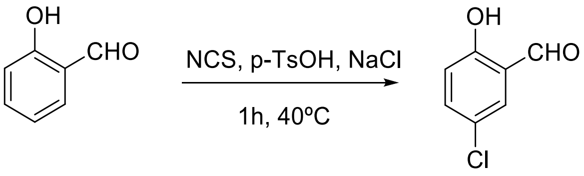

2

Water (4 mL) was added to salicylaldehyde (488 mg, 4.00 mmol, 1 eq) in a 100 mL round-bottom flask. Under magnetic stirring, NCS (536 mg, 4.01 mmol, 1 eq), *p*-TsOH (764 mg, 4.02 mmol, 1 eq) and NaCl (355 mg, 6.07 mmol, 1.5 eq) were added at room temperature. The final solution was stirred at 40 ºC for 1 h. Water (3 mL) was added and the formed precipitate filtered off and washed with water (2x 2mL). Then, the solid was extracted with DCM and dried with sodium sulphate to afford an off-white solid. Pure monochloride product was obtained after column chromatography (Hexane: EtOAc, 6:1). Yield: 85 mg (14%). **^{1}H NMR** (360 MHz, $CDCl_3$, **Figure A2**): δ 10.94 (s, 1H), 9.87 (s, 1H), 7.56 (s, 1H), 7.49 (d, J = 8.4 Hz, 1H), 6.99 (d, J = 8.2 Hz, 1H).

c) *p*-bromo-*o*-hydroxybenzaldehyde (3)[311]

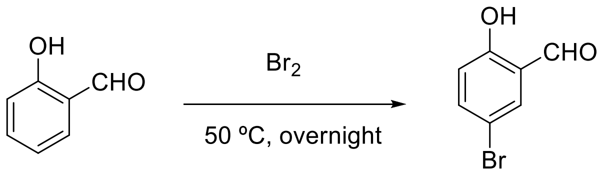

3

To a solution of salicylaldehyde (0.5 g, 4.0 mmol, 1 eq) in chloroform (10 mL), bromine (0.65 g, 4.0 mmol, 1 eq) in chloroform (5 mL) was dropwise added over a period of 15 minutes at 0 ºC. The resulting mixture was stirred overnight at 50 ºC. Then, the reaction was diluted with water (20 mL) and extracted with chloroform (3x8 mL). The organic phases were combined, extracted with water (8 mL) and brine solution (8 mL), dried over sodium sulphate and the solvent removed under reduced pressure. The crude solid was triturated and washed with hexane (2x2 mL) and ether (2x3 mL) and the solvents decanted. **3** was obtained without further purification. Yield: 430 mg (55%). **^{1}H NMR** (250 MHz, *d$_6$*-DMSO, **Figure A3**): δ 10.95 (s, 1H), 10.22 (s, 1H), 7.72 (d, *J* = 2.6 Hz, 1H), 7.65 (dd, *J* = 8.8, 2.6 Hz, 1H), 6.99 (d, *J* = 8.8 Hz, 1H).

d) 3-formyl-4-hydroxybenzenesulfonic acid (4)[243]

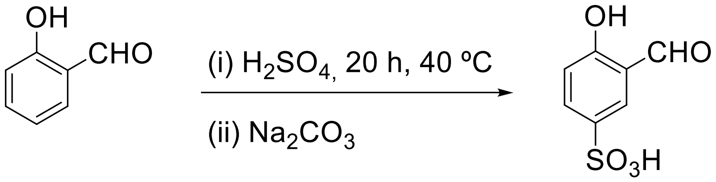

4

Salicylaldehyde (600 mg, 4.90 mmol, 1 eq) was added dropwise into 5 mL of concentrated sulfuric acid at 0 ºC. The reaction was stirred for 24 h at 40-45 °C. The reaction was cooled down to room temperature and poured into 20 mL of ice. Sodium carbonate (5 g, 47.17 mmol, 10 eq) was slowly added at 0 ºC. The mixture was stirred at room temperature for 2 hours.

The carnation precipitate was filtered off and washed with EtOH 96% (3 x 1 mL) and acetone (3 x 2 mL). Crude product was dissolved in absolute EtOH (40 mL) and filtered. The solvent was removed to yield pure **4**. Yield: 108 mg (11%). **^{1}H NMR** (250 MHz, *d$_6$*-DMSO, **Figure A24**): δ 10.86 (s, 1H), 10.26 (s, 1H), 7.89 (d, *J* = 2.2 Hz, 1H), 7.71 (dd, *J* = 8.6, 2.3 Hz, 1H), 6.93 (d, *J* = 8.6 Hz, 1H).

e) (S)-2-amino-5-(3-(2,2,4,6,7-pentamethyl-2,3-dihydrobenzofuran-5-ylsulfonyl)-guanidino)pentanamide resin: Arg(Pbf)-Resin (6)

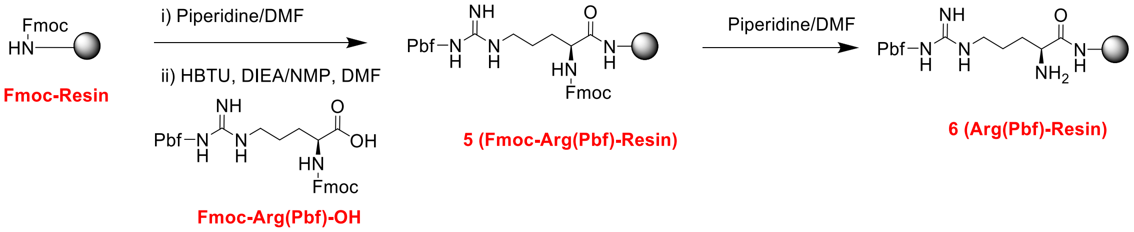

DCM (2 x 15 mL) was added to Rink Amide MBHA (2 g resin scale synthesis, 0.59 mmol/g, 1 eq) for 5 min. The solvent was filtered and the Fmoc group was removed with piperidine (20% in DMF, 2 x 20 mL) for 20 min each. Removal of the Fmoc group was monitored by TLC (Hexane:Et_2O, 1:1.5). The resin was filtered out to remove the excess of piperidine and washed with DMF (2 x 10 mL). A solution of Fmoc-Arg(Pbf)-OH (2.3 g, 3.54 mmol, 3 eq) and HBTU (1.3 g, 3.42 mmol, 2.9 eq) in DMF (6 mL) was then added to the resin in DMF (10 mL) and stirred for 1 min, after which DIEA (1.23 mL, 7.08 mmol, 6 eq) in NMP (2 mL) was also added. The mixture was stirred for 1.5 h at room temperature.

The resin was filtered out and washed with DMF (3 x 5 mL) and DCM (3 x 5 mL). The resin was dried to get **5**. Fmoc protecting group was then removed with piperidine (20% in DMF, 2 cycles x 20 mL) for 20 min each cycle to obtain compound **6**.

To characterize the obtained coupling, an aliquot of **6** was simultaneously cleaved and deprotected with a TFA/TIS/H_2O (95/2.5/2.5, (v/v/v)) mixture for 2 h at room temperature. The resin was filtered out and rinsed with TFA. The filtrate and rinses were combined and concentrated with a nitrogen stream. After precipitation with cold Et_2O, the crude was recovered by centrifugation, dissolved in water and lyophilized. Yield: > 90%. **Analytical HPLC** (8-36% B in 20 min, 1 mL/min): R_t = 15 min. **^{1}H NMR** (300 MHz, D_2O, **Figure A28**): δ 4.50 – 4.35 (m, 1H), 3.15 (t, *J* = 6.8 Hz, 2H), 2.13 (s, 1H), 1.99 – 1.73 (m, 2H), 1.72 – 1.55 (m, 2H).

f) 3-formyl-4-hydroxybenzoic acid (7)[312]

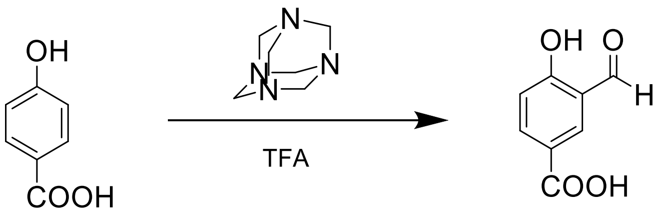

7

A solution of hexamethylenetetramine (7.5 g, 54.5 mmol, 1 eq) in TFA (20 mL) was added dropwise to *p*-hydroxybenzoic acid (7.5 g, 54.0 mmol, 1 eq) in TFA (20 mL) under N_2 atmosphere and refluxed overnight.

The reaction mixture was then cooled to room temperature and HCl 4 M added (150 mL). The reaction mixture was allowed to stir for 4 h at room temperature. The yellow precipitate was filtered off, washed with an excess of water and dissolved in MeOH. The MeOH solution was dried with anhydrous Na_2SO_4 and the solvent removed to obtain a white-yellowish solid. Yield: 3.99 g (44%) **^{1}H NMR** (300 MHz, *d₆*-DMSO, **Figure A29**): 12.75 (bs, 1H), 11.51 (bs, 1H), 10.30 (s, 1H), 8.25 (d, *J* = 2.3 Hz, 1H), 8.05 (dd, *J* = 8.7, 2.3 Hz, 1H), 7.09 (d, *J* = 8.7 Hz, 1H).

g) 3-formyl-4-(methoxymethoxy)benzoic acid (10)[313]

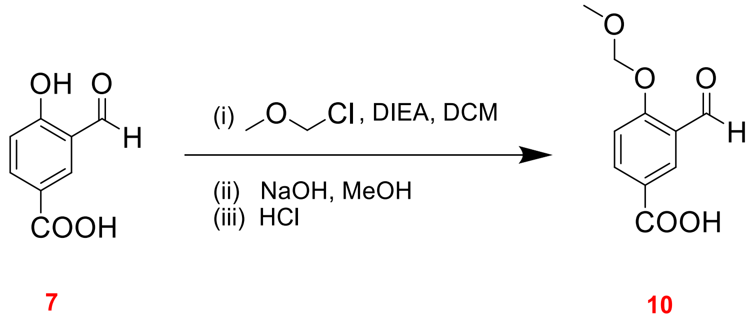

A solution of chloromethyl methyl ether (3.7 mL, 49.7 mmol, 5.5 eq) in anhydrous DCM (120 mL) was added dropwise for 45 min to a solution of **7** (1.5 g, 9 mmol, 1 eq) and DIEA (8.6 mL, 49.7 mL, 5.5 eq) in anhydrous DCM (80 mL) at 0 °C. The resulting reaction mixture was stirred for 48 h at room temperature. Then, it was quenched with saturated NH_4Cl (250 mL) and extracted with DCM (3x150 mL). The organic layer was dried under reduced pressure to provide the intermediate ether ester compound, a dark orange oil.

To a solution of this crude ether ester in MeOH (500 mL), NaOH 15% (400 mL) was added at 0 C and then let stir at room temperature during 3 h. Reaction progress was controlled by TLC. pH was then adjusted to 3 with HCl 6 M at 0 °C. The solution was extracted with EtOAc (2 x 250 mL). The organic layer was washed with water (2 x 50 mL) and brine (2 x 50 mL), and dried under reduced pressure to yield a white-yellowish solid. The solid was recrystallized in EtOAc to obtain pure **10**. Yield: 1.1 mg (59 %). **^{1}H NMR** (360 MHz, *d₆*-DMSO, **Figure A31**): δ 13.05 (bs, 1H), 10.39 (s, 1H), 8.26 (d, *J* = 2.1 Hz, 1H), 8.17 (dd, *J* = 8.8, 2.1 Hz, 1H), 7.39 (d, *J* = 8.8 Hz, 1H), 5.45 (s, 2H), 3.46 (s, 3H).

h) (*E*)-3-((2-acetamidophenylimino)methyl)-4-(methoxymethoxy)benzoic acid (14)

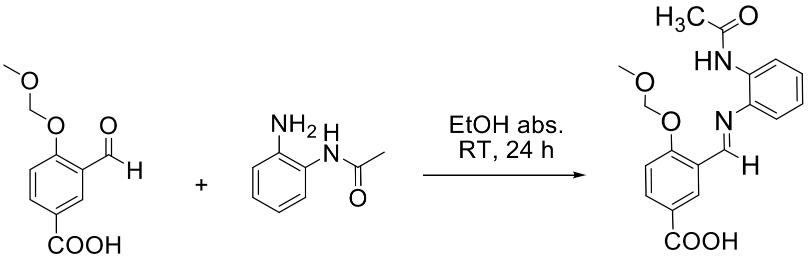

10 **1** **14**

A solution of compound **1** (0.108 g, 0.71 mmol, 1.01 eq) in absolute EtOH (20 mL) was added dropwise to compound **10** (0.150 g, 0.71 mmol, 1 eq) in absolute EtOH (20 mL) and molecular sieve. The reaction mixture was stirred for 24 h at room temperature. Then, it was filtered under vacuum and the filtrate dried under reduced pressure to render a yellowish solid. Yield: 0.236 g (96%). **ESI-MS** (ESI$^-$, MeOH) for [**14**-H]$^-$ = 341.1138 (theoretical = 341.1132). **^{1}H NMR** (250 MHz, *d*$_6$-DMSO, **Figure A33**): δ 12.93 (s, 1H), 9.21 (s, 1H), 8.86 (s, 1H), 8.70 (d, *J* = 2.0 Hz, 1H), 8.07 (dd, *J* = 8.7, 2.2 Hz, 1H), 8.01 (d, *J* = 7.6 Hz, 1H), 7.35 (d, *J* = 8.8 Hz, 1H), 7.28 – 7.10 (m, 3H), 5.43 (s, 2H), 3.45 (s, 3H), 2.09 (s, 3H). **^{13}C NMR** (400 MHz, *d*$_6$-DMSO, **Figure A34**): δ 168.78, 167.21, 160.41, 155.76, 142.68, 134.42, 132.87, 129.82, 126.96, 125.09, 124.96, 124.80, 122.39, 118.69, 115.19, 94.83, 56.70, 24.41.

i) (*R*)-*N*-(1-amino-5-guanidino-1-oxopentan-2-yl)-3-formyl-4-hydroxybenzamide (11)

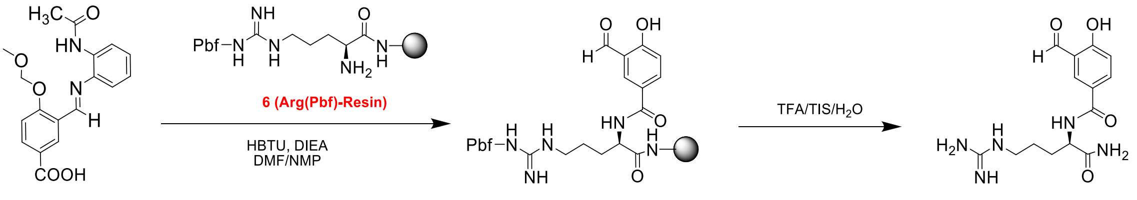

14 **9** **11**

A solution of **14** (262 mg, 0.77 mmol, 1.3 eq) and HBTU (269 mg, 0.71 mmol, 1.2 eq) in DMF (6 mL) were added into **6** (1 g, 0.59 mmol/g, 1 eq) in DMF (8 mL). After 1 min of stirring, DIEA (198 mg, 1.53 mmol, 2.6 eq) in NMP (2 mL) was added and the mixture was stirred at room temperature for 1.5 h. The resin was filtered out and washed with DMF (3 x 5 mL) and DCM (3 x 5 mL), letting the resin dry to get **9**. Then, it was simultaneously cleaved and deprotected with a TFA/TIS/H_2O (95/2.5/2.5, (v/v/v)) mixture for 2 h at room temperature. The resin was filtered out and rinsed with TFA. The filtrate and rinses were combined and concentrated with a nitrogen stream. After precipitation from the filtrate with cold Et_2O, the crude **11** was recovered by centrifugation, dissolved in water and lyophilized. It was purified through reversed-phase preparative HPLC in a C12 Axia column (250 mm x 21.20 mm, 4 µm, 90 Å) with the two-solvent gradient A and B to render pure product **11**. Yield: 55 mg (30%). **Preparative HPLC** (8-36% B in 30 min, 10 mL/min): R_t = 17.3 min. **Analytical HPLC** (8-36% B in 20 min, 1 mL/min): R_t = 11.4 min (purity > 95%). **ESI-MS** (ESI^+, ACN-H_2O) for [**11**+H]$^+$ = 322.2 (theoretical: 322.15). **^{1}H NMR** (300 MHz, D_2O, **Figure A32**): δ 9.99 (s, 1H), 8.18 (d, *J* = 2.3 Hz, 1H), 7.98 (dd, *J* = 8.8, 2.3 Hz, 1H), 7.08 (d, *J* = 8.8 Hz, 1H), 4.48 (m, 1H), 3.23 (t, *J* = 6.7 Hz, 2H), 2.11 – 1.61 (m, 4H).

j) (*β*-Ala)-TAT$_{49\text{-}57}$(*)-Resin (16)

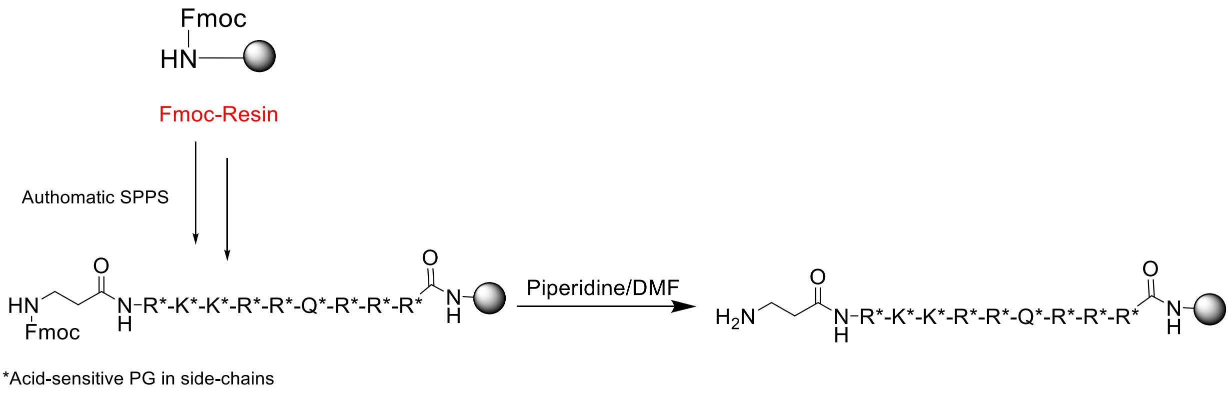

15 (Fmoc-(β-Ala)-TAT$_{49\text{-}57}$(*)-Resin)

16 ((β-Ala)-TAT$_{49\text{-}57}$(*)-Resin)

15 was automatically synthesized on a Rink Amide MBHA (0.424 g resin scale synthesis, 0.59 mmol/g, 0.25 mmol scale) on a Biotage Initiator+ Alstra synthesizer. Namely, amino acids were coupled using HBTU, DIEA as detailed in section 7.2 (*Peptide Synthesis*). The Fmoc group of **15** was removed with piperidine (20% in DMF, 2 x 20 mL, 20 min each) at room temperature. Removal of the Fmoc group was monitored by TLC (Hexane:Et_2O, 1:1.5). The resin was filtered out to remove the excess of piperidine and washed with DMF (2 x 10 mL) and DCM (3 x 10 mL) to get **16**.

The peptide was characterized and its purity assessed by taking aliquots of **15** and **16** and simultaneously cleaved and deprotected by using a TFA/TIS/H_2O (95/2.5/2.5, (v/v/v)) mixture for 2 h at room temperature. The resin was filtered out and rinsed with TFA. The filtrate and rinses were combined and concentrated with a nitrogen stream. After precipitation from the filtrate with cold Et_2O, both crudes were recovered by centrifugation, dissolved in water and lyophilized. They were purified through HPLC preparative. Attachment was considered to be quantitative (> 90% yield).

<u>From **15**:</u>

Preparative HPLC (14-37%B in 30 min, 10 mL/min): R$_t$ = 22.5 min. **Analytical HPLC** (8-36%B in 20 min, 1 mL/min): R$_t$ =19.1 min (purity > 95%). **ESI-MS** (ESI$^+$, H$_2$O-MeOH) for [{Fmoc-(*β*-Ala)-TAT$_{49\text{-}57}$}+4H]$^{4+}$ = 408.8 and for [{Fmoc-(*β*-Ala)-TAT$_{49\text{-}57}$}+5H]$^{5+}$ = 327.4 (theoretical: 408.75 and 327.20, respectively).

<u>From **16**</u>

Preparative HPLC (8-15%B in 10 min, 10 mL/min): R$_t$ = 14.0 min. **Analytical HPLC** (8-36%B in 20 min, 1 mL/min): R$_t$ = 6.9 min (purity > 95%). **^{1}H NMR** (400 MHz, D$_2$O, **Figure A42**): δ 4.26 – 4.10 (m, 9H), 3.92 (t, *J* = 6.7 Hz, 1H), 3.09 (m, 12H), 2.86 (t, *J* = 7.3 Hz, 4H), 2.60 (t, *J* = 6.8 Hz, 2H), 2.23 (t, *J* = 7.6 Hz, 2H), 1.93 (s, 1H), 1.83 – 1.18 (m, 40H).

k) 7 conjugated to (*β*-Ala)-TAT$_{49\text{-}57}$ (17)

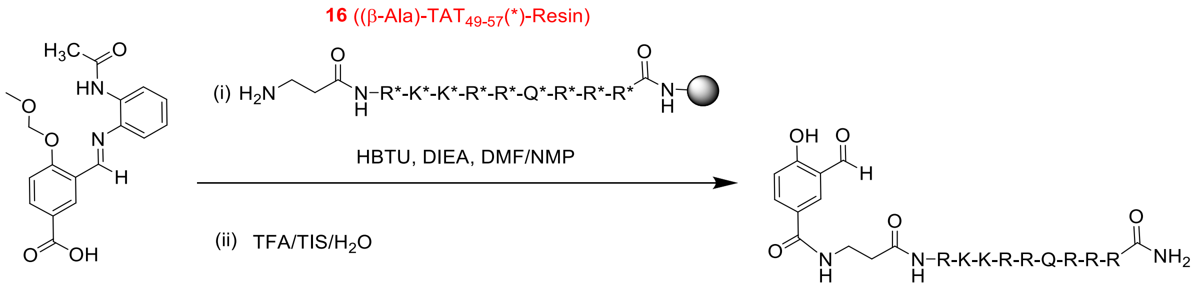

14

17

A solution of **14** (243 mg, 0.71 mmol, 1.3 eq) and HBTU (248 mg, 0.66 mmol, 1.2 eq) in DMF (6 mL) were added into **16** (925 mg, 0.59 mmol/g, 1 eq) in DMF (8 mL). After 1 min of stirring, DIEA (183 mg, 1.53 mmol, 2.6 eq) in NMP (2 mL) was added and the mixture was stirred at room temperature for 1.5 h. The resin was filtered out and washed with DMF (3 x 5 mL) and DCM (3 x 5 mL). Then, it was simultaneously cleaved and deprotected with a TFA/TIS/H$_2$O (95/2.5/2.5, (v/v/v)) mixture for 2 h at room temperature. The resin was filtered out and rinsed with TFA. The filtrate and rinses were combined and concentrated with a nitrogen stream. After precipitation from the filtrate with cold Et$_2$O, the crude **17** was recovered by centrifugation, dissolved in water and lyophilized. It was purified through reversed-phase preparative HPLC in a C12 Axia column (250 mm x 21.20 mm, 4 µm, 90 Å) with the two-solvent gradient A and B to render pure product **17**. **Preparative HPLC** (13.5-21% B in 17 min, 10 mL/min): R$_t$ = 14.0 min. **Analytical HPLC** (8-36% B in 20 min, 1 mL/min): R$_t$ = 10.8 min (purity > 95%). **ESI-MS** (ESI$^+$, H$_2$O-

MeOH) for [**17**+3H]$^{3+}$ = 520.0 (theoretical: 520.0), [**17**+4H]$^{4+}$ = 390.2 (theoretical: 390.2) and [**17**+5H]$^{5+}$ = 312.4 (theoretical: 312.4). ^{1}**H NMR** (300 MHz, D_2O, **Figure A43**): δ 10.05 (s, 1H), 8.18 (d, *J* = 2.3 Hz, 1H), 7.98 (dd, *J* = 8.7, 2.3 Hz, 1H), 7.12 (d, *J* = 8.8 Hz, 1H), 4.42 – 4.16 (m, 9H), 3.78 – 3.60 (m, 2H), 3.19 (dd, *J* = 12.2, 5.4 Hz, 10H), 3.00 (dd, *J* = 16.4, 9.5 Hz, 6H), 2.75 – 2.54 (m, 2H), 2.36 (t, *J* = 7.6 Hz, 2H), 2.14 – 1.31 (m, 38H).

I) R_9(*)-Resin (18) and $(Gly)_4$-R_9(*)-Resin (20)

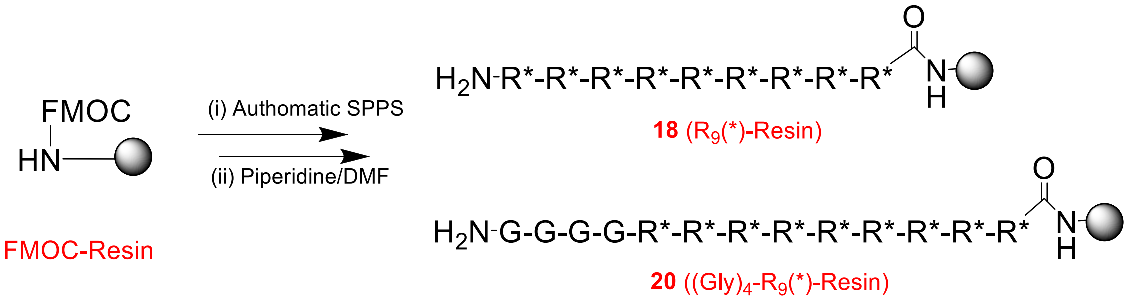

FMOC-Resin

18 (R_9(*)-Resin)

20 ($(Gly)_4$-R_9(*)-Resin)

*Acid-sensitive PG in side-chains

Fmoc-protected (in the *N*-terminus) **18** and **20** were automatically synthesized assisted by a Biotage Initiator+ Alstra synthesizer, and following the same procedure as for Arg(Pbf)-Resin (**6**). Fmoc deprotection was carried out by using piperidine (20% in DMF, 2 x 20 mL, 20 min) at room temperature to render **18** and **20**, as previously reported for **16**. Peptide synthesis yield was considered > 90%.

Aliquots of Fmoc-protected **18** and **20** were simultaneously cleaved and the side-chain protecting groups of the Arg residues removed with the TFA/H_2O/TIS mixture. Following the same procedure as for the aliquot of **6**, they were collected and lyophilized, and characterized without any purification. For the NMR characterization, Fmoc deprotected peptide aliquots (**18** and **20**) were used, following the same protocol.

From Fmoc-protected **18**

Analytical HPLC (0-50%B in 30 min, 1 mL/min, **Figure A44**): R_t = 20.2 min (crude purity > 90%). ^{1}**H NMR** of Fmoc-deprotected (300 MHz, D_2O, **Figure A45**): δ 4.42-4.21 (9H, bs), 3.29-3.10 (18H, bs), 1.9-1.5 (38H, m).

From Fmoc-protected **20**

Analytical HPLC (0-50%B in 30 min, 1 mL/min, **Figure A46**): R_t =18.6 min (crude purity > 90%). ^{1}**H NMR** of Fmoc-deprotected (300 MHz, D_2O, **Figure A47**): δ 4.31-4.10 (9H, bs), 3.95-3.7 (4H, m), 3.20-3.02 (18H, bs), 1.85-1.5 (38H, m).

m) 7 conjugated to R_9 peptide (19)

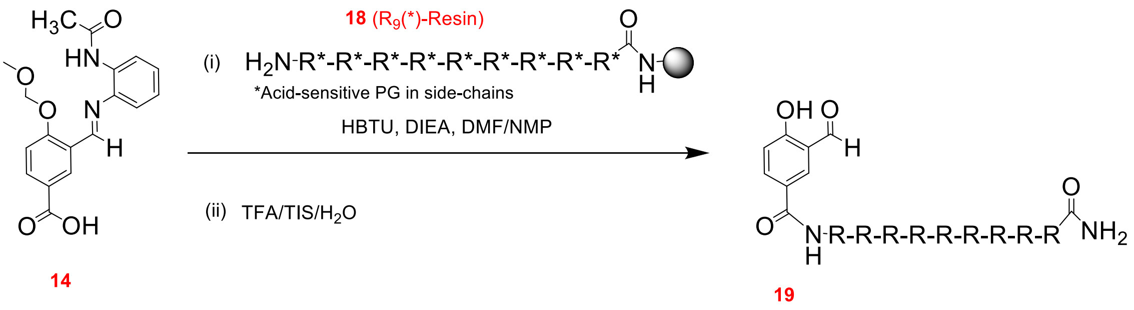

A solution of **14** (66 mg, 0.192 mmol, 1.1 eq) and HBTU (70 mg, 0.184 mmol, 1.05 eq) in DMF (6 mL) were added into **18** (300 mg, 0.59 mmol/g, 1 eq) in DMF (8 mL). After 1 min of stirring, DIEA (52 mg, 0.403 mmol, 2.2 eq) in NMP (2 mL) was added and the mixture was stirred at room temperature for 1.5 h. The resin was filtered out and washed with DMF (3 x 5 mL) and DCM (3 x 5 mL). Then, it was simultaneously cleaved and deprotected with a TFA/TIS/H_2O (95/2.5/2.5, (v/v/v)) mixture for 2 h at room temperature, following the same procedure as that for **17**. The crude of **19** was purified through reversed-phase preparative HPLC. Yield: 42 mg (15%). **Preparative HPLC** (10-22% B in 20 min, 10 mL/min): R_t = 22.1 min. **Analytical HPLC** (0-50%B in 30 min, 1 mL/min): R_t = 15.0 min (purity > 95%). **ESI-MS** (ESI^+, H_2O-MeOH, **Figure A49**) for [**19**+4H]$^{4+}$ = 393.5 (theoretical: 393.5), [**19**+5H]$^{5+}$ = 315.0 (theoretical: 315.0) and [**19**+6H]$^{6+}$ = 262.7 (theoretical: 262.7). **^{1}H NMR** (360 MHz, D_2O, **Figure A48**): δ 9.98 (s, 1H), 8.20 (s, 1H), 7.99 (d, *J* = 8.3 Hz, 1H), 7.10 (d, *J* = 8.2 Hz, 1H), 4.30 (s, 9H), 3.18 (s, 18H), 2.00 – 1.35 (m, 36H).

n) 7 conjugated to $(Gly)_4$-R_9 peptide (21)

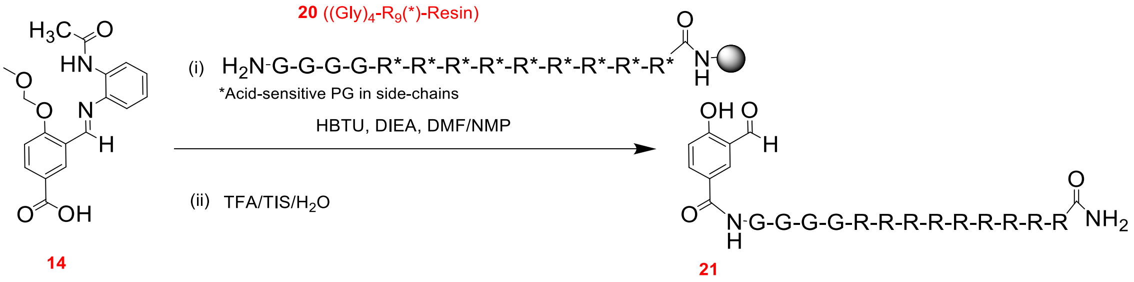

A solution of **14** (330 mg, 0.964 mmol, 1.1 eq) and HBTU (352 mg, 0.929 mmol, 1.05 eq) in DMF (8 mL) were added into **20** (1.5 g, 0.59 mmol/g, 1 eq) in DMF (10 mL). After 1 min of stirring, DIEA (252 mg, 1.95 mmol, 2.2 eq) in NMP (2 mL) was added and the mixture was stirred at room temperature for 1.5 h. The resin was filtered out and washed with DMF (3 x 5 mL) and DCM (3 x 5 mL). Then, it was simultaneously cleaved and deprotected with a TFA/TIS/H_2O (95/2.5/2.5, (v/v/v)) mixture for 2 h at room temperature, following the same procedure as that for **17**. The crude of **21** was purified through reversed-phase preparative HPLC. Yield: 37 mg (11%). **Preparative HPLC** (10-23% B in 20 min, 10 mL/min): R_t = 19.6 min. **Analytical HPLC** (0-50% B in 30 min, 1 mL/min): R_t = 14.5 min (purity > 95%). **HR ESI-MS** (ESI^+, H_2O-MeOH, **Figure A51**) for $[\mathbf{21}+5H]^{5+}$ = 360.6182 (theoretical: 360.6150) and $[\mathbf{21}+3Na+2H+CH_3OH]^{5+}$ = 380.2105 (theoretical: 380.2094). **^{1}H NMR** (400 MHz, D_2O, **Figure A50**): δ 9.94 (s, 1H), 8.15 (d, *J* = 2.4 Hz, 1H), 7.94 (dd, *J* = 8.8, 2.4 Hz, 1H), 7.02 (d, *J* = 8.8 Hz, 1H), 4.26 – 4.12 (m, 9H), 4.08 (s, 2H), 3.97 – 3.74 (m, 6H), 3.14 – 2.99 (m, 18H), 1.80 – 1.42 (m, 36H).

o) 7 conjugated to the DTPA-4Ac-NH_2 platform (23)

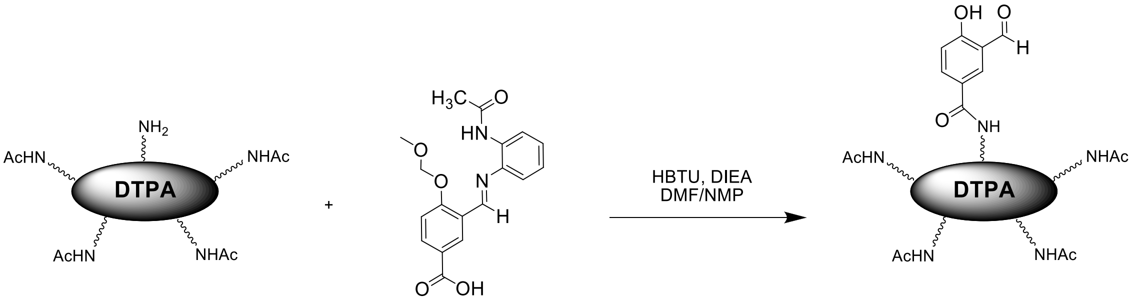

DTPA-4Ac-NH_2 14 23

A solution of **14** (11.88 mg, 0.035 mmol, 2.7 eq) and HBTU (11.57 mg, 0.031 mmol, 2.4 eq) in DMF (4 mL) was added to a solution of DTPA-4Ac-NH_2 (20 mg, 0.013 mmol, 1 eq) in DMF (8 mL). DIEA (8.85 mg, 0.068 mmol, 5.3 eq) in NMP (2 mL) was then added and the reaction mixture stirred for 2h at room temperature.

The reaction mixture was diluted with water (100 mL) and then lyophilized. The remaining crude was washed with EtOAc and filtered under vacuum. The solid was collected with water and lyophilized. 5% TFA in DCM (10 mL) was added to the crude and stirred at room temperature for 1.5 h. The solvent was removed under reduced pressure. The crude **23** was purified by reversed-phase preparative HPLC to provide a colorless oil. Yield: 8 mg (35 %). **Preparative HPLC** (19-41% B in 36 min, 10 mL/min): R_t = 29.6 min. **Analytical HPLC** (0-50% B in 30 min, 1 mL/min): R_t = 25.7 min (purity > 95%). **HR-MS** (ESI^+, MeOH-H_2O) for $[\mathbf{23}+K+H]^{2+}$ = 880.0032 (theoretical= 880.0039). **^{1}H NMR** (400 MHz, D_2O, **Figure A62**): δ 10.05 (s, 1H), 8.16 (d, *J* = 2.2 Hz, 1H), 7.96 (dd, *J* = 8.8, 2.3 Hz, 1H), 7.10 (d, *J* = 8.8 Hz, 1H), 3.67 – 3.57 (m, 40H), 3.56 – 3.51 (m, 22H), 3.34 (s, 12H), 3.28 – 3.14 (m, 20H), 3.09 – 3.02 (m, 4H), 1.93 (s, 12H), 1.91 – 1.85 (m, 2H), 1.82 – 1.68 (m, 18H).

Synthesis of ligands **L1**-**L9**

a) (*E*)-*N*-(2-(2-hydroxybenzylideneamino)phenyl)acetamide (L1)

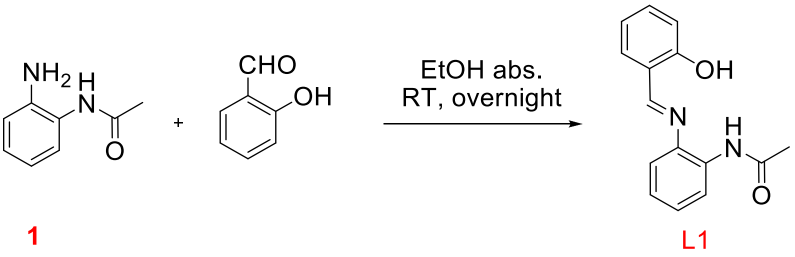

Salicylaldehyde (43.5 mg, 0.36 mmol, 1 eq) in absolute EtOH (6 mL) was added dropwise to a solution of **1** (58.4 mg, 0.39 mmol, 1.1 eq) in absolute EtOH (22 mL) at 0° C and under strong agitation. The final mixture was stirred for 15 min at 0 °C and then overnight (12 h) at room temperature. The solution was filtered, and the solvent of the filtrate removed under vacuum to afford the crude iminic product. Pure **L1** was obtained after purification with column chromatography in SiO_2 using a gradient elution (DCM:Hexane, 1:1 to remove the unreacted aldehyde and then EtOAc:Hexane, 1:1 to elute the desired product). Yield: 36 mg (39%). **R_f** (EtOAc:Hexane, 2:1) = 0.7. **HR ESI-MS** (ESI$^+$, MeOH, **Figure A7**) for [**L1**+H]$^+$ = 255.1104 (theoretical = 255.1128). ^{1}**H NMR** (360 MHz, *d*$_6$-DMSO, **Figure A4**): δ 12.76 (s, 1H), 9.54 (s, 1H), 8.87 (s, 1H), 7.77 – 7.57 (m, 2H), 7.49 – 7.33 (m, 2H), 7.27 (s, 2H), 6.97 (d, *J* = 7.7 Hz, 2H), 2.05 (s, 3H). ^{13}**C NMR** (400 MHz, *d*$_6$-DMSO, **Figure A5**): δ 168.80, 163.70, 160.72, 142.32, 133.77, 132.93, 132.58, 127.33, 126.22, 125.41, 120.29, 119.58, 119.41, 117.10, 23.83. **FTIR-ATR** (**Figure A6**, wavenumber, cm^{-1}): 3294.31, 3055.63, 1662.29, 1613.70, 1589.52, 1573.64, 1515.92, 1443.20, 1365.24, 1304.59, 1278.20, 1225.08, 1180.92, 1150.51, 1108.70, 1033.13, 1005.30, 965.08, 939.91, 909.25, 854.86, 829.27, 779.77, 752.58, 723.25, 674.22, 642.06.

b) (*E*)-*N*-(2-(5-chloro-2-hydroxybenzylideneamino)phenyl)acetamide (L2)

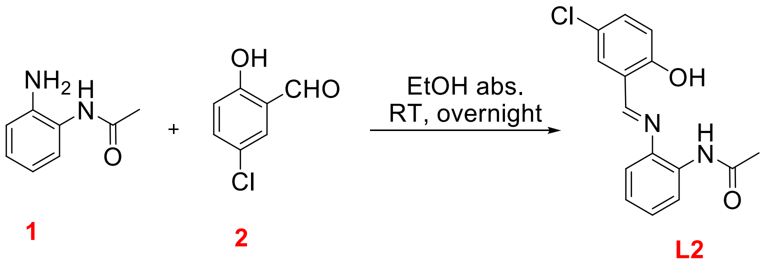

2 (20 mg, 0.13 mmol, 1 eq) in absolute EtOH (4 mL) was added dropwise to a solution of **1** (20 mg, 0.13 mmol, 1 eq) in absolute EtOH (10 mL) at 0 °C and under strong agitation. The final mixture was stirred for 15 min at 0 ºC and at room temperature overnight. The solution was filtered, and the solvent of the filtrate removed to afford the crude iminic product. Pure **L2** was obtained after purification with column chromatography in SiO$_2$ using a gradient elution (DCM:Hexane, 3:4 ratio, to remove the unreacted aldehyde and then Hexane:DCM:EtOAc, 1:1:0.5 ratio, to elute the desired product). Yield: 16 mg (43%). **R$_f$** (EtOAc:Hexane, 2:1) = 0.7. **HR ESI-MS** (ESI$^+$, MeOH, **Figure A17A**) for [**L2**+H]$^+$ = 289.0708 (theoretical = 289.0738). **^{1}H NMR** (360 MHz, d_6-DMSO, **Figure A11**): δ 12.66 (bs, 1H), 9.55 (s, 1H), 8.86 (s, 1H), 7.83 (s, 1H), 7.68 (d, *J* = 7.4 Hz, 1H), 7.45 (d, *J* = 8.7 Hz, 1H), 7.35 (d, *J* = 7.2 Hz, 1H), 7.28 (m, 2H), 7.01 (d, *J* = 8.8 Hz, 1H), 2.05 (s, 3H). **^{13}C NMR** (400 MHz, d_6-DMSO, **Figure A12**): δ 168.81, 161.85, 159.28, 142.18, 133.21, 132.73, 131.26, 127.65, 126.11, 125.15, 122.97, 121.81, 119.19, 119.09, 23.87. **FTIR-ATR** (**Figure A13**, wavenumber, cm^{-1}): 3274.78, 2361.39, 1662.26, 1515.30, 1593.63, 1529.51, 1479.28, 1452.05, 1358.29, 1303.45, 1280.16, 1220.51, 1176.62, 1109.38, 1090.29, 1048.24, 1011.05, 959.80, 922.81, 870.39, 819.90, 760.15, 739.44, 697.78, 654.92, 641.38.

c) (*E*)-*N*-(2-(5-bromo-2-hydroxybenzylideneamino)phenyl)acetamide (L3)

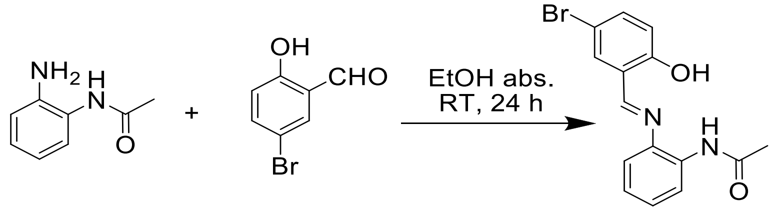

1 3 L3

Compound **3** (150 mg, 0.75 mmol, 1 eq) in absolute EtOH (5 mL) was added dropwise to a solution of **1** (123 mg, 0.76 mmol, 1 eq) in absolute EtOH (10 mL) at 0 ºC and under strong agitation. The final mixture was stirred for 15 min at 0 ºC and at room temperature for 24 h. The solution was filtered, the precipitate washed with DMC (2 x 3 mL) and the solvent of the filtrate removed to afford the crude iminic product. **L3** was obtained after purification by flash column chromatography in SiO$_2$ (DCM:EtOAc, 1:1). Yield: 125 mg, (52%). **R$_f$** (EtOAc:Hexane, 2:1) = 0.7. **HR ESI-MS** (ESI$^+$, MeOH, **Figure A17B**) for [**L3**+H]$^+$ = 333.0193 (theoretical = 333.0233). **^{1}H NMR** (250 MHz, d_6-DMSO, **Figure A14**): δ 12.67 (s, 1H), 9.53 (s, 1H), 8.85 (s, 1H), 7.95 (d, *J* = 2.5 Hz, 1H), 7.67 (d, *J* = 6.9 Hz, 1H), 7.56 (dd, *J* = 8.8, 2.5 Hz, 1H), 7.40 – 7.22 (m, 3H), 6.96 (d, *J* = 8.8 Hz, 1H), 2.07 (d, *J* = 8.4 Hz, 3H). **^{13}C NMR** (400 MHz, d_6-DMSO, **Figure A15**): δ 171.03, 164.07, 161.92, 144.15, 138.20, 136.48, 134.93, 129.88, 128.37, 127.44, 124.46, 121.74, 121.43, 112.57, 26.07. **FTIR-ATR** (**Figure A16**, wavenumber, cm^{-1}): 3295.33, 1661.38, 1614.48, 1587.78, 1566.65, 1528.15, 1472.56, 1451.73, 1368.30, 1355.88, 1307.60, 1277.36, 1219.00, 1175.25, 1130.46, 1111.42, 1076.79, 1038.90, 1016.55, 960.34, 937.67, 914.61.

d) (*E*)-3-((2-acetamidophenylimino)methyl)-4-hydroxybenzenesulfonic acid (L4)

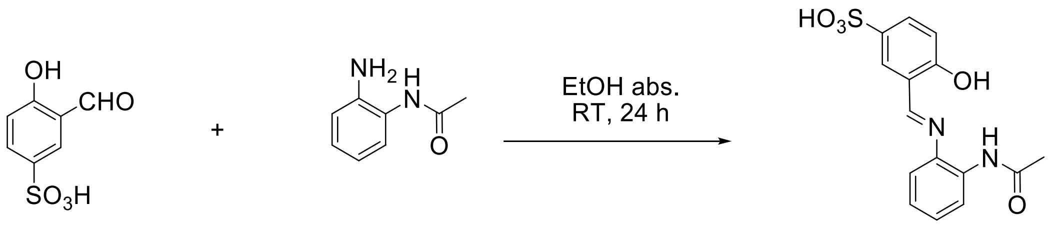

4 **1** **L4**

Compound **4** (50 mg, 0.247 mmol, 1 eq) in absolute EtOH (20 mL) was dropwise added to a solution of **1** (45 mg, 0.297 mmol, 1.2 eq) in absolute EtOH (10 mL) at 0 ºC under stirring and with molecular sieve. The mixture was stirred for 15 min at 0 ºC and then overnight at room temperature. Molecular sieve was filtered off and the solvent of the filtrate removed to obtain crude **L4**. The product was washed with DCM (3 x 5 mL) to obtain pure ligand **L4**. Yield: 43 mg (53%). **ESI-MS** (ESI$^-$, MeOH, **Figure A27**) for [**L4**-H]$^-$ = 333.1 (theoretical = 333.1). ^{1}**H NMR** (360 MHz, d_6-DMSO, **Figure A25**): δ 13.03 (s, 1H), 9.56 (s, 1H), 8.94 (s, 1H), 7.95 (s, 1H), 7.62 (d, *J* = 7.0 Hz, 2H), 7.46 – 7.36 (m, 1H), 7.31 – 7.19 (m, 2H), 6.90 (d, *J* = 8.3 Hz, 1H), 2.05 (s, 3H). ^{13}**C NMR** (400 MHz, d_6-DMSO, **Figure A26**): δ 168.94, 164.03, 161.24, 142.45, 140.48, 132.61, 131.21, 130.19, 127.53, 126.53, 125.88, 119.97, 118.92, 116.26, 24.38.

e) (*R*,*E*)-3-((2-acetamidophenylimino)methyl)-*N*-(1-amino-5-guanidino-1-oxopentan-2-yl)-4-hydroxybenzamide (L5)

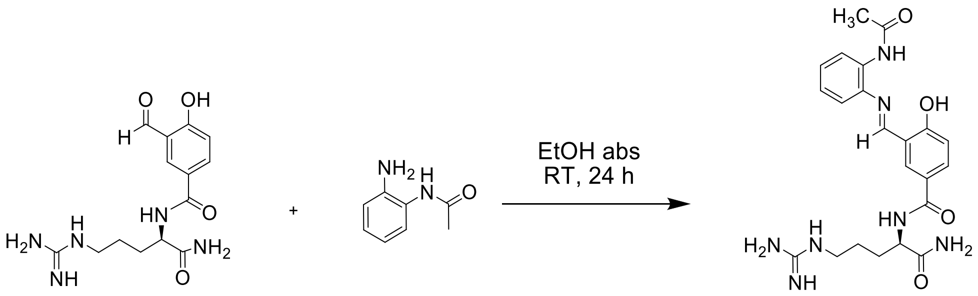

11 **1** **L5**

Compound **1** (13 mg, 0.087 mmol, 1.4 eq) in absolute EtOH (12 mL) was dropwise added to a solution of **11** (20 mg, 0.062 mmol, 1 eq) in absolute EtOH (10 mL) at 0 ºC under stirring and with molecular sieve. The mixture was stirred for 15 min at 0 ºC and then 24 h at room temperature.

Molecular sieve was filtered off and the solvent of the filtrate removed to obtain crude **L5**. The crude was washed with EtOAc (3 x 5 mL) to obtain pure ligand **L5**. Yield: 19 mg (68%). **HR ESI-MS** (ESI$^+$, MeOH) for [**L5**+H]$^+$ = 454.2198 (theoretical = 454.2197). ^{1}**H NMR** (250 MHz, D_2O, **Figure A36**): δ 9.97 (s, 1H), 8.08 (d, *J* = 2.4 Hz, 1H), 7.84 (dd, *J* = 8.9, 2.3 Hz, 1H), 7.18 – 7.07 (m, 1H), 7.02 (d, *J* = 6.5 Hz, 1H), 6.87 (d, *J* = 9.1 Hz, 1H), 6.80 (t, *J* = 7.7 Hz, 1H), 4.40 (m, 1H), 3.17 (t, *J* = 6.7 Hz, 2H), 2.12 (s, *J* = 5.6 Hz, 2H), 1.96 – 1.55 (m, 4H). ^{13}**C NMR** (500 MHz, D_2O, **Figure A37**): δ 192.82, 176.88, 173.94, 169.68, 162.79, 156.70, 142.01, 135.71, 132.04, 128.73, 127.63, 122.82, 121.65, 119.76, 117.76, 117.45, 115.15, 53.80, 40.45, 28.07, 24.55, 21.89.

f) L6

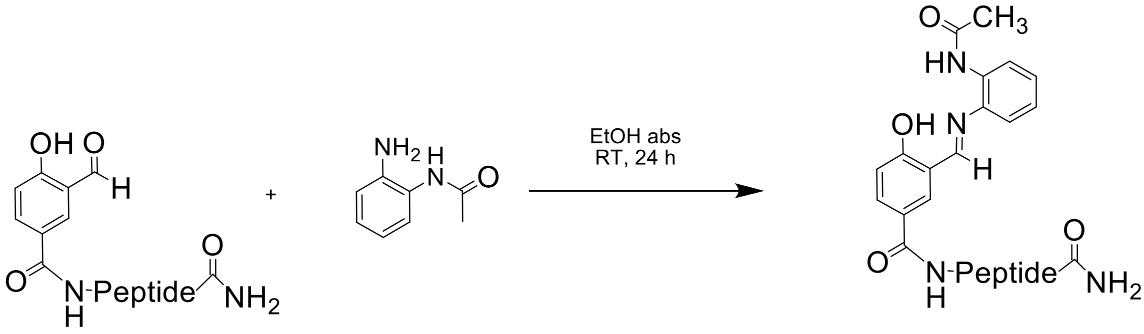

19: ***Peptide= R$_9$*** **1** **L6**: ***Peptide= R$_9$***

Compound **1** (2 mg, 0.013 mmol, 2.1 eq) in absolute EtOH (5 mL) was dropwise added to a solution of **19** (10 mg, 0.0064 mmol, 1 eq) in absolute EtOH (5 mL) at 0 ºC under stirring and with molecular sieve. The mixture was stirred for 15 min at 0 ºC and then 24 h at room temperature.

Molecular sieve was filtered off and the solvent of the filtrate removed to obtain crude **L6**. The crude was washed with EtOAc (3 x 5 mL), recovered with H_2O and lyophilized to obtain pure ligand **L6**. Yield: 9.6 mg (88%). **HR ESI-MS** (ESI$^+$, MeOH) for [**L6**+4H]$^{4+}$ = 426.5133 (theoretical = 426.5126). ^{1}**H NMR** (400 MHz, D_2O, **Figure A52**): δ 10.08 (s, 1H), 8.02 (s, 1H), 7.73 (d, *J* = 8.3 Hz, 1H), 7.14 (t, *J* = 7.5 Hz, 1H), 7.04 (d, *J* = 7.0 Hz, 1H), 6.89 (d, *J* = 6.7 Hz, 1H), 6.82 (t, *J* = 6.5 Hz, 1H), 6.67 (d, *J* = 7.8 Hz, 1H), 4.26 (s, 9H), 3.13 (s, 18H), 2.14 (s, 3H), 1.85 – 1.50 (m, 36H).

g) L7

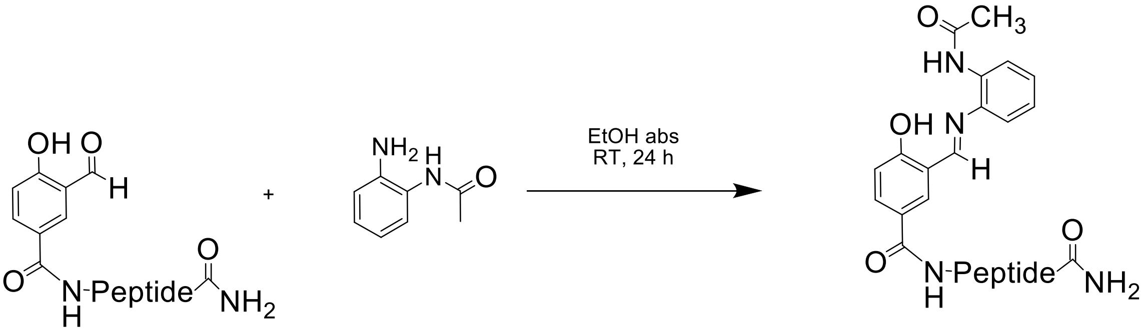

21: *Peptide= (Gly)$_4$-R$_9$* **1** **L7: *Peptide= (Gly)$_4$-R$_9$***

Compound **1** (2 mg, 0.013 mmol, 2.4 eq) in absolute EtOH (5 mL) was dropwise added to a solution of **21** (20 mg, 0.053 mmol, 1 eq) in absolute EtOH (5 mL) at 0 ºC under stirring and with molecular sieve. Pure ligand **L7** was obtained following the same protocol as for **L6**. Yield: 8.0 mg (78%). **HR ESI-MS** (ESI$^+$, MeOH) for [**L7**+4H]$^{4+}$ = 483.5343 (theoretical = 483.5341), for [**L7**+5H]$^{5+}$ = 387.0305 (theoretical = 387.0287). **^{1}H NMR** (500 MHz, D$_2$O, **Figure A53**): δ 10.08 (s, 1H), 8.08 (s, 1H), 7.78 (d, *J* = 9.0 Hz, 1H), 7.20 (t, *J* = 7.6 Hz, 1H), 7.10 (d, *J* = 7.8 Hz, 1H), 6.95 (d, *J* = 8.0 Hz, 1H), 6.88 (t, *J* = 7.5 Hz, 1H), 6.71 (d, *J* = 9.0 Hz, 1H), 4.37 – 4.24 (m, 9H), 4.17 – 3.84 (m, 8H), 3.28 – 3.06 (m, 18H), 2.20 (s, 3H), 1.88 – 1.52 (m, 36H).

h) DTPA-based ligand L9

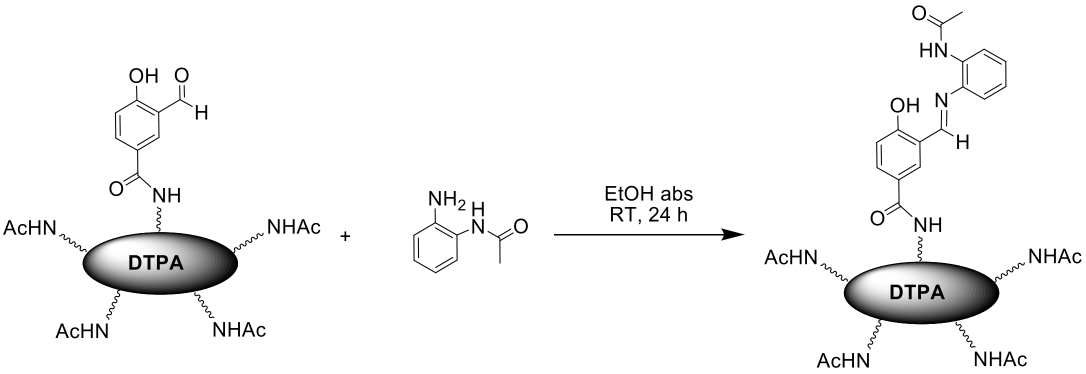

23 **1** **L9**

A solution of **1** (2 mg, 0.013 mmol, 2 eq) in absolute EtOH (5 mL) was added dropwise to a solution of **23** (10 mg, 0.006 mmol, 1 eq) and molecular sieve in absolute EtOH (5 mL). The reaction mixture was stirred for 24 h at room temperature. It was then filtered and dried under vacuum. The reaction crude was washed with EtOAc (4 x 8 mL) and filtered. The solid was collected with water, and lyophilized to provide a clear brown product. Yield: 8 mg (78%). **HR-MS** (ESI$^+$, MeOH) for [**L9**+K+H]$^{2+}$ = 946.0406 (theoretical= 946.0382) and for [**L9**+K+Na+H]$^{3+}$ = 638.3575 (theoretical= 638.3552).**^{1}H NMR** (400 MHz, D_2O, **Figure A64**) δ 9.99 (s, 1H), 7.92 (d, *J* = 2.4 Hz, 1H), 7.65 (dd, *J* = 9.2, 2.5 Hz, 13H), 7.14 – 7.09 (t, *J* = 7.8, 1H), 7.01 (dd, *J* = 7.9, 1.5 Hz, 1H), 6.86 (dd, *J* = 7.9, 1.0 Hz, 1H), 6.81 (t, *J* = 7.6, 1H), 6.61 (d, *J* = 9.1 Hz, 1H), 3.65 – 3.48 (m, 42H), 3.48 – 3.32 (m, 28H), 3.23 – 3.04 (m, 30H), 2.11 (s, 3H), 1.87 (s, 12H), 1.81 (m, 2H), 1.72 – 1.56 (m, 18H).

Synthesis of complexes **C1**-**C9**

All complexes (except **C8**) have been synthesized following the general scheme shown below, where Y refers to the functionalizations carried out (Cl, Br, SO_3^-, Arg, R_9, $(Gly)_4$-R_9) and X to a solvent molecule or a counterion:

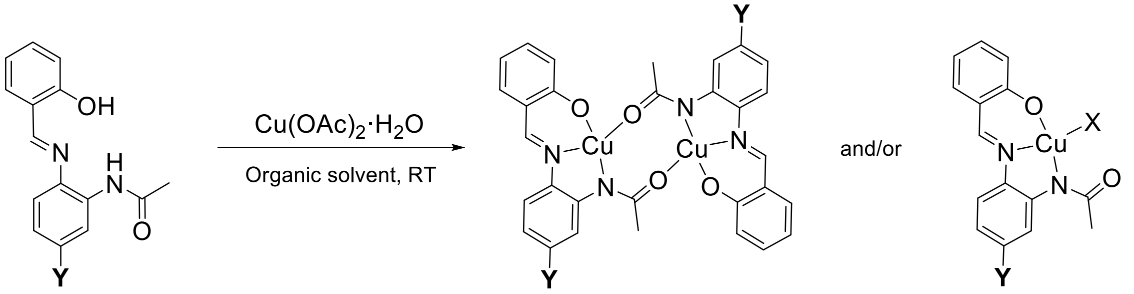

a) *Y: H* (Complex C1)

$Cu(OAc)_2 \cdot 2H_2O$ (15.7 mg, 0.08 mmol, 1 eq) in ACN (3 mL) was slowly added to a solution of **L1** (20 mg, 0.08 mmol, 1 eq) in ACN (8 mL) at room temperature. The final mixture was stirred for 2h and the formed precipitate was filtered off, washed with ACN (2 x 3 mL) and with Et_2O (2 x 3 mL) to get C1. Yield: 17 mg (68%). **HR-MS** (ESI$^+$, DMSO-MeOH) for [**C1**+H]$^+$ = 631.0456 (theoretical = 631.0462), for [**C1**+Na]$^+$ = 653.0194 (theoretical = 653.0282). **Elemental analysis** calc. for **C1** ($C_{30}H_{24}Cu_2N_4O_4$): C, 57.05; H, 3.83; N, 8.87. Found: C, 56.61; H, 3.81; N, 8.56. **FTIR-ATR** (wavenumber, cm^{-1}, **Figure A8**): 2363.09, 1610.64, 1477.82, 1458.40, 1429.20, 1401.49, 1376.22, 1353.19, 1326.39, 1281.82, 1244.19, 1217.10, 1173.53, 1145.83, 1126.54, 1026.08, 961.53, 922.74, 849.42, 793.31, 747.55, 679.15, 649.79, 620.37.

b) *Y: Cl* (Complex C2)

$Cu(OAc)_2{\cdot}2H_2O$ (6.0 mg, 0.03 mmol, 1 eq) in ACN (2 mL) was slowly added to a solution of **L2** (9 mg, 0.03 mmol, 1 eq) in ACN (5 mL) at room temperature. The same procedure as for **C1** was followed to obtain pure **C2**. Yield: 8 mg (73%). **HR-MS** (ESI^+, DMSO-MeOH) for [**C2**-H]$^+$ = 698.9670 (theoretical = 698.9683). **Elemental analysis** calc. for **C2** ($C_{30}H_{22}Cl_2Cu_2N_4O_4$): C, 51.44; H, 3.17; N, 8.00. Found: C, 51.47; H, 3.18; N, 7.66. **FTIR-ATR** (wavenumber, cm^{-1}, **Figure A18**): 1614.62, 1492.27, 1475.85, 1406.65, 1375.34, 1318.32, 1281.53, 1240.53, 1201.84, 1159.66, 1129.77, 1027.64, 988.20, 960.72, 932.29.

c) *Y: Br* (Complex C3)

$Cu(OAc)_2{\cdot}2H_2O$ (24.0 mg, 0.12 mmol, 1 eq) in ACN (3 mL) was slowly added to a solution of **L3** (40 mg, 0.12 mmol, 1 eq) in ACN:DCM (1:1, 12 mL) at room temperature. The same procedure as for **C1** was followed to obtain pure **C3**. Yield: 35 mg (74%). **HR-MS** (ESI^+, DMSO-MeOH) for [**C3**+H]$^+$ = 786.8678 (theoretical = 786.8673). **Elemental analysis** calc. for **C3** ($C_{30}H_{22}Br_2Cu_2N_4O_4$): C, 45.64; H, 2.81; N, 7.10. Found: C, 45.41; H, 2.81; N, 6.82. **FTIR-ATR** (wavenumber, cm^{-1}, **Figure A19**): 1613.76, 1492.89, 1475.85, 1454.37, 1436.29, 1408.34, 1374.91, 1317.00, 1281.65, 1241.56, 1203.98, 1159.97, 1133.05, 1070.82, 1028.23, 988.61, 961.31.

d) *Y: SO_3^-* (Complex C4)

A solution of **L4** (22 mg, 0.066 mmol, 1 eq) and AcONa (5.4 mg, 0.066 mmol, 1 eq) in MeOH (4 mL) was dropwise added to a solution of $Cu(OAc)_2{\cdot}H_2O$ (13.15 mg, 0.066 mmol, 1 eq) in MeOH (4 mL) at 0 ºC under stirring. The mixture was stirred for 24 h at room temperature. Yield: 19 mg (73%). The precipitate was filtered off and washed with MeOH (3 x 1 mL) and DCM (3 x 3 mL). **HR-MS** (ESI^+, MeOH-DMSO) for [**C4**+H]$^+$ = 792.9392 (theoretical =790.9599).

e) *Y: -CO-NH-Arg* (Complex C5)

A solution of $Cu(OAc)_2{\cdot}H_2O$ (6.6 mg, 0.033 mmol, 1.5 eq) in ACN (5 mL) was added to a solution of **L5** (10 mg, 0.022 mmol, 1 eq) in MeOH (5 mL) under stirring. The mixture was stirred for 24 h at room temperature. Solvent was removed under reduced pressure and the solid washed with ACN (4 x 5 mL). Yield: 8 mg (78%) **HR-MS** (ESI^+, MeOH) for [**C5**+H]$^+$ = 1029.2550 (theoretical =1029.2601) and for [**C5**+Na]$^+$ = 1051.2376 (theoretical =1051.2420).

f) *Y: -CO-NH-R$_9$* (Complex C6)

A solution of $Cu(OAc)_2 \cdot H_2O$ (1.1 mg, 0.0055 mmol, 1.9 eq) in ACN (5 mL) was added to a solution of **L6** (5 mg, 0.0029 mmol, 1 eq) in MeOH (5 mL) under stirring. The mixture was stirred for 24 h at room temperature. Solvent was removed under reduced pressure and the solid washed with ACN (4 x 5 mL). Yield: 4.6 mg (88%). **HR-MS** (ESI^+, H_2O-MeOH) for [**C6**+2H]$^{2+}$ = 882.4696 (theoretical = 882.4749), for [**C6**+CH_3OH+3Na]$^{3+}$ = 621.3068 (theoretical = 621.3097), for [**C6**+3H]$^{3+}$ = 588.6500 (theoretical =588.6524), for [**C6**+4H]$^{4+}$ = 441.7483 (theoretical = 441.7411).

g) *Y: -CO-NH- (Gly)$_4$-R$_9$* (Complex C7)

A solution of $Cu(OAc)_2 \cdot H_2O$ (1.1 mg, 0.0055 mmol, 2 eq) in ACN (2.5 mL) was added to a solution of **L7** (5 mg, 0.0026 mmol, 1 eq) in MeOH (2.5 mL) under stirring. The mixture was stirred for 24 h at room temperature. Solvent was removed under reduced pressure and the solid washed with ACN (4 x 5 mL). Yield: 4.8 mg (90%) **HR-MS** (ESI^+, H_2O-MeOH) for [**C7**+3H]$^{3+}$ = 664.6829 (theoretical = 664.6810), for [**C7**+CH_3OH+H+3Na]$^{4+}$ = 523.2568 (theoretical = 523.2566), for [**C7**+4H]$^{4+}$ = 498.7642 (theoretical = 498.7626), for [**C7**+CH_3OH+2H+3Na]$^{5+}$ = 418.8074 (theoretical = 418.8059), for [**C7**+5H]$^{5+}$ = 399.2147 (theoretical = 399.2115).

h) [Cu(DTPA-5Ac)]$^{n+}$ (C8)

Ligand **L8** (16.1 mg, 0.01 mmol, 1 eq) and $Cu(NO_3)_2$ (0.01 mmol, 1 eq) were dissolved in 5 mL of H_2O and NaOH was added to adjust the apparent pH ≥ 7.2. Yield: > 95 %. **MS** (ESI^+, H_2O-MeOH) for [**C8**-H+Na]$^{2+}$ = 849.5 (theoretical = 849.5), for [**C8**]$^{2+}$ = 838.5 (theoretical = 838.5), for [**C8**-H+2Na]$^{3+}$ = 574.0 (theoretical = 574.0), for [**C8**+Na]$^{3+}$ = 566.6 (theoretical = 566.6).

i) *Y:* -CO-NH-DTPA-4Ac (C9)

A solution of $Cu(OAc)_2 \cdot H_2O$ (0.6 mg, 0.003 mmol, 2.5 eq) in MeOH (5 mL) was added to a solution of **L9** (2 mg, 0.0011 mmol, 1 eq) in MeOH (5 mL) under stirring. The mixture was stirred for 24 h at room temperature. Solvent was removed under reduced pressure and the solid washed with ACN (4 x 5 mL). Yield: 1.9 mg (92%) **HR-MS** (ESI^+, DMSO-MeOH) for [**C9**]$^{2+}$ = 987.9684 (theoretical = 987.9742), for [**C9**-H+Na]$^{2+}$ = 998.9641 (theoretical = 998.9652).

References

Bibliography that have been consulted for this work is shown here.

REFERENCES

[1] “WHO | World Health Organization”, **2019**. Available at: http://www.who.int/en/ [Accessed 22 May 2019].

[2] F. Bray, J. Ferlay, I. Soerjomataram, R. L. Siegel, L. A. Torre, A. Jemal, *CA. Cancer J. Clin.* **2018**, *68*, 394–424.

[3] G. M. Cooper, *The Cell A Molecular Approach*, 2nd Edition, Sinauer Associates, **2000**.

[4] American Cancer Society. *Cancer Facts and Figures 2000,* Atlanta: American Cancer Society, **2000**.

[5] American Cancer Society. *Cancer Facts and Figures 2014*, Atlanta: American Cancer Society, **2014**.

[6] *Drug Delivery in Oncology. From Basic Research to Cancer Therapy* (Eds. F. Kratz, P. Senter, H. Steinhagen), WILEY-VCH, **2012**.

[7] D. Hanahan, R. A. Weinberg, *Cell* **2000**, *100*, 57–70.

[8] D. Hanahan, R. A. Weinberg, *Cell* **2011**, *144*, 646–674.

[9] G. Bergers, L. E. Benjamin, *Nat. Rev. Cancer* **2003**, *3*, 401–410.

[10] N. Petrovic, *J. Pharm. Pharm. Sci.* **2016**, *19*, 226–238.

[11] Y. Zhao, A. A. Adjei, *Oncologist* **2015**, *20*, 660–673.

[12] M. G. Vander Heiden, L. C. Cantley, C. B. Thompson, *Science* **2009**, *324*, 1029–1033.

[13] M. V Liberti, J. W. Locasale, *Trends Biochem. Sci.* **2016**, *41*, 211–218.

[14] O. Warburg, *Science* **1956**, *123*, 309.

[15] V. R. Fantin, J. St-Pierre, P. Leder, *Cancer Cell* **2006**, *9*, 425-434.

[16] R. Moreno-Sanchez, S. Rodriguez-Enrique, A. Marin-Hernandez, E. Saavedra, *FEBS J.* **2007**, *274*, 1393.

[17] E. J. Holmayard, *Alchemy*, Dover Publications, **1990**.

[18] V. T. DeVita, E. Chu, *Cancer Res.* **2008**, *68*, 8643–8653.

[19] C. Orvig, M. J. Abrams, *Chem. Rev.* **1999**, *99*, 2201–2204.

[20] S. P. Fricker, *Dalton Trans.* **2007**, 4903–4917.

[21] C. L. Spurr, T. R. Smith, M. Block, L. O. Jacobson, *Am. J. Med.* **1950**, *8*, 710–723.

[22] P. J. Sadler, *Adv. Inorg. Chem.* **1991**, *36*, 1–48.

[23] G. J. Higby, *Gold Bull.* **1982**, *15*, 130–140.

[24] K. H. Thompson, C. Orvig, in *Concepts and Models in Bioinorganic Chemistry* (Eds.: H.-B. Kraatz, N. Metzler-Nolte), Wiley-VCH, **2006**, pp. 25–47.

[25] B. Rosenberg, L. Van Camp, T. Krigas, *Nature* **1965**, *205*, 698–699.

[26] P. Workman, I. Collins, in *Cancer Drug Design and Discovery* (Ed.: S. Neidle), Academic Press, **2013**, p. 640.

[27] K. D. Mjos, C. Orvig, *Chem. Rev.* **2014**, *114*, 4540–4563.

[28] M. J. Hannon, *Pure Appl. Chem.* **2007**, *79*, 2242–2261.

[29] Z. Guo, P. J. Sadler, *Angew. Chemie Int. Ed.* **1999**, *38*, 1512–1531.

[30] J. S. Casas, V. Moreno, Á. Sánchez, J. L. Sánchez, J. Sordo, *Química Bioinorgánica*, Editorial Síntesis, S.A., **2002**.

[31] L. Kelland, *Nat. Rev. Cancer* **2007**, *7*, 573–584.

[32] A. Zamora, V. Rodríguez, N. Cutillas, G. S. Yellol, A. Espinosa, K. G. Samper, M. Capdevila, O. Palacios, J. Ruiz, *J. Inorg. Biochem.* **2013**, *128*, 48–56.

[33] A. Presa, R. F. Brissos, A. B. Caballero, I. Borilovic, L. Korrodi-Gregório, R. Pérez-Tomás, O. Roubeau, P. Gamez, *Angew. Chem. Int. Ed.* **2015**, *54*, 4561–4565.

[34] J. Ruiz, J. Lorenzo, C. Vicente, G. López, J. María López-de-Luzuriaga, M. Monge, F. X. Avilés, D. Bautista, V. Moreno, A. Laguna, *Inorg. Chem.* **2008**, *47*, 6990–7001.

[35] V. Brabec, O. Nováková, *Drug Resist. Updat.* **2006**, *9*, 111–122.

[36] K. G. Samper, S. C. Marker, P. Bayón, S. N. MacMillan, I. Keresztes, Ò. Palacios, J. J. Wilson, *J. Inorg. Biochem.* **2017**, *174*, 102–110.

[37] K. M. Deo, D. L. Ang, B. McGhie, A. Rajamanickam, A. Dhiman, A. Khoury, J. Holland, A. Bjelosevic, B. Pages, C. Gordon, J. R. Aldrich-Wright, *Coord. Chem. Rev.* **2018**, *375*, 148–163.

[38] T. Karasawa, M. Sibrian-Vazquez, R. M. Strongin, P. S. Steyger, *PLoS One* **2013**, *8*, e66220.

[39] K. G. Samper, C. Vicente, V. Rodríguez, S. Atrian, N. Cutillas, M. Capdevila, J. Ruiz, Ò. Palacios, *Dalton Trans.* **2012**, *41*, 300–306.

[40] R. P. Perez, *Eur. J. Cancer* **1998**, *34*, 1535–1542.

[41] K. G. Samper, V. Rodríguez, E. Ortega-Carrasco, S. Atrian, J. D. Maréchal, N. Cutillas, A. Zamora, C. de Haro, M. Capdevila, J. Ruiz, Ò. Palacios, *Biometals* **2014**, *27*, 1159–1177.

[42] J. García-Tojal, R. Gil-García, V. I. Fouz, G. Madariaga, L. Lezama, M. S. Galletero, J. Borrás, F. I. Nollmann, C. García-Girón, R. Alcaraz, M. Cavia-Saiz, P. Muñiz, Ò. Palacios, K. G. Samper, T. Rojo, *J. Inorg. Biochem.* **2018**, *180*, 69–79.

[43] M. Ohmichi, J. Hayakawa, K. Tasaka, H. Kurachi, Y. Murata, *Trends Pharmacol. Sci.* **2005**, *26*, 113–116.

[44] L. Galluzzi, L. Senovilla, I. Vitale, J. Michels, I. Martins, O. Kepp, M. Castedo, G. Kroemer, *Oncogene* **2012**, *31*, 1869–1883.

[45] Z. H. Siddik, *Oncogene* **2003**, *22*, 7265–7279.

[46] U. Ndagi, N. Mhlongo, M. E. Soliman, *Drug Des. Devel. Ther.* **2017**, *11*, 599–616.

[47] T. Lazarević, A. Rilak, Ž. D. Bugarčić, *Eur. J. Med. Chem.* **2017**, *142*, 8–31.

[48] Y. Shi, S.-A. Liu, D. J. Kerwood, J. Goodisman, J. C. Dabrowiak, *J. Inorg. Biochem.* **2012**, *107*, 6–14.

[49] D. Gibson, *Dalt. Trans.* **2016**, *45*, 12983–12991.

[50] T. C. Johnstone, J. J. Wilson, S. J. Lippard, *Inorg. Chem.* **2013**, *52*, 12234–12249.

[51] W. Zheng, Y. Zhao, Q. Luo, Y. Zhang, K. Wu, F. Wang, *Curr. Top. Med. Chem.* **2017**, *17*, 3084–3098.

[52] Y. Yu, Q. Xu, S. He, H. Xiong, Q. Zhang, W. Xu, V. Ricotta, L. Bai, Q. Zhang, Z. Yu, J. Ding, H. Xiao, D. Zhou, *Coord. Chem. Rev.* **2019**, *387*, 154–179.

[53] *Photodynamic Therapy: Basic Principles and Clinical Applications* (Eds.: B. W. Henderson, T. J. Dougherty), 1st Edition, CRC Press, **1992**.

[54] K. Morales, K. G. Samper, Q. Peña, J. Hernando, J. Lorenzo, A. Rodríguez-Diéguez, M. Capdevila, M. Figueredo, Ò. Palacios, P. Bayón, *Inorg. Chem.* **2018**, *57*, 15517–15525.

[55] W. Han Ang, P. J. Dyson, *Eur. J. Inorg. Chem.* **2006**, *20*, 4003–4018.

[56] G. Sava, G. Jaouen, E. A. Hillard, A. Bergamo, *Dalt. Trans.* **2012**, *41*, 8226.

[57] C.-T. Poon, P.-S. Chan, C. Man, F.-L. Jiang, R. N. S. Wong, N.-K. Mak, D. W. J. Kwong, S.-W. Tsao, W.-K. Wong, *J. Inorg. Biochem.* **2010**, *104*, 62–70.

[58] Z. Liu, A. Habtemariam, A. M. Pizarro, S. A. Fletcher, A. Kisova, O. Vrana, L. Salassa, P. C. A. Bruijnincx, G. J. Clarkson, V. Brabec, et al., *J. Med. Chem.* **2011**, *54*, 3011–3026.

[59] I. Ott, *Coord. Chem. Rev.* **2009**, *253*, 1670–1681.

[60] E. Z. Jahromi, A. Divsalar, A. A. Saboury, S. Khaleghizadeh, H. Mansouri-Torshizi, I. Kostova, *J. Iran. Chem. Soc.* **2016**, *13*, 967–989.

[61] A. R. Kapdi, I. J. S. Fairlamb, *Chem. Soc. Rev.* **2014**, *43*, 4751–4777.

[62] N. Muhammad, Z. Guo, *Curr. Opin. Chem. Biol.* **2014**, *19C*, 144–153.

[63] A. Bergamo, G. Sava, *Dalt. Trans.* **2007**, *13*, 1267–1272.

[64] A. Tzubery, E. Y. Tshuva, *Inorg. Chem.* **2011**, *50*, 7946–7948.

[65] O. Rackham, S. J. Nichols, P. J. Leedman, S. J. Berners-Price, A. Filipovska, *Biochem. Pharmacol.* **2007**, *74*, 992–1002.

[66] F. Darabi, H. Hadadzadeh, J. Simpson, A. Shahpiri, *New J. Chem.* **2016**, *40*, 9081–9097.

[67] Z. Liu, I. Romero-Canelón, A. Habtemariam, G. J. Clarkson, P. J. Sadler, *Organometallics* **2014**, *33*, 5324–5333.

[68] C. G. Hartinger, M. Groessl, S. M. Meier, A. Casini, P. J. Dyson, *Chem. Soc. Rev.* **2013**, *42*, 6186.

[69] C. G. Hartinger, N. Metzler-Nolte, P. J. Dyson, *Organometallics* **2012**, *31*, 5677–5685.

[70] R. E. Aird, J. Cummings, A. A. Ritchie, M. Muir, R. E. Morris, H. Chen, P. J. Sadler, D. I. Jodrell, *Br. J. Cancer* **2002**, *86*, 1652–1657.

[71] A. L. Noffke, A. Habtemariam, A. M. Pizarro, P. J. Sadler, *Chem. Commun.* **2012**, *48*, 5219.

[72] F. Schmitt, P. Govindaswamy, G. Süss-Fink, W. H. Ang, P. J. Dyson, L. Juillerat-Jeanneret, B. Therrien, *J. Med. Chem.* **2008**, *51*, 1811–1816.

[73] D. Havrylyuk, D. K. Heidary, L. Nease, S. Parkin, E. C. Glazer, *Eur. J. Inorg. Chem.* **2017**, *2017*, 1842–1842.

[74] H. Chan, J. B. Ghrayche, J. Wei, A. K. Renfrew, *Eur. J. Inorg. Chem.* **2017**, *2017*, 1538–1538.

[75] E. Y. Tshuva, M. Miller, in *Metallo-Drugs: Development and Action of Anticancer Agents* (Eds.: A. Sigel, H. Sigel, E. Freisinger, R.K.O. Sigel), De Gruyter GmbH, **2018**, pp. 219–250.

[76] A. Casini, R. W.-Y. Sun, I. Ott, in *Met. Dev. Action Anticancer Agents* (Eds.: A. Sigel, H. Sigel, E. Freisinger, R.K.O. Sigel), De Gruyter GmbH, **2018**, pp. 199–218.

[77] Z. Liu, P. J. Sadler, *Acc. Chem. Res.* **2014**, *47*, 1174–1185.

[78] M. E. Sears, *The Scientific World Journal.* **2013**, *2013*, 219840–219853.

[79] K. Suntharalingam, D. J. Hunt, A. A. Duarte, A. J. P. White, D. J. Mann, R. Vilar, *Chemistry* **2012**, *18*, 15133–15141.

[80] C. Marzano, M. Pellei, F. Tisato, C. Santini, *Anticancer. Agents Med. Chem.* **2009**, *9*, 185–211.

[81] C. Santini, M. Pellei, V. Gandin, M. Porchia, F. Tisato, C. Marzano, *Chem. Rev.* **2014**, *114*, 815–862.

[82] A. R. Chakravarty, P. A. N. Anreddy, B. K. Santra, A. M. Thomas, *Proc. Indian Acad. Sci. - Chem. Sci.* **2002**, *114*, 391–401.

[83] R. F. Brissos, E. Torrents, F. M. dos Santos Mello, W. Carvalho Pires, E. de P. Silveira-Lacerda, A. B. Caballero, A. Caubet, C. Massera, O. Roubeau, S. J. Teat, P. Gamez, *Metallomics* **2014**, *6*, 1853–1868.

[84] R. Tabti, N. Tounsi, C. Gaiddon, E. Bentouhami, L. Desaubry, *Med. Chem. (Los Angeles)* **2017**, *7*, 875-879.

[85] W. A. Wani, U. Baig, S. Shreaz, R. A. Shiekh, P. F. Iqbal, E. Jameel, A. Ahmad, S. H. Mohd-Setapar, M. Mushtaque, L. Ting Hun, *New J. Chem.* **2016**, *40*, 1063–1090.

[86] L. Xie, Z. Luo, Z. Zhao, T. Chen, *J. Med. Chem.* **2017**, *60*, 202–214.

[87] S. Saha, R. Majumdar, A. Hussain, R. R. Dighe, A. R. Chakravarty, *Philos. Trans. R. Soc. A Math. Phys. Eng. Sci.* **2013**, *371*, 20120190.

[88] T. Sarkar, A. Hussain, *Enzym. Eng.* **2016**, *5*, 143.

[89] P. Köpf-Maier, H. Köpf, E. W. Neuse, *J. Cancer Res. Clin. Oncol.* **1984**, *108*, 336–340.

[90] R. P. Hong Enriquez, T. N. Do, *Life (Basel)* **2012**, *2*, 274–285.

[91] J. J. R. Fraústo da Silva, R. J. P. Williams, *The Biological Chemistry of the Elements: The Inorganic Chemistry of Life*, Oxford University Press, **2001**.

[92] *Concepts and Models in Bioinorganic Chemistry* (Eds.: H.-B. Kraatz, N. Metzler-Nolte), Wiley-VCH, **2006**.

[93] S. J. Lippard, J. M. Berg, *Principles of Bioinorganic Chemistry*, University Science Books, University Science Books, **1994**.

[94] P. Atkins, T. Overton, J. Rourke, M. Weller, F. Armstrong, *Shriver and Atkins' Inorganic Chemistry*, Oxford University Press, **2009**.

[95] R. R. Crichton, *Biological Inorganic Chemistry. An Introduction*, Elsevier, **2012**.

[96] M. Vallet, J. Faus, E. García-España, J. Moratal, *Introducción a La Química*

Bioinorgánica, Editorial Síntesis, S.A., **2003**.
[97] S. Larsson, B. Källebring, P. Wittung, B. G. Malmström, *Proc. Natl. Acad. Sci. U. S. A.* **1995**, *92*, 7167–7171.
[98] D. Strausak, J. F. Mercer, H. H. Dieter, W. Stremmel, G. Multhaup, *Brain Res. Bull.* **2001**, *55*, 175–185.
[99] T. B. Bartnikas, J. D. Gitlin, *Nat. Struct. Biol.* **2001**, *8*, 733–734.
[100] B. R. McAuslan, W. Reilly, *Exp. Cell Res.* **1980**, *130*, 147–157.
[101] G. Hu, *J. Cell. Biochem.* **1998**, *69*, 326–335.
[102] J. Folkman, *Ann. Surg.* **1972**, *175*, 409–416.
[103] V. L. Goodman, G. J. Brewer, S. D. Merajver, *Endocr. Relat. Cancer* **2004**, *11*, 255–263.
[104] B. M. Paterson, P. S. Donnelly, *Chem. Soc. Rev.* **2011**, *40*, 3005.
[105] V. Antoniades, A. Sioga, E. M. Dietrich, S. Meditskou, L. Ekonomou, K. Antoniades, *Med. Hypotheses* **2013**, *81*, 1159–1163.
[106] D. Denoyer, S. A. S. Clatworthy, M. A. Cater, in *Metallo-Drugs: Development and Action of Anticancer Agents* (Eds.: A. Sigel, H. Sigel, E. Freisinger, R.K.O. Sigel), De Gruyter GmbH, **2018**, pp. 469–506.
[107] R. F. Brissos, A. Caubet, P. Gamez, *Eur. J. Inorg. Chem.* **2015**, *2015*, 2633–2645.
[108] F. E. para la C. y la Tecnología, “Web of Science”. Available at: http://webofknowledge.com, **2019**. [Accessed: 25 May 2019]
[109] K. Laws, G. Bineva-Todd, A. Eskandari, C. Lu, N. O’Reilly, K. Suntharalingam, *Angew. Chemie Int. Ed.* **2018**, *57*, 287–291.
[110] S. M. G. Leite, L. M. P. Lima, S. Gama, F. Mendes, M. Orio, I. Bento, A. Paulo, R. Delgado, O. Iranzo, *Inorg. Chem.* **2016**, *55*, 11801–11814.
[111] Z. Molphy, A. Prisecaru, C. Slator, N. Barron, M. McCann, J. Colleran, D. Chandran, N. Gathergood, A. Kellett, *Inorg. Chem.* **2014**, *53*, 5392–5404.
[112] C. H. Ng, S. M. Kong, Y. L. Tiong, M. J. Maah, N. Sukram, M. Ahmad, A. S. B. Khoo, *Metallomics* **2014**, *6*, 892–906.
[113] Q. Peña, J. Lorenzo, G. Sciortino, S. Rodríguez-Calado, J.-D. Maréchal, P. Bayón, A. J. Simaan, O. Iranzo, M. Capdevila, Ò. Palacios, *J. Inorg. Biochem.* **2019**, *195*, 51–60.
[114] J. Deng, P. Yu, Z. Zhang, J. Wang, J. Cai, N. Wu, H. Sun, H. Liang, F. Yang, *Eur. J. Med. Chem.* **2018**, *158*, 442–452.
[115] K. Ohui, E. Afanasenko, F. Bacher, R. L. X. Ting, A. Zafar, N. Blanco-Cabra, E. Torrents, O. Dömötör, N. V. May, D. Darvasiova, Éva A. Enyedy, A. Popović-Bijelić, J. Reynisson, P. Rapta, M. V. Babak, G. Pastorin, V. B. Arion, *J. Med. Chem.* **2019**, *62*, 512–530.
[116] J. M. Veal, R. L. Rill, *Biochemistry* **1991**, *30*, 1132–1140.
[117] F. Tisato, M. Porchia, C. Santini, V. Gandin, C. Marzano, in *Copper(I) Chem. Phosphines, Funct. Phosphines Phosphorus Heterocycles* (Ed.: M. Balakrishna) **2019**, pp. 61–82.
[118] M. P. Cervantes-Cervantes, J. V. Calderón-Salinas, A. Albores, J. L. Muñoz-Sánchez, *Biol. Trace Elem. Res.* **2005**, *103*, 229–248.
[119] J. C. García-Ramos, Y. Toledano-Magaña, L. G. Talavera-Contreras, M. Flores-Álamo, V. Ramírez-Delgado, E. Morales-León, L. Ortiz-Frade, A. G. Gutiérrez, A. Vázquez-Aguirre, C. Mejía, J. C. Carrero, J. P. Laclette, R. Moreno-Esparza, L. Ruiz-Azuara, *Dalton Trans.* **2012**, *41*, 10164–10174.
[120] S. Dhar, D. Senapati, P. A. N. Reddy, P. K. Das, A. R. Chakravarty, *Chem. Commun.* **2003**, *19*, 2452.
[121] P. U. Maheswari, S. Roy, H. den Dulk, S. Barends, G. van Wezel, B. Kozlevcar, P. Gamez, J. Reedijk, *J. Am. Chem. Soc.* **2006**, *128*, 710–711.
[122] K. C. Park, L. Fouani, P. J. Jansson, D. Wooi, S. Sahni, D. J. R. Lane, D. Palanimuthu, H. C. Lok, Z. Kovačević, M. L. H. Huang, D. S. Kalinowski, D. R. Richardson, *Metallomics* **2016**, *8*, 874–886.
[123] D. İnci, R. Aydın, Ö. Vatan, D. Yılmaz, H. M. Gençkal, Y. Zorlu, T. Cavaş,

Spectrochim. Acta. A. Mol. Biomol. Spectrosc. **2015**, *145*, 313–324.
[124] D. Hedley, A. Shamas-Din, S. Chow, D. Sanfelice, A. C. Schuh, J. M. Brandwein, M. D. Seftel, V. Gupta, K. W. L. Yee, A. D. Schimmer, *Leuk. Lymphoma* **2016**, *57*, 2437–2440.
[125] L. Ruiz-Azuara, G. Bastian, M. E. Bravo-Gómez, R. C. Cañas, M. Flores-Alamo, I. Fuentes, C. Mejia, J. C. García-Ramos, A. Serrano. *Phase I study of one mixed chelates copper(II) compound, Casiopeína CasIIIia with antitumor activity and its mechanism of action*, in Proceedings of the 105th Annual Meeting of the American Association For Cancer Research, **2014**, Abstract nr. CT408.
[126] B. B. Hasinoff, X. Wu, A. A. Yadav, D. Patel, H. Zhang, D.-S. Wang, Z.-S. Chen, J. C. Yalowich, *Biochem. Pharmacol.* **2015**, *93*, 266–276.
[127] B. B. Hasinoff, A. A. Yadav, D. Patel, X. Wu, *J. Inorg. Biochem.* **2014**, *137*, 22–30.
[128] R. K. Blackman, K. Cheung-Ong, M. Gebbia, D. A. Proia, S. He, J. Kepros, A. Jonneaux, P. Marchetti, J. Kluza, P. E. Rao, Y. Wada, G. Giaever, C. Nislow, *PLoS One* **2012**, *7*, e29798.
[129] J. R. Kirshner, S. He, V. Balasubramanyam, J. Kepros, C.-Y. Yang, M. Zhang, Z. Du, J. Barsoum, J. Bertin, *Mol. Cancer Ther.* **2008**, *7*, 2319–2327.
[130] S. Garattini, *Eur. J. Cancer* **2007**, *43*, 271–282.
[131] B. Meibohm, H. Derendorf, *Int. J. Clin. Pharmacol. Ther.* **1997**, *35*, 401–413.
[132] J. E. Davies, *Occup. Environ. Med.* **2007**, *64*, e2.
[133] D. R. Lu, S. Øie, *Cellular Drug Delivery : Principles and Practice*, Humana Press, **2004**.
[134] K. Nurgali, R. T. Jagoe, R. Abalo, *Front. Pharmacol.* **2018**, *9*, 245.
[135] M. W. Tibbitt, J. E. Dahlman, R. Langer, *J. Am. Chem. Soc.* **2016**, *138*, 704–717.
[136] T. Peters, *Adv. Protein Chem.* **1985**, *37*, 161–245.
[137] D. C. Carter, J. X. Ho, *Adv. Protein Chem.* **1994**, *45*, 153–203.
[138] U. Testa, E. Pelosi, C. Peschle, *Crit. Rev. Oncog.* **1993**, *4*, 241–276.
[139] A. Sułkowska, *J. Mol. Struct.* **2002**, *614*, 227–232.
[140] K. Yamasaki, V. T. G. Chuang, T. Maruyama, M. Otagiri, *Biochim. Biophys. Acta - Gen. Subj.* **2013**, *1830*, 5435–5443.
[141] R. R. Wakaskar, *Int. J. Drug Dev. Res.* **2017**, *9*, 37–41.
[142] R. A. Firestone, *Bioconjug. Chem.* **1994**, *5*, 105–113.
[143] F. Kratz, *J. Control. Release* **2008**, *132*, 171–183.
[144] Y. Matsumura, H. Maeda, *Cancer Res.* **1986**, *46*, 6387–6392.
[145] A. Warnecke, in *Drug Delivery in Oncology: From Basic Research to Cancer Therapy* (Eds.: F. Kratz, P. Senter, H. Steinhagen), WILEY-VCH, **2012**, pp. 747–803.
[146] H. Maeda, in *Drug Delivery in Oncology: From Basic Research to Cancer Therapy* (Eds.: F. Kratz, P. Senter, H. Steinhagen), WILEY-VCH, **2012**, pp. 65–84.
[147] J. K. Vasir, V. Labhasetwar, *Technol. Cancer Res. Treat.* **2005**, *4*, 363–374.
[148] H. Maeda, J. Wu, T. Sawa, Y. Matsumura, K. Hori, *J. Control Release* **2000**, *65*, 271–284.
[149] F. M. Muggia, *Clin. Cancer Res.* **1999**, *5*, 7–8.
[150] G. Gregoriadis, *Trends Biotechnol.* **1995**, *13*, 527–537.
[151] P. E. Thorpe, *Clin. Cancer Res.* **2004**, *10*, 415–427.
[152] W. Arap, R. Pasqualini, E. Ruoslahti, *Science* **1998**, *279*, 377–380.
[153] W. Arap, R. Pasqualini, E. Ruoslahti, *Curr. Opin. Oncol.* **1998**, *10*, 560–565.
[154] J.-Y. Zhang, K. S. Looi, E. M. Tan, *Methods Mol. Biol.* **2009**, *520*, 1–10.
[155] J. Sudimack, R. J. Lee, *Adv. Drug Deliv. Rev.* **2000**, *41*, 147–162.
[156] N. S. Chung, K. M. Wasan, *Adv. Drug Deliv. Rev.* **2004**, *56*, 1315–1334.
[157] Y. H. Yun, B. K. Lee, K. Park, *J. Control. Release* **2015**, *219*, 2–7.
[158] G. Tiwari, R. Tiwari, B. Sriwastawa, L. Bhati, S. Pandey, P. Pandey, S. K. Bannerjee, *Int. J. Pharm. Investig.* **2012**, *2*, 2–11.
[159] Z.-R. Lu, P. Qiao, *Mol. Pharm.* **2018**, *15*, 3603–3616.

[160] T. M. Allen, P. R. Cullis, *Adv. Drug Deliv. Rev.* **2013**, *65*, 36–48.

[161] A. Samad, Y. Sultana, M. Aqil, *Curr. Drug Deliv.* **2007**, *4*, 297–305.

[162] S. Tran, P.-J. DeGiovanni, B. Piel, P. Rai, *Clin. Transl. Med.* **2017**, *6*, 44.

[163] Y. Zhou, J. Kopeček, *J. Drug Target.* **2013**, *21*, 1–26.

[164] H. Kobayashi, B. Turkbey, R. Watanabe, P. L. Choyke, *Bioconjug. Chem.* **2014**, *25*, 2093–2100.

[165] G. Guidotti, L. Brambilla, D. Rossi, *Trends Pharmacol. Sci.* **2017**, *38*, 406–424.

[166] T. M. Allen, P. R. Cullis, *Science* **2004**, *303*, 1818–1822.

[167] O. C. Farokhzad, R. Langer, *ACS Nano* **2009**, *3*, 16–20.

[168] R. Langer, *Nature* **1998**, *392*, 5–10.

[169] W. M. Saltzman, W. L. Olbricht, *Nat. Rev. Drug Discov.* **2002**, *1*, 177–186.

[170] D. A. LaVan, T. McGuire, R. Langer, *Nat. Biotechnol.* **2003**, *21*, 1184–1191.

[171] Z. Zhu, D. J. Hicklin, in *Cellular Drug Delivery*, Humana Press, **2004**, pp. 311–344.

[172] T. Ghose, S. T. Norvell, A. Guclu, D. Cameron, A. Bodurtha, A. S. MacDonald, *BMJ* **1972**, *3*, 495–499.

[173] D. A. Davies, G. J. O'Neill, *Br. J. Cancer. Suppl.* **1973**, *1*, 285–298.

[174] U. Bulbake, S. Doppalapudi, N. Kommineni, W. Khan, *Pharmaceutics* **2017**, *9*, 12.

[175] M. Cagel, F. C. Tesan, E. Bernabeu, M. J. Salgueiro, M. B. Zubillaga, M. A. Moretton, D. A. Chiappetta, *Eur. J. Pharm. Biopharm.* **2017**, *113*, 211–228.

[176] H. Ringsdorf, *J. Polym. Sci. Polym. Symp.* **2007**, *51*, 135–153.

[177] S. Nazir, T. Hussain, A. Ayub, U. Rashid, A. J. MacRobert, *Nanomedicine Nanotechnology, Biol. Med.* **2014**, *10*, 19–34.

[178] S. K. Libutti, G. F. Paciotti, A. A. Byrnes, H. R. Alexander, W. E. Gannon, M. Walker, G. D. Seidel, N. Yuldasheva, L. Tamarkin, L. Tamarkin, *Clin. Cancer Res.* **2010**, *16*, 6139–6149.

[179] K. Madaan, S. Kumar, N. Poonia, V. Lather, D. Pandita, *J. Pharm. Bioallied Sci.* **2014**, *6*, 139–150.

[180] N. K. Jain, A. Asthana, *Expert Opin. Drug Deliv.* **2007**, *4*, 495–512.

[181] N. D. James, R. J. Coker, D. Tomlinson, J. R. Harris, M. Gompels, A. J. Pinching, J. S. Stewart, *Clin. Oncol. (R. Coll. Radiol).* **1994**, *6*, 294–296.

[182] J. W. Valle, A. Armstrong, C. Newman, V. Alakhov, G. Pietrzynski, J. Brewer, S. Campbell, P. Corrie, E. K. Rowinsky, M. Ranson, *Invest. New Drugs* **2011**, *29*, 1029–1037.

[183] M. Wadleigh, P. G. Richardson, D. Zahrieh, S. J. Lee, C. Cutler, V. Ho, E. P. Alyea, J. H. Antin, R. M. Stone, R. J. Soiffer, et al., *Blood* **2003**, *102*, 1578–1582.

[184] Q. Hu, W. Sun, C. Wang, Z. Gu, *Adv. Drug Deliv. Rev.* **2016**, *98*, 19–34.

[185] H. Pelicano, D. Carney, P. Huang, *Drug Resist. Updat.* **2004**, *7*, 97–110.

[186] S. M. El Sayed, A. A. Mahmoud, S. A. El Sawy, E. A. Abdelaal, A. M. Fouad, R. S. Yousif, M. S. Hashim, S. B. Hemdan, Z. M. Kadry, M. A. Abdelmoaty, A. G. Gabr, F. M. Omran, M. M. Nabo, N. S. Ahmed, *Med. Hypotheses* **2013**, *81*, 866–870.

[187] C. Santini, M. Pellei, G. Papini, B. Morresi, R. Galassi, S. Ricci, F. Tisato, M. Porchia, M. P. Rigobello, V. Gandin, et al., *J. Inorg. Biochem.* **2011**, *105*, 232–240.

[188] P. T. Schumacker, *Cancer Cell* **2006**, *10*, 175–176.

[189] S. Misra, M. Boylan, A. Selvam, J. Spallholz, M. Björnstedt, S. Misra, M. Boylan, A. Selvam, J. E. Spallholz, M. Björnstedt, *Nutrients* **2015**, *7*, 3536–3556.

[190] V. C. da Silveira, J. S. Luz, C. C. Oliveira, I. Graziani, M. R. Ciriolo, A. M. da Costa Ferreira, *J. Inorg. Biochem.* **2008**, *102*, 1090–1103.

[191] D. L. J. Broere, R. Plessius, J. I. van der Vlugt, *Chem. Soc. Rev.* **2015**, *44*, 6886–6915.

[192] Z. Shirin, J. Thompson, L. Liable-Sands, G. P. A. Yap, A. L. Rheingold, A. S. Borovik, *J. Chem. Soc. Dalt. Trans.* **2002**, 1714–1720.

[193] E. Garribba, G. Micera, *J. Chem. Educ.* **2006**, *83*, 1229.

[194] B. W. E. Peisach J., *Arch. Biochem. Biophys* **1974**, *165*, 691–708.

[195] M. Abdolahad, H. Taghinejad, A. Saeidi, M. Taghinejad, M. Janmaleki, S. Mohajerzadeh, *RSC Adv.* **2014**, *4*, 7425.

[196] N. N. Greenwood, A. Earnshaw, *Chemistry of the Elements*, Butterworth-Heinemann, **1997**.

[197] K. P. Butin, E. K. Beloglazkina, N. V Zyk, *Russ. Chem. Rev.* **2005**, *74*, 531–553.

[198] M. D. Ward, J. A. McCleverty, *J. Chem. Soc. Dalt. Trans.* **2002**, 275–288.

[199] A. J. Bard, L. R. Faulkner, *Electrochemical Methods : Fundamentals and Applications*, WILEY, **2001**.

[200] W. R. Hagen, *Biomolecular EPR Spectroscopy*, CRC Press, Taylor& Francis Group, **2009**.

[201] H. R. López-Mirabal, J. R. Winther, *Biochim. Biophys. Acta* **2008**, *1783*, 629–640.

[202] H. Østergaard, C. Tachibana, J. R. Winther, *J. Cell Biol.* **2004**, *166*, 337–345.

[203] M. C. Elvington and K. J. Brewer in *Applications of Physical Methods to Inorganic and Bioinorganic Chemistry* (Eds.: R. A. Scott, C. M. Lukehart), Wiley, **2007**, pp. 17–38.

[204] D. Voet, J. Voet, C. Pratt, *Fundamentals of Biochemistry*, WILEY, **2013**.

[205] W. Gołebiewski, M. Gucma, *Synthesis (Stuttg).* **2007**, *2007*, 3599–3619.

[206] *Comprehensive Organic Transformations : A Guide to Functional Group Preparations* (Ed.: R. C. Larock), WILEY, **2018**.

[207] T. Mahajan, L. Kumar, K. Dwivedi, D. D. Agarwal, *Ind. Eng. Chem. Res.* **2012**, *51*, 3881–3886.

[208] J. Clayden, N. Greeves, S. Warren, *Organic Chemistry*, Oxford University Press, 2n Edition, **2012**.

[209] B. Halliwell, J. M. Gutteridge, *Methods Enzymol.* **1990**, *186*, 1–85.

[210] A. E. Vickers, T. C. Sloop, G. W. Lucier, *Environ. Health Perspect.* **1985**, *59*, 121.

[211] W. F. Greenlee, R. Osborne, K. M. Dold, L. G. Hudsont, W. A. Toscano, *Environ. Health Perspect.* **1985**, *60*, 69-76.

[212] L. S. Birnbaum, *Environ. Health Perspect.* **1994**, *102 Suppl 9*, 157–67.

[213] J. Grau, C. Renau, A. B. Caballero, A. Caubet, M. Pockaj, J. Lorenzo, P. Gamez, *Dalt. Trans.* **2018**, *47*, 4902–4908.

[214] P. U. Maheswari, M. van der Ster, S. Smulders, S. Barends, G. P. van Wezel, C. Massera, S. Roy, H. den Dulk, P. Gamez, J. Reedijk, *Inorg. Chem.* **2008**, *47*, 3719–3727.

[215] M. Vorlíčková, I. Kejnovská, K. Bednářová, D. Renčiuk, J. Kypr, *Chirality* **2012**, *24*, 691–698.

[216] G. R. Bishop, J. B. Chaires, in *Current Protocols in Nucleic Acid Chemistry*, WILEY, **2002**, p. 7.11.1-7.11.8.

[217] M. Sirajuddin, S. Ali, A. Badshah, *J. Photochem. Photobiol. B.* **2013**, *124*, 1–19.

[218] T. Pivetta, F. Isaia, G. Verani, C. Cannas, L. Serra, C. Castellano, F. Demartin, F. Pilla, M. Manca, A. Pani, *J. Inorg. Biochem.* **2012**, *114*, 28–37.

[219] V. Rajendiran, R. Karthik, M. Palaniandavar, H. Stoeckli-Evans, V. S. Periasamy, M. A. Akbarsha, B. S. Srinag, H. Krishnamurthy, *Inorg. Chem.* **2007**, *46*, 8208–8221.

[220] P. C. A. Bruijnincx, P. J. Sadler, *Curr. Opin. Chem. Biol.* **2008**, *12*, 197–206.

[221] H. A. Benesi, J. H. Hildebrand, *J. Am. Chem. Soc.* **1949**, 2703–2707.

[222] A. K. Williams, S. C. Dasilva, A. Bhatta, B. Rawal, M. Liu, E. A. Korobkova, *Anal. Biochem.* **2012**, *422*, 66–73.

[223] N. P. Bazhulina, A. M. Nikitin, S. A. Rodin, A. N. Surovaya, Y. V Kravatsky, V. F. Pismensky, V. S. Archipova, R. Martin, G. V Gursky, *J. Biomol. Struct. Dyn.* **2009**, *26*, 701–718.

[224] A. Bhattacharyya, A. Dixit, S. Banerjee, B. Roy, A. Kumar, A. A. Karande, A. R. Chakravarty, *RSC Adv.* **2016**, *6*, 104474–104482.

[225] D. V. Krysko, T. Vanden Berghe, K. D'Herde, P. Vandenabeele, *Methods* **2008**, *44*, 205–221.

[226] S. L. Fink, B. T. Cookson, *Infect. Immun.* **2005**, *73*, 1907–1916.

[227] V. M. Gonzalez, M. A. Fuertes, C. Alonso, J. M. Perez, C. Dive, *Mol. Pharmacol.* **2001**, *59*, 657–663.

[228] M. G. Ormerod, C. F. O'Neill, D. Robertson, K. R. Harrap, *Exp. Cell Res.* **1994**, *211*, 231–237.

[229] Y. Liu, H. Xing, X. Han, X. Shi, F. Liang, G. Cheng, Y. Lu, D. Ma, *J. Huazhong Univ. Sci. Technol. Medical Sci.* **2008**, *28*, 197–199.

[230] A. Coates, S. Abraham, S. B. Kaye, T. Sowerbutts, C. Frewin, R. M. Fox, M. H. N. Tattersall, *Eur. J. Cancer Clin. Oncol.* **1983**, *19*, 203–208.

[231] A. Pearce, M. Haas, R. Viney, S.-A. Pearson, P. Haywood, C. Brown, R. Ward, *PLoS One* **2017**, *12*, e0184360.

[232] R. Z. Lockart, H. Eagle, *Science* **1959**, *129*, 252–254.

[233] R. Dulbecco, G. Freeman, *Virology* **1959**, *8*, 396–397.

[234] L. Casella, M. Gullotti, *J. Inorg. Biochem.* **1983**, *18*, 19–31.

[235] H. Sigel, D. B. McCormick, *J. Am. Chem. Soc.* **1971**, *93*, 2041–2044.

[236] X. Liu, C. N. Kim, J. Yang, R. Jemmerson, X. Wang, *Cell* **1996**, *86*, 147–157.

[237] S. Orrenius, B. Zhivotovsky, *Nat. Chem. Biol.* **2005**, *1*, 188–189.

[238] W. Bal, M. Sokołowska, E. Kurowska, P. Faller, *Biochim. Biophys. Acta - Gen. Subj.* **2013**, *1830*, 5444–5455.

[239] C. Harford, B. Sarkar, *Acc. Chem. Res.* **1997**, 30, 123-130.

[240] Y. Matsumura, H. Maeda, *Cancer Res.* **1986**, *46*, 6387–6392.

[241] A. S.-Y. Law, M. C.-L. Yeung, V. W.-W. Yam, *ACS Appl. Mater. Interfaces* **2017**, *9*, 41143–41150.

[242] N. Schmidt, A. Mishra, G. H. Lai, G. C. L. Wong, *FEBS Lett.* **2010**, *584*, 1806–1813.

[243] G. W. Kirker, *Org. Prep. Proced. Int.* **1980**, *12*, 246–249.

[244] E. Rossini, A. D. Bochevarov, E. W. Knapp, *ACS Omega* **2018**, *3*, 1653–1662.

[245] W. C. Chan, P. D. White, *Fmoc Solid Phase Peptide Synthesis : A Practical Approach*, Oxford University Press, **2000**.

[246] R. B. Merrifield, *Science* **1965**, *150*, 178–185.

[247] "The Nobel Prize in Chemistry 1984 - NobelPrize.org". Available at: https://www.nobelprize.org/. [Accessed 15 August 2019]

[248] I. Abeldemonty, F. Albericio, L. Carpino, D. Foxman, S. Kates, *Lett. Pept. Sci.* **1994**, *1*, 57–67.

[249] W. Dixon, D. Murphy, *J. Chem. Soc. Faraday Trans. 2* **1976**, *72*, 1221–1230.

[250] P. G. M. Wuts, T. W. Greene, *Greene's Protective Groups in Organic Synthesis*, WILEY, **2006**.

[251] C. G. Swain, A. L. Powell, T. J. Lynch, S. R. Alpha, R. P. Dunlap, *J. Am. Chem. Soc.* **1979**, *101*, 3584–3587.

[252] P. Rajkumar, B. S. Mathew, S. Das, R. Isaiah, S. John, R. Prabha, D. H. Fleming, *J. Clin. Diagn. Res.* **2016**, *10*, XC01- XC04.

[253] H. Eichholtz-Wirth, B. Hietel, *Br. J. Cancer* **1986**, *54*, 239–243.

[254] *Cellular Drug Delivery : Principles and Practice* (Eds.: D. R. Lu, S. Øie), 2n Edition, Humana Press, **2010**.

[255] S. Tran, P.-J. DeGiovanni, B. Piel, P. Rai, *Clin. Transl. Med.* **2017**, *6*, 44.

[256] Z. Guo, H. Peng, J. Kang, D. Sun, *Biomed. reports* **2016**, *4*, 528–534.

[257] A. Borrelli, A. Tornesello, M. Tornesello, F. Buonaguro, *Molecules* **2018**, *23*, 295.

[258] J. R. Marks, J. Placone, K. Hristova, W. C. Wimley, *J. Am. Chem. Soc.* **2011**, *133*, 8995–9004.

[259] F. Milletti, *Drug Discov. Today* **2012**, *17*, 850–860.

[260] D. Raucher, J. S. Ryu, *Trends Mol. Med.* **2015**, *21*, 560–570.

[261] M. Green, P. M. Loewenstein, *Cell* **1988**, *55*, 1179–1188.

[262] A. D. Frankel, C. O. Pabo, *Cell* **1988**, *55*, 1189–1193.

[263] E. Vivès, P. Brodin, B. Lebleu, *J. Biol. Chem.* **1997**, *272*, 16010–16017.

[264] S. Y. Choi, E. Y. Choi, K. Han, J. Park, K.-A. Kim, J. H. Bahn, H. Y. Kwon, H. J.

Lee, J. Ryu, K. S. Lee, *J. Gen. Virol.* **2002**, *83*, 1173–1181.
[265] J. B. Rothbard, T. C. Jessop, R. S. Lewis, B. A. Murray, P. A. Wender, *J. Am. Chem. Soc.* **2004**, *126*, 9506–9507.
[266] J. Vellinga, M. J. W. E. Rabelink, S. J. Cramer, D. J. M. van den Wollenberg, H. Van der Meulen, K. N. Leppard, F. J. Fallaux, R. C. Hoeben, *J. Virol.* **2004**, *78*, 3470–3479.
[267] E. Pretsch, P. Bühlmann, M. Badertscher, in *Structure Determination of Organic Compounds*, Springer, **2009**, pp. 1–86.
[268] I. André, S. Linse, F. A. A. Mulder, *J. Am. Chem. Soc.* **2007**, 129, 15805-15813.
[269] G. Tünnemann, G. Ter-Avetisyan, R. M. Martin, M. Stöckl, A. Herrmann, M. C. Cardoso, *J. Pept. Sci.* **2008**, *14*, 469–476.
[270] P. A. Wender, D. J. Mitchell, K. Pattabiraman, E. T. Pelkey, L. Steinman, J. B. Rothbard, *Proc. Natl. Acad. Sci.* **2000**, *97*, 13003–13008.
[271] X. Chen, J. L. Zaro, W.-C. Shen, *Adv. Drug Deliv. Rev.* **2013**, *65*, 1357–1369.
[272] M. van Rosmalen, M. Krom, M. Merkx, *Biochemistry* **2017**, *56*, 6565–6574.
[273] G. Tesei, M. Vazdar, M. R. Jensen, C. Cragnell, P. E. Mason, J. Heyda, M. Skepö, P. Jungwirth, M. Lund, *Proc. Natl. Acad. Sci. U. S. A.* **2017**, *114*, 11428–11433.
[274] R. Brock, *Bioconjug. Chem.* **2014**, *25*, 863–868.
[275] K. Madaan, S. Kumar, N. Poonia, V. Lather, D. Pandita, *J. Pharm. Bioallied Sci.* **2014**, *6*, 139–150.
[276] D. Soto-Castro, J. Cruz-Morales, M. Ramirez Apan, P. Guadarrama, *Bioorg Chem* **2012**, *41*, 13–21.
[277] D. Patton, Y. Cosgrove Sweeney, T. McCarthy, S. Hilier, *Antimicrob Agents Chemother* **2006**, *50*, 1696–1700.
[278] A. Chauhan, *Molecules* **2018**, *23*, 938.
[279] L. Palmerston Mendes, J. Pan, V. P. Torchilin, *Molecules* **2017**, *22*, 1401.
[280] R. Duncan, L. Izzo, *Adv Drug Deliv Rev* **2005**, *57*, 2215–2237.
[281] U. Gupta, O. Perumal, *Nat. Synth. Biomed. Polym.* **2014**, 243–257.
[282] S. Svenson, D. Tomalia, *Adv. Drug Deliv. Rev.* **2005**, *57*, 2106–2129.
[283] A. Kesavan, P. Ilaiyaraja, W. Sofi Beaula, V. Veena Kumari, J. Sugin Lal, C. Arunkumar, G. Anjana, S. Srinivas, A. Ramesh, S. K. Rayala, D. Ponraju, G. Venkatraman, *Eur. J. Pharm. Biopharm.* **2015**, *96*, 255–263.
[284] S. P. Kuruvilla, G. Tiruchinapally, A. C. Crouch, M. E. H. El Sayed, J. M. Greve, *PLoS One* **2017**, *12*, e0181944.
[285] T. U. Ly, N. Q. Tran, T. K. D. Hoang, K. N. Phan, H. N. Truong, C. K. Nguyen, *J. Biomed. Nanotechnol.* **2013**, *9*, 213–220.
[286] S. Zhu, M. Hong, L. Zhang, G. Tang, Y. Jiang, Y. Pei, *Pharm. Res.* **2010**, *27*, 161–174.
[287] L. M. Kaminskas, V. M. McLeod, B. D. Kelly, G. Sberna, B. J. Boyd, M. Williamson, D. J. Owen, C. J. H. Porter, *Nanomedicine Nanotechnology, Biol. Med.* **2012**, *8*, 103–111.
[288] P. Kesharwani, A. K. Iyer, *Drug Discov. Today* **2015**, *20*, 536–547.
[289] D. Pulido, F. Albericio, M. Royo, *Org. Lett.* **2014**, *16*, 1318–1321.
[290] M. A. Brown, A. Paulenova, A. V. Gelis, *Inorg. Chem.* **2012**, *51*, 7741–7748.
[291] C. Hershko, *J. Lab. Clin. Med.* **1975**, *85*, 913–921.
[292] A. Eivazihollagh, J. Bäckström, M. Norgren, H. Edlund, *J. Chem. Technol. Biotechnol.* **2018**, *93*, 1421–1431.
[293] A. Safavy, D. C. Smith,Jr., A. Bazooband, D. J. Buchsbaum, *Bioconjug. Chemistry* **2002**, *13,* 317-326.
[294] J. Lim, B. Turkbey, M. Bernardo, L. H. Bryant, M. Garzoni, G. M. Pavan, T. Nakajima, P. L. Choyke, E. E. Simanek, H. Kobayashi, *Bioconjug. Chem.* **2012**, *23*, 2291–2299.
[295] E. J. Durham, D. P. Ryskiewich, *J. Am. Chem. Soc.* **1958**, *80*, 4812–4817.
[296] T. J. Manning, E. D. Gravley, *Spectrosc. Lett.* **1995**, *28*, 291–300.
[297] J. L. Submeier, C. N. Reilley, *Anal. Chem.* **1964**, *36*, 1698–1706.

[298] Z. Baranyai, Z. Pálinkás, F. Uggeri, E. Brücher, *Eur. J. Inorg. Chem.* **2010**, *2010*, 1948–1956.
[299] K. A. Krot, A. F. D. De Namor, A. Aguilar-Cornejo, K. B. Nolan, *Inorganica Chim. Acta* **2005**, *358*, 3497–3505.
[300] H. Maumela, R. D. Hancock, L. Carlton, J. H. Reibenspies, K. P. Wainwright, *J. Am. Chem. Soc.* **1995**, *117*, 6698–6707.
[301] C. F. G. C. Geraldes, R. Delgado, A. M. Urbano, J. Costa, F. Jasanada, F. Nepveu, *J. Chem. Soc. Dalt. Trans.* **1995**, 327–335.
[302] T. Ackermann, *Berichte der Bunsengesellschaft für Phys. Chemie* **1987**, *91*, 1398–1398.
[303] J. L. Atwood, J.-M. Lehn, *Comprehensive Supramolecular Chemistry*, Pergamon, 1st Edition, **1996**.
[304] P. Thordarson, *Chem. Soc. Rev.* **2011**, *40*, 1305–1323.
[305] M. Sokołowska, W. Bal, *J. Inorg. Biochem.* **2005**, *99*, 1653–1660.
[306] H. Monti, G. Léandri, M. Klos-ringuet, C. Corriol, *Synth. Commun.* **1983**, *13*, 1021–1026.
[307] A. Rockenbauer, L. Korecz, *Appl. Magn. Reson.* **1996**, *10*, 29–43.
[308] P. Gans, A. Sabatini, A. Vacca, *Talanta* **1996**, *43*, 1739–1753.
[309] G. Schwarzenbach, H. A. Flaschka, *Complexometric Titrations*, 2nd Edition, Methuen, **1969**.
[310] N. J, Z. Shirin, J. Thompson, L. Liable-sands, G. P. A. Yap, L. Rheingold, A. S. Borovik, *J. Chem. Soc., Dalt. Trans.* **2002**, 1714–1720.
[311] P. Sadanandam, N. Sathaiah, V. Jyothi, M. A. Chari, D. Shobha, P. Das, K. Mukkanti, *Lett. Org. Chem.* **2012**, *9*, 683–690.
[312] R. M. Irfan, D. Jiang, Z. Sun, D. Lu, P. Du, *Dalt. Trans.* **2016**, *45*, 12897–12905.
[313] J. Lampe, C. Biggers, J. Defauw, E. Al, *J. Med. Chem.* **2002**, *45*, 2624–2643.
[314] U. Sakaguchi, A. W. Addison, *J. Chem. Soc. Dalt. Trans.* **1979**, 600.
[315] M. T. Albelda, M. A. Bernardo, E. García-España, M. L. Godino-Salido, S. V. Luis, J. Melo, Maria, F. Pina, C. Soriano, *J. Chem. Soc., Perkin Trans. 2* **1999**, 2545–2549.

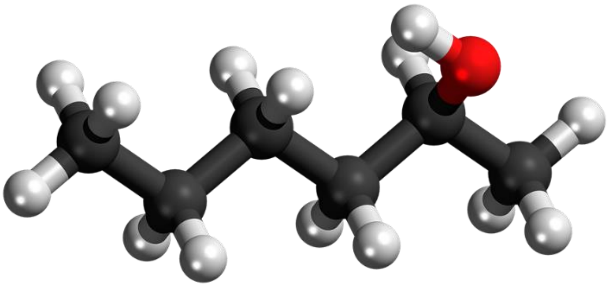

Formula Index

The different compounds shown in this work are listed here.

FORMULA INDEX

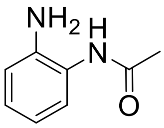

1

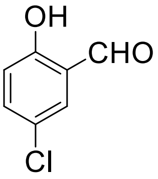

2

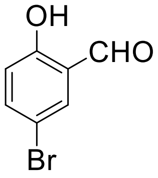

3

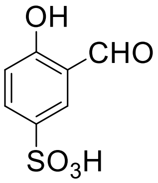

4

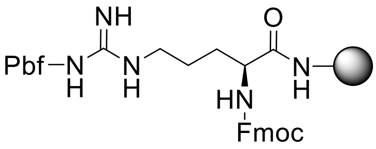

5 (Fmoc-Arg(Pbf)-Resin)

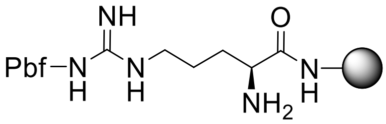

6 (Arg(Pbf)-Resin)

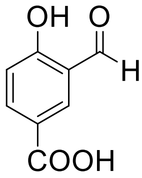

7

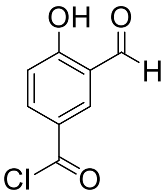

8

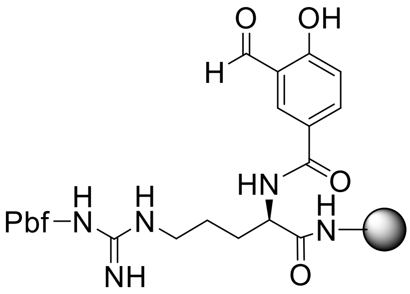

9

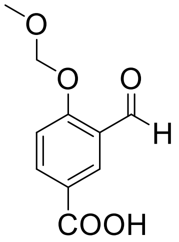

10

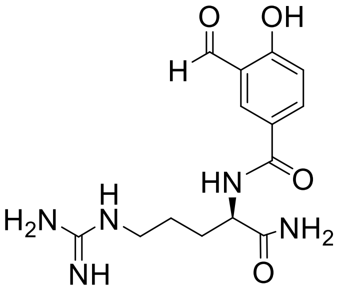

11

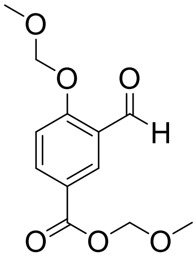

12

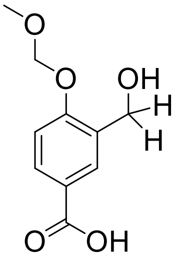

13

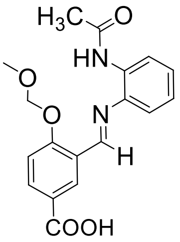

14

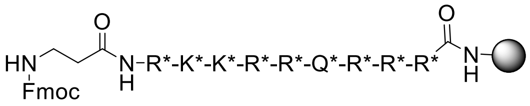

*Acid-sensitive PG in side-chains

15 (Fmoc-(β-Ala)-TAT$_{49-57}$(*)-Resin)

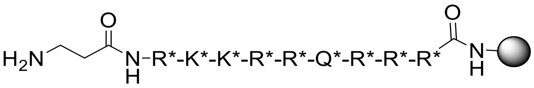

*Acid-sensitive PG in side-chains

16 ((β-Ala)-TAT$_{49-57}$(*)-Resin)

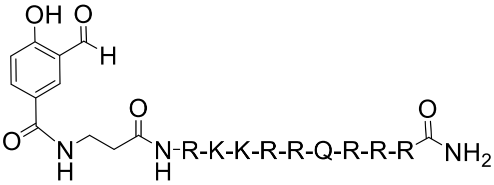

17

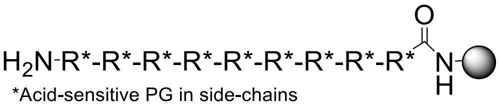

*Acid-sensitive PG in side-chains

18 (R$_9$(*)-Resin)

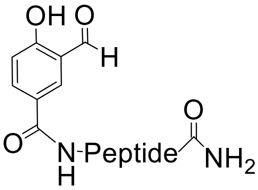

19: ***Peptide= R$_9$***

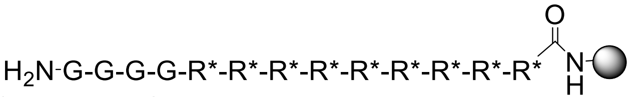

*Acid-sensitive PG in side-chains

20 ((Gly)$_4$-R$_9$(*)-Resin)

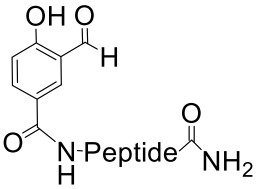

21: ***Peptide= (Gly)$_4$-R$_9$***

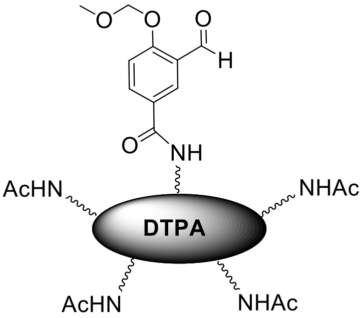

22

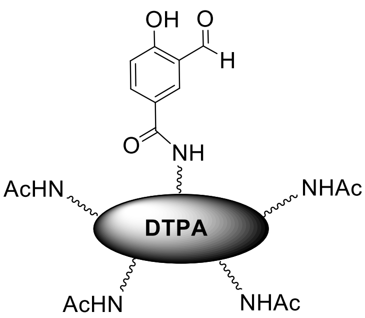

23

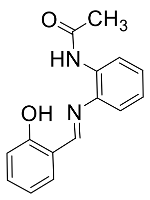

L1

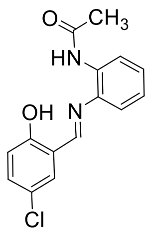

L2

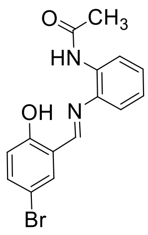

L3

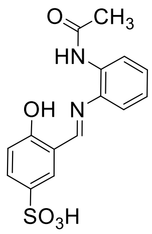

L4

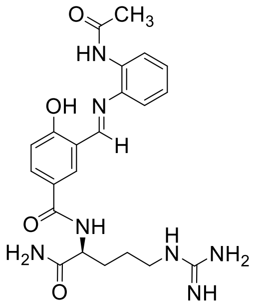

L5

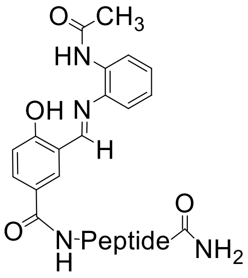

L6: *Peptide*= R_9

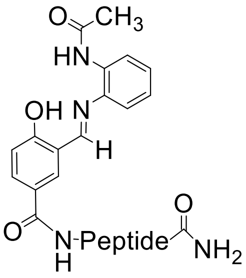

L7: *Peptide*= $(Gly)_4$-R_9

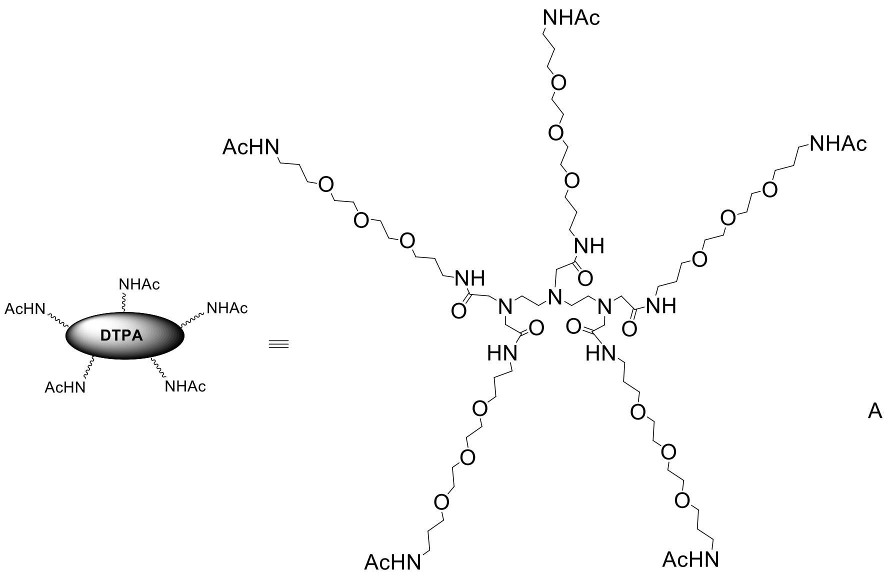

L8
(DTPA-5Ac)

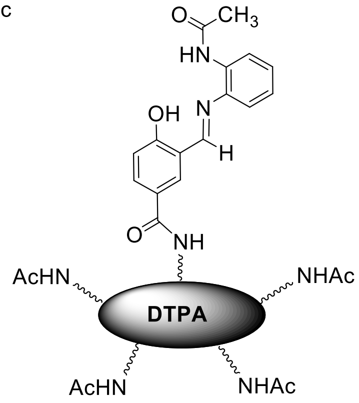

L9

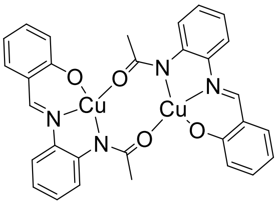

C1

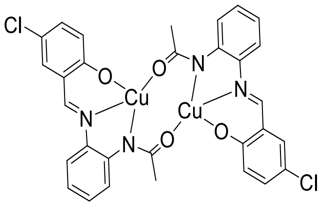

C2

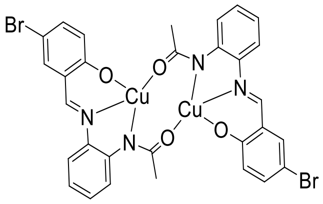

C3

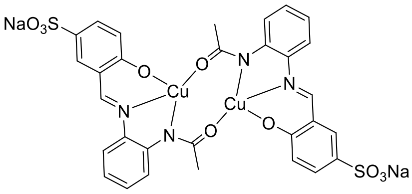

C4

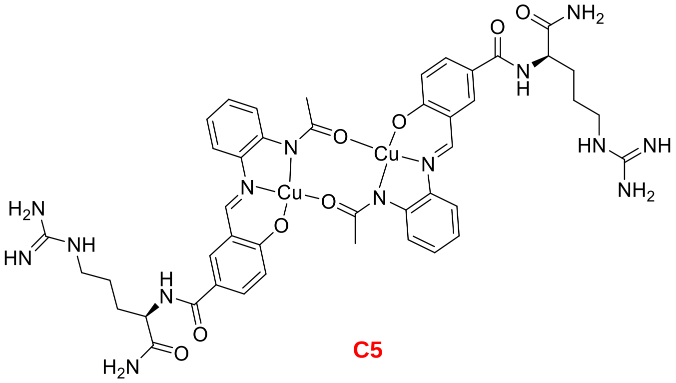

C5

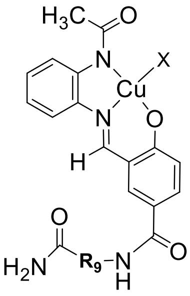

C6

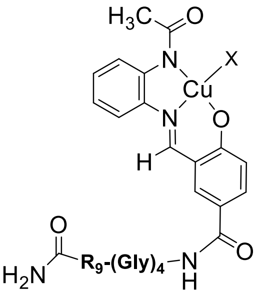

C7

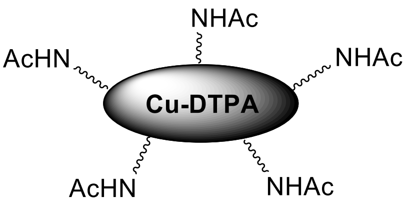

C8
[Cu(DTPA-5Ac)]

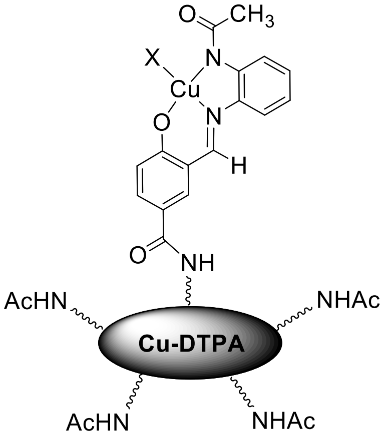

C9

Annex

Supplementary information and NMR spectra to characterize the obtained compounds are collected in this part.

ANNEX CHAPTER 3

a) Ligands L1, L2 and L3 precursors: compounds 1, 2 and 3

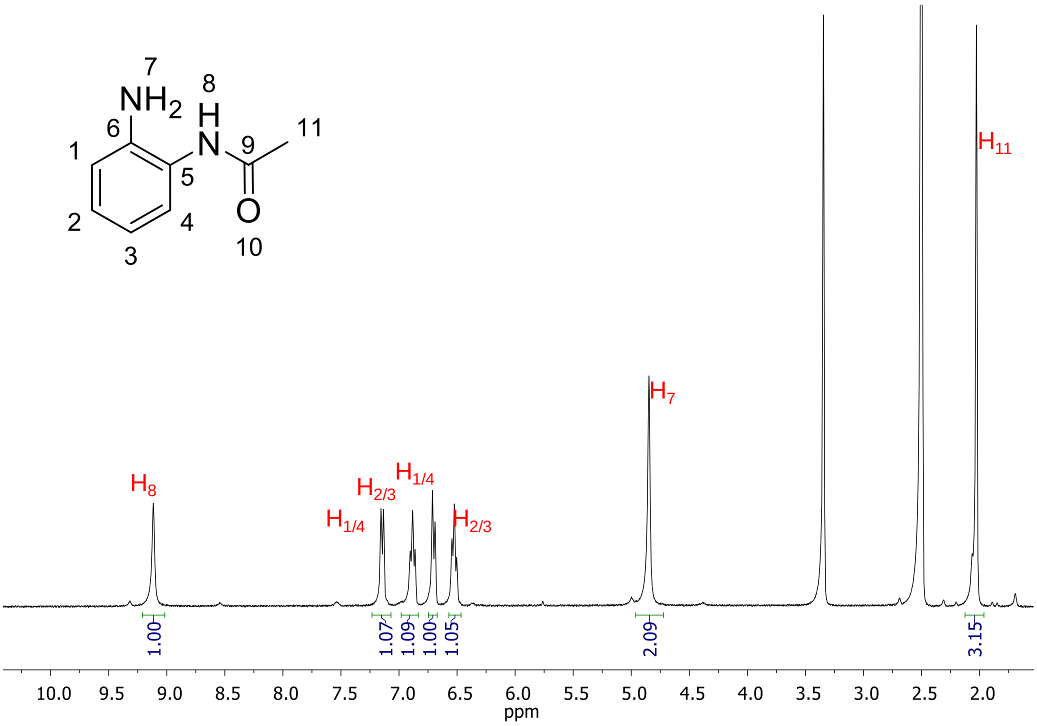

Figure A1. ^1H NMR (360 MHz, d_6-DMSO) spectrum of compound **1**.

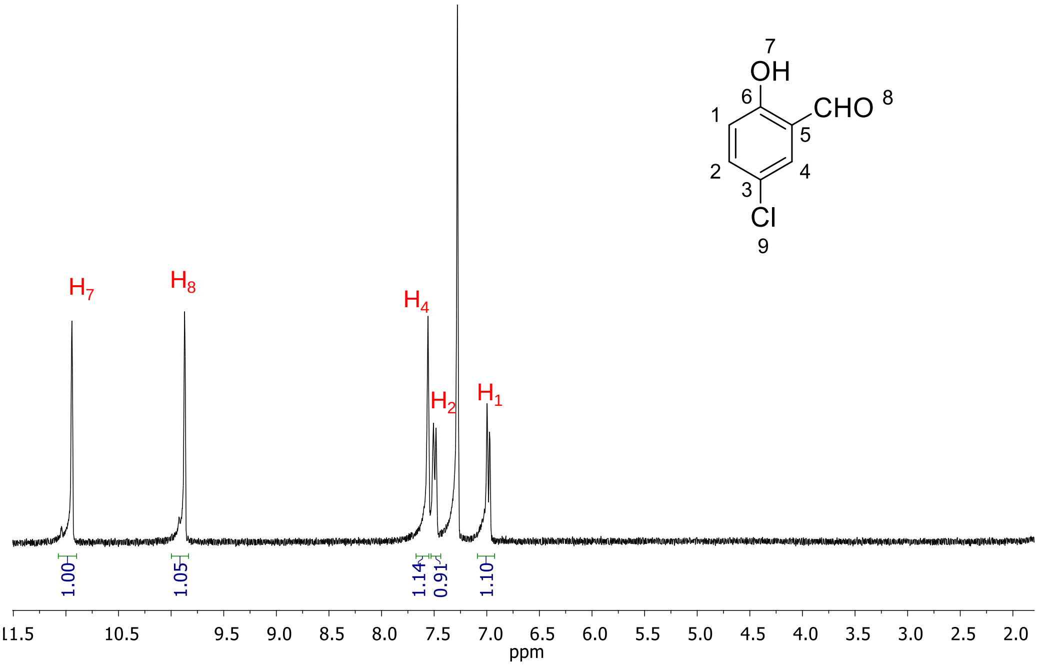

Figure A2. ^1H NMR (360 MHz, $CDCl_3$) spectrum of compound **2**.

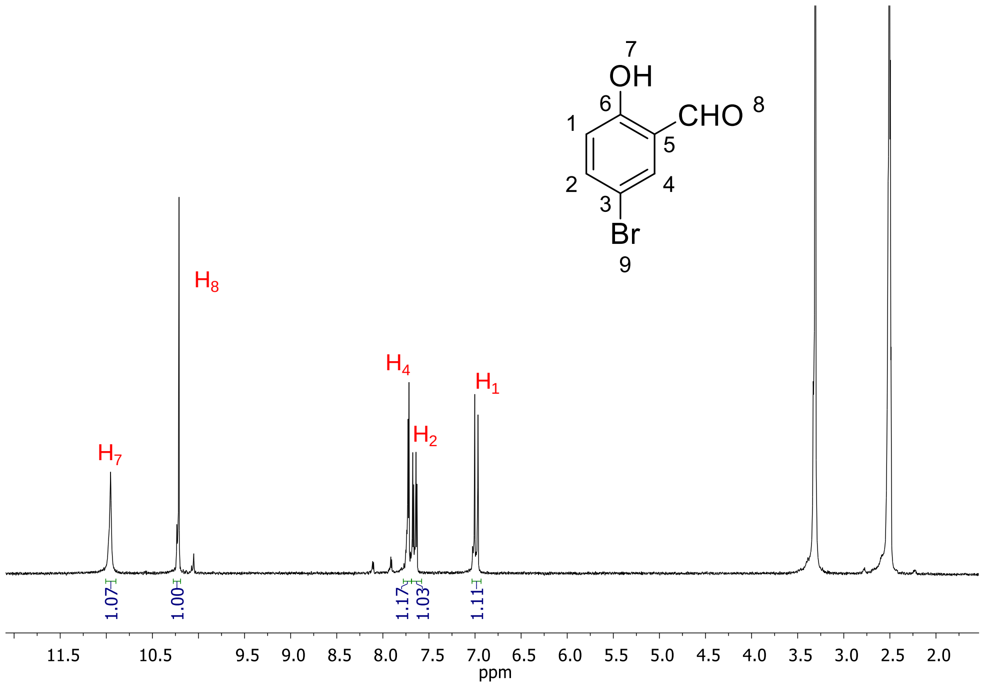

Figure A3. ^{1}H NMR (250 MHz, d_6-DMSO) spectrum of compound **3**.

b) Ligand L1

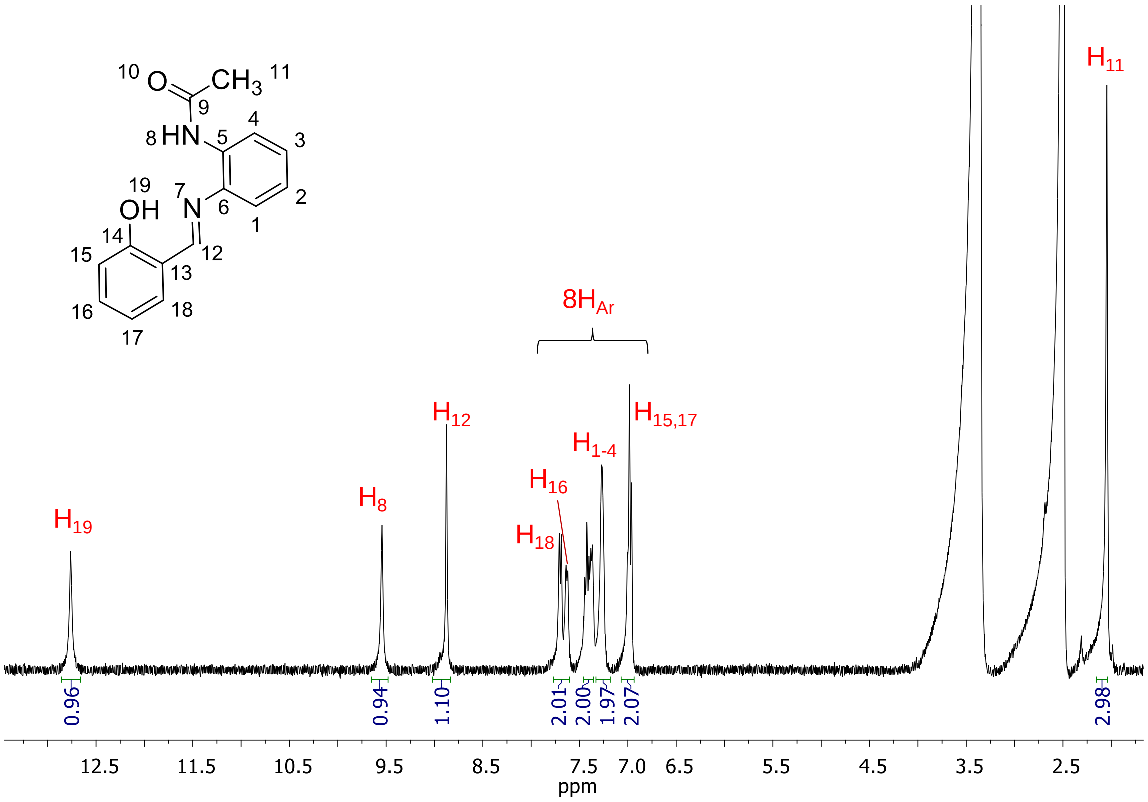

Figure A4. ^{1}H NMR (360 MHz, d_6-DMSO) spectrum of compound **L1**.

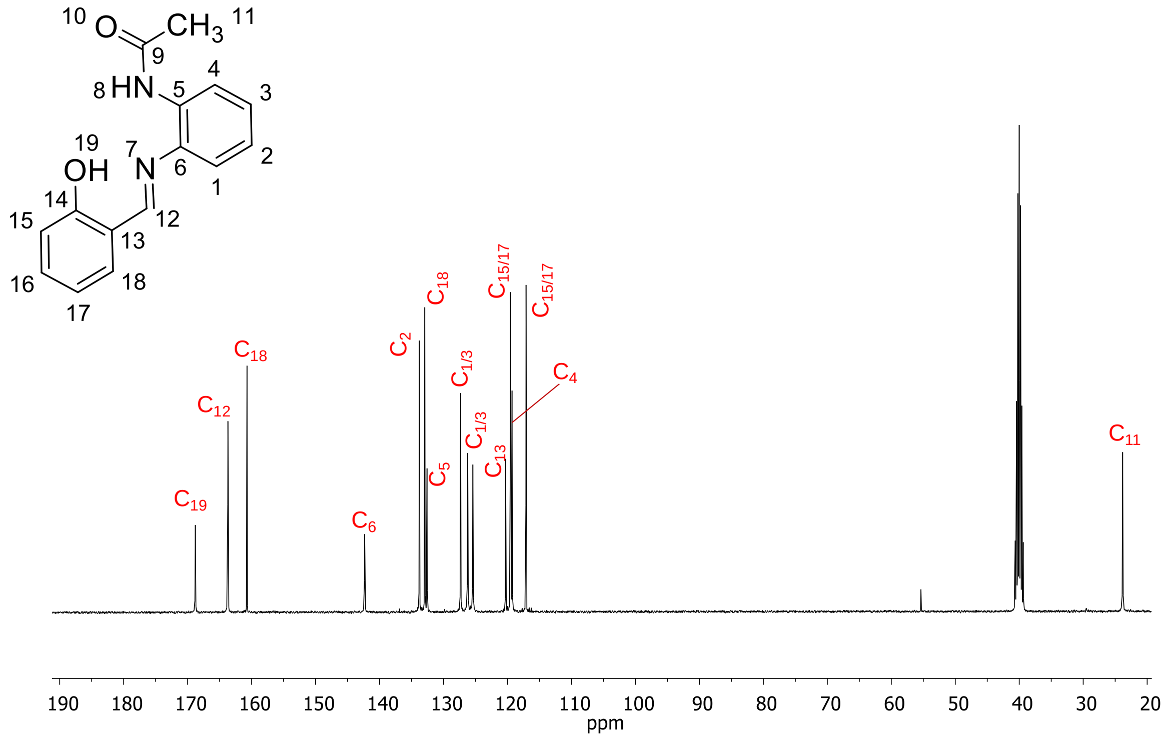

Figure A5. ^{13}C NMR (400 MHz, d_6-DMSO) of ligand **L1**.

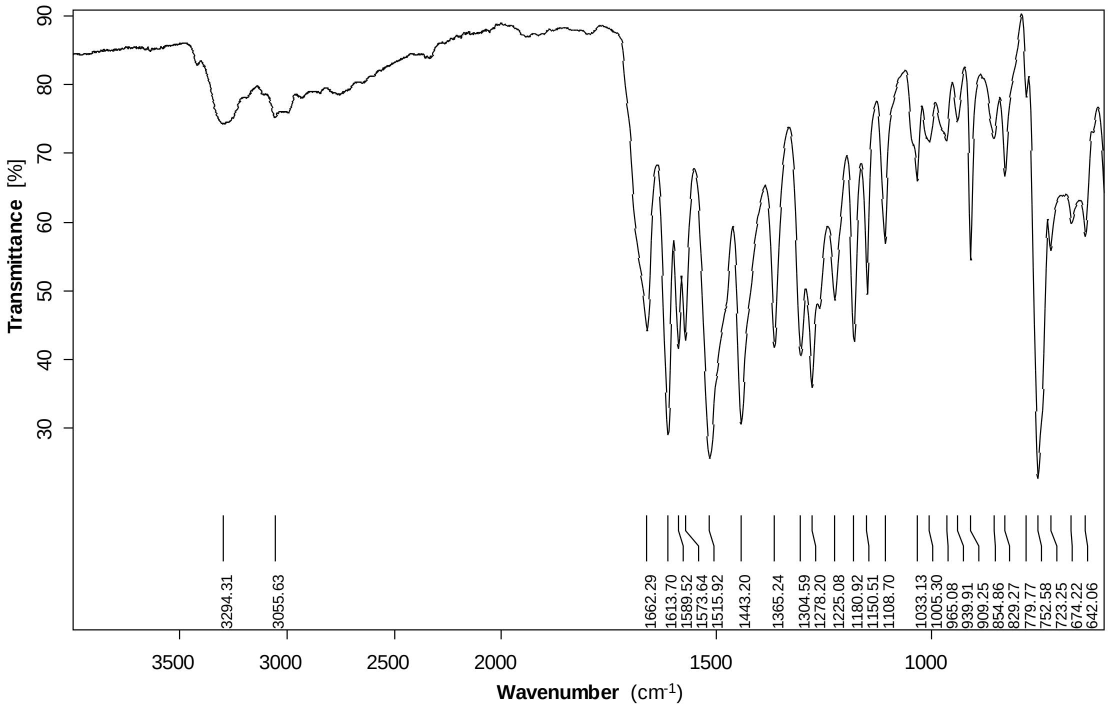

Figure A6. FT-IR spectrum of **L1**.

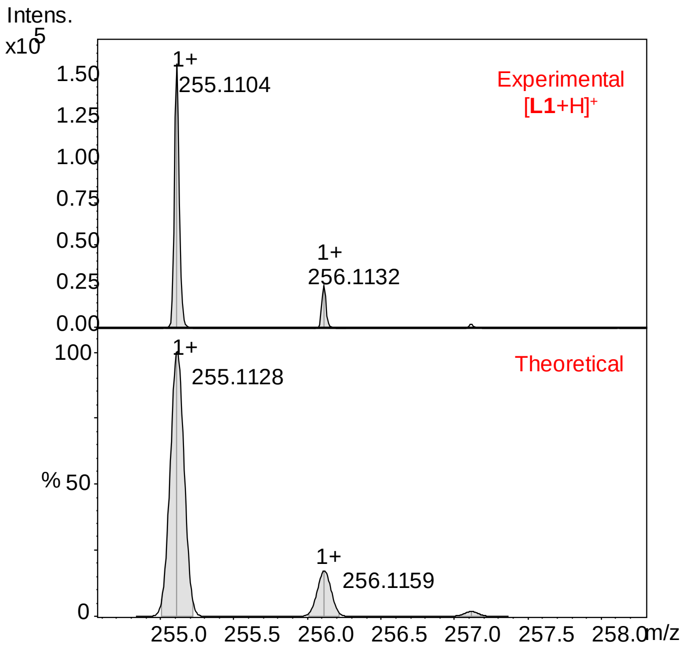

Figure A7. Experimental (top) and theoretical (down) HR-MS (ESI$^+$, MeOH) spectrum of [**L1**+H]$^+$.

c) C1

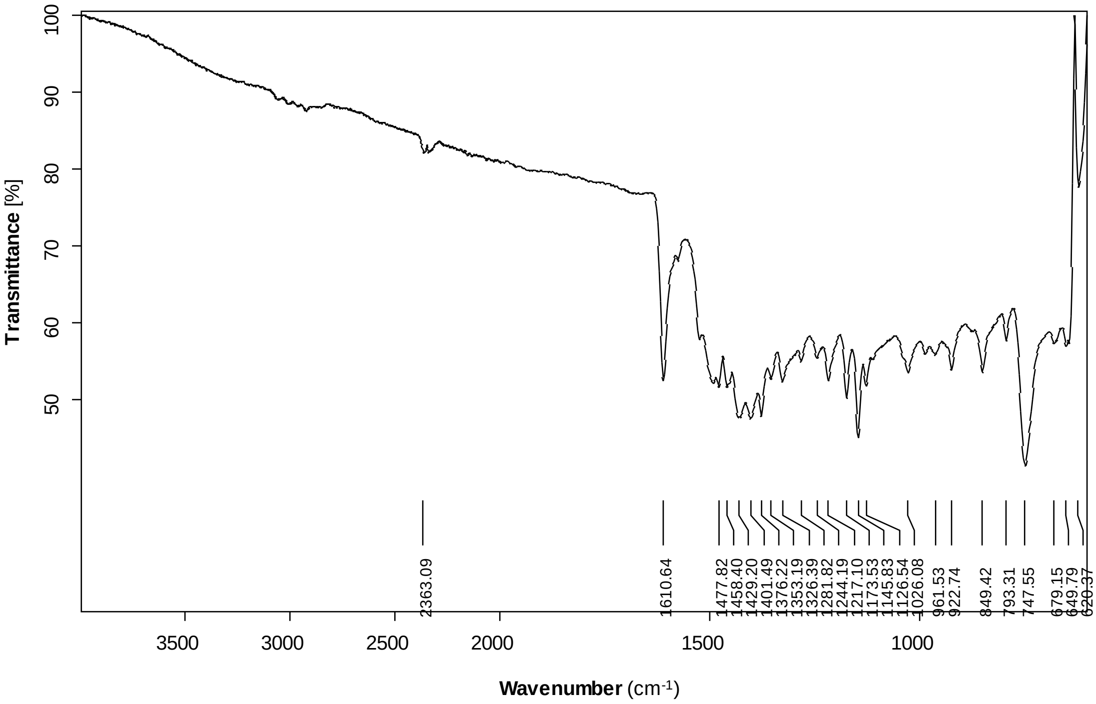

Figure A8. FT-IR of complex **C1**.

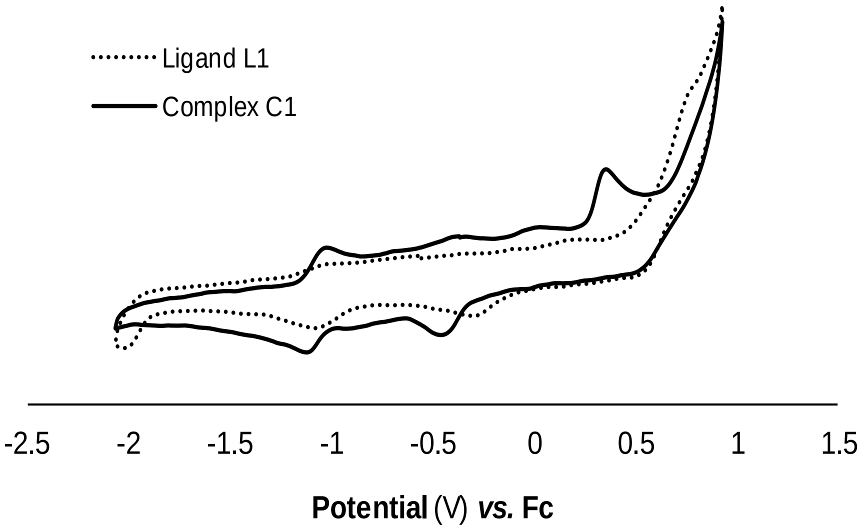

Figure A9. Cyclic voltammograms of **L1** (1.5 mM, dashed line) and **C1** (1.5 mM, solid line) in DMSO at a scan rate of 100 mV/s with 0.1 M TBAP *vs.* Fc^+/Fc.

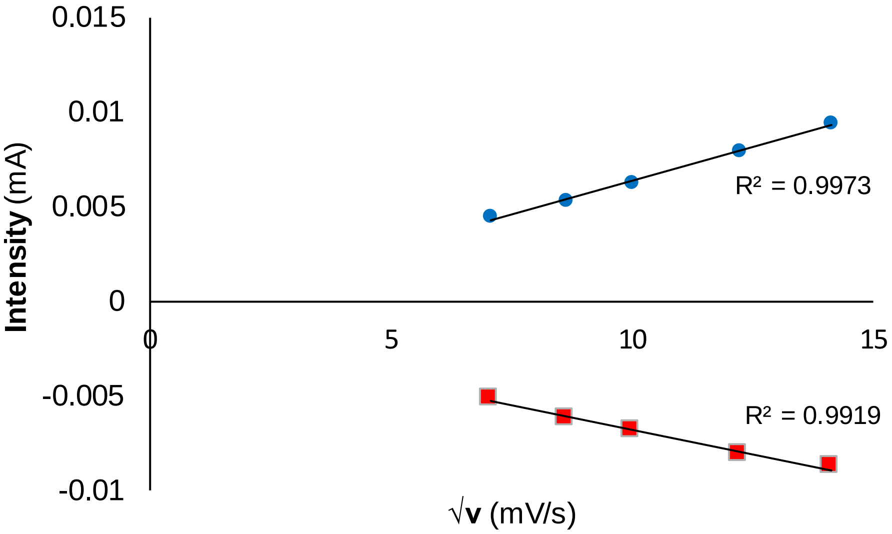

Figure A10. Linear plots of I_{pc} (red) and I_{pa} (blue) *vs.* the root square of the scan rate (*v*) for complex **C1** in DMSO with 0.1 M TBAP.

d) Ligands L2 and L3

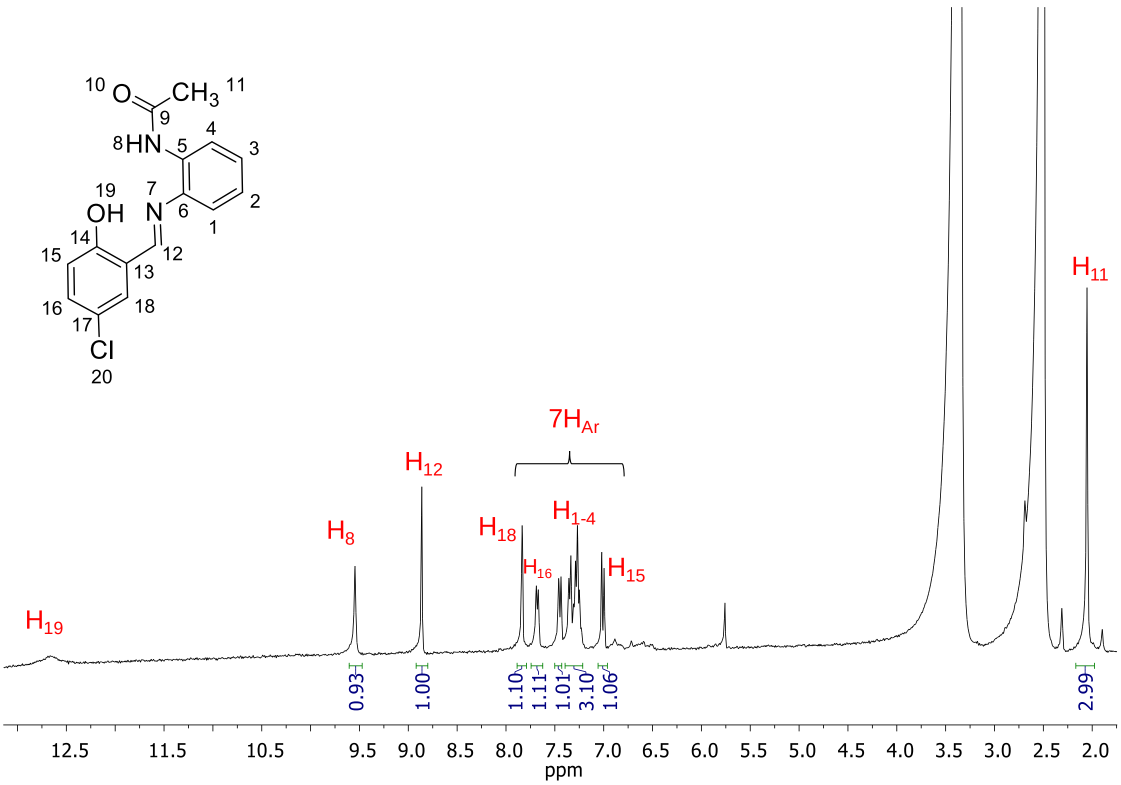

Figure A11. ^1H NMR (360 MHz, d_6-DMSO) spectrum of ligand **L2**.

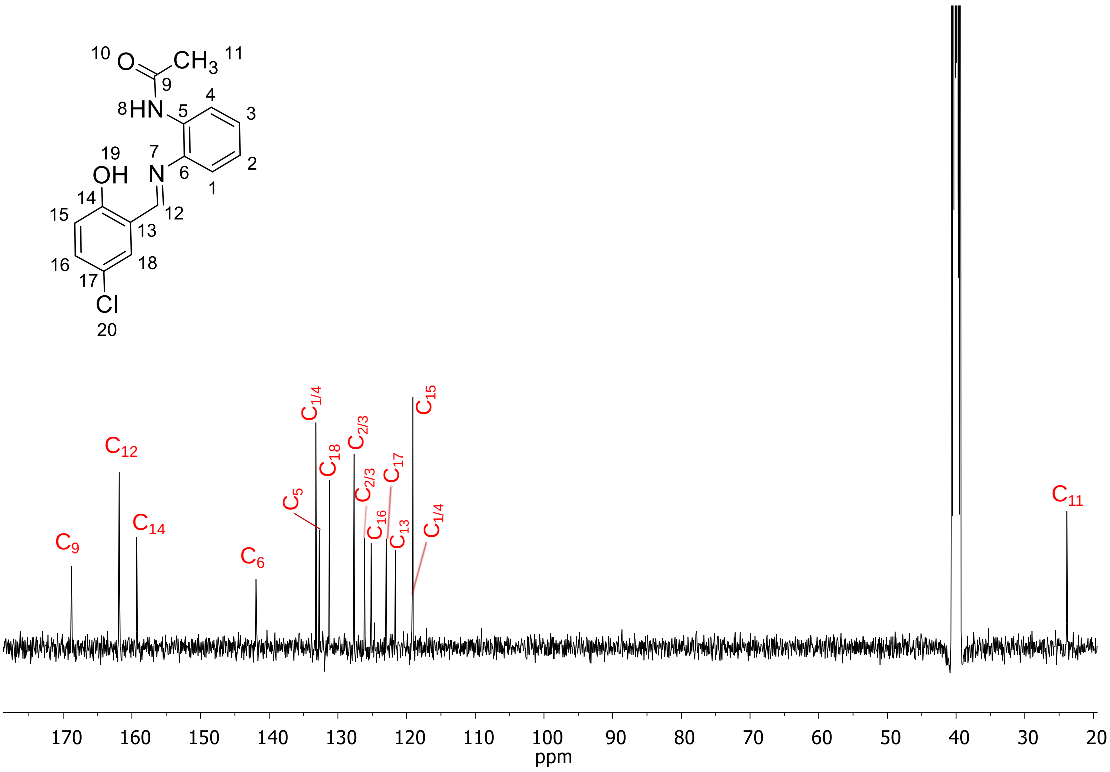

Figure A12. ^{13}C NMR (400 MHz, d_6-DMSO) of ligand **L2**.

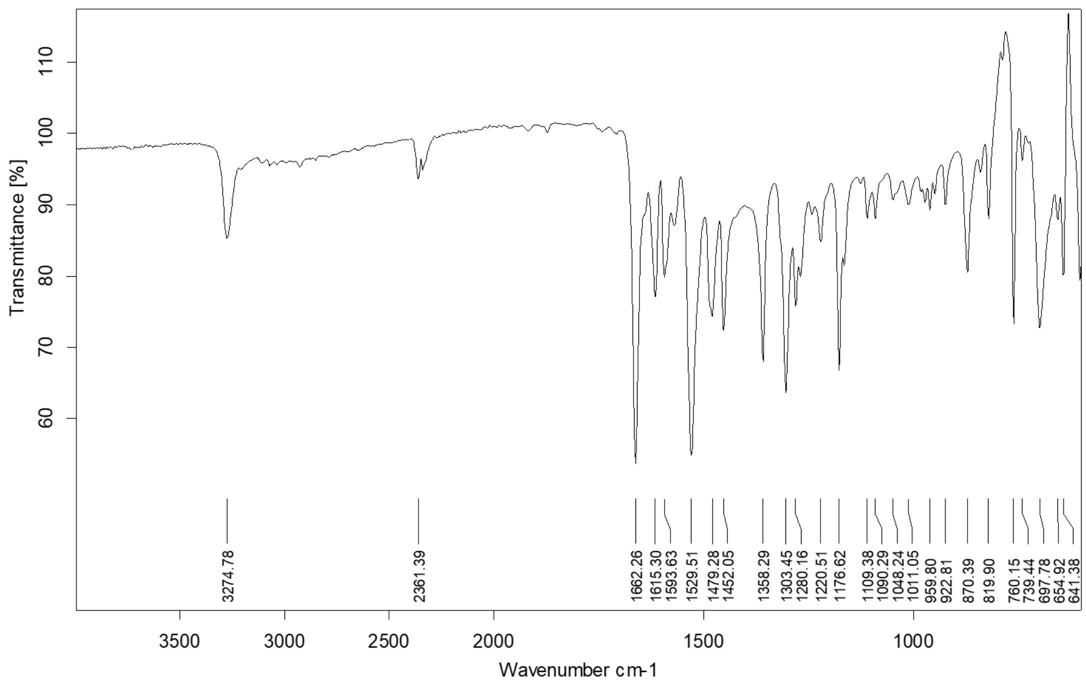

Figure A13. FT-IR of ligand **L2**.

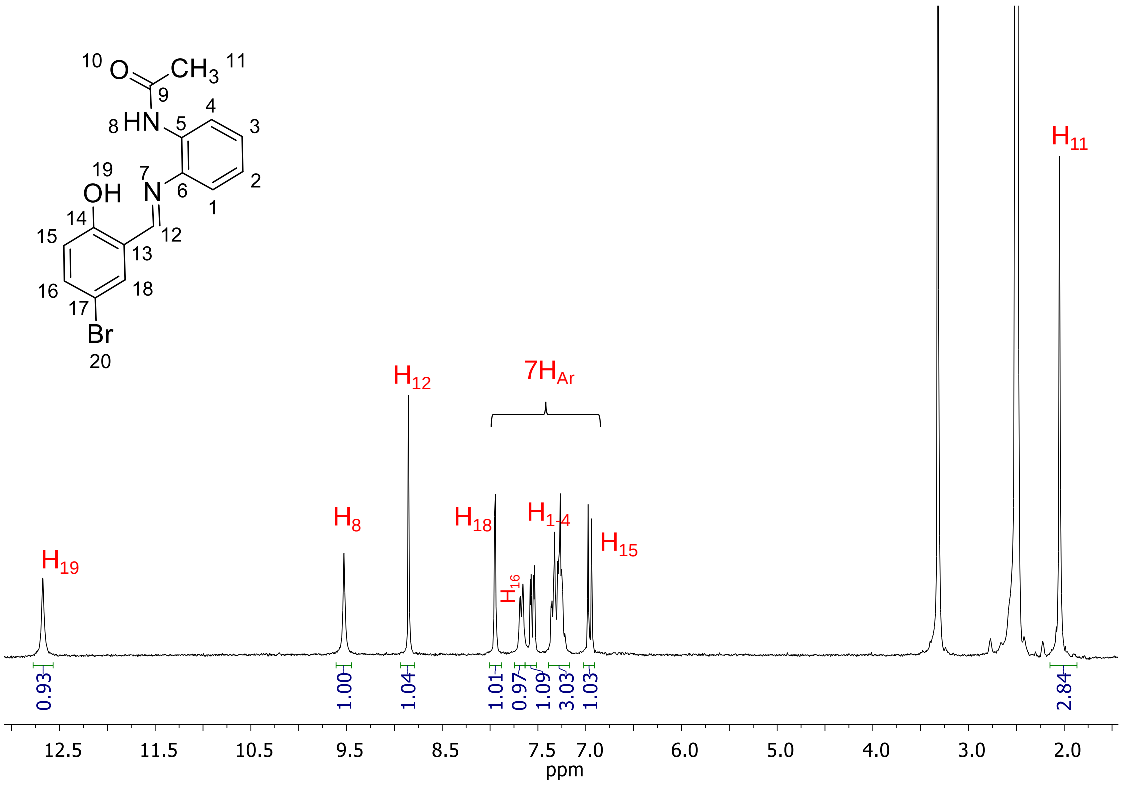

Figure A14. ^{1}H NMR (250 MHz, d_6-DMSO) spectrum of ligand **L3**.

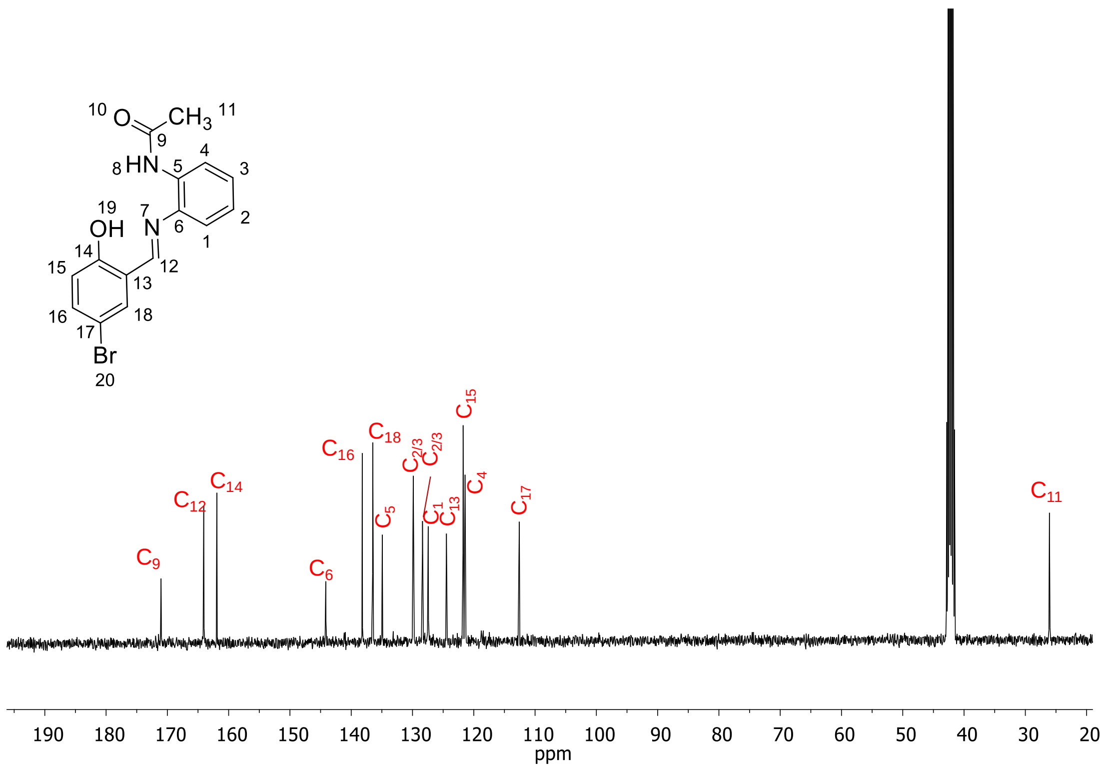

Figure A15. ^{13}C NMR (400 MHz, *d*$_6$-DMSO) of ligand **L3**.

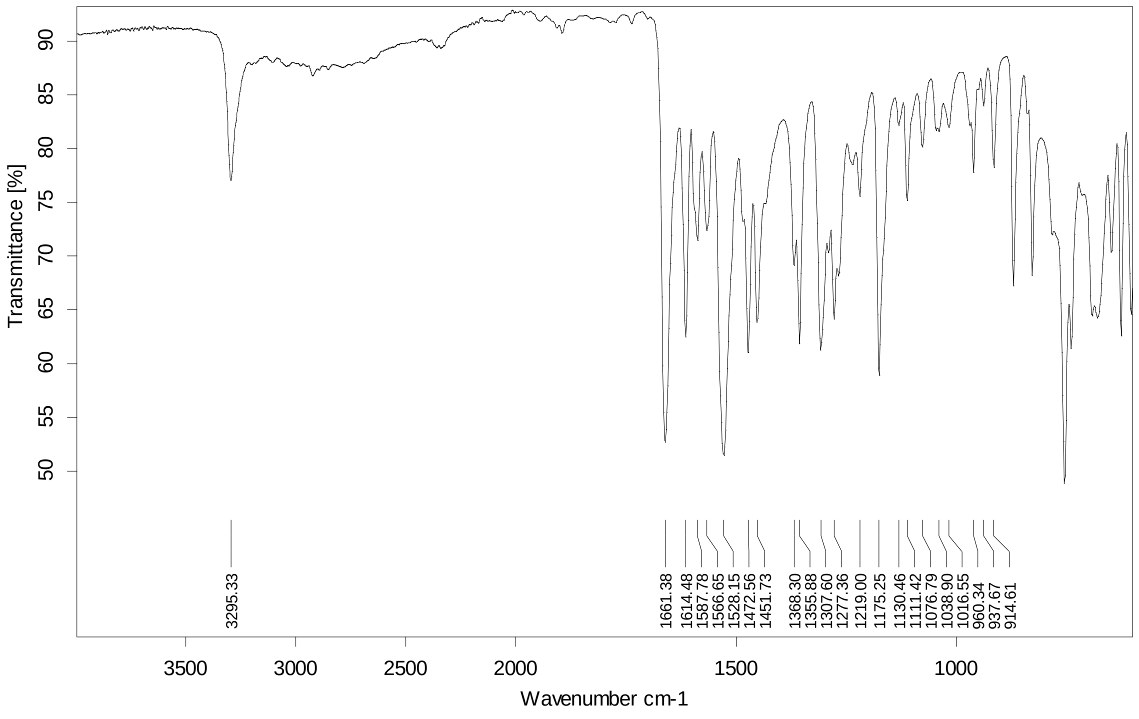

Figure A16. FT-IR spectrum of ligand **L3**.

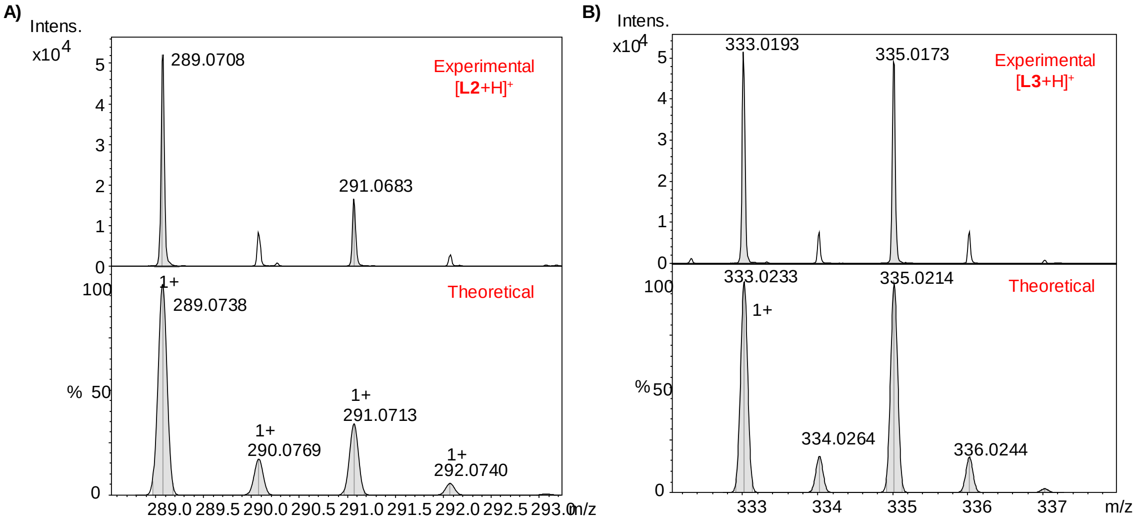

Figure A17. Experimental (top) and theoretical (down) HR-MS (ESI$^+$, MeOH) of (**A**) **L2**: [**L2**+H]$^+$, and (**B**) **L3**: [**L3**+H]$^+$.

e) Characterization of C2 and C3

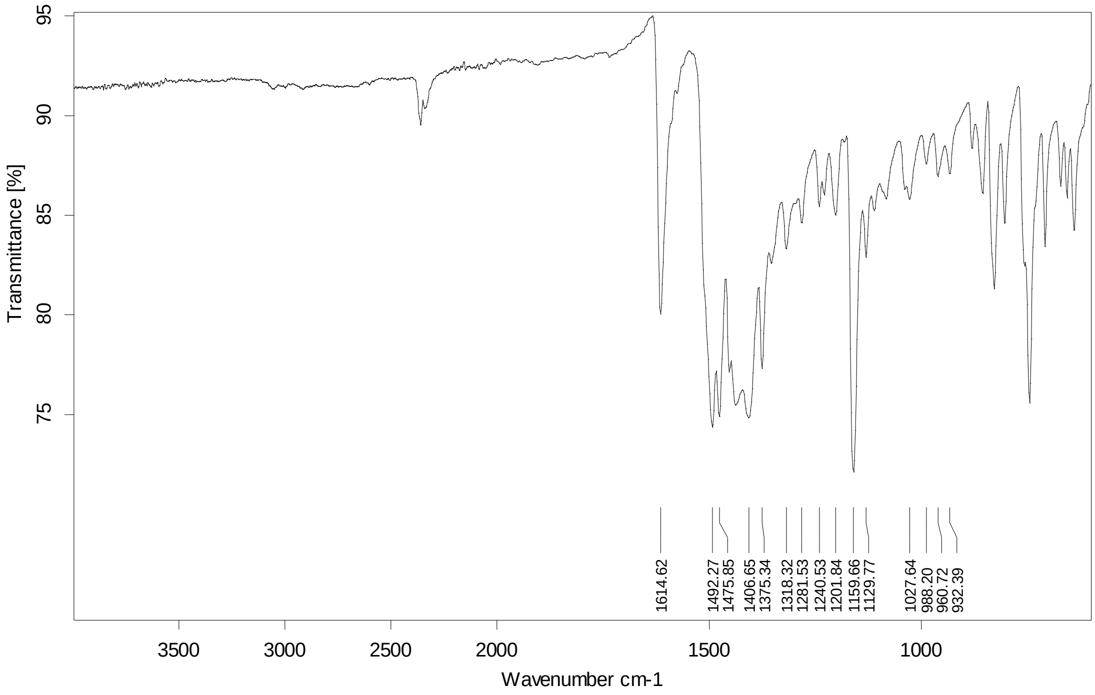

Figure A18. FT-IR spectrum of **C2**.

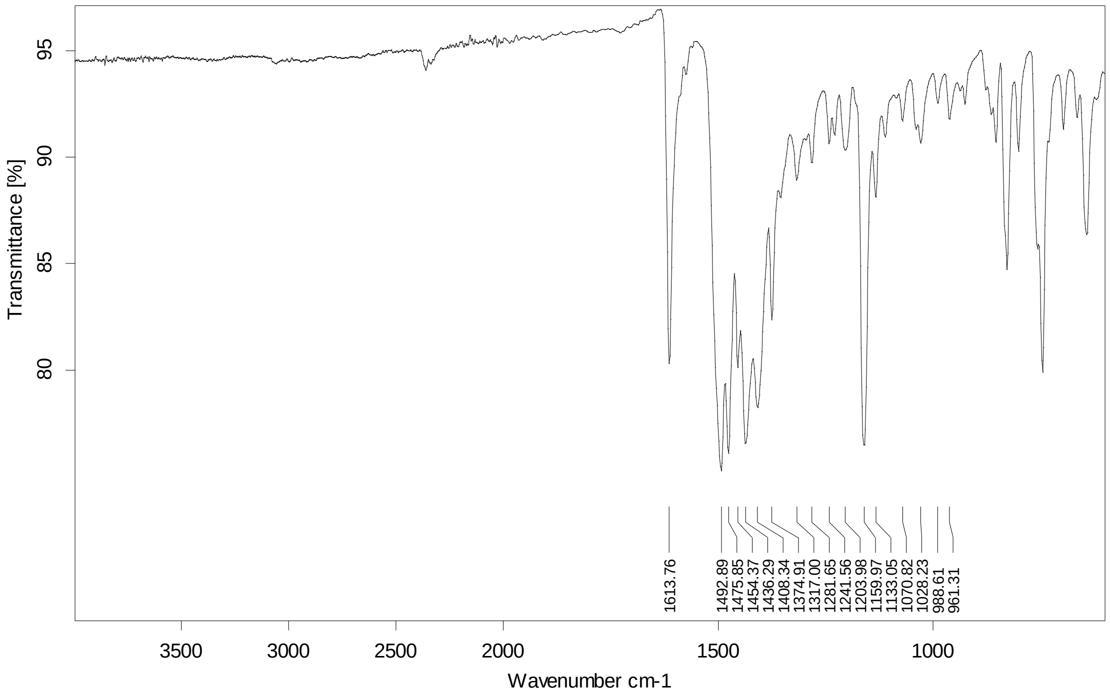

Figure A19. FT-IR spectrum of **C3**.

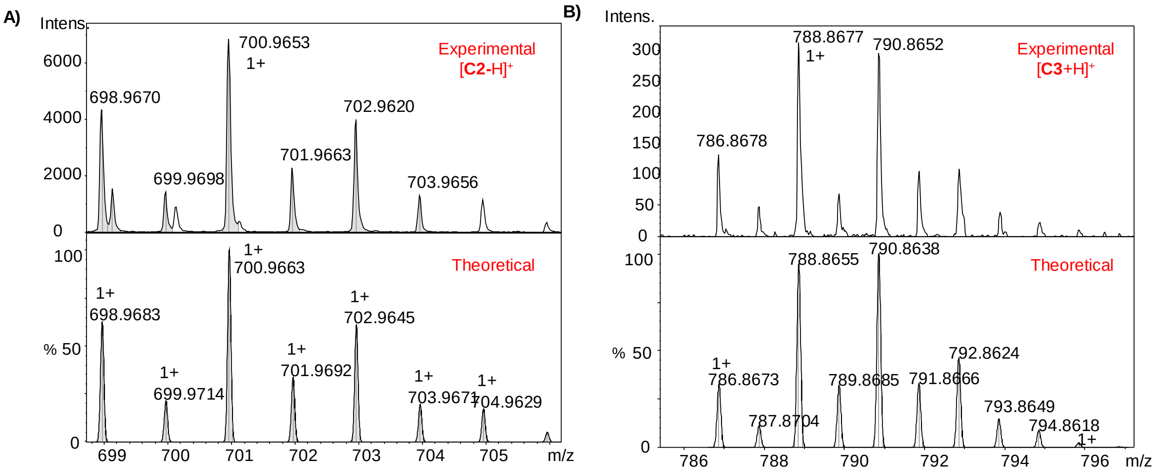

Figure A20. Experimental (top) and theoretical (down) HR-MS (ESI$^+$, MeOH) of complexes (**A**) **C2**: [**C2**-H]$^+$, and (**B**) **C3**: [**C3**+H]$^+$.

Table A1. Summary of the Cu(II)/Cu(I) redox potentials obtained for complexes **C1**, **C2** and **C3** in DMSO with 0.1 M TBAP at a scan rate of 100 mV/s *vs.* Fc$^+$/Fc.

	$E_{1/2}$(V)	E_{pc}(V)	E_{pa}(V)	I_a/I_c	ΔE_p (mV)
Complex C1	-1.07	-1.15	-0.99	1.1	130
Complex C2	-1.03	-1.09	-0.97	0.9	110
Complex C3	-1.03	-1.08	-0.97	0.9	90

f) Biological assays and protein interactions

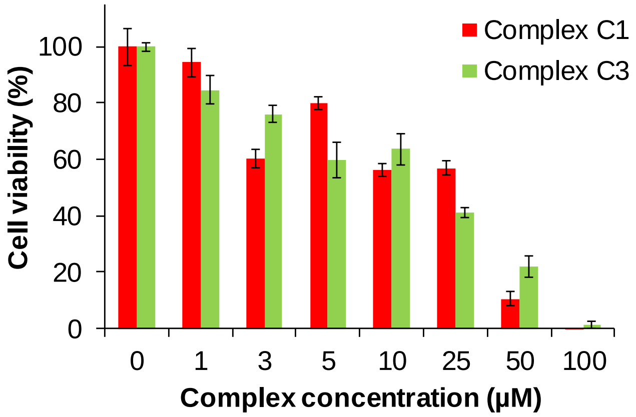

Figure A21. Cell-viability assays in MCF7 at different concentrations at 72 h for **C1** and **C3**. Free ligands have been also tested (data not shown). **C2** was not able to be assessed due to solubility issues in MCF7 culture medium.

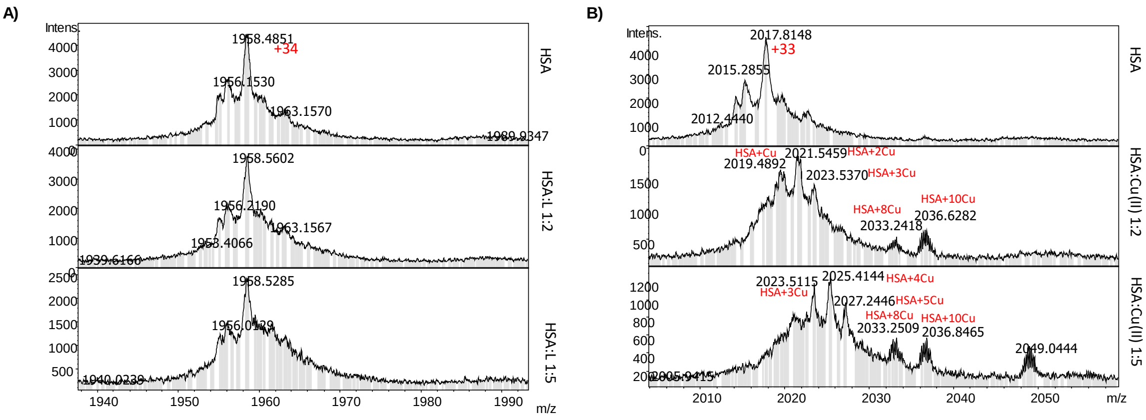

Figure A22. ESI-MS spectra of (**A**) HSA:**L1** incubations and (**B**) HSA:Cu(II) incubations at 1:2 and 1:5 ratios. Samples were incubated for 24 h at 37 ºC previous to MS experiments.

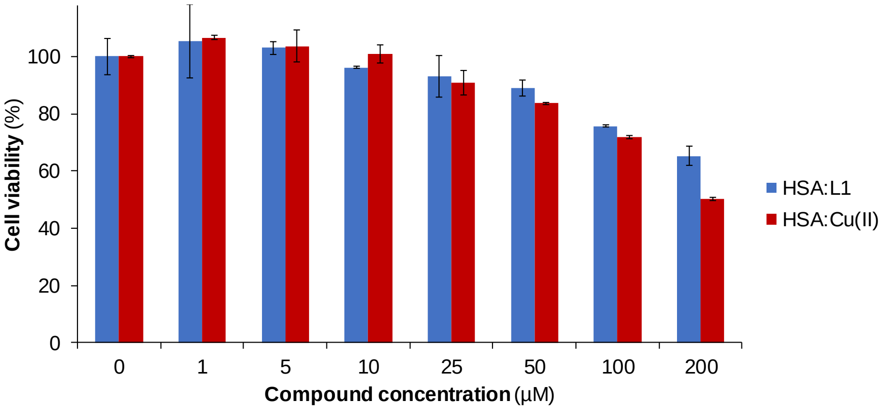

Figure A23. Cell-viability diagrams in HeLa cell lines at 72 h of treatment of the previously incubated HSA:Cu(II) and HSA:**L1** samples for 24 h at 37 ºC.

ANNEX CHAPTER 4

a) Compound 4

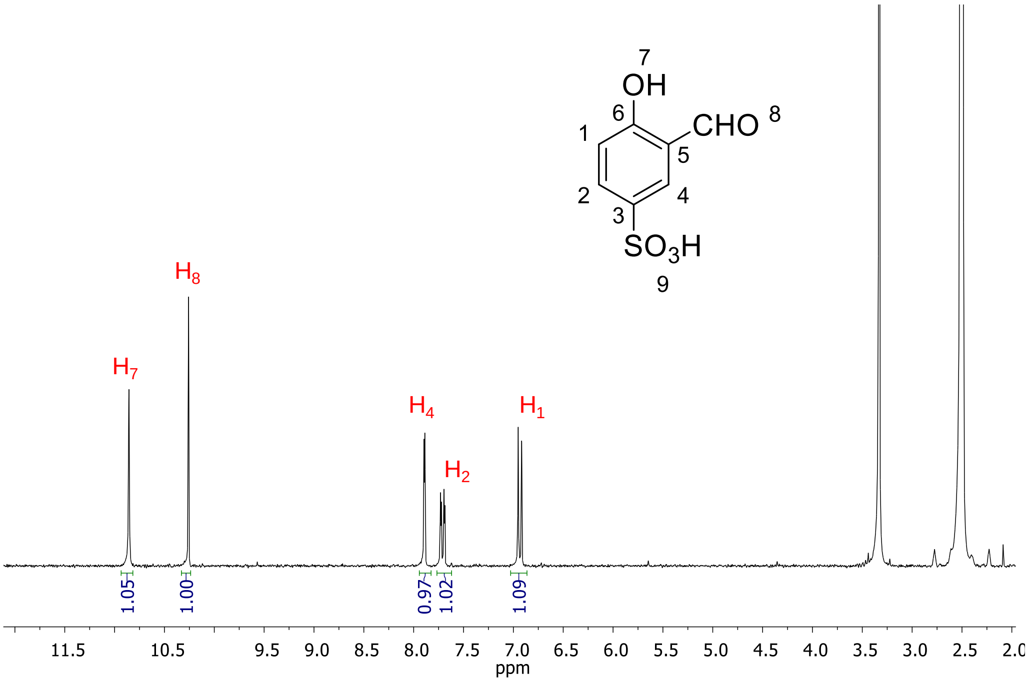

Figure A24. ^{1}H NMR (250 MHz, d_6-DMSO) spectrum of compound **4**.

b) Ligand L4

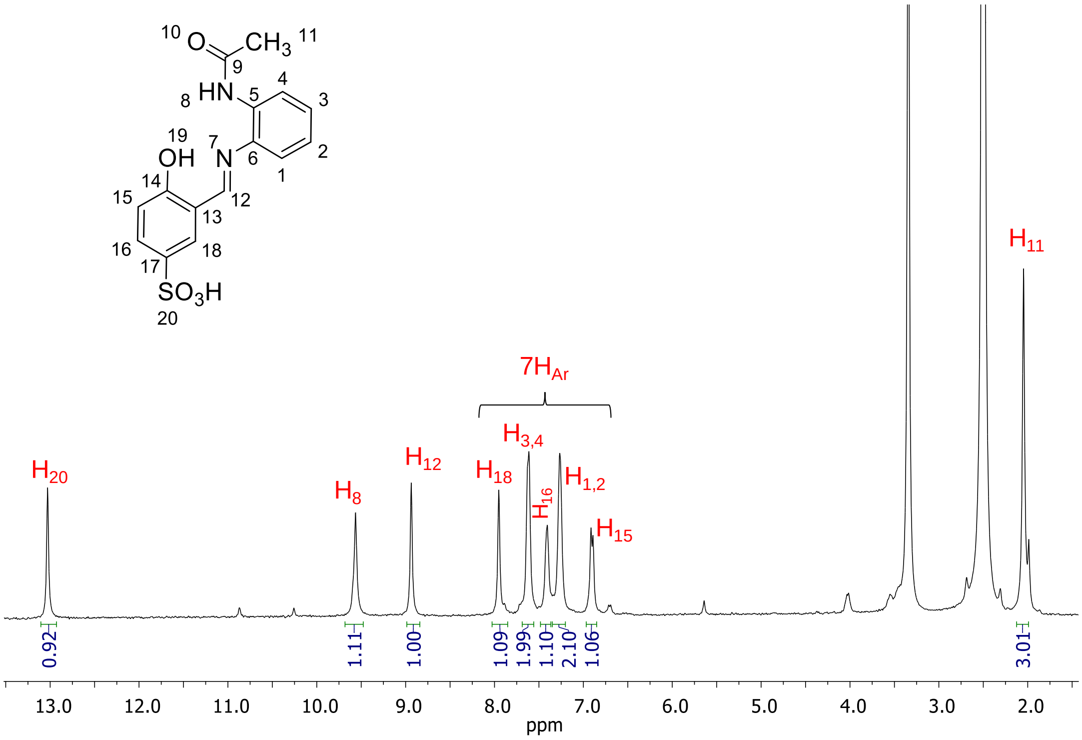

Figure A25. ^{1}H NMR spectrum (360 MHz, d_6-DMSO) of ligand **L4**.

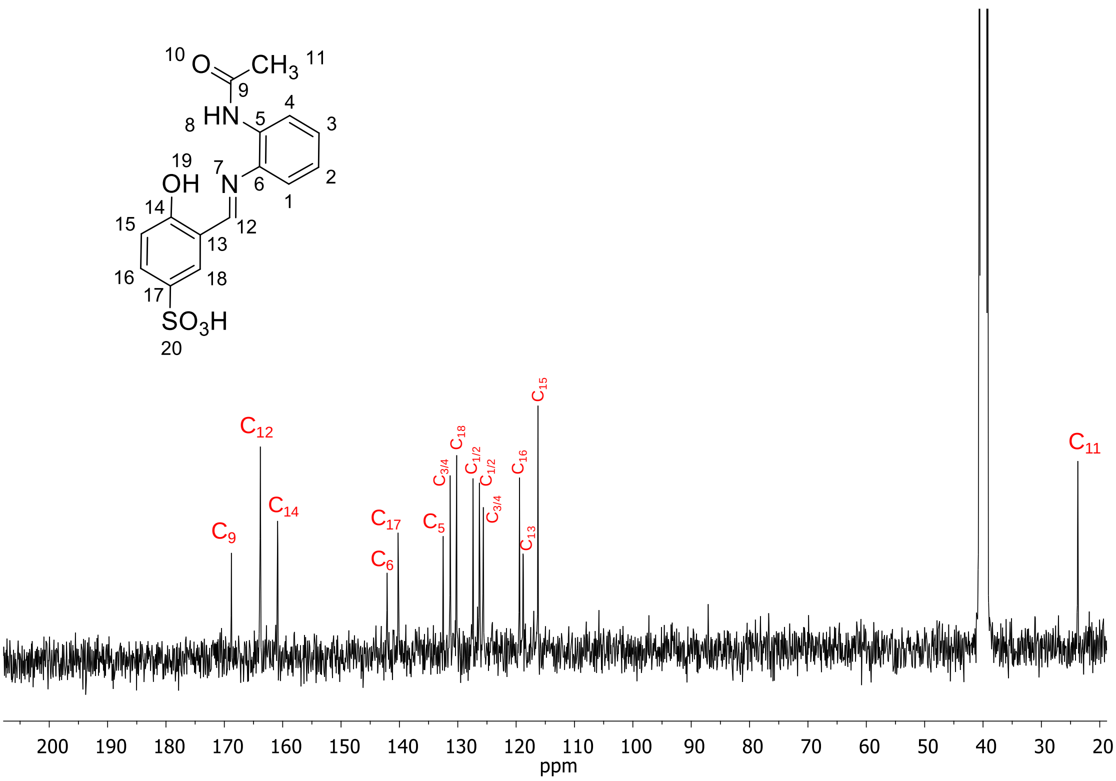

Figure A26. ^{13}C NMR (360 MHz, *d*$_6$-DMSO) of ligand **L4**.

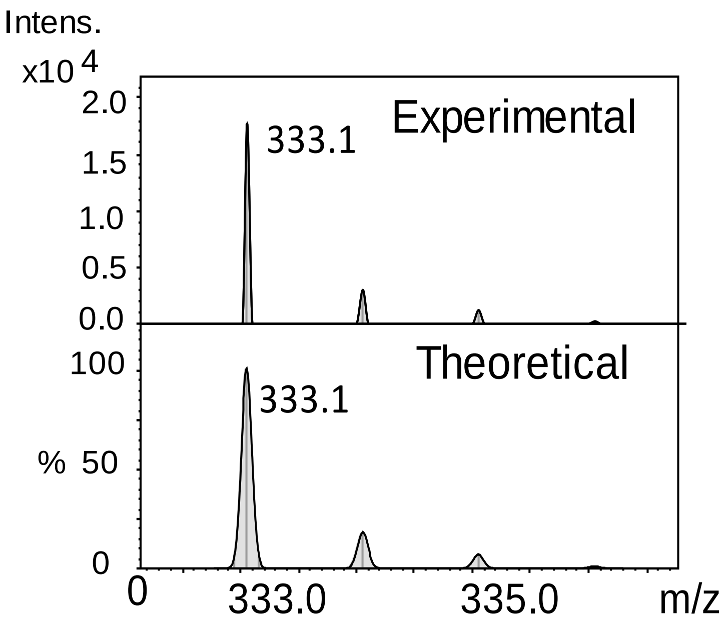

Figure A27. Experimental (top) and theoretical (down) MS (ESI$^-$, MeOH) of [**L4**-H]$^-$.

c) Arg conjugation precursors. Compounds 6, 7, 10, 11 and 14

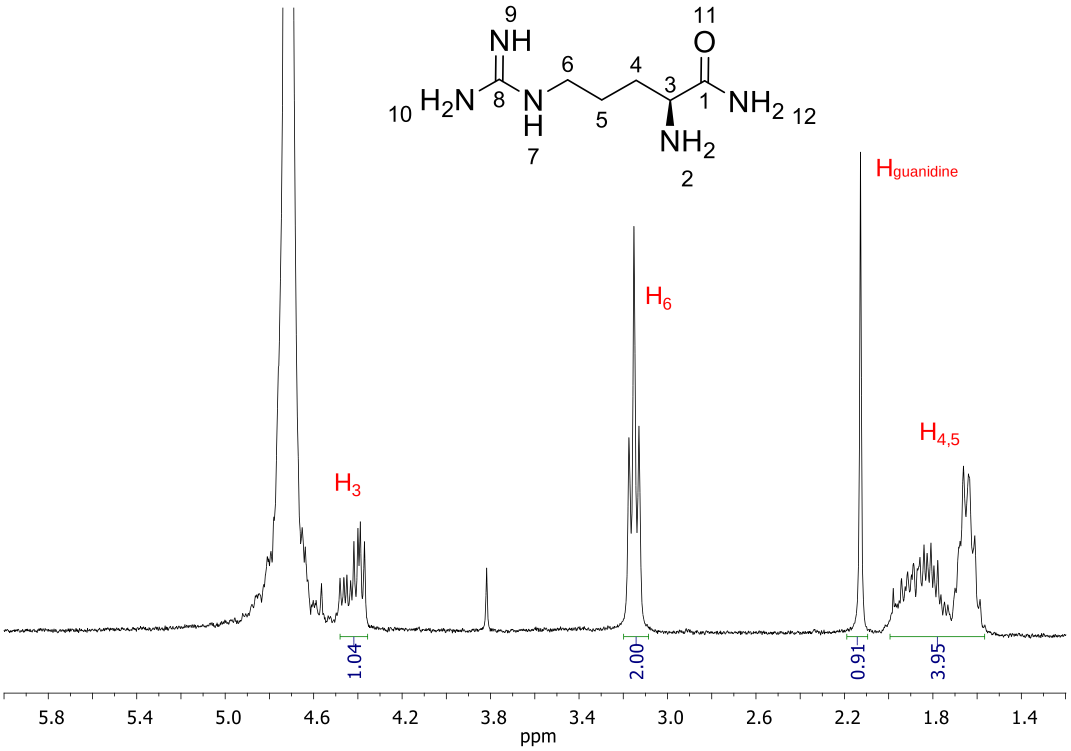

Figure A28. ^{1}H NMR spectrum (300 MHz, D_2O) of compound **6** after cleavage and deprotection with the TFA/TIS/H_2O mixture.

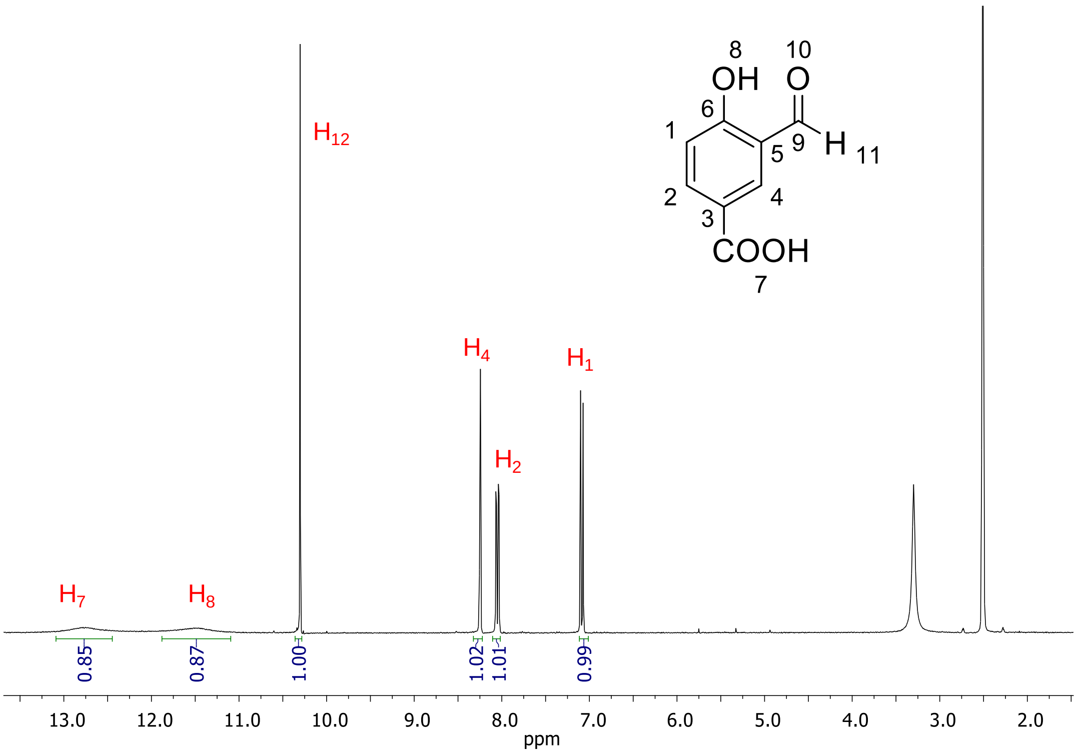

Figure A29. ^{1}H NMR spectrum (300 MHz, d_6-DMSO) of compound **7**.

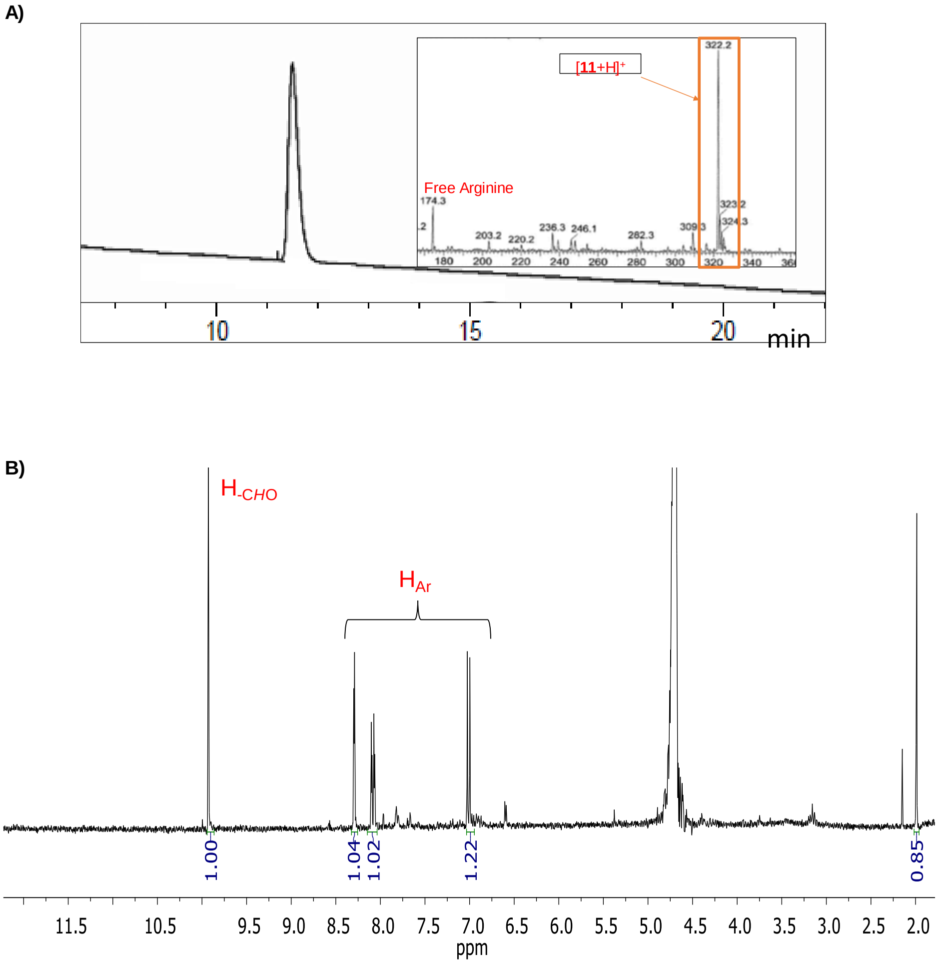

Figure A30. (**A**) Analytical reversed-phase HPLC (8-36%B in 20 min) of the purified compound *P* of the crude **11** (**Figure 4.5**). In the inset, its MS spectrum (ESI$^+$, ACN-H_2O). (**B**) ^{1}H NMR (D_2O, 300 MHz) of the purified compound *Q* from the crude **11** (**Figure 4.5**).

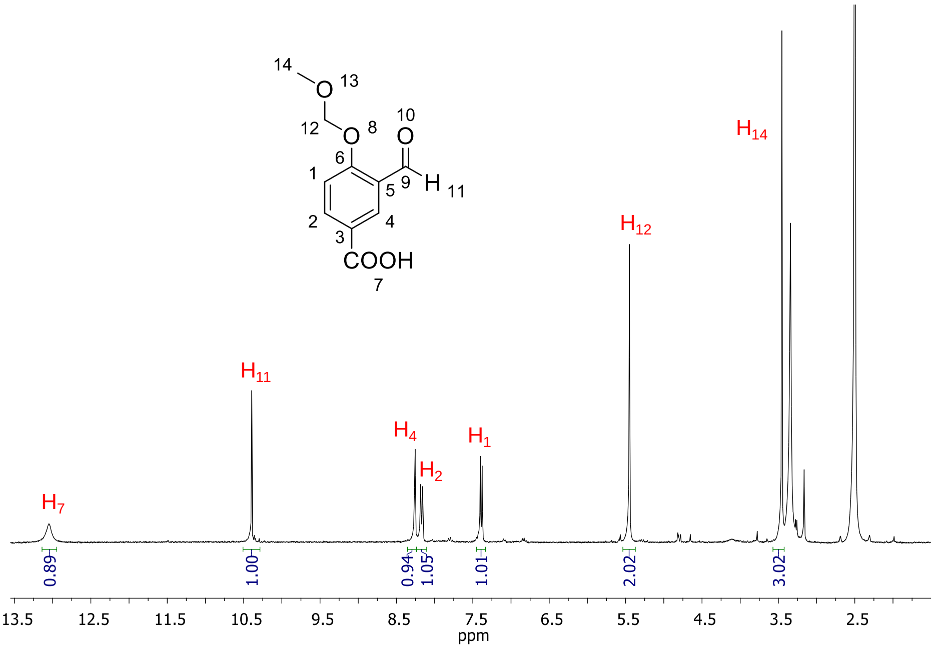

Figure A31.^{1}H NMR spectrum (360 MHz, d_6-DMSO) of compound **10**.

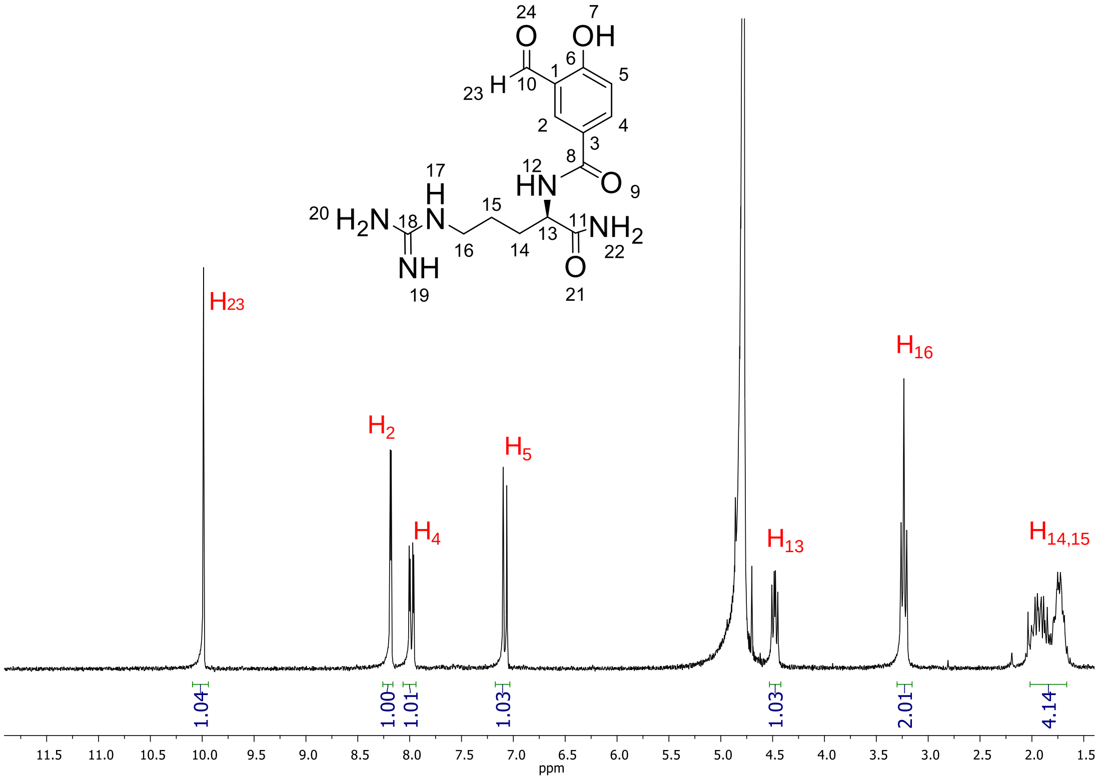

Figure A32.^{1}H NMR spectrum (250 MHz, D_2O) of compound **11**.

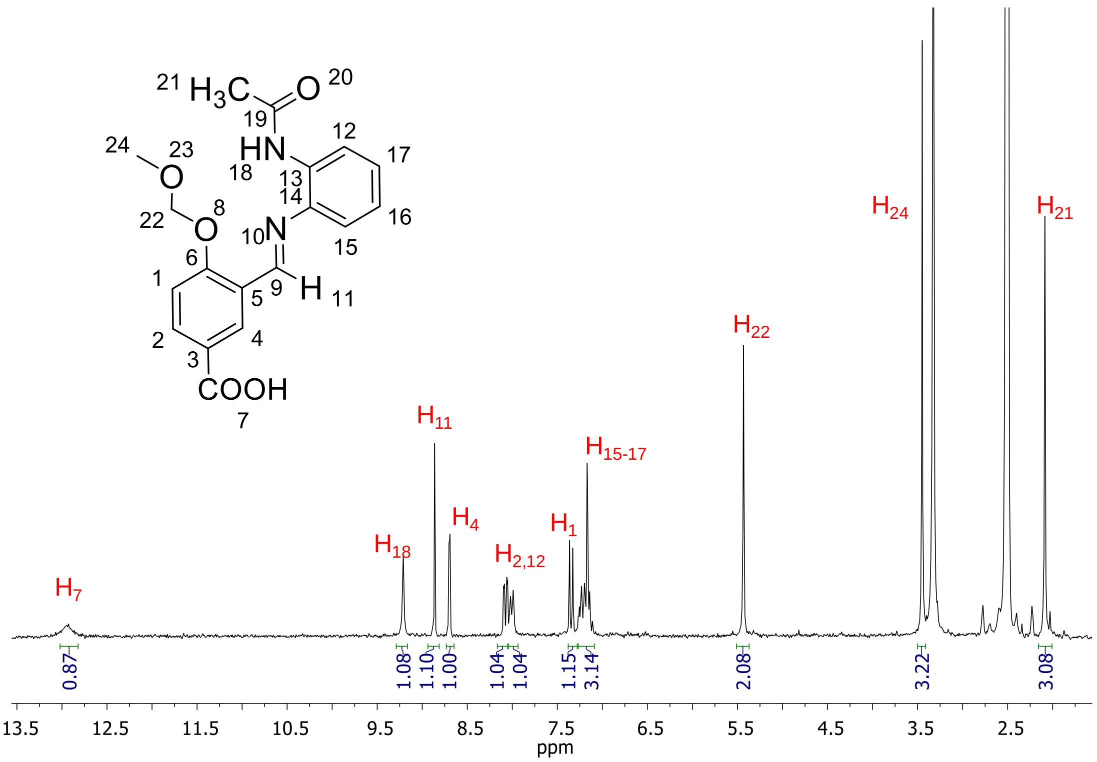

Figure A33.^{1}H NMR spectrum (250 MHz, *d*$_6$-DMSO) of compound **14**.

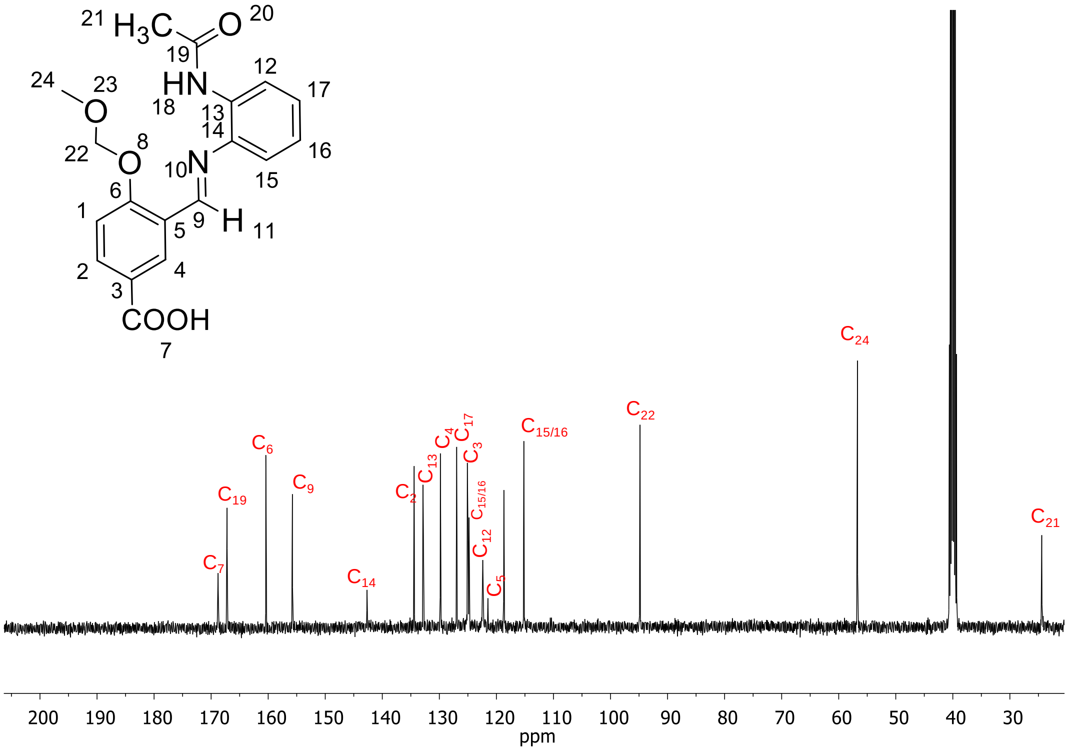

Figure A34. ^{13}C NMR (400 MHz, d_6-DMSO) of **14**.

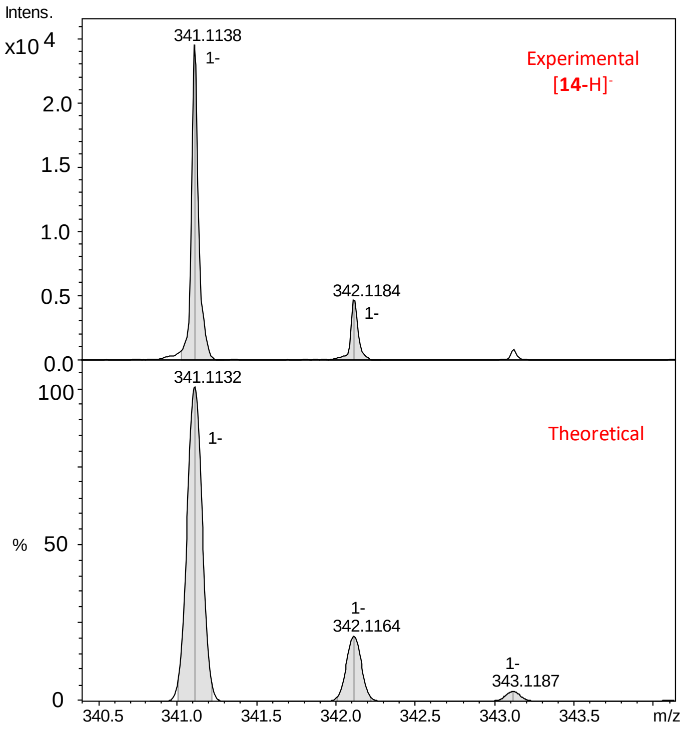

Figure A35. Experimental (top) and theoretical (down) HR-MS (ESI$^-$, MeOH) of [**14**-H]$^-$.

d) Ligand L5

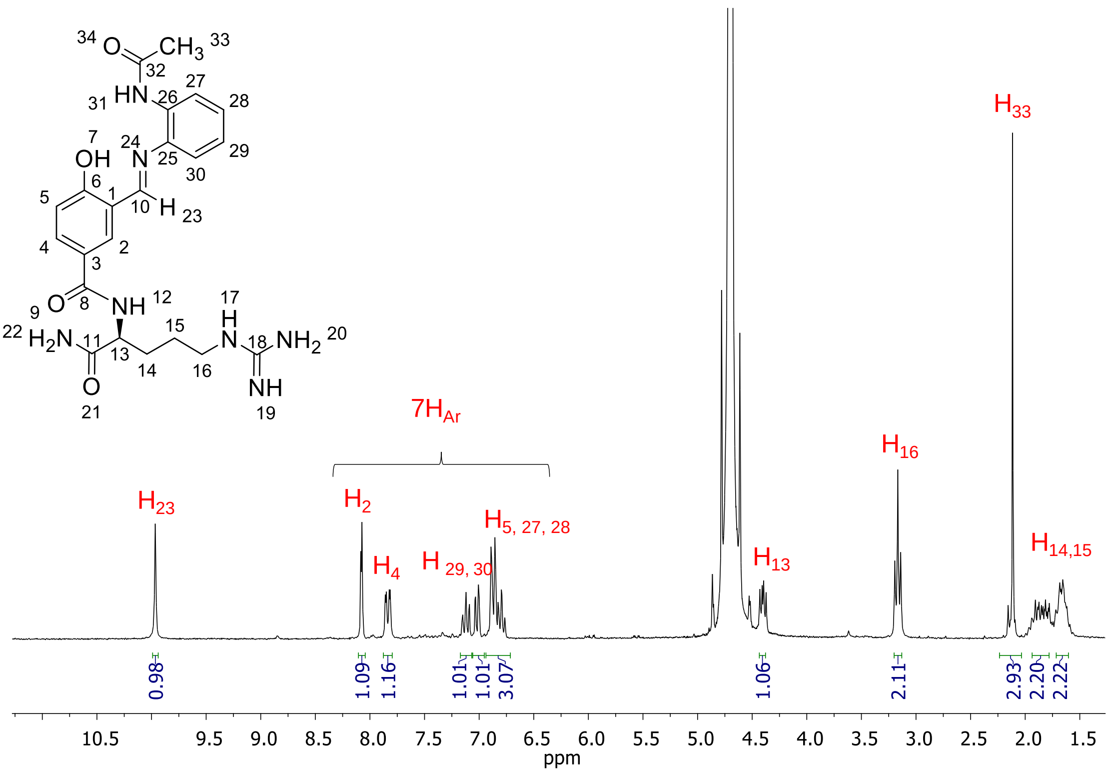

Figure A36. ^{1}H NMR spectrum (250 MHz, D_2O) of **L5**.

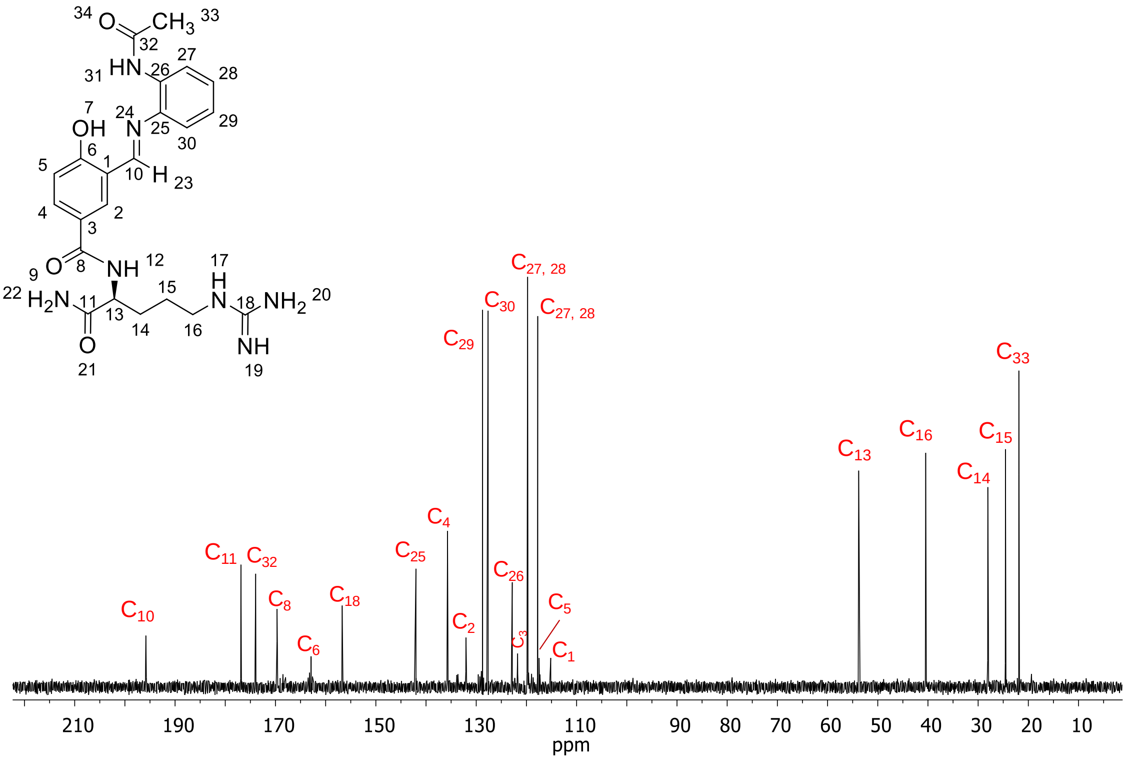

Figure A37. ^{13}C NMR (500 MHz, D_2O) of ligand **L5**.

e) CV of C4

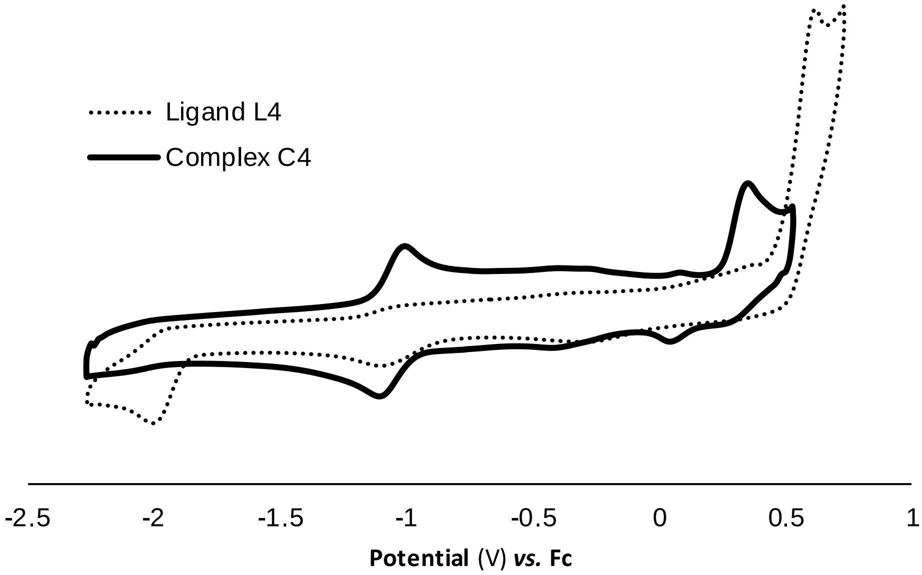

Figure A38. Cyclic voltammograms of **L4** (1 mM, dashed line) and **C4** (1 mM, solid line) in DMSO 0.1 M TBAP *vs.* Fc/Fc$^+$ at a scan rate of 100 mV/s.

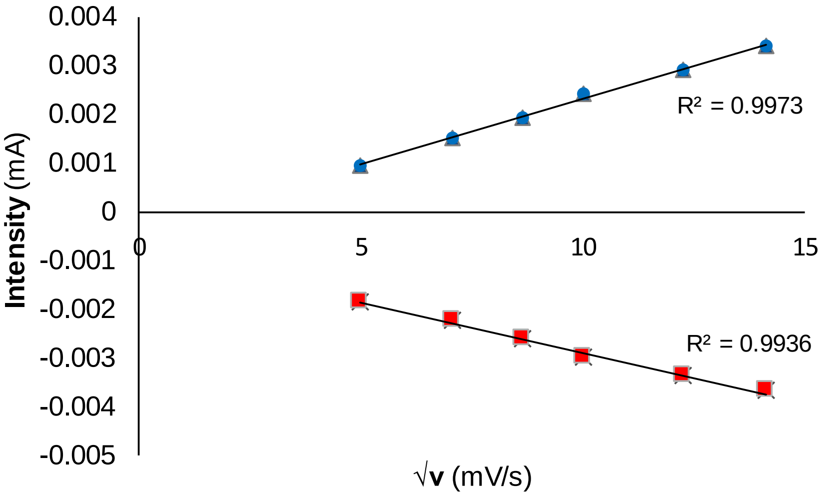

Figure A39. Linear plots of I_{pc} (red) and I_{pa} (blue) *vs.* the root square of the scan rate (*v*) for **C4** in DMSO with 0.1 M TBAP.

f) Biological assays for C4, C5

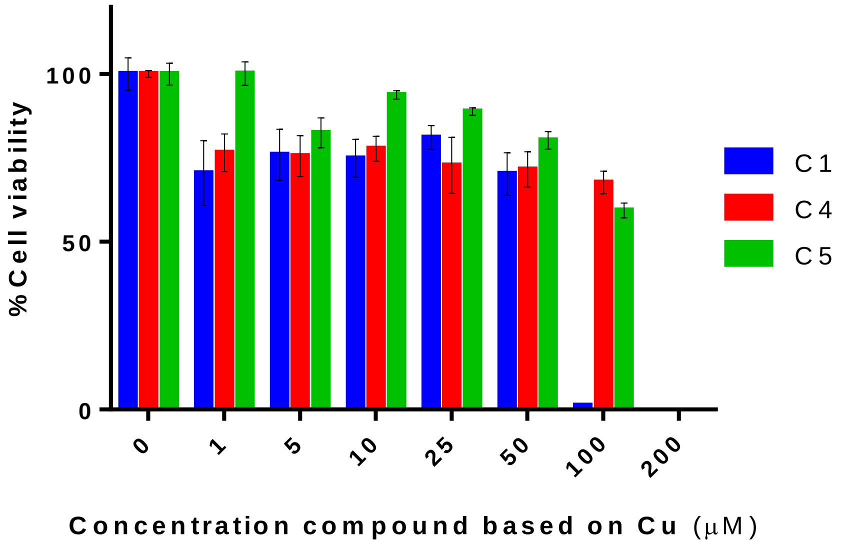

Figure A40. Cell-viability assays for **C1**, **C4** and **C5** at 24 h in HeLa cancer cells. Complexes concentrations were normalized based on Cu concentration.

ANNEX CHAPTER 5

a) (β-Ala)-TAT$_{49-57}$ and compound 17

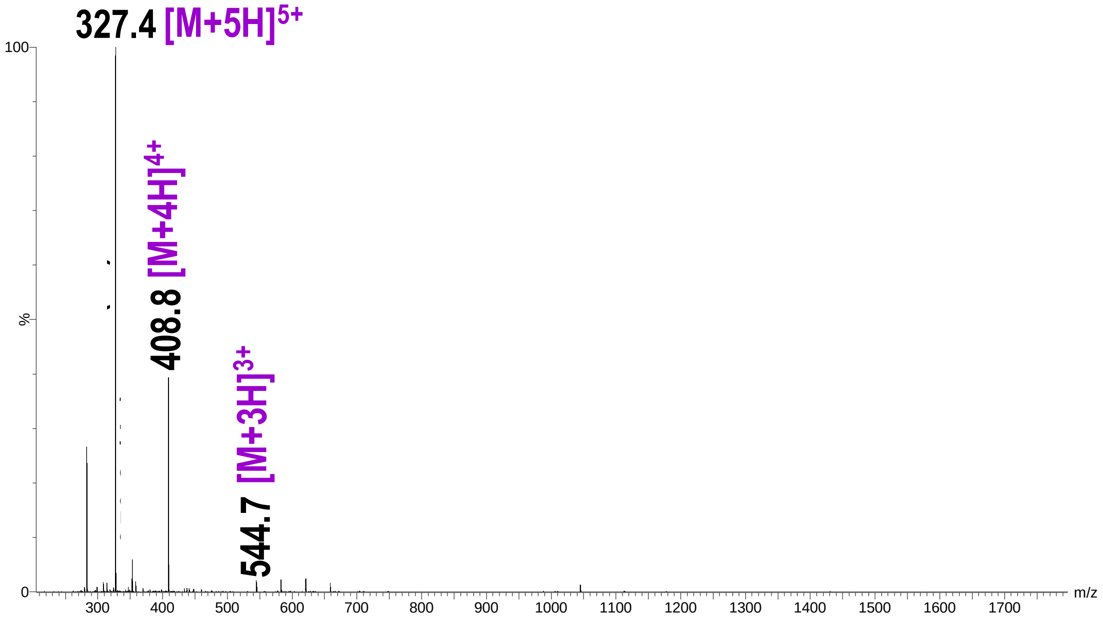

Figure A41. ESI-MS (ESI$^+$, H_2O-MeOH) of a cleaved and deprotected aliquot of **15**: Fmoc-(*β*-Ala)-TAT$_{49-57}$.

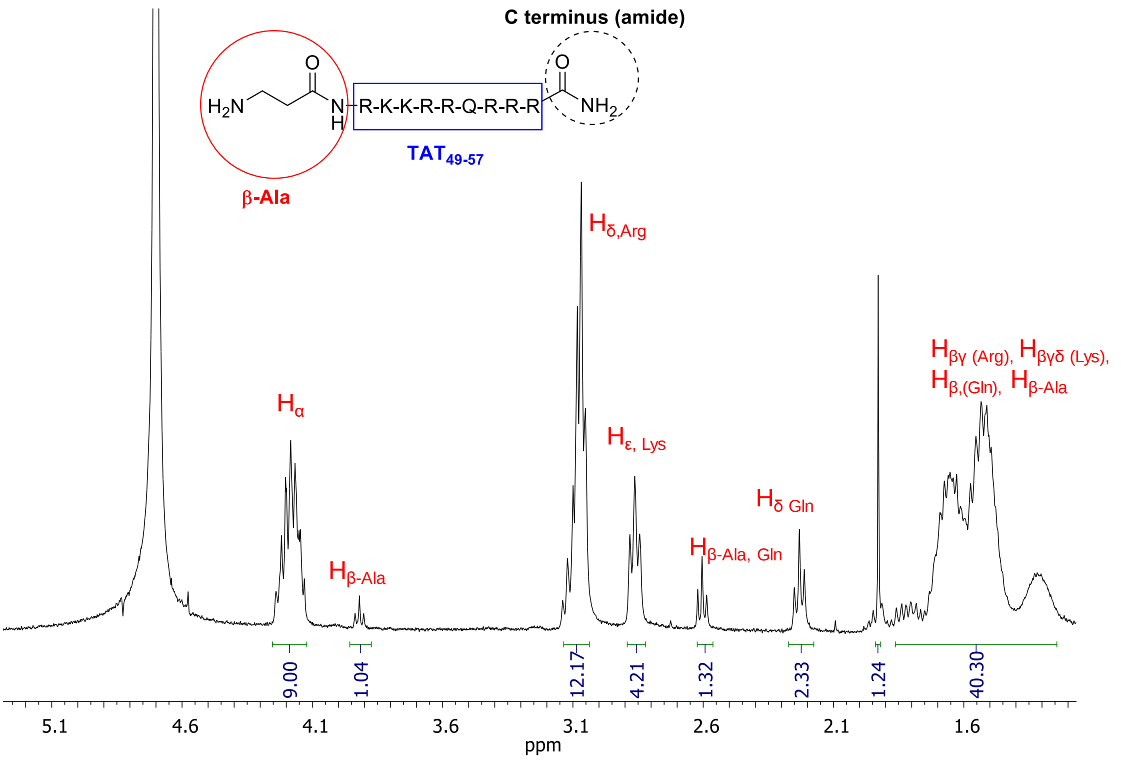

Figure A42. ^{1}H NMR (400 MHz, D_2O) of a cleaved and deprotected aliquot of **16**: (β-Ala)-TAT$_{49-57}$.

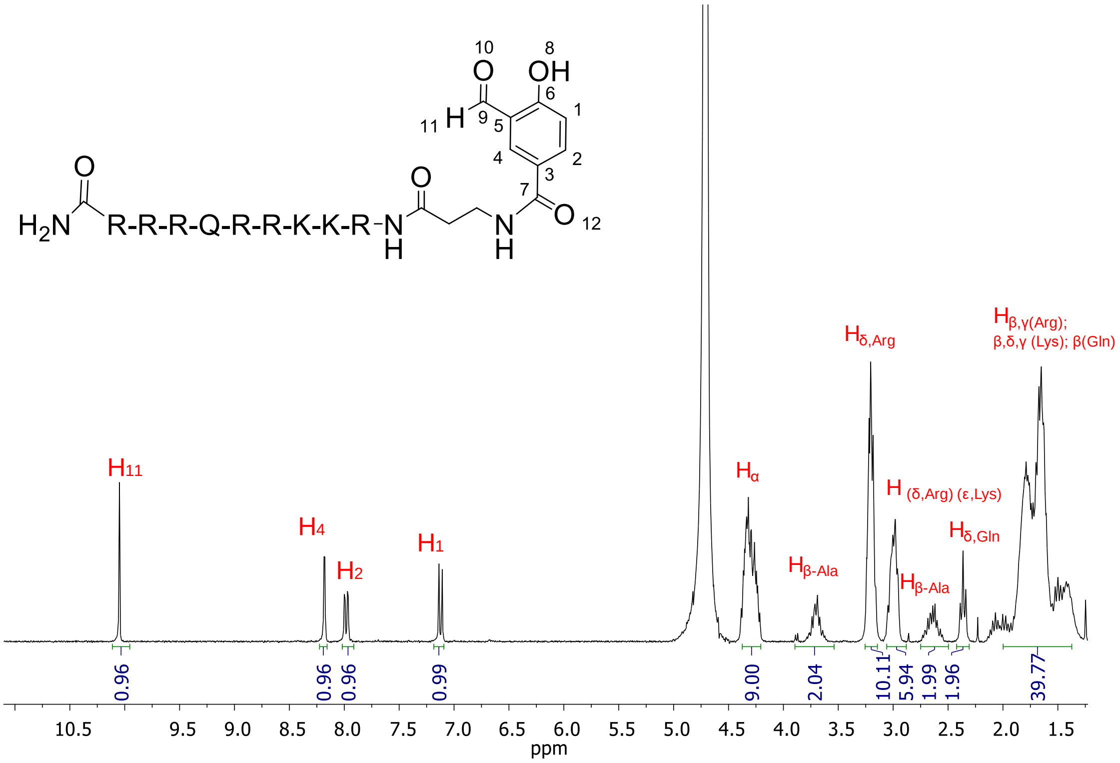

Figure A43. ^{1}H NMR spectrum (300 MHz, D_2O) of **17**.

b) R_9 and $(Gly)_4$-R_9 and precursors 19 and 21

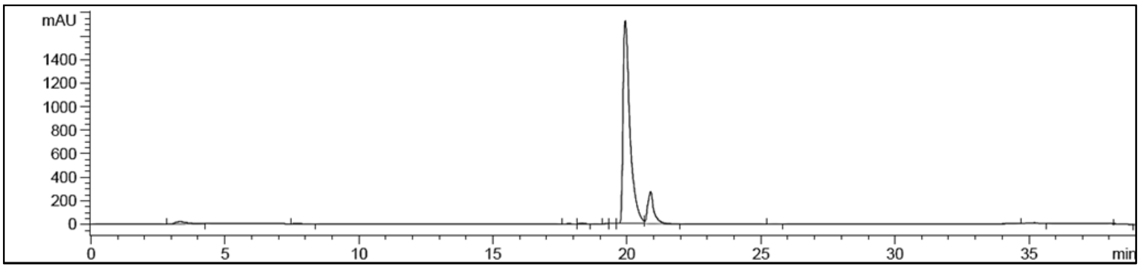

Figure A44. Analytical reversed-phase HPLC of Fmoc-protected R_9. Linear gradient of Solvent A (H_2O with 0.1% TFA) and Solvent B (Acetonitrile/H_2O/TFA (90:9.9:0.1%)): 0-50% Solvent B in 30 min. Absorbance at 220 nm was used.

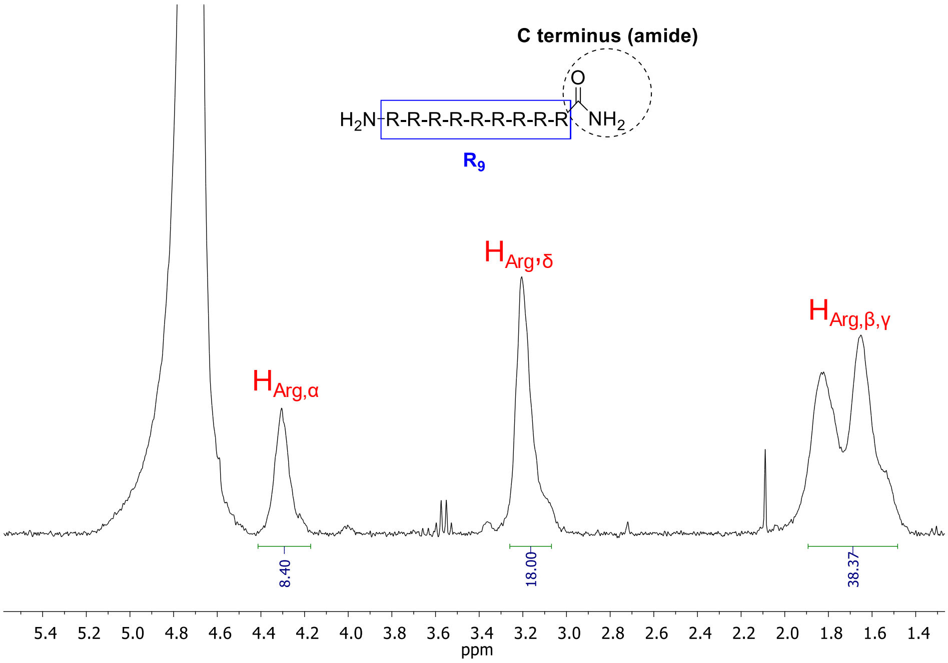

Figure A45. ^1H NMR (300 MHz, D_2O) of the R_9 peptide.

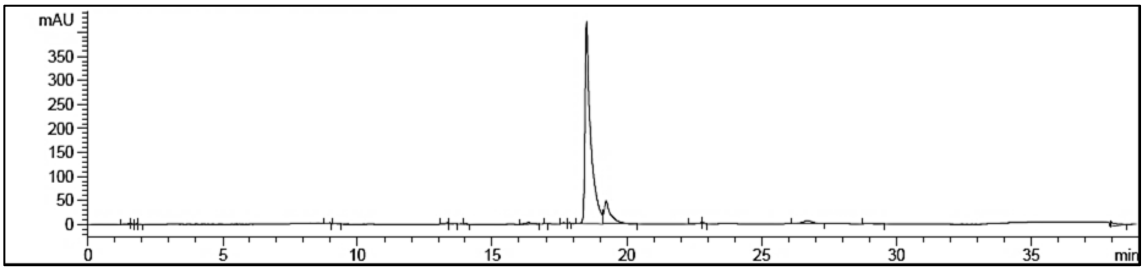

Figure A46. Analytical reversed-phase HPLC of Fmoc-protected $(Gly)_4$-R_9. Linear gradient of Solvent A (H_2O with 0.1% TFA) and Solvent B (Acetonitrile/H_2O/TFA (90:9.9:0.1%)): 0-50% Solvent B in 30 min. Absorbance at 220 nm was used.

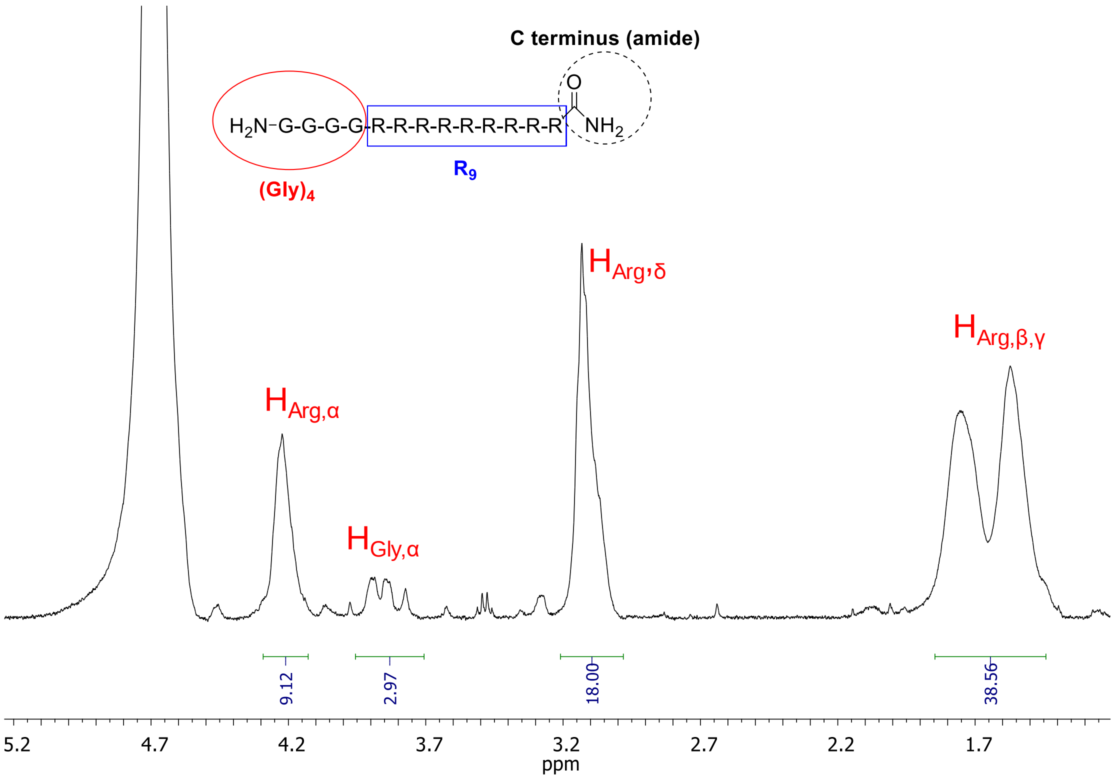

Figure A47. ^{1}H NMR (300 MHz, D_2O) of the $(Gly)_4$-R_9 peptide.

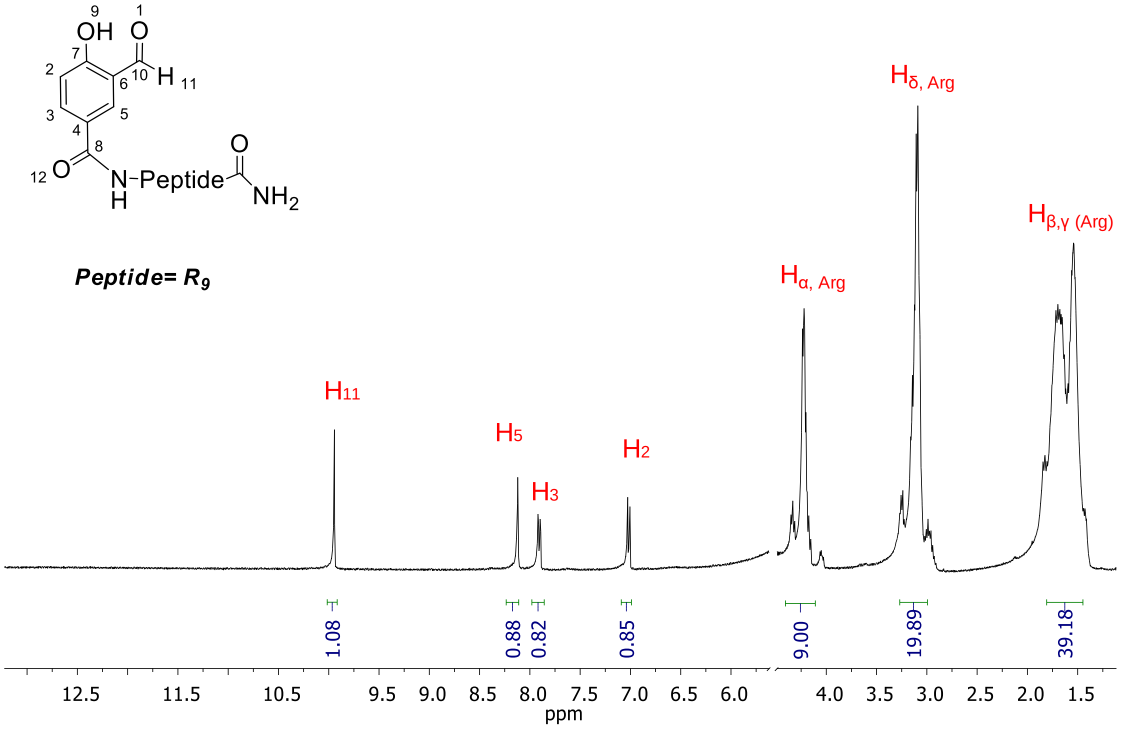

Figure A48. ^{1}H NMR spectrum (360 MHz, D_2O) of **19**.

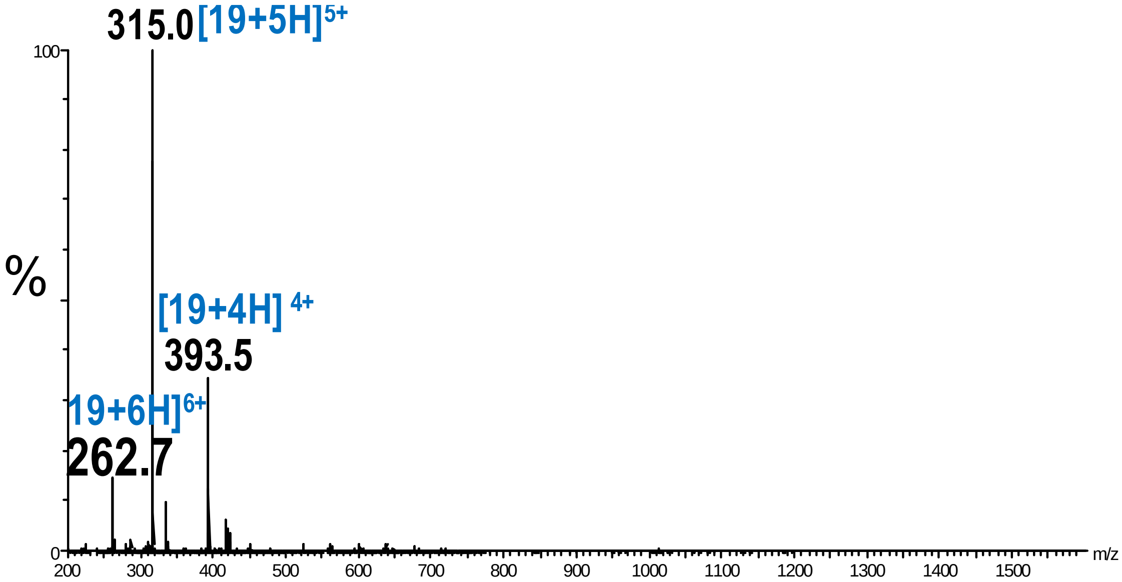

Figure A49. ESI-MS (ESI$^+$, H_2O-MeOH) of **19**.

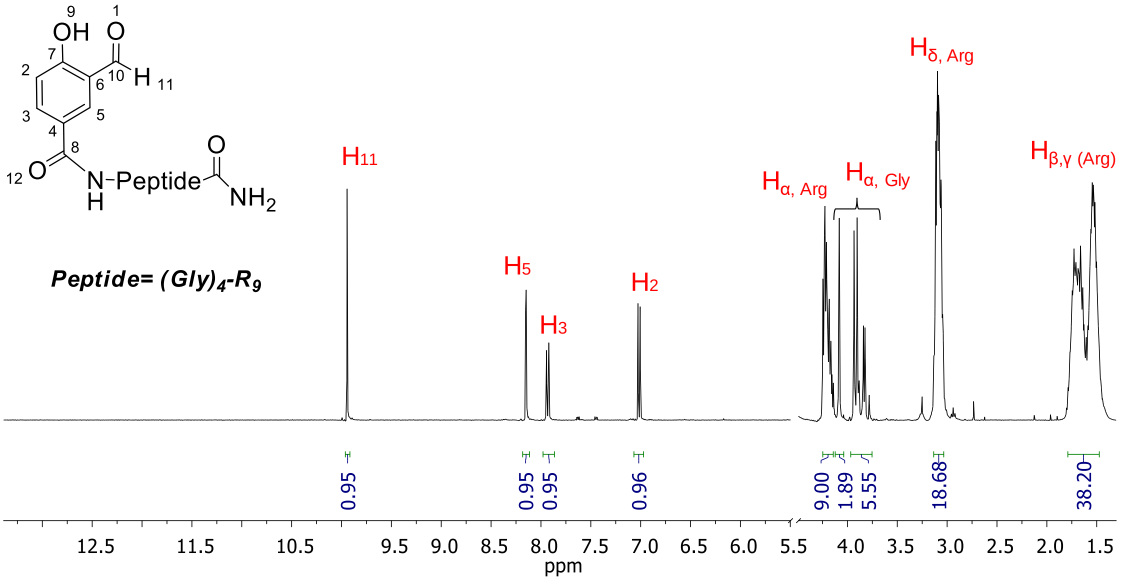

Figure A50. ^1H NMR spectrum (400 MHz, D_2O) of **21**.

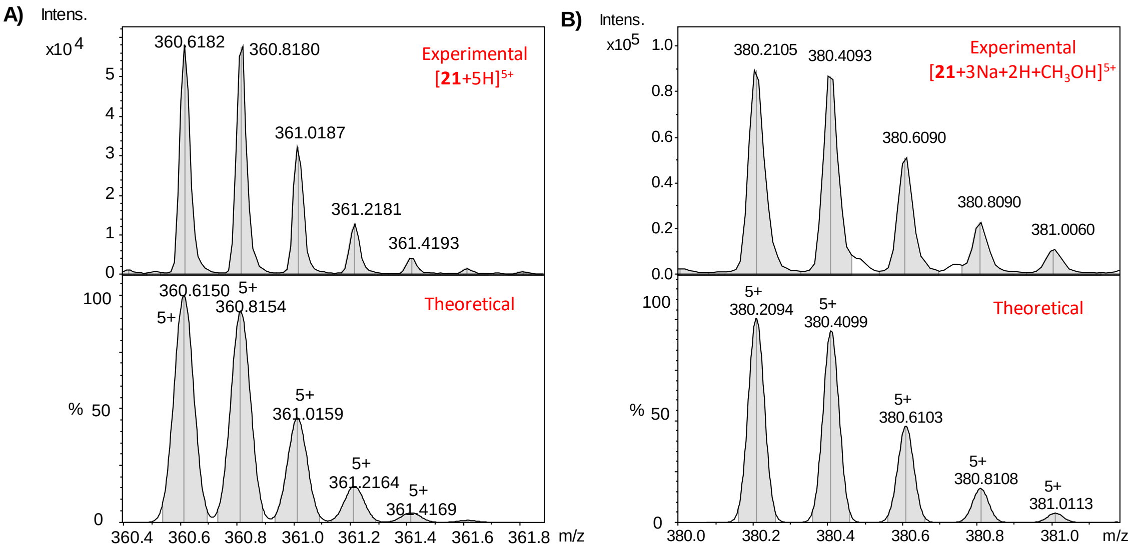

Figure A51. Experimental (top) and theoretical (down) HR ESI-MS (ESI$^+$, H_2O-MeOH) of (**A**) [**21**+5H]$^{5+}$ and (**B**) [**21**+3Na+2H+CH_3OH]$^{5+}$.

c) L6 and L7

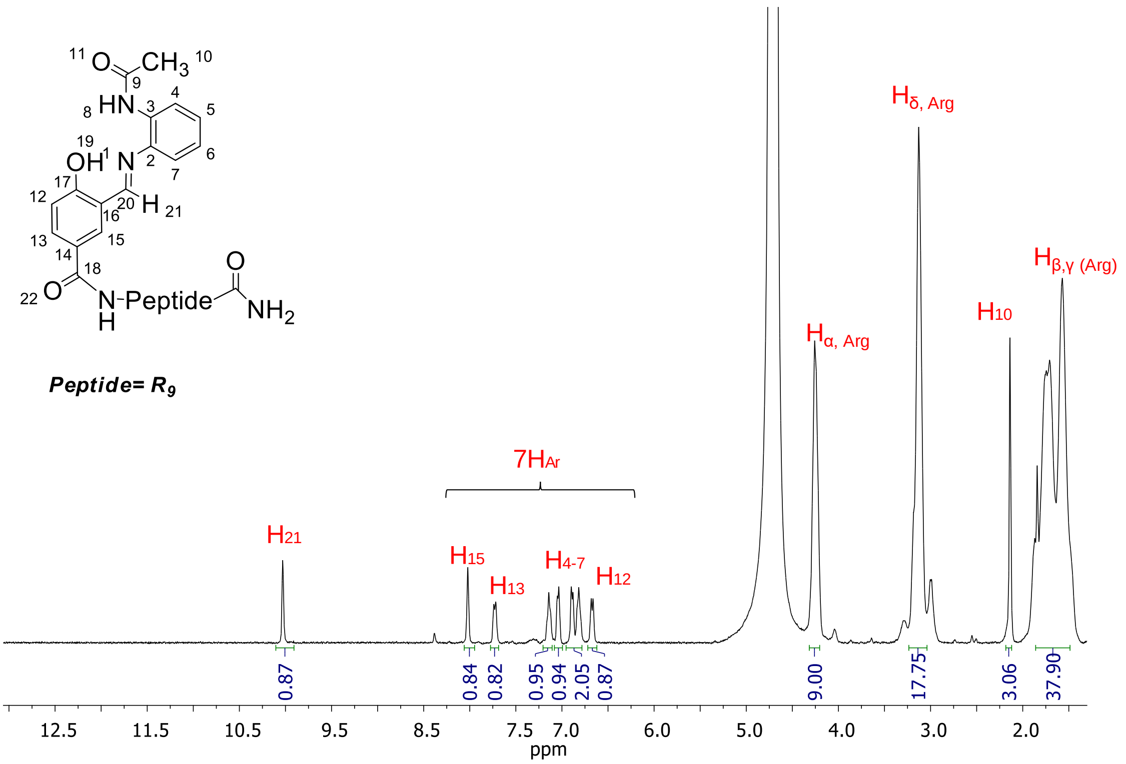

Figure A52. ^{1}H NMR spectrum (400 MHz, D_2O) of ligand **L6**.

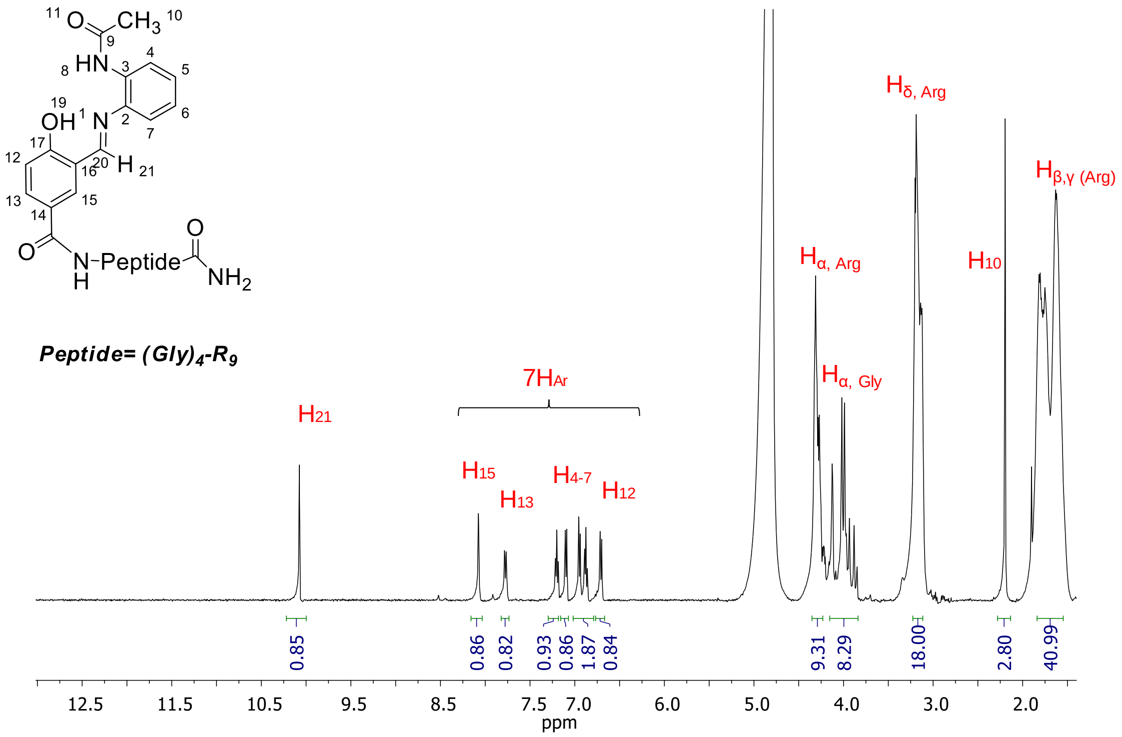

Figure A53. ^{1}H NMR spectrum (500 MHz, D$_2$O) of ligand **L7**.

d) C6 and C7

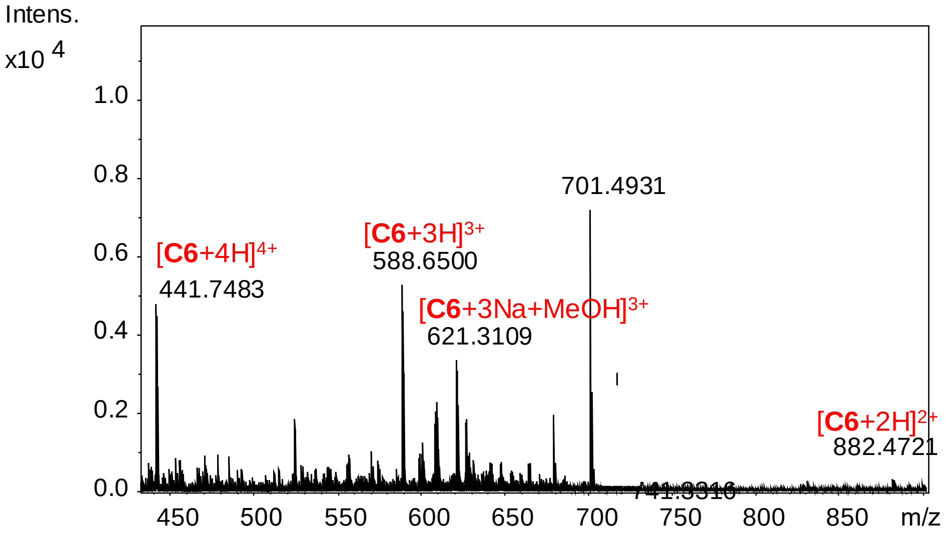

Figure A54. HR-MS (ESI$^+$, H$_2$O-MeOH) of **C6** in the range of m/z 400-900. Peaks at +2, +3 and +4 are indicated in the spectrum. In all the cases, **C6** represents the complex without the fourth coordinating molecule X (**Figure 5.12**).

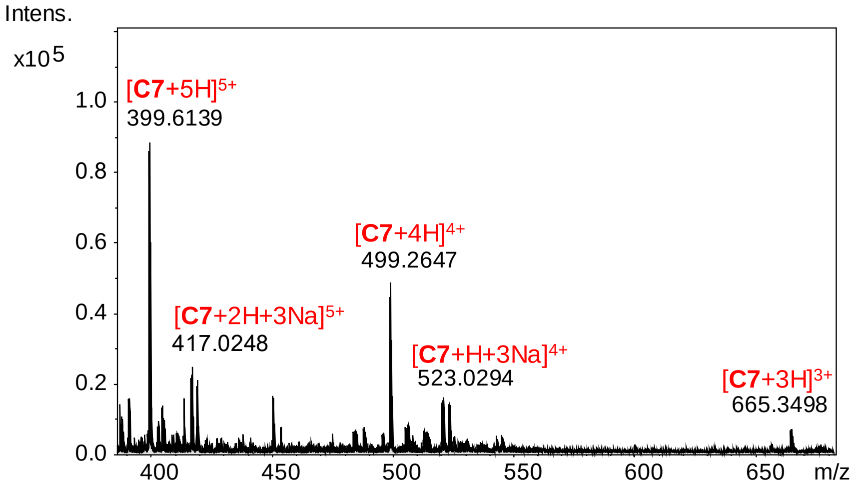

Figure A55. HR-MS (ESI$^+$, H_2O-MeOH) of **C7** in the range of m/z 350-700. Peaks at +3, +4 and +5 are indicated in the spectrum. In all the cases, **C7** represents the complex without the fourth coordinating molecule X (**Figure 5.12**).

e) Biological assays for C6 and C7

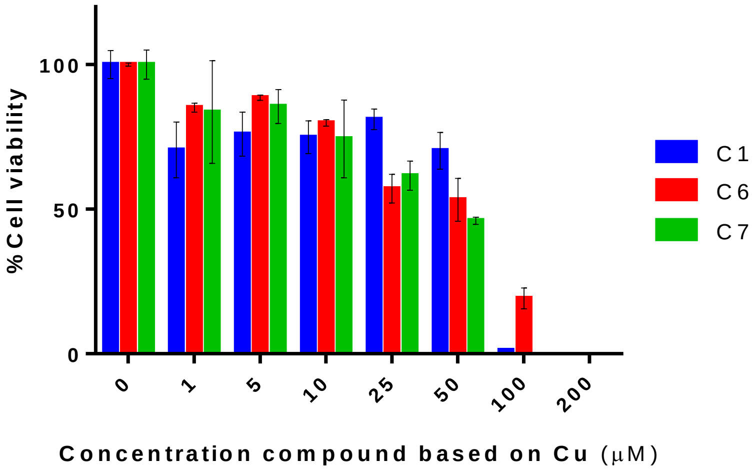

Figure A56. Cell-viability assays for complexes **C1**, **C6** and **C7** in HeLa cell lines after 24 h of treatment. Due to the putative presence of dimeric and monomeric forms of the different assayed complexes in the solid structure, concentrations of the tested compounds have been normalized based on the Cu concentration.

f) DTPA-5Ac

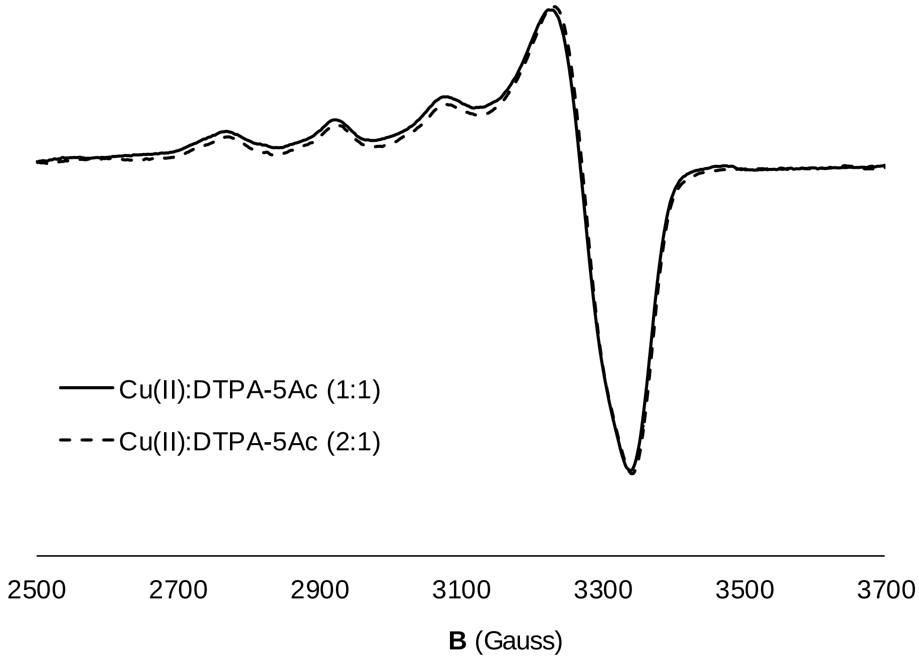

Figure A57. X-ESR band of DTPA-5Ac titrated with 1 (solid line) and 2 (dashed line) equivalents of Cu(II) at pH 7.2.

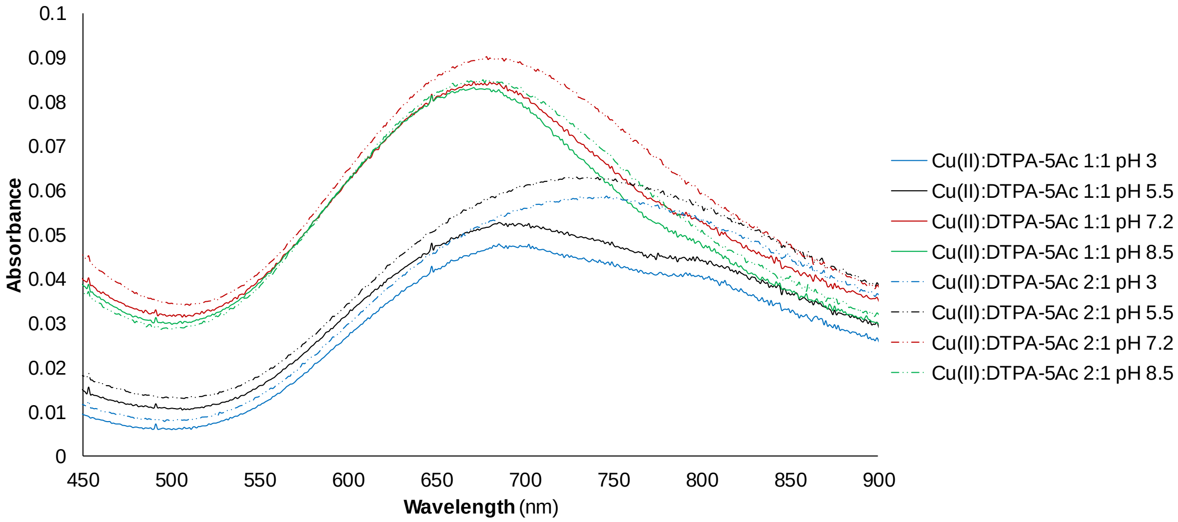

Figure A58. VIS DTPA-5Ac titration experiments with different equivalents of Cu(II) (1 equivalent, solid line; and 2 eq, dashed line) at different pH values.

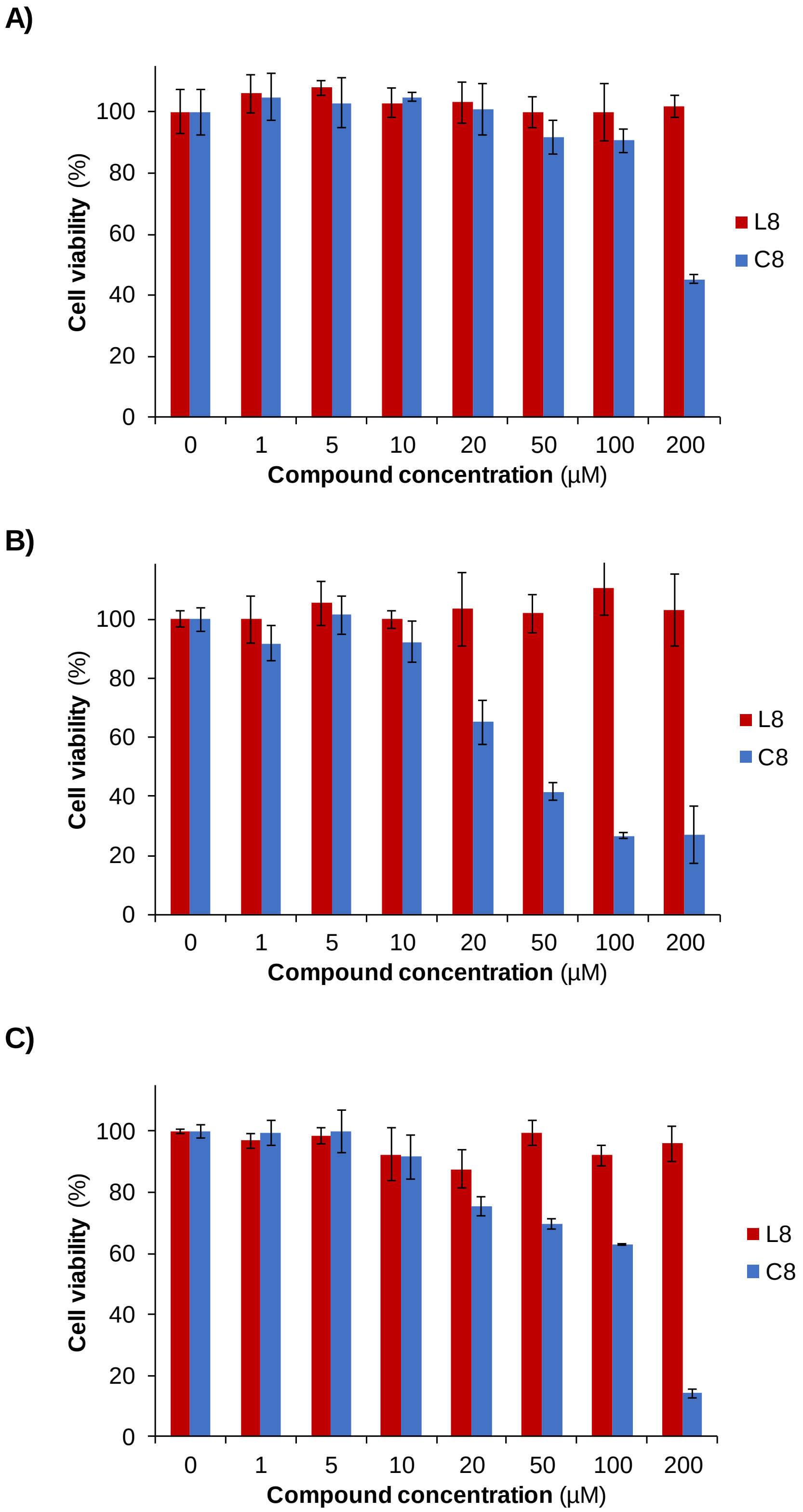

Figure A59. Cell-viability assays for DTPA-5Ac (**L8**) and its corresponding Cu(II) complex (**C8**) in HeLa (**A**), MCF7 (**B**) and NIH 3T3 fibroblasts (**C**) cell lines after 72 h of treatment.

g) DTPA-4Ac-NH$_2$ and precursor 23

A)

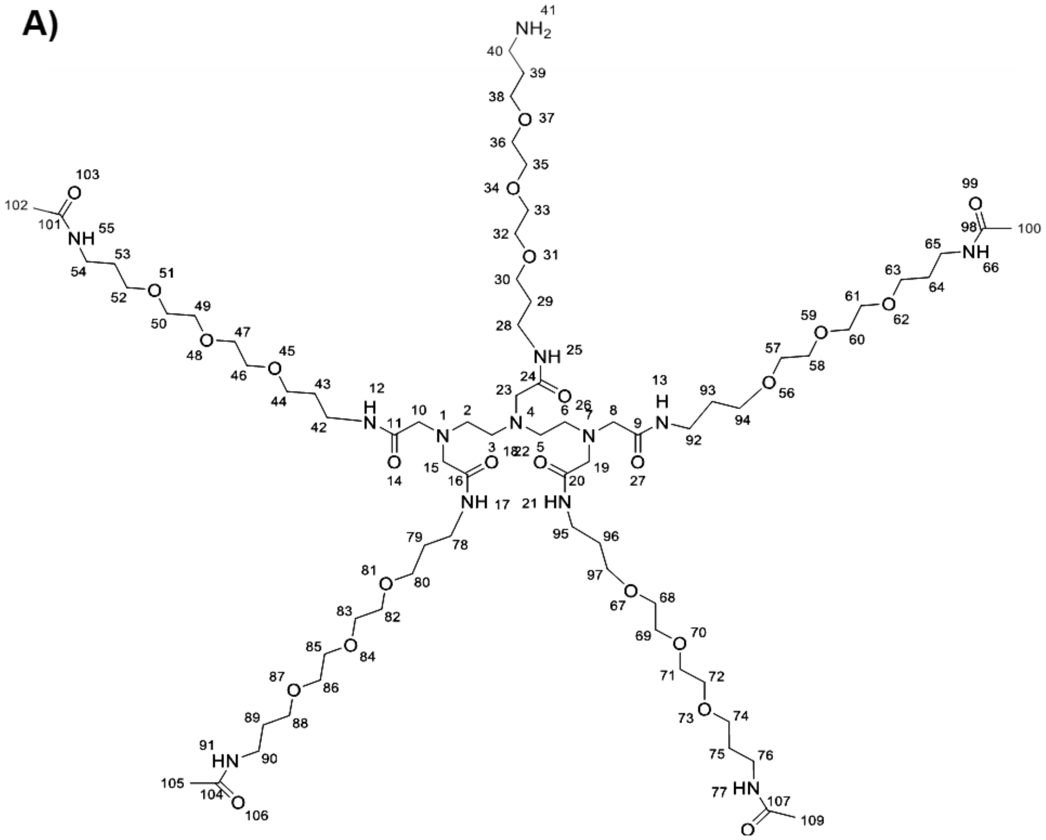

B)

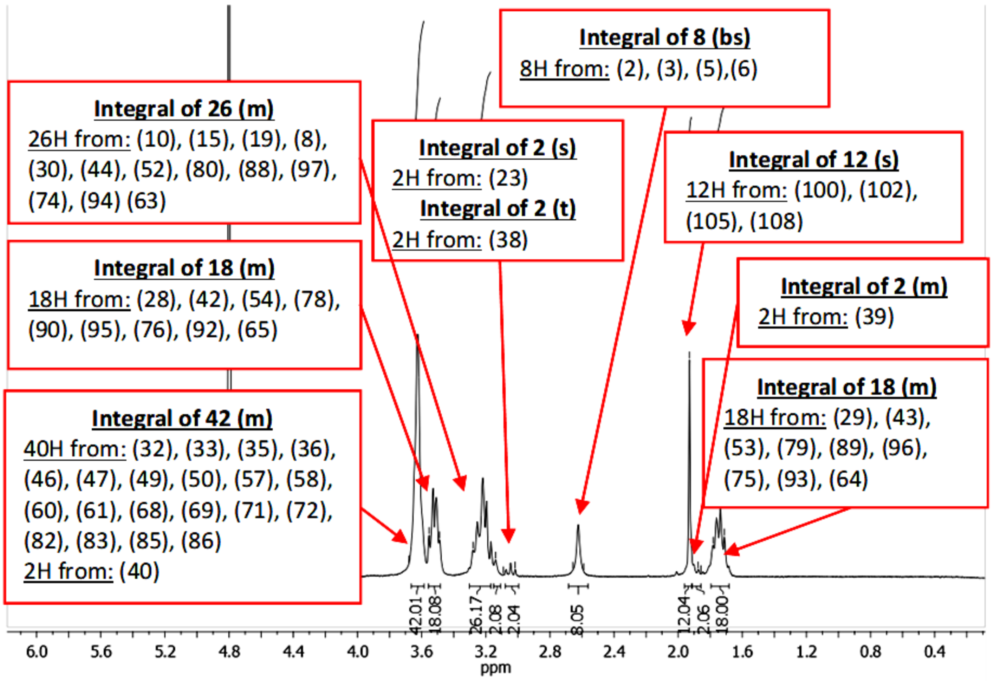
Integral of 26 (m)
26H from: (10), (15), (19), (8), (30), (44), (52), (80), (88), (97), (74), (94) (63)

Integral of 18 (m)
18H from: (28), (42), (54), (78), (90), (95), (76), (92), (65)

Integral of 42 (m)
40H from: (32), (33), (35), (36), (46), (47), (49), (50), (57), (58), (60), (61), (68), (69), (71), (72), (82), (83), (85), (86)
2H from: (40)

Integral of 2 (s)
2H from: (23)
Integral of 2 (t)
2H from: (38)

Integral of 8 (bs)
8H from: (2), (3), (5),(6)

Integral of 12 (s)
12H from: (100), (102), (105), (108)

Integral of 2 (m)
2H from: (39)

Integral of 18 (m)
18H from: (29), (43), (53), (79), (89), (96), (75), (93), (64)

Figure A60. (**A**) Structure of the DTPA-4Ac-NH$_2$ and (**B**) ^{1}H NMR spectrum (400 MHz, D$_2$O) of the DTPA-4Ac-NH$_2$.

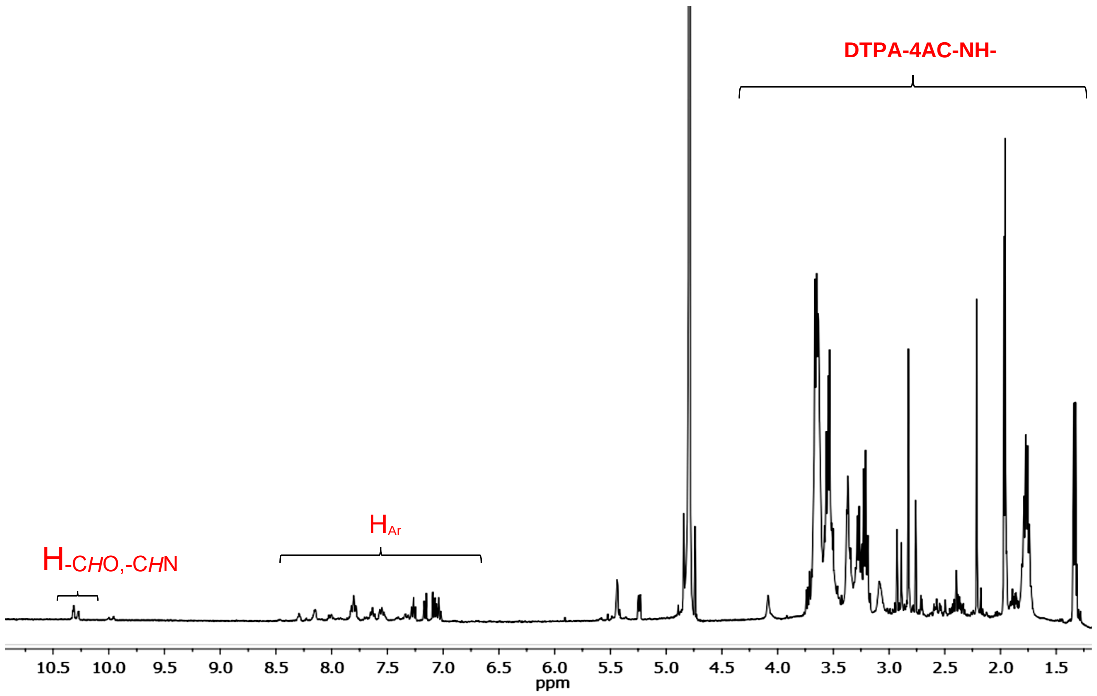

Figure A61. ^{1}H NMR (400 MHz, D_2O) of crude **22**.

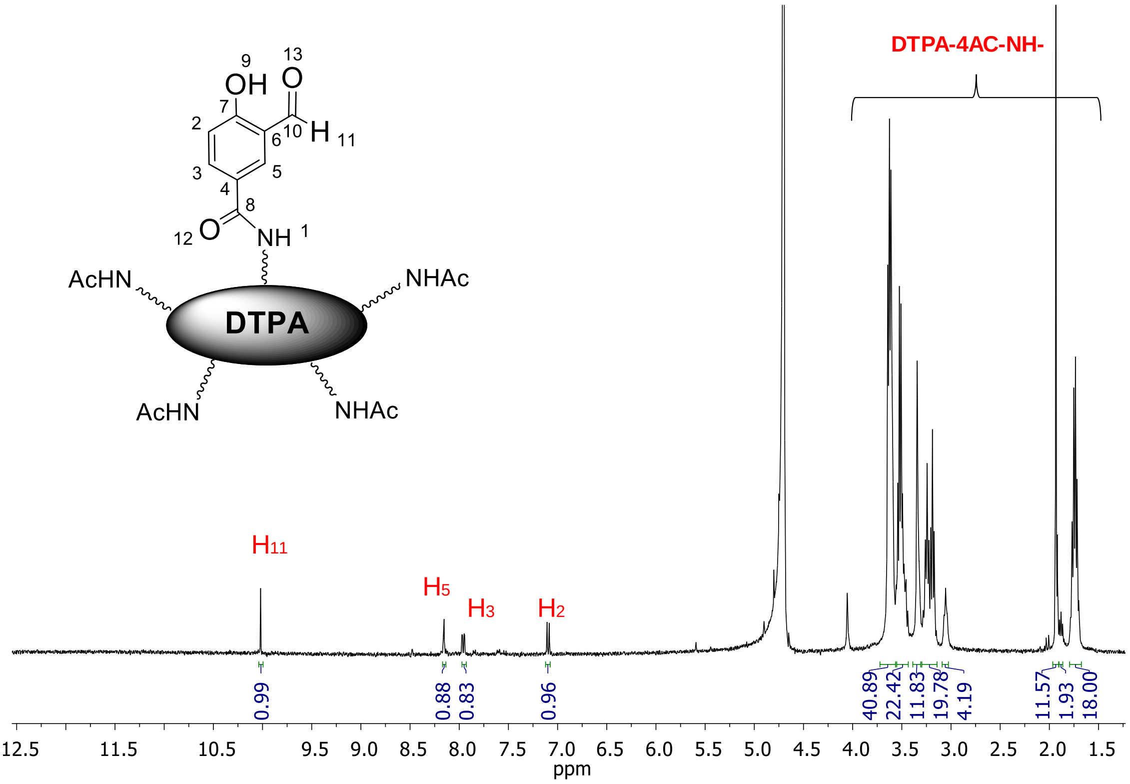

Figure A62. ^{1}H NMR spectrum (400 MHz, D_2O) of compound **23**.

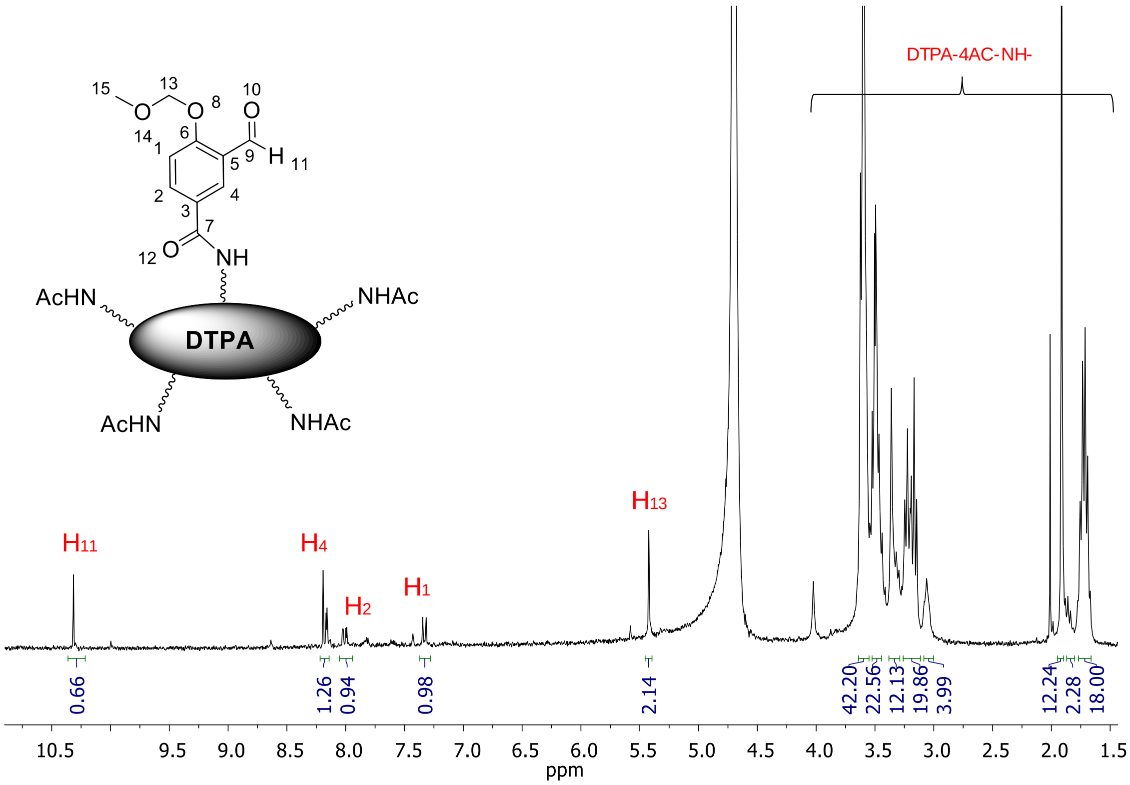

Figure A63. ^{1}H NMR spectrum (300 MHz, D_2O) of compound **22**.

h) Ligand L9 and Complex C9

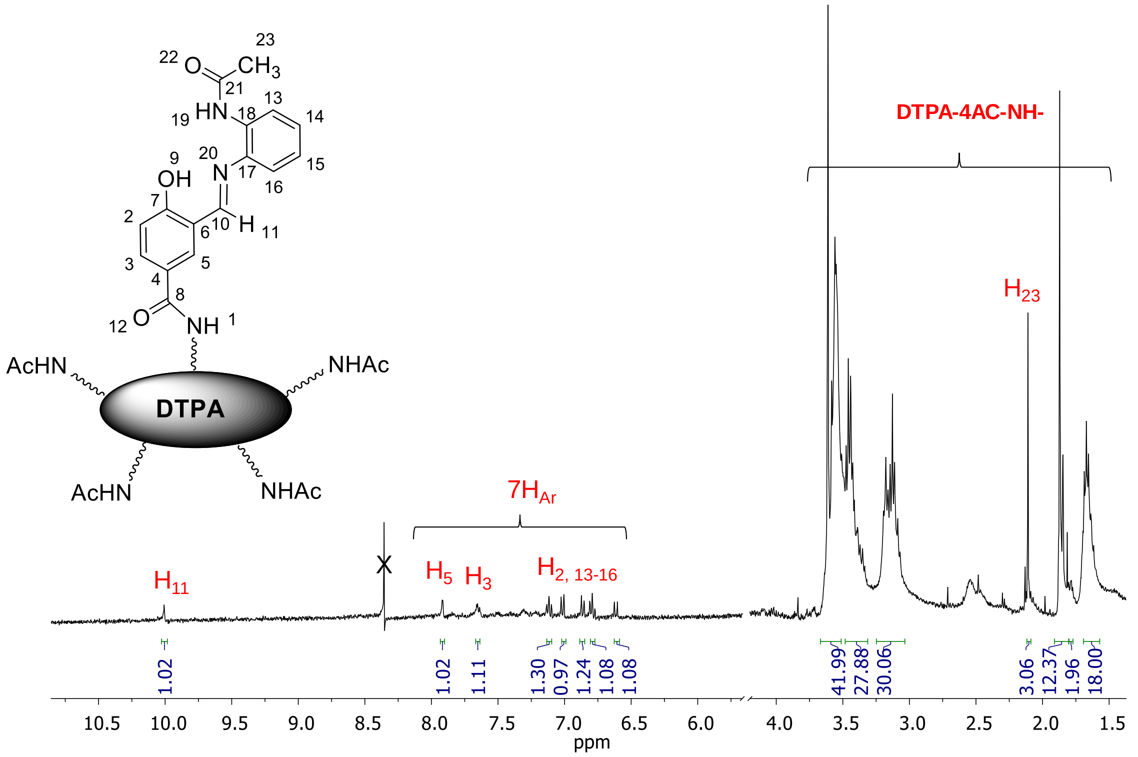

Figure A64. ^{1}H NMR spectrum (400 MHz, D_2O) of ligand **L9**.

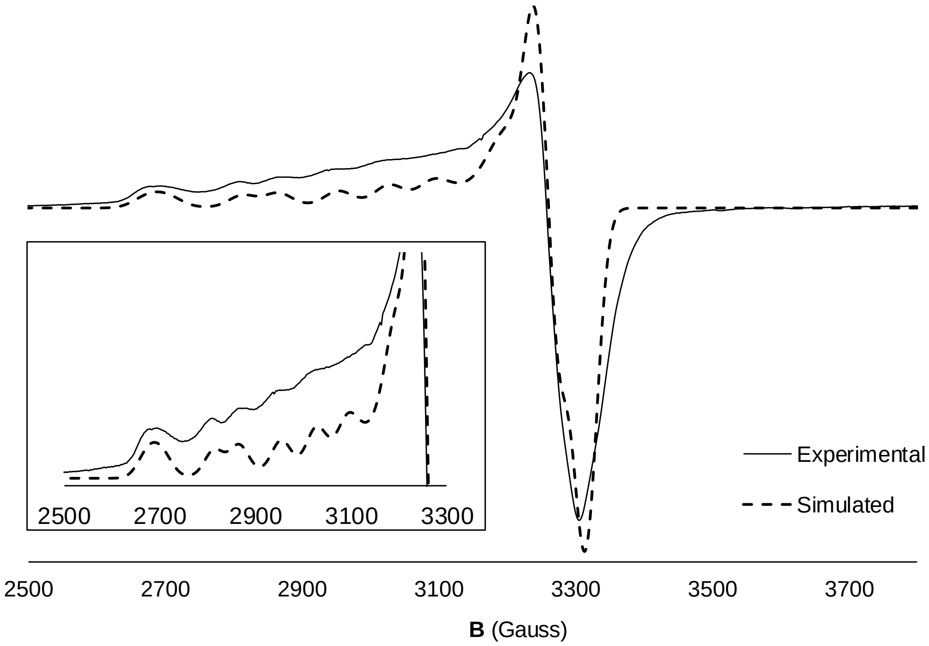

Figure A65. Experimental (solid line) and simulated (dashed line) X-ESR band of **C9** in DMSO solution.

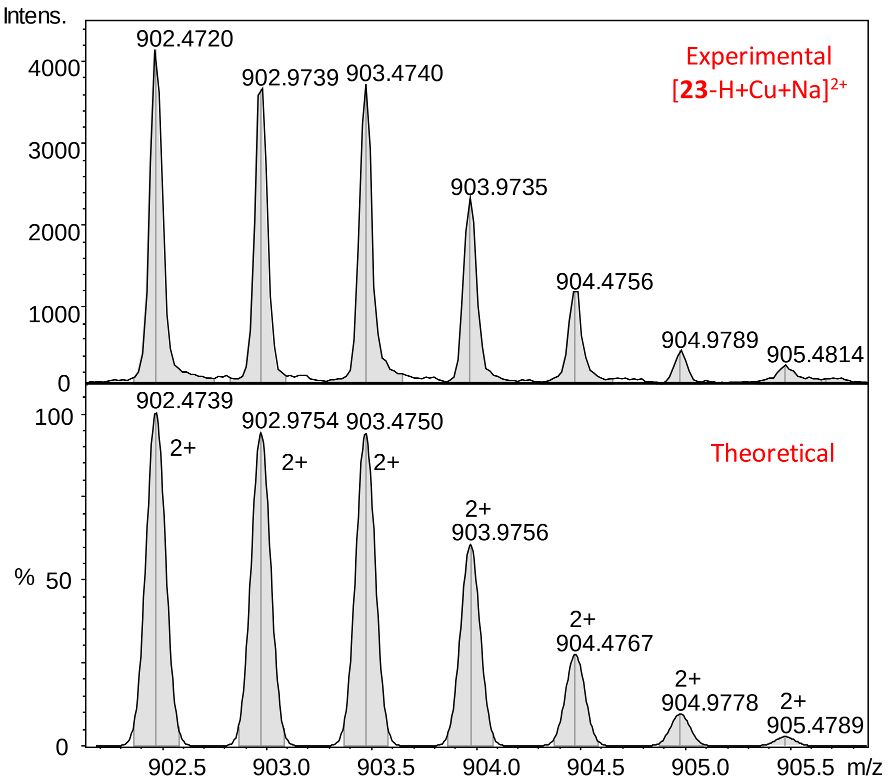

Figure A66. Experimental (top) and theoretical (down) HR-MS (ESI$^+$, MeOH-DMSO) of the peak corresponding to [**23**-H+Cu+Na]$^{2+}$ in the MS spectrum of complex **C9**.